High-resolution atomic force microscopy and current-voltage characterisation of DNA and protein complexes.

Davies, Emma

Davies, Emma (2006) *High-resolution atomic force microscopy and current-voltage characterisation of DNA and protein complexes..* thesis, Swansea University.
http://cronfa.swan.ac.uk/Record/cronfa42320

High-Resolution Atomic Force Microscopy and Current-Voltage Characterisation of DNA and Protein Complexes

A thesis submitted for the degree of Doctor of Philosophy in the
School of Engineering, University of Wales Swansea.

Emma Davies MPhys (Hons)

2006

DECLARATION

This work has not previously been accepted in substance for any degree and is not being concurrently submitted in candidature for any degree.

Signed... .... (Candidate)

Date ....22/12/06...........................

STATEMENT 1

This thesis is the result of my own investigations, except where otherwise stated. Other sources are acknowledged by footnotes giving explicit references. A bibliography is appended.

Signed....... .... (Candidate)

Date ....22/12/06............................

STATEMENT 2

I hereby give consent for my thesis, if accepted, to be available for photocopying and for inter-library loan, and for the title and summary to be made available to outside organisations.

Signed.... .... (Candidate)

Date ....22/12/06...........................

ABSTRACT

Using the technique of non-contact atomic force microscopy (NC-AFM), the structural properties of DNA and protein complexes were studied at the single-molecule level and at high-resolution. The electrical properties of these biomolecules were then investigated using an electrode setup. This work focussed on the visualisation of DNA strands, nucleosomes, PUT3 protein and DNA-PUT3 complexes and the effect of protein on the conductivity of DNA. NC-AFM experiments were performed in vacuum and results were compared to tapping-mode AFM (TM-AFM) experiments performed in air. The detailed structure of DNA strands 2-kilobase-pairs (kbp) in length, deposited on gold substrates, was observed for the first time using NC-AFM without the need for chemical-anchoring techniques. Measurements made on individual DNA molecules revealed a strand length of 700 nm which was in good agreement with the calculated length of 680 nm for a liner 2-kbp DNA molecule. The average height of the DNA was 1.37 nm compared to 2 nm as determined with X-ray crystallography. Images of nucleosomes on mica revealed unprecedented detail with line profiles indicating peaks of 3-4 nm corresponding to DNA wrapped twice around the nucleosome core. DNA-PUT3 complexes were observed using a very high spring constant cantilever for NC-AFM. The measured diameter of PUT3 was 70 nm with corresponding height ~11 nm. Similar diameters were recorded using TM-AFM but with lower height ~2-2.5 nm. The difference in height is possibly attributed to the non-invasive nature of NC-AFM compared to tapping-mode which may have compressed soft samples into the surface. Current-voltage (I-V) measurements were performed on DNA-PUT3 samples and those prepared in binding buffer gave elevated currents at +5 V (I = 73-115 nA) compared to samples containing an equivalent concentration of DNA prepared with water (I = 0.4-3.6 nA). The presence of binding buffer appeared to improve current readings possibly by interacting with molecules via ‘doping’ to give to metallic-DNA (M-DNA) or by promoting DNA-PUT3 complex formation. The preferential bonding of DNA-PUT3 complexes to gold electrodes is suggested as a possible interpretation.

ACKNOWLEDGEMENTS

I would like to express my gratitude to the supervisor of my studies, Prof. Steve P. Wilks, for giving me the opportunity to perform research work within the Multidisciplinary Nanotechnology Centre at Swansea. His guidance and encouragement have been invaluable. In addition, I am extremely grateful to Dr. Vincent Teng for his valuable advice, guidance and involvement throughout the entire research project. Many thanks go to Dr. Steve Conlan for his expertise in preparing samples, discussions of results and also the proof reading of this thesis. Thanks also to Adam Bowen and Deya Gonzalez for their involvement with the preparation of DNA samples, Dr Yumin Teng and Dr. Yachuan Yu at Cardiff for supplying sonicated chromatin samples and Prof. Richard Reece, Manchester for providing PUT3 samples. I thank Dr. Owen Guy for his assistance in preparation of gold substrates and Jeff Kettle for his expertise in the fabrication of gold electrodes. I must also thank the staff at the engineering department, particularly Mark Pritchard, Andrew Jardine and Steve Batcup for their professional advice and technical supports. Finally I'd like to thank my family and friends for their support and encouragement throughout the course of this work. The financial support of the Postgraduate Scholarship Award from University of Wales Swansea is gratefully acknowledged.

LIST OF FIGURES

2.1 Origin of DNA 8
2.2 Nucleotide structure 9
2.3 Nucleotide base-pairing 9
2.4 Polynucleotide chains 10
2.5 Watson Crick double-helix 11
2.6 PCR 12
2.7 PCR primers 13
2.8 Amino acid structure 15
2.9 Protein secondary structure 16
2.10 DNA-binding proteins 20
2.11 Chemical features of DNA grooves 21
2.12 Nucleosome structure 22
2.13 PUT3 schematic 24
2.14 Energy bands for metals, semiconductors and insulators 32
2.15 Atomic p_z orbitals in DNA 34
2.16 Mechanisms of charge transfer in DNA 35
2.17 Coupling of biomolecules to metal electrodes 39

3.1 Schematic of atomic forces 47
3.2 Interaction between two molecules 49
3.3 Frequency response of a dynamic cantilever 51
3.4 AFM instrumentation 52
3.5 Cantilever geometries 53
3.6 Tip geometries 55
3.7 A typical silicon probe 56
3.8 Measurement of cantilever deflections 57
3.9 Modes of AFM and tip-sample separations 58
3.10 Frequency modulation in NC-AFM 62
3.11 Frequency shifts in NC-AFM 62
3.12 Schematic of an oscillating cantilever 64
3.13 Piezoelectric scanners 68

4.1 NC-AFM of mica 71
4.2 TM-AFM of thin gold films 72
4.3 Fabrication process of flat gold substrates 72
4.4 NC-AFM of flat gold 73
4.5 Electron beam lithography 74
4.6 Plasmid DNA Map 77
4.7 AFM base plate 78
4.8 Photograph of STM/AFM system 79
4.9 AFM tip scanner 81
4.10 Cantilever tips for NC-AFM 81
4.11 Optical deflection for NC-AFM 83
4.12 Laser alignment 83
4.13 Photodiode output signal definition 84
4.14 Regulation of NC-AFM and feedback electronics 85

4.15 Optical deflection for TM-AFM 86
4.16 Amplitude modulation for TM-AFM 87
4.17 Feedback electronics for TM-AFM 88

5.1 STM of DNA on graphite and gold 92
5.2 Examples of others' STM images 93
5.3 TM-AFM of DNA networks on mica 94
5.4 TM-AFM of DNA strands on mica 95
5.5 NC-AFM of DNA network on mica 97
5.6 NC-AFM of DNA strands on mica 98
5.7 High-resolution NC-AFM of DNA strands 99
5.8 High-resolution NC-AFM of DNA network 10
5.9 NC-AFM of DNA strands on gold 104
5.10 Examples of others' AFM images of DNA 106
5.11 Examples of others' AFM images of nucleosomes 107
5.12 NC-AFM of single and di-nucleosomes 108
5.13 NC-AFM of nucleosome array 110
5.14 Schematic of PUT3 113
5.15 DNA-PUT3 recognition sites 114
5.16 NC-AFM of buffer 115
5.17 NC-AFM of PUT3 116
5.18 TM-AFM of PUT3 117
5.19 Histograms for PUT3 dimensions with TM-AFM 118
5.20 NC-AFM of DNA with buffer 119
5.21 NC-AFM of DNA with PUT3 120
5.22 DNA with PUT3, high spring constant cantilever 122
5.23 DNA with PUT3, high spring constant cantilever (2) 123
5.24 DNA with PUT3, high spring constant cantilever (3) 124
5.25 Histograms for PUT3 dimensions with NC-AFM 125
5.26 TM-AFM of DNA with protein on mica 126
5.27 TM-AFM of DNA with protein on mica (2) 127
5.28 TM-AFM of DNA with protein on gold 130

6.1 SEM images of gold electrodes 137
6.2 Optical microscope images of electrodes 138
6.3 AFM images of electrodes 139
6.4 AFM of SiO_2 140
6.5 AFM of electrodes with DNA 140
6.6 AFM of electrodes with DNA (2) 141
6.7 AFM of electrodes with DNA (3) 142
6.8 AFM of electrodes with DNA (4) 143
6.9 Setup for I-V measurements 144
6.10 Summary of current readings 146
6.11 I-V data for bare electrodes 147
6.12 I-V data for DNA 148
6.13 I-V data for DNA (2) 149
6.14 I-V data for DNA (3) 149
6.15 I-V data for protein 151
6.16 I-V data for DNA with protein mixed in water 152
6.17 I-V data for DNA with protein mixed in water (2) 152

6.18 I-V data for DNA with protein mixed in buffer 153
6.19 I-V data for DNA with protein mixed in buffer (2) 153
6.20 Results Tables 155

ABBREVIATIONS

dsDNA	Double-stranded Deoxyribonucleic Acid
A-DNA	Dehydrated DNA
B-DNA	Biologically significant DNA
M-DNA	Metallic DNA
kbp	Kilo-base pair
Gbp	Giga-base pair
PCR	Polymerase Chain Reaction
dNTP	Deoxy 'Nucleotide' Triphosphate
Taq	Thermus aquaticus
PUT3	Proline Utilization Transcription 3
CRYO-EM	Cryo-Electron Microscopy
SPM	Scanning Probe Microscopy
STM	Scanning Tunnelling Microscopy
AFM	Atomic Force Microscopy
NC-	Non-Contact
TM-	Tapping-Mode
AM	Amplitude Modulation
FM	Frequency Modulation
PSPD	Position-Sensitive Photodiode
VdW	Van der Waals
UHV	Ultra-High Vacuum
EBL	Electron Beam Lithography
Q-factor	Quality factor
TSG	Template-Stripped Gold
HOPG	Highly Ordered Pyrolytic Graphite
I-V	Current-Voltage

CONTENTS

Declaration i

Abstract ii

Acknowledgements iii

List of Figures iv

Abbreviations vi

Chapter 1: Introduction 1
- 1.1 General Introduction 1
- 1.2 Thesis Organisation 4
- 1.3 References 6

Chapter 2: Bio-Molecules for Bio-Electronics 7
- 2.1 Introduction 7
- 2.2 DNA 8
  - 2.2.1 Biological Importance 8
  - 2.2.2 Structure of Nucleic Acids 8
  - 2.2.3 The Double Helix 11
  - 2.2.4 Replication, Cloning and PCR 11
- 2.3 Protein 14
  - 2.3.1 Biological Role 14
  - 2.3.2 Structure of Proteins 14
  - 2.3.3 Levels of Organization 16
  - 2.3.4 Additional Properties 18
- 2.4 DNA-Protein Complexes 20
  - 2.4.1 General Description 20
  - 2.4.2 Nucleosomes 22
  - 2.4.3 Proline Utilization Trans-activator (PUT3) 23
    - 2.4.3.1 Structure 23
    - 2.4.3.2 Binding Conditions 25
- 2.5 Literature Review 26
  - 2.5.1 Current Methods of Structure Determination of Bio-Molecules 26
  - 2.5.2 SPM Studies of DNA 27
  - 2.5.3 Charge Transfer Studies of DNA 29
- 2.6 Theory of Conducting Polymers 31
- 2.7 Theory of Charge Transfer in DNA 33
- 2.8 Molecules-Substrate Coupling 37
- 2.9 Summary 41
- 2.10 References 41

Chapter 3: Scanning Probe Microscopy 45
- 3.1 Introduction 45
- 3.2 STM 45
- 3.3 Principles of Tip-Sample Forces 46
  - 3.3.1 Short-Range Interactions 47
  - 3.3.2 Long-Range Interactions 49
  - 3.3.3 AFM Imaging 50
- 3.4 AFM Instrumentation 52
  - 3.4.1 General Description 52
  - 3.4.2 The Force Sensor 52
    - 3.4.2.1 Cantilever Properties 53
    - 3.4.2.2 Tip Shape 54
    - 3.4.2.3 Signal Measurement 56
- 3.5 Modes of Operation 58
  - 3.5.1 Static AFM 59
  - 3.5.2 Dynamic AFM 59
    - 3.5.2.1 Amplitude Modulation 59
    - 3.5.2.2 Frequency Modulation 61
- 3.6 Additional Features 67
  - 3.6.1 Piezoelectric Scanners 67
  - 3.6.2 Vibration Isolation 68
  - 3.6.3 Data Analysis and Image Processing 68
- 3.7 Summary 69
- 3.8 References 69

Chapter 4: Experimental Techniques 70
- 4.1 Introduction 70
- 4.2 Substrate Preparation 70
  - 4.2.1 Mica 69
  - 4.2.2 Template-Stripped Gold 71
  - 4.2.3 Gold Electrodes 73
  - 4.2.4 Bio-Molecules 75
- 4.3 The Omicron VT Beam Deflection AFM 78
  - 4.3.1 General Description 78
  - 4.3.2 Sample and Tip Positioning 80
  - 4.3.3 Tip Scanner 80
  - 4.3.4 Feedback Control System 81
  - 4.3.5 AFM Electronics and Software 84
- 4.4 The Dimension 3100 AFM 85
  - 4.4.1 General Description 85
  - 4.4.2 Sample and Tip Positioning 86
  - 4.4.3 Feedback Control System 86
  - 4.4.4 AFM Electronics and Software 87
- 4.5 Summary 88
- 4.6 References 89

Chapter 5: Visualisation of Biological Molecules 90
5.1 Introduction 91
5.2 Sample Preparation 91
5.3 STM Studies of DNA on Graphite and Gold Substrates 94
5.4 AFM Studies of DNA on Mica Substrates 94
  5.4.1 TM-AFM Imaging 94
  5.4.2 NC-AFM Imaging 97
  5.4.3 Comparison of TM- and NC-AFM Imaging 101
5.5 High-Resolution NC-AFM Studies of DNA on Gold Substrates 103
5.6 High-Resolution NC-AFM Studies of Nucleosome Proteins 106
  5.6.1 Single and Di-Nucleosomes 107
  5.6.2 Array of Nucleosomes 110
5.7 AFM Studies of DNA-Binding Proteins 112
  5.7.1 Preparation of DNA, Protein and Buffer 110
  5.7.2 Imaging PUT3 115
    5.7.2.1 NC-AFM on Mica 115
    5.7.2.2 TM-AFM on Mica 117
  5.7.3 NC-AFM of DNA strands with Protein Binding Sites 118
  5.7.4 DNA with PUT3 Protein 119
    5.7.4.1 NC-AFM on Mica: Comparison of Normal and High Frequency Cantilevers 119
    5.7.4.2 TM-AFM on Mica 126
    5.7.4.3 TM-AFM on Gold 128
5.8 Summary 131
5.9 References 132

Chapter 6: Electrical Measurement of Biological Molecules 134
6.1 Introduction 134
6.2. Sample Preparation 135
  6.2.1 DNA and Protein 135
  6.2.2 Electrodes 136
6.3 AFM of Studies of Nano-Spaced Electrodes 139
  6.3.1 Bare Electrodes 139
  6.3.2 Electrodes with DNA 140
6.4 I-V Measurement of DNA-Protein Complexes 144
  6.4.1 General Description 144
  6.4.2 I-V Measurements 145
    6.4.2.1 Bare Electrodes 147
    6.4.2.2 Electrodes with DNA across Gap 148
    6.4.2.3 Electrodes with Protein and DNA across Gap 150
  6.4.3 Comparison of I-V Measurements 154
6.5 Discussion 159
6.6 References 160

Chapter 7: Conclusions 162
  Future Work 167

CHAPTER 1

Introduction

1.1 General Introduction

Silicon microchips provide the backbone of today's technology. They are products of momentous developments in electronics over the past four decades. At present fabrication of these microchips is big business and the worldwide silicon industry estimated at some $300 billion[1]. The number of transistors interconnected on an individual chip has grown to hundreds of millions from just a few tens of transistors and metal-oxide-semiconductor (MOS) transistors now measure a thousandth of their original size. In 1965, Gordon Moore made a famous prediction that the number of transistors on a single chip would double every two years. In actual fact, the average number of transistors doubled every 18 months. In 2005, the Intel "Itanium 2" processor contained some 410 million transistors each having a size of 45 nm, concentrated in a 3 cm^2 chip, processing hundreds of millions of commands per second[2]. In 2006, up-to-date figures reveal that the transistor with feature size ~30 nm is in high production with an average cost per transistor seven orders of magnitude less than those of size 10 μm forty years ago[1].

Although exponential growth is good news for chip manufacturers, it is unclear how long this miniaturisation trend can continue. It is increasingly difficult to fabricate smaller and smaller device components using conventional 'top-down' approaches to silicon-based devices. For example, traditional photolithography is physically limited by the wavelength of the radiation used. Furthermore device components have practical limits set by the emergence of current leakages (*i.e.* at small gate lengths) and parasitic effects (small contact sizes lead to higher contact resistances and problems with contact-to-gate capacitance). For nanoscale devices, these effects are disastrous if other factors are not scaled accordingly[1,3]. Even if improved fabrication methods allow device components to shrink, complications may still arise when actually trying to connect billions of tiny components. Since this economically-driven industry is continually pushing towards '*smaller, faster, cheaper*' devices and fundamental size limits do indeed exist, the future of silicon microchips is uncertain.

The timescale for implementation of drastically new materials in devices is estimated at 30 years[1] and therefore intense research is required during this time if alternatives to silicon are to be found and sufficiently developed.

Much research is indeed directed towards finding alternative materials and/or alternative fabrication methods to overcome these envisaged difficulties and to encourage the next micro-electronics revolution. Instead of shaping matter into smaller and smaller pieces as in 'top-down' processes, one interesting concept is to assemble devices using an interdisciplinary 'bottom-up' approach. This involves the placing of atoms and molecules precisely where needed, atom-by-atom or molecule-by-molecule using knowledge gained from biology, chemistry and physics. Indeed these 'bottom-up' approaches are elegantly demonstrated with uttermost complexity in the biological world as a result of billions of years of evolution. Nucleic acids assemble into chains several thousands of units long; pre-programmed molecular-based sequences of amino acids form complex proteins and information is processed in transcription of DNA sequences. Self-assembly is just one of the unique capabilities of biomolecules but is one that is being actively sought for exploitation in future nano-devices.

Materials for molecular wires are of particular interest. When one considers DNA as a potential candidate, the prospect of a self-assembling molecular wire having a diameter of just 2 nm becomes irresistibly attractive. DNA interactions can be reliably predicted such as the complementary base-pairing. The simple but effective properties of DNA ensure genetic information is efficiently stored and passed on to future generations via its precise replication. Significant developments in the biotechnology industry have given rise to superior handling of DNA and related molecules by predictable enzyme manipulation and automated methods that allow DNA sequences to be amplified in macroscopic amounts with relative ease. Of course biomolecules do have limitations and these may include a limited supply of initial materials, performance degradation at elevated temperatures and possibly poor structural performance over long time spans. Such issues may be overcome or even avoided in many applications if, for example, supplies of molecules are maintained, self-repair mechanisms are incorporated and the temperature of the environment is controlled. Novel techniques for studying structure and behaviour of biomolecules are becoming increasingly valuable. The revolution of scanning probe microscopy (SPM) allows physical and electrical properties of single molecules to be examined perhaps for the first time. Non-contact atomic force microscopy (NC-AFM) is one of the more recently developed modes of AFM operation where a cantilever tip is oscillated above the substrate in a UHV environment and does not make contact with the substrate under normal imaging conditions. Compared to other modes such as contact-mode and tapping-mode AFM which are performed in the repulsive force regime, non-contact mode uses the weak attractive tip-sample forces. In NC-AFM, samples are less prone to lateral forces caused by tip-sample interactions and the structural integrity of samples is maintained so that chemical modifications for fixation to substrate may not be necessary. The present level of knowledge in molecular biology and electronics implies bio-molecular electronics (or bio-electronics) is indeed a viable option and one worth pursuing[4,5,6]. It is envisaged that realistic design approaches based on bio-molecular structures interacting with external macroscopic structures will aid their subsequent implementation into electronic devices. Even if the inherent properties of molecules such as DNA are unsuitable, it may be possible to manipulate the structure and even metallize them since it is the self-assembling property of molecules that molecular electronics aims to exploit for wires, diodes, interconnects, switches, gates, transistors and sensors[7].

Charge transport properties of molecules do not only depend on those inherent to the molecule but also on external factors. For instance, the metal-molecule contact is targeted during charge injection before charge can be transferred along the structure core. The ideal molecule-substrate should not induce additional electrical barriers against electron transport at the interface.

The first step in considering bio-molecular components for future devices is to study their structural and electrical properties under non-physiological conditions. Countless experiments have been performed by others to measure the conductivity of DNA but no definitive answer has been unveiled. The general consensus is that conductivity is highly dependent on sample preparation, composition and method of probing[8]. In contrast, the number of reports considering the attachment of DNA to electrodes is relatively small in comparison to these other investigated factors. Electrode contacts that facilitate electron transport are highly desirable in all situations and since there may be some question as to whether the DNA molecule is actually in 'intimate' contact with metal electrodes further research is desirable. DNA-binding proteins bind site-specifically to DNA and may provide the necessary 'intimate' contact between DNA molecular wires and external substrates and electrodes.

To embark on such research, a detailed study into the underlying structures of DNA and proteins is performed. Non-contact AFM is the technique chosen for the study due to its high resolution capabilities and non-invasive nature. Since this is a relatively new technique especially in its application to bio-molecular analyses, experiments are performed on a variety of different samples to determine its overall capabilities. Results of well-known structures can be compared to those from more established methods (*e.g.* X-ray crystallography) and those lesser well-known can be correlated with that of recent journals. Naturally this study aids the development of appropriate techniques for successful structure analysis of single molecules. Such imaging studies are designed to provide an awareness of DNA's interactions with substrates and binding proteins and the accuracy to which data is recorded. To the knowledge of the author, research into the effect of proteins on the conductivity of DNA is a novel concept which makes use of the pre-programmed self-assembly of biomolecules. Therefore, the aim of the project is extended to perform current-voltage (I-V) measurements on DNA strands with protein molecules attached. This approach is very much in its infancy but ultimately such an approach may improve the nature of the DNA-electrode contact which may then affect the overall measurements of DNA's conductivity.

1.2 Thesis Organisation

Chapter 1 has presented a summary of the current state of miniaturization of semi-conductor devices to-date and addresses the problem of future fabrication processes. The objectives of this project were expressed, aiming to develop the techniques necessary for performing an in-depth, high-resolution study of single molecules and to determine their I-V characteristics. The project seeks to determine the feasibility of using protein anchoring groups for improvement of the DNA-electrode contact which then may affect the overall conductivity measured for DNA.

Chapter 2 explores the structure and roles of both DNA and protein and their present-day laboratory handling techniques. Their self-assembling properties are discussed alongside the anticipated advantages and possible disadvantages of incorporating them into nano-devices. A literature review of DNA electronics is provided and the current theories of DNA's charge transport are given.

Chapter 3 addresses the principles of Atomic Force Microscopy. Principles of atomic forces are described with their application to AFM. The theory of frequency and amplitude modulation for signal detection is given which govern non-contact and tapping-modes. The unique advantages particular to each mode are discussed and their suitable applications.

Chapter 4 describes the main experimental techniques of the project. Details concerning sample preparation are given as well as practicalities of AFM operation (VT Beam Deflection AFM and Dimension 3100 AFM systems) and their feedback mechanisms and the logging of experimental data.

Chapter 5 presents high-resolution imaging results of DNA, protein and DNA-protein complexes. The high-resolution capabilities of NC-AFM are demonstrated and data is compared with expected values of well-known structures. Preparation of lesser well-known samples is discussed, along with the difficulties encountered and the particular methods for overcoming them. Results of the imaging study are reviewed and compared with other techniques commonly used in structure analysis in molecular biology.

Chapter 6 presents results of electrical conductivity measurements made on DNA and protein structures. Electrodes are used in conjunction with such work and were fabricated with electron-beam lithography. These were subject to AFM analysis for verification of gap size and cleanliness. A comparison study is performed amongst the different samples and an in-depth discussion of results given.

Chapter 7 expresses the conclusion of this work. Results are discussed in terms of the overall success of the project. Future works are suggested which may build on the ideas and results presented in this thesis.

1.3 References

[1] Thompson, S.E. and Parthasarathy S. (2006) Moore's law: the future of Si microelectronics. Materials Today 9(6), 20-25.

[2] Wong, H. and Iwai H. (2005) The road to miniaturization. Physics World (Sept) 40-44.

[3] Ieong, M., Narayanan, V., Singh, D., Topol, A., Chan, V. and Zhibin, R. (2006) Transistor scaling with novel materials. Materials Today 9(6), 26-31.

[4] Niemeyer, C. (2000) Self-assembled nanostructures based on DNA: towards the development of nanobiotechnology. Curr. Opin. Chem. Biol. 4, 609-618.

[5] Cingolani, R., Rinaldi, R., Maruccio, G. and Biasco, A. (2002) Nanotechnology approaches to self-organized bio-molecular devices. Physica E 13, 1229-1235.

[6] Maruccio, G., Cingolani, R. and Rinaldi, R. (2004) Projecting the nanoworld: Concepts, results and perspectives of molecular electronics. J. Mater. Chem. 14, 542-554.

[7] Gu, O., Cheng, C., Gonela, R., Suryanarayanan, S., Anabathula, S., Dai, K. and Haynie, D.T. (2006) DNA nanowire fabrication. Nanotechnology 17, R14-R25.

[8] Di Ventra M. and Zwolak, M. (2004) DNA Electronics. Encyclopedia of Nanoscience and Nanotechnology, X, 1-19. www.aspbs.com/enn.

CHAPTER 2

Bio-Molecules for Bio-Electronics

2.1 Introduction

The organisation of biological molecules in space influences their behaviour. Once it is known it may be possible to predict their reactions and apply it to different situations. Individual biological molecules that are relatively well understood in the biological world may provide a solution to the problems associated with nano-fabrication of electronics devices. Compared with traditional semiconductor electronics which is based on the behaviour of atoms, biological macro-molecules self-assemble using sophisticated molecular machinery and contain many diverse structural motifs. Fundamental mechanisms of charge transport will also depend on the molecule's organisation in space and so it vital to firstly determine their structure. The strand-like nature of DNA implies it may be suited for a molecular wire. Studies into DNA's conductivity have already been performed by others and a myriad of results have been reported. It appears that DNA's conductivity is very much dependent on factors such as sample composition and choice of experimental apparatus.

Protein is a second potentially useful component for nano-devices. Proteins exist with different electronic charges and in principle one could utilise or even 'engineer' its properties in a future design process. Protein's affinity for particular substrates could possibly be controlled by inducing conformational changes or by shifting its native charge.

In this chapter, the structural aspects of DNA and protein are addressed which are paramount for their understanding in nanoscience, a literature review of others' work is performed regarding the current theories of charge transfer in DNA, and the effects of molecule-substrate contact are discussed. This chapter aids interpretation of scanning probe microscopy (SPM) results and provides the background necessary for investigating DNA's conductivity.

2.2 DNA

2.2.1 Biological Importance

Deoxyribonucleic Acid (DNA) is the storage medium for genetic information[1,2]. It is typically found in the nucleus of human cells where it undergoes many degrees of coiling as shown in Figure 2.1. Strands are protected and preserved for maximum space efficiency and stability.

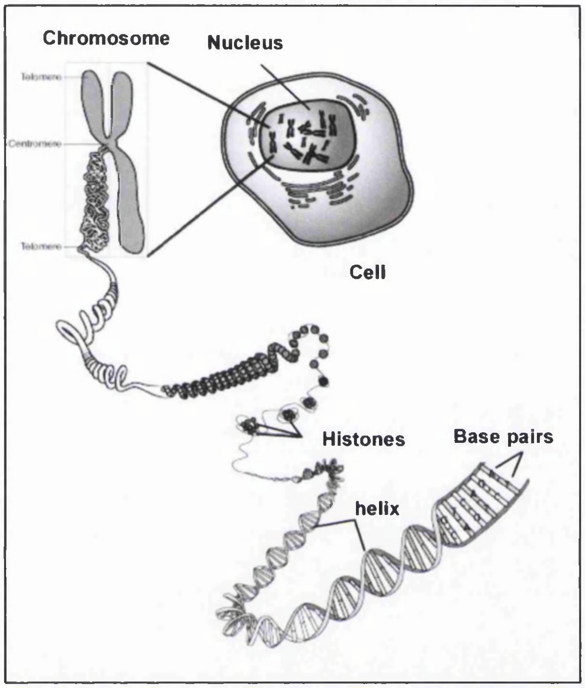

Figure 2.1. DNA is typically found in the nucleus of cells and associates with basic histone proteins during its compaction into the nucleus.

Genetic information encoded in the chemical language of DNA contributes to all organisms' physiological, anatomical properties and behavioural characteristics and therefore preservation of DNA sequences is crucial.

2.2.2 Structure of Nucleic Acids

DNA is a linear unbranched polymeric structure made from monomeric subunits or nucleotides[1,3]. Each nucleotide consists of a phosphate group, a 2′-deoxyribose (a 5-carbon sugar) and one of four nitrogenous bases (Figure 2.2). Note that *nucleoside* refers to the base-sugar combination only. A numbering terminology is derived from carbon atoms in the sugar ring: the sugar is a pentose composed of five carbon atoms numbered 1′, 2′ … (Fig. 2.2A). For DNA, '2′ -deoxyribose' indicates that this particular sugar is a derivative of ribose but the hydroxyl (-OH) group attached to the 2′ -carbon of ribose has been replaced by a hydrogen (-H) group. The four bases are adenine (**A**), cytosine (**C**), guanine (**G**) and thymine (**T**) (Fig. 2.2B).

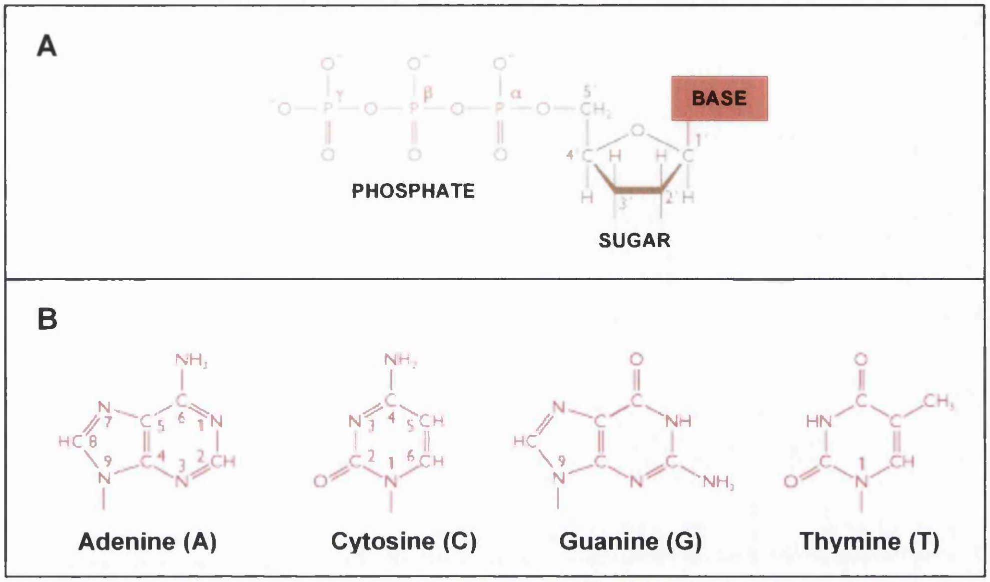

Figure 2.2. (A) The nucleotide consists of a phosphate group, a sugar and a base. (B) In DNA, the four bases are A, C, G and T.

Adenine and guanine are purine bases and contain a double-ring made of carbon and nitrogen. Cytosine and thymine are pyrimidine bases and are single-ringed. Purines and pyrimidines differ in their number and placement of hydrogen bond donor and acceptor groups thereby giving bases unique structural identities to serve as genetic information. The carbon and nitrogen atoms in the pyrimidine and purine rings are numbered 1 to 6 and 1 to 9 respectively. Figure 2.3 shows hydrogen bonding which takes place between complementary bases: **A** pairs with **T** and **C** pairs with **T**.

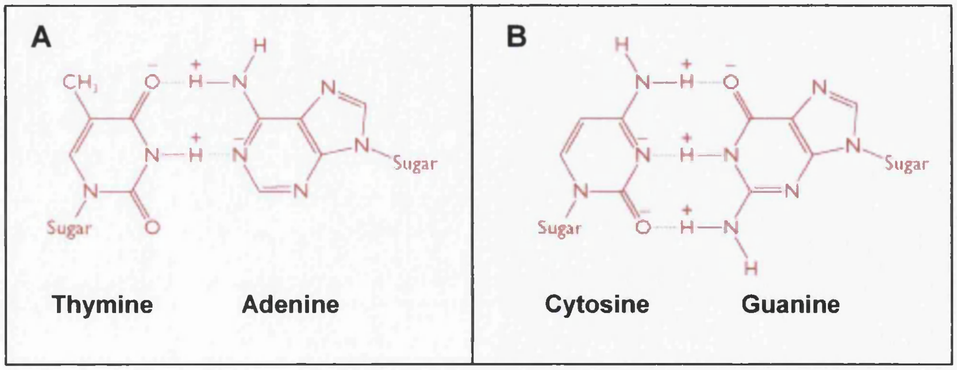

Figure 2.3. Complementary base-pairing of nucleotides. (A) T bonds with A via two hydrogen bonds. (B) C bonds with G via hydrogen three bonds.

Carbonyl oxygens and ringed nitrogens provide hydrogen bond acceptors for the amino groups' hydrogen bond donors. Bonding between bases **G** and **C** is more stable than **A** and **T** as one more hydrogen bond is involved. The aromatic nature of the bases means they are rigid planar molecules which allow uniform stacking within the helix. Such stacking provides protection for the chemical identity of bases. The presence of phosphate groups in DNA gives it an overall negative charge when in solution at physiological pH.

Nucleotides are linked through phosphodiester bonds to form polynucleotides. A single DNA chain begins with a free phosphate group at the 5′ carbon of the deoxyribose ring; additional nucleotides join via phosphodiester bonds linking hydroxyl groups at the 3′ carbon atom of one sugar with the phosphate 5′ carbon atom of a neighbouring sugar; the chain ends in a free hydroxyl group at the 3′ carbon in the last sugar. By convention DNA sequences are written in the 5′-to-3′ direction. Two polynucleotide chains are wound around each other creating an antiparallel double-stranded helix. One polynucleotide chain runs in the 5′-to-3′ direction while the second runs in the 3′-to-5′ direction (Figure 2.4).

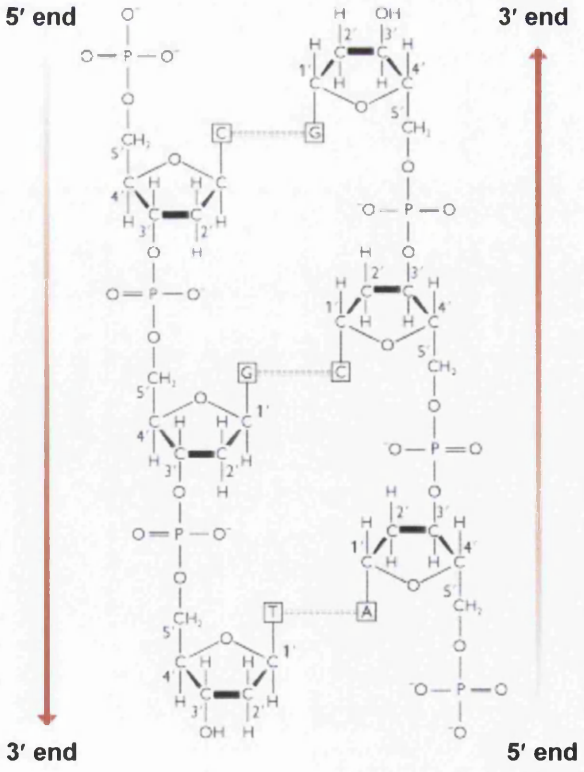

Figure 2.4. Two polynucleotide chains are wound around each in an antiparallel helix.

2.2.3 The Double Helix

James Watson and Francis Crick first proposed the double helix structure for DNA in 1953[4] (Figure 2.5). This is B-DNA, a right-handed helix which is the most common conformation and probably the most biologically significant[2]. The two linear polynucleotide chains are coiled in anti-parallel fashion around a central axis so that each base lies perpendicular to the axis and is covalently bound to the backbone and hydrogen-bonded to its complementary counterpart.

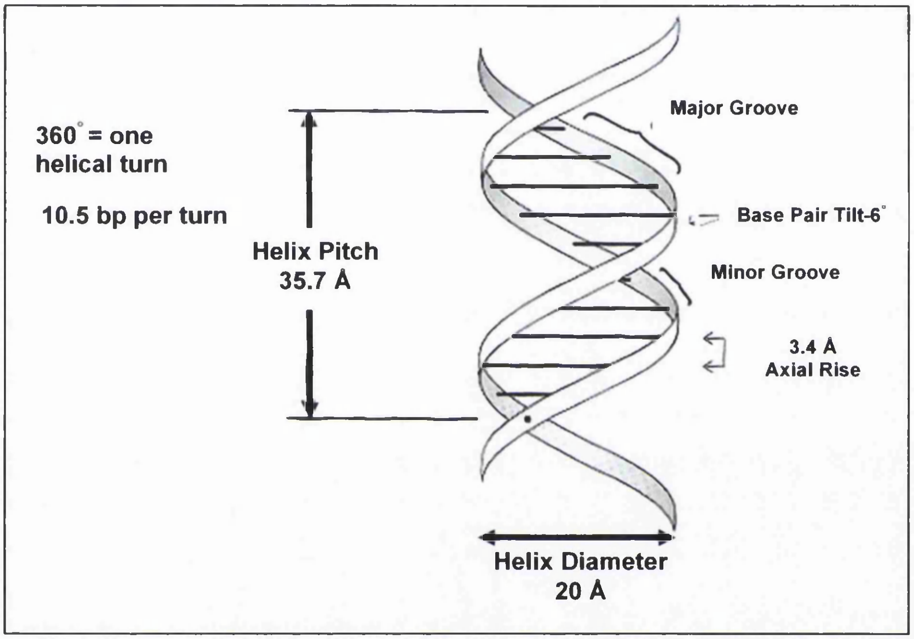

Figure 2.5. The double helix contains 10.5-bp per helical turn[2]. The helix diameter is 20 Å with pitch 35.7 Å for 10.5-bp (or ~3.4 nm for 10-bp).

The diameter of the DNA molecule is 2 nm (20 Å). Inside the helix, bases are stacked vertically 0.34 nm apart. One complete helix turn contains 10.5 base pairs (-bp) and is 3.57 nm in length. Major and minor grooves alternate throughout the structure and are used as recognition sites for other molecules. Different salt concentrations can induce different conformations and it is possible for the DNA to undergo a reversible change from B-DNA to A-DNA which is composed of relatively dehydrated fibres; Z-DNA is a left-handed helix.

2.2.4 Replication, Cloning and PCR

Standard biological laboratory techniques allow straightforward handling and manipulation of DNA so that individual genes can be studied with immense convenience[1]. For cloning, DNA and cloning vectors are digested by either restriction enzymes or sonication. Digests are then cloned or fragmented further and purified by removal from an agarose gel. Both DNA fragment and vector should have compatible ends to be ligated together to form a recombinant molecule. Recombinant DNA molecules are introduced into a bacterium (*e.g. Escherichia coli* or *Saccharomyces cerevisiae*) and then replicated as directed by the vector to give identical copies.

The polymerase chain reaction (PCR) was developed in 1985 and is a powerful and convenient method of isolating and creating pure multiple copies of specific DNA sequences. Enzymatic amplification increases the number of copies for DNA fragments up to ~6000 base pairs in length and can take just a few hours. Amplification of the whole human genome comprising approximately 3,000,000,000 -bp is attainable by PCR if it is split into Gkb segments. PCR is especially sensitive and allows small samples of DNA to be copied numerous times so it can be used in medical and biological applications (*e.g.* genetic identification, cloning of genes and detection of hereditary diseases). The first cycle of PCR is shown in Figure 2.6.

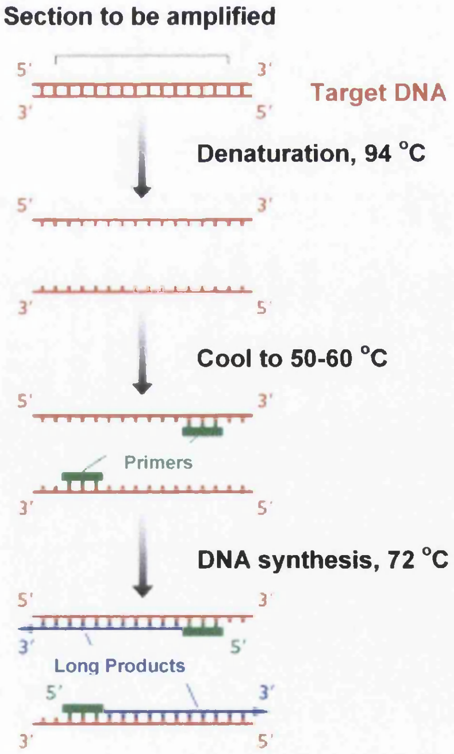

Figure 2.6. The first cycle of PCR: double strands are split, annealed with primers and new copies are synthesised.

One or more target DNA molecules are mixed in a buffer reaction containing a supply of single nucleotides (dNTPs), a thermostable DNA polymerase 'Taq' (*Thermus aquaticus)* and oligonucleotide primers [forward (F) and reverse (R)] whose sequences of 17-30 nucleotides are designed to be complimentary to the target DNA. Heating to 94 °C causes *denaturation* and strands separate. Cooling to 45-60 °C allows primers to hybridise to complementary target DNA. Primers attach at either side of the segment that is to be copied provided their sequences are complimentary to the DNA. Primers cannot anneal at the correct locations if the sequences are not complimentary (Figure 2.7).

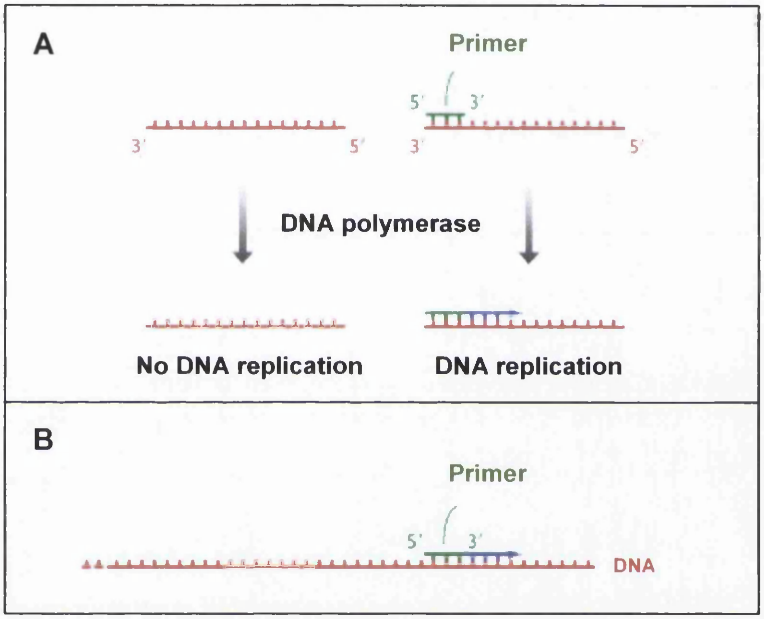

Figure 2.7. (A) Primers are designed to complement sections of DNA. (A) If primers cannot anneal no replication occurs. (B) Primers determine which part of DNA is copied.

Annealing temperature depends on primer length and sequence. Heating to 72 °C allows the Taq polymerase to bind at the free 3′-end of each bound oligonucleotide, and free dNTPs are used for synthesis of a new DNA strand in the 5′-to-3′ direction extending the sequence beyond that of the primers. For one strand of DNA the heating-cooling-heating process results in 2 copies of target DNA (or one set of 'long products'). The polynucleotides have identical 5′ ends and randomly terminated 3′ ends and act as templates for the next DNA synthesis. 'Short products' are formed in subsequent cycles with 5′ and 3′ ends both set by the primer annealing locations.

Cycles are automated and repeated numerous times to give exponential yield of

DNA. The expected amplification is 30 million-fold after 25 cycles and such quantities are achieved. PCR products can be analysed using agarose gel electrophoresis: a single band is revealed if the target DNA sequence has been successfully amplified.

For the work of this thesis, 30-35 cycles of PCR were carried out for the fabrication of DNA strands with protein PUT3 binding sites.

2.3 Protein

2.3.1 Biological Role

Proteins are fundamental structural elements found in all cells and tissues, and play a key role in all life processes (*i.e.* catalysis, structure, motion, recognition, and regulation)[5]. Proteins in the form of enzymes, digest food; those in the form of collagen, actin, myosin and intermediate filaments determine structure and motion of cells and organisms; antibody proteins provide protection from disease; membrane proteins control ion transport and intercellular recognition, and proteins also regulate gene expression. Mechanisms for protein self-assembly have evolved with extreme accuracy since even small defects in their structure can be disastrous for the individual (*e.g.* disease). The intricate structures of protein play the decisive role in their destined biological activity and compared to DNA which uses one-dimensional positioning along its strands proteins perform lock and key bonding in three dimensions. To understand how proteins fulfil their vital roles in life and how they could possibly be exploited for bio-electronics, it is necessary to study the arrangement of proteins in space. The basic properties of protein are therefore described in the following sections.

2.3.2 Structure of Proteins

Proteins are genetically encoded by DNA and contain 20 different α-amino acid building blocks[3]. Nineteen of these amino acids contain a central (α) carbon atom with a hydrogen atom attached, an amino group (NH_2), a carboxyl group (COOH) and a side chain (R) group, as shown in Figure 2.8. Amino acids are categorized into acidic, basic, hydrophilic (polar), and hydrophobic (non-polar) depending on their R

group. The chemical reactivity of polypeptides depends on the *R* groups present and such groups dictate the final shape that the polypeptide assumes from their stabilizing and repulsive forces with other groups.

The *R* groups of the non-polar, alipathic amino acids (Gly, Ala, Val, Leu, Ile and Pro) are without chemically reactive functional groups. When these amino acids are present in a polypeptide's backbone, they interact via hydrophobic interactions. Six amino acids are polar but uncharged: two of these, cysteine and methionine contain a sulphur atom. The side chain of methionine is non-polar and fairly unreactive although susceptible to oxidation.

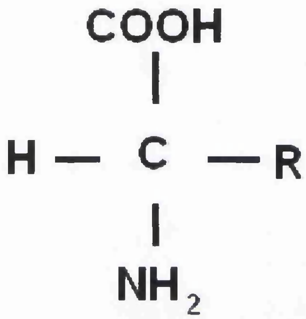

$$\mathrm{H-\overset{\displaystyle COOH}{\underset{\displaystyle NH_2}{C}}-R}$$

Figure 2.8. The general structure of an amino acid. *R* groups are different for each amino acid.

The thiol (-C-SH) portion of cysteine's *R* group is the most reactive functional group of any amino acid side-chain and can form complexes with various metal ions. Covalent linkages called disulphide bridges can form between two cysteine amino acids at different positions in the polypeptide. The amino acid proline is unusual in that its *R* group forms a direct covalent bond with the nitrogen atom of the free amino group in other amino acids.

Amino acids join to form short polymer chains or *peptides* and *polypeptides*. The currently accepted nomenclature states that *polypeptides* contain approximately 15-50 amino acid residues whilst those composed of fewer than 15 are termed *oligopeptides*. Peptides are assembled into proteins which contain 50 or more amino acids. Whole proteins vary from peptides of a few amino acids with molecular weight of a few hundred daltons to large proteins with over 3000 amino acids in excess of 300,000 daltons. The majority of proteins have molecular weight within the range of 10,000-150,000 daltons. Multi-subunit aggregates (*e.g.* dimers or tetrameters) may also be formed. Proteins can be spherical, globular, or asymmetric in shape. Fibrous proteins tend to adopt simpler 3D shapes and are usually elongated compared to globular proteins. Typical globular polypeptides have diameter 50-100 Å.

2.3.3 Levels of Organisation

Different levels of organisation exist within proteins[1,5]. *Primary structure* refers to the number and sequence of amino acids sequentially linked through peptide bonds. *Secondary structure* expresses the local three-dimensional arrangement of the peptide backbone. Two common forms of secondary structure are the α-helix and β-sheet (Figure 2.9). Both structures are stabilized by hydrogen bonds between different amino acids in the polypeptide.

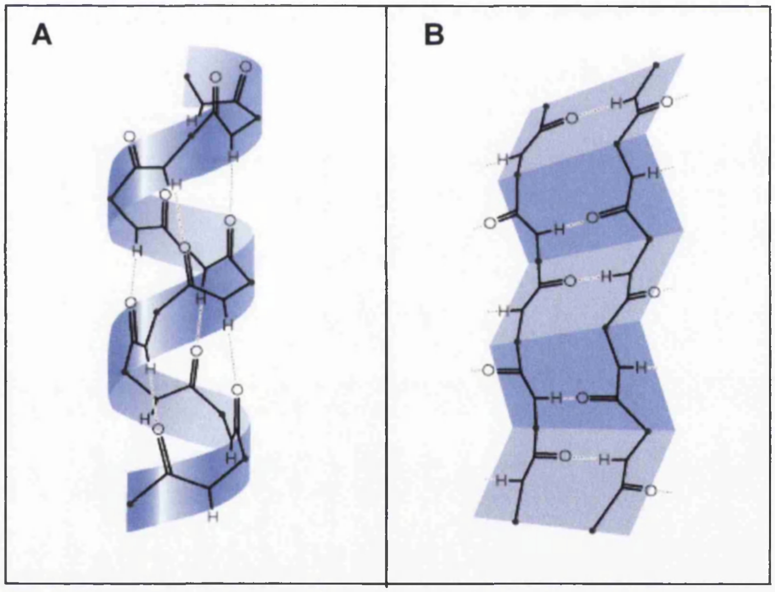

Figure 2.9. The secondary structures of protein[3]. (A) An α-helix (B) A β-pleated sheet.

For the α-helix, intramolecular hydrogen bonds are aligned parallel with helix axis and it is characterized through a well-defined amino acid residue per turn or helix pitch (Fig. 2.9A). The most common form has ~3.6 amino acid residues per turn. For β-sheets, hydrogen bonds are formed between neighboring polypeptide chains (Fig. 2.9B). Chains can be aligned parallel or anti-parallel to each other. For both secondary structures, the polypeptide chain conformation is determined primarily by hydrogen bonds.

Tertiary structure refers to the overall shape of an individual peptide chain resulting from secondary structure elements. Globular clusters within proteins are termed *domains* consisting of up to 200 amino acids. These are typically tightly folded regions of single polypeptides. Domains make up *motifs* that are composed of stretches of secondary structure linked through loops making up a specific 3D conformation. *Quaternary structure* refers to the spatial arrangement of two or more chains associated by non-covalent interactions or disulfide bonds.

At present most of the high-resolution structural information of whole proteins is attained using diffraction of X-rays through macromolecular crystals[6]. X-ray wavelengths (~1 Å) approximately match atomic dimensions (1.5 Å for C-C single bonds) and are therefore diffracted. Collected X-rays cannot be focussed so images are reconstructed computationally using the theory of diffraction using intensities of diffracted waves that are recorded experimentally. Crystals are required for X-ray diffraction analysis and a typical protein crystal contains more than 10^{14} aligned molecules and the averaging of diffraction intensities is very accurate. The process of determining molecular structure consists firstly of growing crystals and secondly measuring diffraction data. Phases for structure factors are determined and electron density maps produced. Atomic models are fitted with the map to provide a structure model which may be refined through repeated experiments.

Crystal growth of protein macromolecules is challenging[6]. Two crucial factors are protein concentration and purity. The protein mass of a single X-ray-quality crystal is small, 10-20 μg but at least 10 mg of pure material is required at the onset of a successful experiment. Micro-techniques (*e.g.* micro-dialysis, vapour diffusion) are therefore necessary to make suitable crystals. Practical implementation of X-ray diffraction is described elsewhere[7].

Nuclear Magnetic Resonance (NMR) offers a second approach for studying protein chemistry[7]. This spectroscopic technique is applied to small proteins and site-specific information can be routinely obtained (*e.g.* conformation alterations, pK_a values, hydrogen bonding patterns). In a one-dimensional pulse-Fourier transform NMR experiment, a sample is placed in a uniform magnetic field and subject to a quick pulse of electromagnetic energy with frequency centred at the spectral region of interest. The pulse excites all nuclei of interest (*i.e.* all ^1H or all ^{13}C). The brief magnetization of sample perpendicular to the static magnetic field generates a signal at a receiver coil and is detected in the audio frequency range as an offset from the transmitter radio frequency. The signal is digitised and stored. Fourier transformation of this single yields a NMR spectrum where signal intensity is plotted as a function of offset frequency from a reference. The frequency is divided by the spectrometer carrier frequency and shown as a *chemical shift* in dimensionless units of parts per million.

Other approaches include Circular Dichroism (CD) spectroscopy and Fourier transform infrared (FTIR) spectroscopy[8]. Both are used for secondary structure estimations. UV Fluorescence Spectroscopy is based on intrinsic fluorophor observations. At present, recombinant DNA techniques allow scarce proteins to be advantageously 'manufactured' in large quantities and so an abundance of inherently rare proteins means the rate at which structures are determined has improved. On solving protein structures, their coordinate sets are held at the Protein Data Bank[9,10].

2.3.4 Additional Properties

It is notoriously difficult to predict protein properties. For a protein with 100 amino acids, there are three possible conformations per amino acid residue; the time for a single conformation transition is 10^{-13} sec, so the optimum conformation after searching through all potential ones is 10^{27} years. Ultimately energy minimization and dynamics will determine the overall protein structure. Additional features that are inherent to proteins are listed below:

- **Enzyme proteins** will bind substrates, effector molecules, cofactors, DNA templates and some metal ions tightly (*e.g.* Cu^{2+}, Zn^{2+}, Ca^{2+}, Co^{2+}).
- **Protein charge** is determined by the sum of positively and negatively charged amino acid residues. Many aspartic and glutamic acid residues give rise to an overall negative charge, an *acid* protein. An abundance of lysine, arginine and possibly histidine gives rise to a *basic* protein. The pH of the buffer solution influences protein charge. The isoelectric point (pI) is that pH for which the

charge on a protein is zero and it can be determined from the positively and negatively charged amino acid residues on the protein. In general pI values range from 4.5-8.5. Charged amino acid residues may be distributed evenly over the protein surface or can be clustered forming highly positive or highly negative regions. Non-random distributions can be a discriminating factor between proteins.

- **Protein solubility** varies tremendously depending on the solvent from effectively insoluble to soluble to a level of hundreds of mg/ml. Ionic strength, nature of ions, pH, and solvent polarity are key factors affecting solubility.
- **Protein density** is ~1.4 g/cm^3. High quantities of phosphate in proteins are considerably denser than average proteins whilst lipid moieties are substantially less dense. Proteins may be separated using this density gradient factor.
- **Protein folding** is self-assembling in the right conditions. Linear polypeptide chains rotate about single bonds thereby aiding 3D structure formation. Hydrophobic, folded proteins ensure their interiors are compacted as organic crystals which are protected from the solvent. Folded states must be kinetically accessible and have lower free energy than unfolded states. Free energies of the folded states are determined by physical interactions occurring inside the protein molecule and with the solvent and all entropic factors. The folded state has less surface area in contact with the solvent allowing non-polar groups to interact more favourably with each other than with water. The balance between folded and unfolded states is delicate and determined by the range of conditions such as solvent, ionic strength, temperature, pH and pressure.
- **Proteins are constantly moving** even at subzero temperatures or in their crystalline state. Their atoms undergo vibrations, rotations and small translations (0.2 –0.5 Å). At higher temperatures (0-60 $^{\circ}$C) reversible displacements of whole sections of the protein are observed in aqueous solution. Motion is determined via the fine balance of intramolecular, non-covalent interactions such as hydrogen bonds, hydrophobic, ionic and Van der Waals interactions. At elevated temperatures (45-85 $^{\circ}$C) drastic intramolecular movement may occur. Non-covalent bonds may not withstand the increase in temperature and the protein loses its secondary and tertiary structure via denaturation.

- **Proteins with Cysteine residues** are synthesised in a thiol form so that folding accompanies disulfide bond formation. The redox reaction involves electron donors and/or acceptors: 2-SH ↔ -S-S- $+ 2H^+$ $+ 2e^-$ and reducing disulfides unfolds proteins without cause for other denaturants.

2.4 DNA-Protein Complexes

2.4.1 General Description

DNA carries the information necessary for the manufacture of proteins via its linear sequencing of nucleotides[1,3]. Genetic information is expressed at specific times during development of cells through interactions of regulatory proteins with short DNA sequences (Figure 2.10). These DNA-binding proteins are able to recognise specific DNA base sequences from the entire genome and interact with them accordingly during genome expression. Other proteins, such as histones are assembled into nucleosome core particles which are involved with the structural organization of DNA.

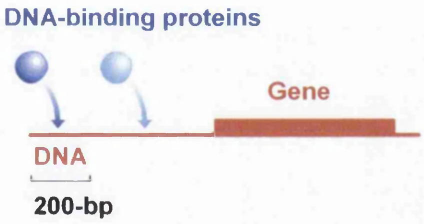

Figure 2.10. DNA-binding proteins attach to DNA immediately upstream from a gene.

The contact bonds created between DNA and binding proteins are non-covalent[1,3]. The presence of major and minor grooves aid site recognition without unravelling of the helix: major grooves are wide (~0.22 nm) and deep, and minor grooves are narrow (~0.12 nm) and shallow[1]. *Direct readout* of the DNA sequence is possible if a protein contacts the DNA helix at one or more of the grooves: at the bottom of the major groove are mainly nitrogen and oxygen atoms belonging to unique regions of each base pair; at the bottom of the minor groove are nitrogen and oxygen atoms that are common to both purines and pyrimidine bases. The nucleotide sequence can therefore be recognised at the major groove whilst at the minor groove only the base pair (A-T or C-G) can be identified. Figure 2.11 shows the recognition features of an A-T base pair[3].

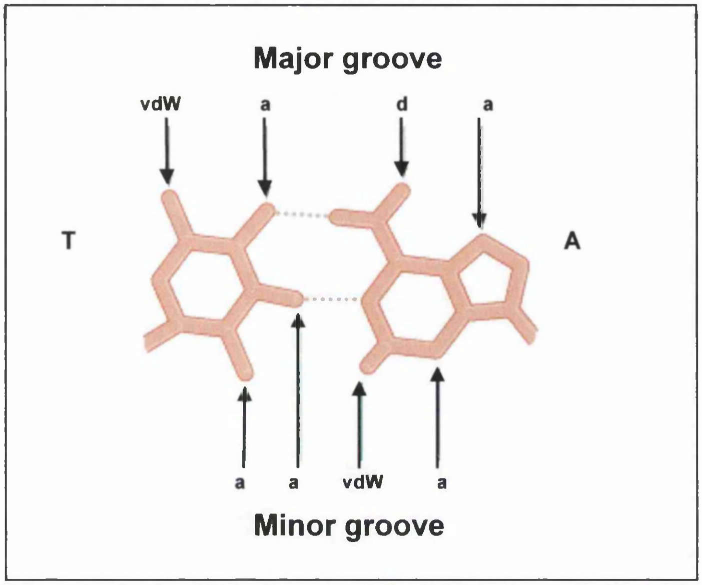

Figure 2.11. Chemical features of DNA grooves: a= hydrogen bond acceptor, d= hydrogen bond donor, VdW= Van der Waals interaction. Chemical features are asymmetric at the major groove.

At the major groove, hydrogen bonds form between the nucleotide bases and *R* groups of amino acids in the protein recognition segment and in the minor groove, hydrophobic interactions are more significant. At the helix surface, electrostatic interactions are created between the negatively charged phosphate components at each nucleotide site and the positive charges on *R* groups of amino acids (*e.g.* lysine, arginine). Hydrogen bonding may also occur at the surface of the helix as well as in the major groove between protein and DNA directly or mediated by water molecules depending on the particular DNA-protein interaction.

DNA-binding proteins which bind predominantly to specific sites may also bind non-specifically[1]. Since the quantity of DNA in a cell is large compared to the number of binding proteins it is indeed feasible that proteins spend the majority of their time attached non-specifically although site-specific binding is likely to be favoured thermodynamically[11]. To fulfil this thermodynamic preference, the binding process must induce maximum contact between the protein and DNA. DNA-binding motifs appear to fit neatly at the major groove where DNA-protein contact is actually greatest and at this position the base sequence should be recognisable[3]. Furthermore, conformational changes can occur to either the protein or DNA which increases the area of contact and strengthens the interaction -many DNA-binding proteins bind to DNA in dimer form to maximise the contact and achieve this site-specificity.

2.4.2 Nucleosomes

In mammalian cells, 2-3 billion bases of DNA encode some 30,000 genes in a strand of corresponding length 2.1 m. Tremendous compaction is achieved via DNA's association with small basic proteins to form chromatin and to condense it into the nucleus with diameter 5-10 μm. The structure of nucleosomes is relatively well-defined from X-ray crystallography[12,13] and electron microscopy studies[14]. Eight small basic proteins associate with DNA to form a disk-shaped nucleosome core particle (Figure 2.12). Two copies of each protein (H2A, H2B, H3 and H4) form the octamer and are stabilised by a linker (H1). DNA is wrapped around the core particle 1.7 times using up 145-147 base pairs, resulting in a nucleosome with diameter 12-13 nm. The periodicity is reduced from 10.6-bp of free B-DNA to 10.2-bp due to torsion of wrapping and allows minor grooves to bind with histones[15].

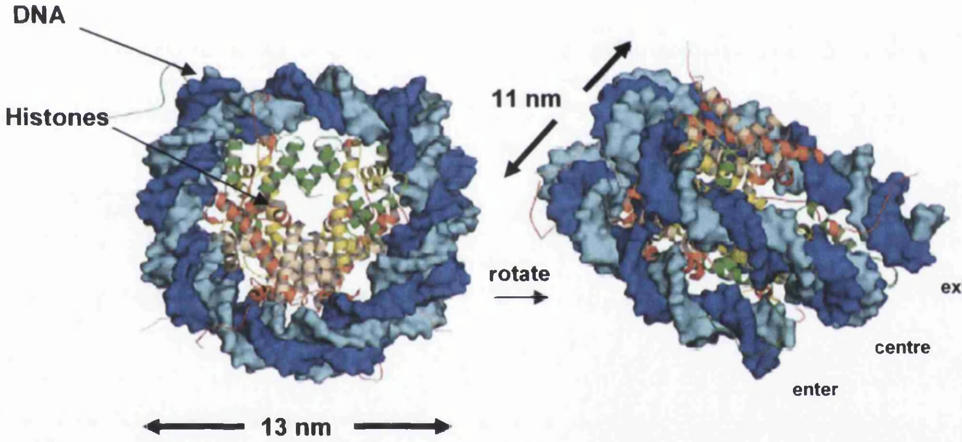

Figure 2.12. The atomic structure of the nucleosome core particle. DNA (blue) makes 1.7 turns to surround the histone core and form a disk-like shape[15].

Histones have large amounts of lysine and arginine (positively charge amino acids) which give rise to binding with negatively charged phosphate groups. Histones are involved in many modifications (*e.g. acetylation of lysines, methylation of lysines and arginines, phosphorylation of serines and threonines, ubiquitination of lysines*[15]) and one future challenge is to ascertain how covalent modifications may regulate the disease states in mammals.

Nucleosomes appear as spherical complexes regularly spaced along a chromatin axis in linear arrays, also termed '*beads on a string*'. They are dynamic units, not only involved in DNA compaction but with genomic regulation. In turn, nucleosomes are folded into a higher order 30 nm chromatin fibre for further compaction. The degree of compaction may influence whether or not genes are expressed and varies with cell cycles. The process is always reversible.

For the work of this thesis, DNA-binding proteins were especially interesting for applications in bio-electronics. The next section discusses a protein *PUT3* which has high affinity for particular DNA base sequences.

2.4.3 Proline Utilization Trans-activator (PUT3)

2.4.3.1 Structure

A family of DNA-binding proteins target specific nucleotide sequences and bind accordingly to DNA molecules[3]. The process is self-assembling in a suitable environment. The protein first contacts DNA in order to recognize its nucleotide sequence. Part of the protein may penetrate a major or a minor groove of the helix to distinguish between bases. Additional DNA-protein interactions can stabilise the DNA-protein complex or aid access to indirect information of the sequence provided by the helix conformation. DNA-binding proteins are sub-divided into groups depending on the structure of the DNA-binding motif and the protein segment interacting with DNA. Examples of these are firstly the helix-turn-helix (HTH) domain, consisting of a 20-amino-acid motif that has evolved to fit into major grooves of DNA, and secondly the zinc finger motif for proteins containing zinc (Zn) binding domains. The Zn binding domain must recognise regulatory regions or specific bases pairs upstream from genes for transcription to occur. At least 79 fungal DNA-binding proteins contain a Binuclear Zinc Cluster [$Zn_2(Cys_6)$] where two zinc ions are held with six cysteine residues. Such proteins, termed *transcription factors*, can recognise CGG triplet sites within DNA in different orientations with characteristic spacing. Two cysteines bind each atom of Zn while the two Zn atoms are bridged through the third pair of cysteines (Cys_2-Zn-Cys_2-Zn-Cys_2) and certain regions of the zinc clusters may play a part directing the protein to the preferred site[16]. Cysteines are arranged around the binuclear Zn cluster with two short α-helices joined by a loop on opposite sites of the Zn atoms. One of these helices interacts through the major groove with DNA.

Yeast cells are able to use proline from their environment as a source of nitrogen and the protein '*Proline Utilization Trans-activator*' (PUT3), a member of the C_6 cluster family of yeast transcriptional activators, regulates the process of converting proline to glutamate so that it can be used as a source of nitrogen[17]. The structure of the PUT3p DNA-binding motif (denoted by *PUT3* in literature) has been resolved using X-ray crystallography[18] but this is small compared to the size of the whole protein which consists of a total of 979 amino acids and whose structure is yet to be determined (*PUT3p*). Simple models are given in Figure 2.13 to show the PUT3 binding domain with and without DNA.

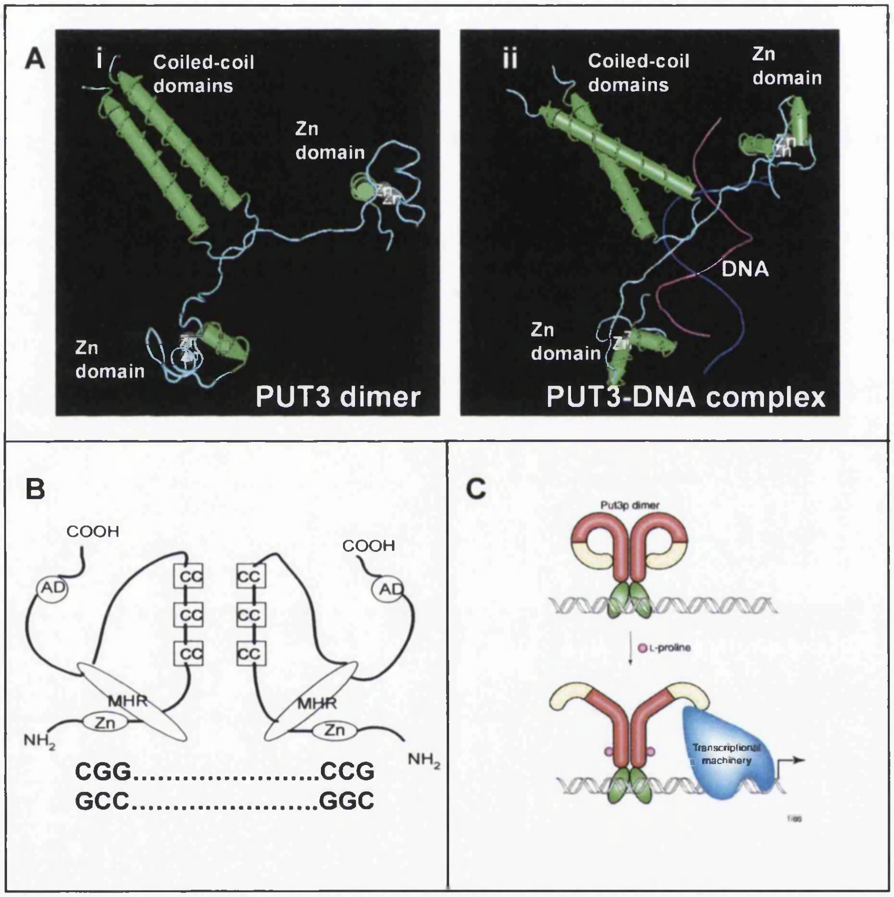

Figure 2.13. Models of the PUT3 dimer with DNA (Cn3D 4.1 software) (A)(i) PUT3 dimer only (ii) PUT3 dimer with DNA. (B) Schematic of a prototypic C_6 zinc cluster (Zn) protein[19]. Abbreviations: coiled coils (CC), middle homology region (MHR) The MHR regions interact with the C_6 cluster and linker region to allows binding with DNA to occur if the sequence is correct (*i.e.* $CGGn_{10}CCG$). Binding is prevented for sequences with the incorrect middle sequences. (C) Proposed mechanism for proline-specific activation by Put3p[20]. The DNA-bound Put3p dimer functions as a proline sensor.

The dimers wrap asymmetrically around the DNA by one and one-half turns. A β-strand from one protein subunit is positioned into a minor groove of DNA. This gives rise to a partial amino acid-base pair intercalation and extensive direct and water-mediated interactions with the minor groove. Thus, there are two components to DNA recognition by PUT3. Firstly the recognition of CGG DNA half-sites at the ends of the DNA sequence by Zn_2Cys_6 binuclear cluster residues, and secondly the specificity of a 10-bp sequence separating the half-sites by linker and dimerization units.

PUT3 binds to DNA as an asymmetric homodimer, wrapping around the DNA by one and one-half times[18]. The two Zn_2Cys_6 domains lie in major grooves at either end of the DNA; the carboxyl-(C) terminal ends form a *coiled-coil* dimerization interface which is positioned over the minor groove, near the centre of the DNA site (Fig. 2.13A and B). A short stand connects the domain responsible for dimerization to the Zn_2Cys_6 domain. As binding with DNA occurs, strands are inserted deep into the minor groove (near the centre of the DNA site) and a 40° kink is induced in otherwise B-DNA. Thus, both protein and DNA within the PUT3-DNA complex undergo significant structural rearrangements during complex formation[18]. Further information regarding the intricate structure of PUT3 and its binding properties can be found in data published by Swaminathan *et al.*[18]

Data published in 2005 by Sellick and Reece[20] suggests that the conformation of the PUT3p complex may be altered in response to the presence of proline and that the DNA-bound PUT3p dimer acts as a proline sensor (Fig. 2.13C). An addition of a sufficiently high concentration of proline appears to 'activate' PUT3p such that it becomes increasingly resistant to digestion with certain protein digestive enzymes (proteases) and cleavages (*i.e.* thrombin cleavage of the glutathione S-transferase (GST) tagged PUT3p). In other words, the presence of proline appears to contribute to the 'unmasking' of an activation domain in PUT3p. This may result in the conformational change in PUT3 as shown in Fig. 2.13C, which allows the protein to perform its role in subsequent biological processes (*i.e.* activate transcription)[20].

2.4.3.2 Binding Conditions

PUT3 recognises a 16-bp DNA binding site containing CGG triplets: ***CGG-10-bp-CCG***. The characteristic 10-bp spacing between CGG triplets is important for PUT3 binding. It has been shown using other binding proteins that binding affinities may decrease as the characteristic spacing is altered[16]. Note, 'GAL4' and 'PPR1' contain C_6 clusters like PUT3 and recognise the rotationally symmetric CGG triplets that are separated by 11-bp and 6-bp respectively.

The PUT3p unit is known to bind to the DNA site when incubated in a 10 µl reaction mixture containing 20 mM HEPES-KOH (pH 8.0), 150 mM NaCl, 5 mM $MgCl_2$, 10 µM $ZnSO_4$, and 10% (v/v) Glycerol. Binding takes place in 30 minutes at room temperature, 23 °C [16]. Interestingly DNA containing a PUT3 binding site is reported to exhibit a modest 6° bend in the absence of PUT3, whilst after binding a bend of ~46° towards the major groove of the PUT3-bound DNA is observed[18]. Many other transcription factors isolated from organisms bind to DNA and appear to induce bends and the bend-ability of a sequence is thought to be linked to the protein's binding affinity at that site. Comparative gel electrophoresis can be used to detect DNA bending. The location of a bend sequence is mapped by moving the suspected sequences nearer the end and is then used in circular permutation electrophoretic assays. By altering the number of bases the relative orientations of two bends are mapped as well as the difference in phase. Electron microscopy has also been applied to analyse DNA bends although the effect of binding surfaces must be taken into account.

2.5 Literature Review

2.5.1 Current Methods of Structure Determination of Bio-Molecules

As quoted by Feynman in 1959: *'It is very easy to answer many of these fundamental biological questions; you just look at the thing! You will see the order of the bases in the chain; you will see the structure of the microsome. Unfortunately the present microscope sees at a level which is just a bit too crude. Make the microscope a hundred times more powerful, and many problems of biology would be made very much easier'*[21]. The organisation of biological molecules in space is indeed fundamental to their behaviour and various techniques have been developed to elucidate bio-molecular structures with increasing accuracy. X-ray crystallography provides detailed structural information of crystallized samples. However, crystallisation is limited to only a small percentage of known biomolecules at the present time and the fundamental challenge seems to be the growing of suitable quality crystals of a given molecule[6]. The search for crystallization conditions of the protein *cytochrome c oxidase* took around 15 years though once crystallised the structure was solved in approximately one year. A second technique is cryogenic electron microscopy (cryo-EM). Samples are frozen very quickly by vitrification in a thin aqueous film before being exposed to an electron beam[22]. The technique has been successfully applied to an assortment of biological specimens and structural data agrees well with that extracted from X-ray crystallography. One drawback is that the signal-to-noise ratio is relatively low and it can be difficult to detect features when considering a small quantity of images. Typically hundreds of images need to be captured in order to permit accurate molecular modelling.

Scanning probe microscopy (SPM) encompasses a range of techniques for analysing topographic and electronic properties of materials at the nanoscale[23]. Atomic force microscopy (AFM) is particularly favoured for examining 'soft' specimens[24]. Biomolecules contain many diverse structural motifs and since fundamental mechanisms of charge transport depend on their characteristic organisation in space, it is vital to first determine their molecular organisation. At present, the routine use of many SPM systems allow single biological molecules and organic structures to be examined perhaps for the first time for applications in biotechnological and medical research[25, 26].

2.5.2 SPM Studies of DNA

SPM studies of DNA began in 1989 using the revolutionary scanning tunnelling microscopy (STM). Highly ordered pyrolytic graphite (HOPG) was used for mounting DNA due to its flat, electrically conducting nature[27,28]. However, graphite exhibits features resembling DNA that are in fact native to its surface[29]. Alternative substrates such as gold proved more successful[30,31]. In 1999, high resolution STM images of double- and single-stranded DNA were reported by Tanaka *et al.*, captured in ultra-high vacuum (UHV) following their pulse injection onto a copper surface[32]. The internal structures had a periodicity of 2.6-3.7 nm compared to ~3.4 nm for

Watson-Crick DNA. Copper provided an artefact-free, well-defined, electrically conducting substrate for observing DNA and related molecules. However, STM relies on electrons tunnelling from tip to sample through biological material deposited on the conducting surface for the surface topography to be traced out. Therefore, the need for atomically flat, electrically conducting substrates is one potential drawback of using STM for bio-molecular studies. Tunnelling current cannot always flow through bulky molecules such as proteins, especially when the organisation and conductive nature of certain proteins is not yet known.

AFM solves this issue by enabling users to study insulators as well as conductors via atomic force interactions. DNA molecules are typically diluted into a solution of divalent cations (*e.g.* magnesium) then deposited on to mica, allowed to dry or rinsed with water and dried, and then scanned with AFM[33,34,35,36]. Water layers present in high humidity environments can give rise to capillary forces between tip and sample which may affect apparent height and width measurements of molecules[33]. Compression forces may compact DNA in the vertical dimension and can cause structural damage[36]. Salt adsorbate layers aiding DNA binding to the surface can also be problematic for height contrast between DNA and the surrounding background[36]. Imaging in liquid eliminates capillary effects but it is more difficult to achieve good binding of DNA to mica surface[36]. Binding is enhanced with alcohols (*e.g.* propanol) and Hansma *et al.* (1992) used propanol for reproducible imaging and dissection of strands in liquid[37]. Furthermore, Schaper *et al.* (1994) used propanol and non-ionic detergents (*e.g.* 2,4,6-tris(dimethylaminomethyl) phenol) to observe DNA in air[38].

Ions having radii compatible with the oxygen lattice on mica (Co^{2+}, Zn^{2+}, Ni^{2+}) improve DNA binding efficiency for imaging in water[36]. However, it should be noted that while certain cations are efficient at anchoring DNA to mica they may affect the nucleic acid structure by substituting physiological counterions[33] which in turn may prove detrimental to, for example, DNA-binding proteins. Divalent cations may cause variations in contour length or helix winding[33]; Zn^{2+} ions have been linked to kinking in DNA[39].

Numerous experiments have been performed over recent years with the aim of optimising binding of DNA to substrates and increasing image resolution. In 2002, Medalia *et al.*[40] studied DNA-protein complexes on thin-film gold surfaces in liquid. Thiol groups were introduced to the 5'-end of DNA and imaging performed - unmodified DNA could not be visualised. Therefore, the thiol group is a common choice when gold substrates are used. NC-AFM was developed as a less invasive mode of imaging and in 2002, Arai *et al.*[41] used NC-AFM to visualise DNA on silicon in UHV and reported DNA strings lying along surface steps. Maeda *et al.* observed DNA on untreated mica using NC-AFM in UHV[42] and on copper surfaces[43] using a pulse-injection method similar work to that reported by Tanaka *et al.*[32] Hansma *et al.*[44] used AFM to examine long, short, double stranded, single-stranded and even triple-stranded nucleic acids. Their findings showed that very short DNA strands (~25 bases) were globular in appearance and plasmids were highly coiled on oxidised silicon with only 5% being relaxed compared to on mica with 42% being relaxed. As the topological properties of DNA are fixed and cannot change without breaking bonds, coiling was attributed to differences in intramolecular interactions under different conditions.

While many sample preparations involve modifications of either surface or molecule for improved binding, such modifications can affect the properties of molecules and lead to difficulties in interpreting data[33,36]. It is therefore desirable to minimise all factors that could possibly lead to artefacts and incorrect data interpretation.

2.5.3 Charge Transfer Studies of DNA

DNA was first suggested as an electronic conductor by Eley and Spivey[45] in 1962 and since then various experiments have been performed. In 1999, long-range charge transport was investigated by Fink and Schonenberger and results of direct measurements showed DNA ropes consisting of several molecules of length 600 nm to be electrically conducting; an upper limit of resistance 2.5 MΩ was found in vacuum using a low energy electron point source[46]. In 2000, Porath *et al.*[47] reported large band-gap semi-conducting behaviour whilst de Pablo *et al.*[48] found in agreement with several others[49,50,51] that DNA is insulating.

In 2002, Ha *et al.* found that humidity improved DNA's conductivity[52] possibly via ionic conduction through DNA's hydration layers. Similar observations were made in 2004 by Kleine *et al.* so that individual DNA strands that were initially insulating became more conducting with increased humidity, presumably from water capillary condensation and ionic currents[50]. Jo *et al.*[53] also found that by decreasing humidity, DNA's resistance increased, and that the G-C content affected the conductivity level at a given voltage. In 2005, Iqbal *et al.*[54] reported rectifying properties for small thiolated DNA using nanogap break-junctions and found conductivity dependence on temperature where increasing temperature decreased its conductivity. For a comprehensive history of DNA's conductivity, the various experimental setups used and results obtained, the reader is directed to recent review publications[55].

Despite the large numbers of experiments that have been performed by others which investigate the conductivity of DNA, the number of reports considering the attachment of DNA to electrodes is significantly less. Electrode contacts that facilitate electron transport are highly desirable in all situations and since there may be some question as to whether the DNA molecule is actually in *intimate* contact with metal electrodes (as for the cases described above), further research is desirable. DNA-binding proteins bind site-specifically to DNA and may provide the necessary *intimate* contact between DNA molecular wires and external substrates and electrodes. Therefore, this project seeks to determine the feasibility of using protein anchoring groups for improvement of the DNA-electrode contact which then may affect the overall conductivity measured for DNA.

Using similar reasoning behind DNA electronics, proteins have already been suggested for 'bottom-up' building blocks in the fabrication of nano-devices. Rectification has previously been reported for some proteins[56]. Several studies have been performed on metalloproteins that contain metal atoms at their centres to make use of their natural redox properties[57,58,59] and it may be possible to engineer additional charge transfer properties by using different metal atoms as the redox centres. The presence of a disulfide site present on blue copper metalloprotein Azurin's surface implies binding to gold is more straightforward. In 2005, Alessandrini *et al.* reported that Azurin hosted within a nm gap between two gold electrodes, acted as an electrochemically gated single-molecule transistor in aqueous environment and the protein exhibited rectification at room temperature in air. Ferritin proteins (apoferritin and holoferritin) have also been adsorbed on gold surfaces and studied using conductive atomic force microscopy to yield measurable electrical currents[60].

In returning to the topic of DNA's conductivity, results appear to be highly influenced by a range of factors (*e.g.* sample composition, apparatus used, environment *etc*). In order to interpret future results, it is necessary to consider the fundamental, polymer-like nature of DNA. Therefore, it is useful to examine the basic properties of well-known conducting polymers before questioning the effect of external influences on DNA's behaviour. The theory of conducting polymers is discussed in the next section.

2.6 Theory of Conducting Polymers

The electronics industry relies heavily on metal and semiconductors for high electrical conductivity applications. In both metals and semiconductors, the atomic orbitals of each atom overlap creating continuous energy bands as shown in Figure 2.14. Electrons are delocalized from orbitals throughout the structure but are excluded from forbidden energy regions between bands (*i.e.* band gaps). Valence band refers to the highest occupied energy band and conduction band refers to the lowest unoccupied band. If the valence band is partially filled with electrons and an electric field is applied, electrons can move giving rise to metallic behaviour. If the valence band is full, conduction only takes place if electrons are promoted across the forbidden energy gap to the conduction band. Vacancies or holes are left in the valence band as free electrons are added to the conduction band. The extent of orbital interactions and overlap influences the amount of delocalization possible and in turn, the spread of energy levels made available to electrons of each band (bandwidth) is determined. The larger the electron delocalisation, the larger the bandwidth and greater mobility of carriers in that band. For solid state systems, the presence of continuous, overlapping atomic orbitals is ideal for electronic conduction since they create the delocalised states necessary for electron movement if an electric field is applied. Many polymeric structures have highly delocalized electronic states and facilitate electron transport[61].

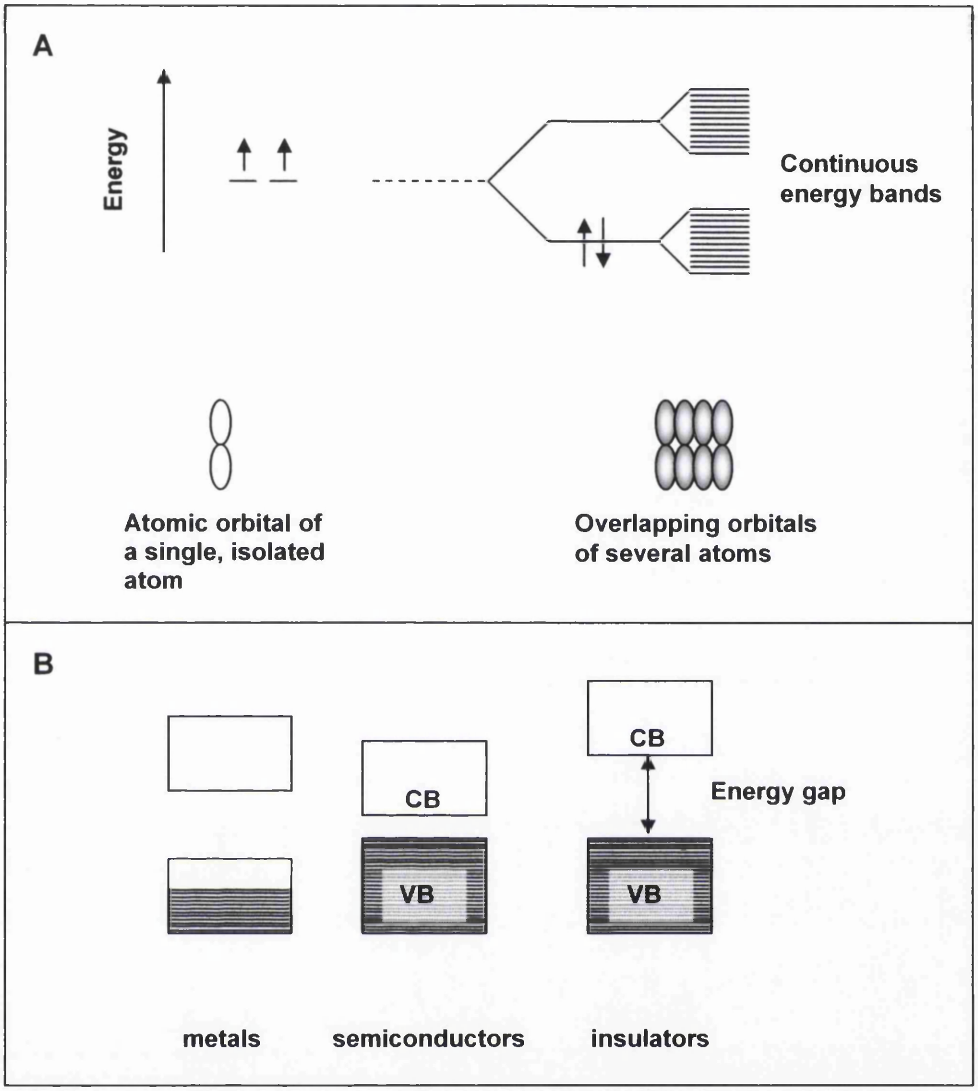

Figure 2.14. (A) Energy bands are created when atomic orbitals overlap. (B) The highest occupied bands are shown for metals, semiconductors and insulators.

For a number of insulating polymers, the molecular orbitals linking chains of atoms do not sufficiently overlap since electrons are highly localised for bonding and cannot easily partake in conduction. A large energy gap exists between highest occupied band and lowest unoccupied band (*e.g.* polyethylene). Conformational changes may be induced if efforts to excite electrons in these polymers are performed.

For conducting polymers, atomic orbitals are arranged so that delocalisation of electronic states takes place whilst the structure is maintained. Polymers containing conjugated unsaturated bonds fulfil this criterion. These (conjugated) polymers are often defined as those containing planar sequences of alternating single and double bonds through its backbone. Carbon atoms equipped with p_z-orbitals perpendicular to the backbone axis may interact or overlap with its neighbours. Assuming the electron wave-function is completely delocalized over the entire length of a linear polymer, that all its bond lengths were matching and that just one electron from each strongly interacting coplanar p_z-orbital contributed to the continuous π-system, the polymer would act as a one-dimensional metal.

Many one-dimensional systems use alternating short and long bonds to conserve energy and this restricts electron delocalisation. Strong-coupling between π-electrons and phonon modes (skeletal vibrations) influence bond alternation and since the energy needed to 'distort' the molecule into alternating bonds is less than the energy needed to maintain a fully delocalised backbone, bond alternation is established. For polymers with alternating bonds, the maximum level of delocalisation is seen for a certain number linked multiple bonds (*e.g.* 20 multiple bonds). Bond alternation ultimately results in a filled valence band and empty conduction band separated by the energy gap at the Fermi level. Conjugated polymers are typically large band gap materials with band gaps >1.5 eV.

Fully aligned chains are strongly affected by the direction of applied optical/electrical fields. (*e.g.* stretched aligned polymers increase their absorbance when an incident light vector is polarized along its chain axis rather than perpendicular to it). Low dimensionality is an important factor in polymers, influencing the electron-phonon interactions (π-electrons-lattice vibrations) and overall electronic properties.

2.7 Theory of Charge Transfer in DNA

Many experiments and theoretical studies have been performed with the universal aim of measuring the electrical properties of single DNA molecules. A direct measurement is performed if two electrodes, separated by a small gap, is bridged by molecules. For example, long lengths of DNA (~1.5 μm) are highly likely to bridge a small electrode (typically tens of nm). The separation should be small enough for molecules to bridge the gap but large enough to avoid tunnelling through electrodes. Molecules can therefore facilitate charge transfer as macroscopic electrodes or SPM tips act as donors and acceptors of electrons. A lack of measurable current is attributed to highly resistive molecules.

Conductivity depends on the electronic energy levels or band structure of a molecule. Localised orbitals give rise to discrete energy levels and delocalised states form continuous energy levels. If a voltage bias is applied across electrodes and charge transport induced through the molecules in a reproducible way without altering their conformation, then it may be considered a wide band-gap semiconductor. If the structure is damaged irreversibly and results not reproducible then it is considered an insulator. The bases of DNA are organic compounds with planar, unsaturated benzene-like rings with π-electrons. Since other organic, aromatic crystals containing π-stacking were found to exhibit metallic behaviour, similar effects were suggested for DNA.

Within DNA, p_z-orbitals exist perpendicular to the bases as shown in Figure 2.15.

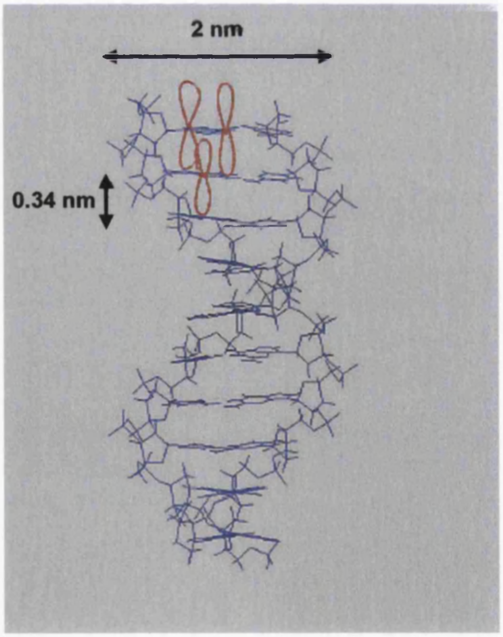

Figure 2.15. The base pairs of B-DNA are stacked within the core of the double helix (blue). The positions of a few atomic p_z orbitals are indicated (red).

Delocalized π-bonding and π*-anti-bonding orbitals are formed, separated by an energy gap. If the interactions between base pairs in the helix axis are sufficiently strong, extended states may exist along the helical axis. Therefore, DNA's energy gap may be reduced via broadening. Vanishing gaps where π and π^* states sufficiently overlap imply metallic behaviour; non-vanishing gaps imply DNA could be doped with electrons/holes as for semiconductors.

There are three mechanisms postulated for charge transport along DNA[55]. These are *thermal hopping, sequential tunnelling* and *coherent tunnelling* as illustrated in Figure 2.16.

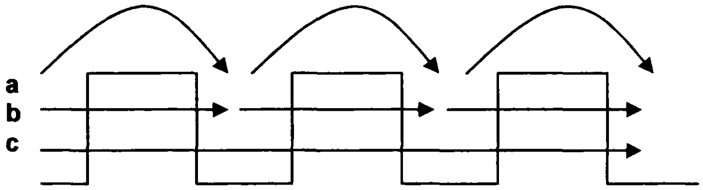

Figure 2.16. The three mechanisms for charge transfer in DNA. (a) thermal hopping, (b) sequential tunnelling and (c) coherent (uni-step) tunnelling. Energy increases along the vertical axis and spatial position increases from left to right.

The dominant mechanism will depend on the experimental setup and the particular conformation of DNA. Thermal hopping (Fig. 2.16, a) is an incoherent process. The electron is localised in the molecule as it exchanges energy with it. Electron transfer can occur in multi-step or diffusive manner over bases although for fluorescence experiments, thermal hopping from base to base is unlikely to occur as the energy required is very large. During sequential tunnelling (Fig. 2.16, b) charge tunnels from site to site. After each tunnelling action, 'dephasing' actions (*e.g.* scattering, molecular vibrations) give rise to a loss of coherence of the charge wave-function. Both thermal hopping and sequential tunnelling are considered largely independent of the length of DNA. Coherent tunnelling (Fig. 2.16, c) occurs when electrons do not exchange any energy with the molecule during transfer and are not localized. Phase coherence is not lost and therefore a strong dependence on distance is expected and it is unlikely to occur over long molecules.

Several theoretical models are based on sequential tunnelling through DNA. Holes are favoured as charge carriers with the base **G** being a favourable site, based on its ionization potential (where **G<A<C<T**). One suggestion is that a hole generated at a

G base gives rise to a $\mathbf{G}^+$ radical; the hole then hops to successive **G** bases throughout the length of the DNA or alternatively the $\mathbf{G}^+$ radical reacts with water. Sites containing multiple **G**'s may act to trap the hole but if large relaxation times are involved then the hole will continue to travel through the DNA. If the distance between **G** bases is too large thermal hopping can take over. Similar explanations are used to interpret experimental data. Single-step charge transfer is unlikely in complex formations so coherent tunnelling and sequential tunnelling have been combined in some models. The strength of dephasing (*e.g.* due to thermal motions of DNA, solvation *etc.*) is used to weigh the effects of each tunnelling process and this approach appears to account for the experimental results of Porath *et al.*[47] and Li *et al.*[62] on DNA molecules with 30 G-C base pairs deposited on two electrodes.

For theoretical models, the degree of inclusion/weighting of certain parameters is important, such as the structural form -whether stretched on substrates or free-standing, in bundles or strands. Tight-binding models have been used to take into account the coupling between bases and the phosphate backbone. The negatively charged backbone coupling may contribute to the large overall resistance and 'polyelectrolyte' behaviour of the helix.

Polaron and soliton formations may contribute to DNA's conducting properties. Polaron formations are linked to the electronic and vibrational mode degrees of freedom, and soliton formations are associated with domain walls in dimerised bonds of DNA[55].

Bundles and networks appear to be more conductive than individual strands and short DNA molecules appear to transfer electrons and holes over a few nm. Conductivity has shown to increase with temperature and at sufficiently high temperatures the dependence is also increased. Although tunnelling and thermally activated hopping are thought to be occurring, a critical temperature may exist where the hopping mechanism is initiated[55].

Indeed many factors appear to influence DNA's conductivity and in light of these findings, it is vital that future experiments are focussed on single factors of influence whilst all other experimental conditions remain equivalent (*e.g.* sample preparation, temperature, humidity). One of the least studied aspects of DNA's conductivity is the molecule-substrate contact. This factor has perhaps the greatest influence on DNA's conductivity and is addressed in the work of this thesis. The next section discusses the various types of molecule-substrate couplings used for both imaging and I-V measurements.

2.8 Molecule-Substrate Coupling

Structure analysis of single biomolecules with SPM requires the attachment of molecules to an underlying substrate[33]. The attachment ideally involves a minimum of structural modifications so that structural (or electronic) data can then be attributed to the biomolecule's inherent features. Biomolecules may be anchored to surfaces in a several ways. DNA is highly negatively charged and bonds non-covalently with positively charged substrates (*e.g.* nylon, nitrocellulose papers, polylysine-coated polystyrene plates). DNA modified with biotin (a small vitamin) has high affinity for surfaces functionalised with avidin or streptavidin molecules and binds to it irreversibly. For combined imaging and I-V measurement studies, metallic electrodes are necessary. The commonly used molecule-substrate couplings are described below.

- **Physisorption** (*i.e.* physical adsorption) occurs when adsorbates are adhered to surfaces or electrodes by attractive Van der Waals forces. This is often sufficient for anchoring biomolecules such as DNA on mica for imaging with AFM. Ions from solution can also adsorb onto oppositely charged surface regions in a process known as *ion exchange* although the final surface charge is balanced by equal and oppositely charged regions of counterions[63]. Counterions are usually transiently bound to the surface or create an atmosphere of ions in brisk thermal motion close to the surface, also known as a *diffuse electric double layer*[63]. Thus, highly polarizable layers can be formed at each interface (*i.e.* between the two 'conducting' layers) which then experience an attractive VdW force (or *ion-correlation force*)[63].

- **Chemisorption** takes place when molecules form chemical bonds with substrates. The thiol sulphur-gold (S-Au) linkage is a popular example and 'SH' groups can be added to ends of DNA for bonding with clean, flat Au substrates. The S-Au link is strong and polar (sulphur is more electronegative than gold). A Schottky barrier is formed and theoretical calculations predict a barrier up to 2 V. This method is useful for anchoring molecules for imaging but it may not be the best metal-molecule linkage for charge transfer studies.

- **Mechanical Coupling** refers to the contact made to molecules adsorbed on substrates. SPM probes may be used as external electrodes (*e.g.* conducting-AFM or STM tips). This is considered weak-coupling since contact is created through the air-gap or vacuum gap in UHV. Molecule compression is one issue affecting the true conductivity of molecules and it has been shown that for metalloproteins the higher the mechanical force applied, the higher the current recorded[64].

- **Protein Coupling** may be a viable option as whole proteins containing cysteine residues or disulfide bridges have been shown to chemisorb directly to Au surfaces[65]. Proteins containing just two residues deposited on gold nanoclusters pinned on to a HOPG background were reported to be easily displaced with a scanning tip and attributed to the inaccessibility of the cysteine residues to the surface. Proteins containing five residues were reported to be strongly anchored to gold nanoclusters and structural analysis matched that of crystallography showing that the 3D conformations of proteins were maintained. This coupling is a form of chemisorption and is based on the affinity of sulphur with gold. In other words, proteins containing cysteine residues that are accessible to the gold may be chemisorbed to gold (*i.e.* strongly bonded) rather than physisorbed (*i.e.* weakly bonded).

- **Electrode Coupling** is needed for I-V characterisation of biomolecules and so metal-molecule-metal junctions are used (Figure 2.17). The nature of the metal-molecule contact influences the overall current measured through the molecular core and is dependent on the chosen metal and the molecule's chemical functionality or 'alligator clip' which links them both.

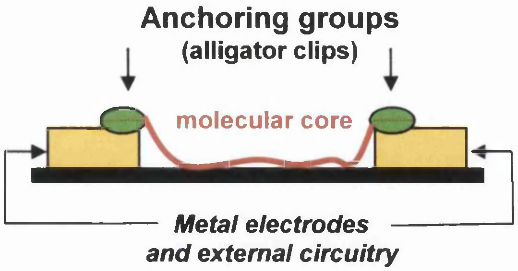

Figure 2.17. I-V measurements of biomolecules. The physical contact formed between a molecule and the electrodes is important.

Sufficient mixing of energy states between discrete molecular orbitals and continuum of electronic states gives rise to strong-coupling. A coulomb blockade effect implies weak-coupling. Both contact size and chemical nature of the molecule affect this phenomenon. The two basic mechanisms for electron transfer across a metal-molecule contact are *thermionic emission* (Schottky emission) and *electron tunnelling*. Thermionic emission is applicable to metal-semiconductor interfaces. A potential barrier forms between the metal and semiconductor contact and thermionic emission occurs when electrons have enough energy to pass over the barrier. For the simple case, barrier height is given by difference in work functions of metal and semiconductor. For real junctions interface dipole layers and surface states influence barrier height. For solid-state experiments, electrical measurements are recorded when molecules are under the influence of an external field. Electron tunnelling becomes the dominant mechanism when electrons do not have high enough energy to pass over the potential barrier. A number of theoretical models exist for such tunnelling through barriers[55] (*e.g.* Fowler Nordheim (FN) and Simmons tunnelling).

Whereas metal-semiconductor contacts are relatively well-understood, the same cannot be said for metal-molecule contacts. Aside from DNA, the sulphur bridge formed between a gold cluster contact and a short, unsaturated molecular wire (a phenyl molecule with a thiol group) has indicated ohmic behaviour in theoretical models where molecular orbitals of gold clusters extend into the π- system[66]. A dipole layer is created along with an associated electrostatic potential which is needed for charge transport through the interface. This type of state is unlikely to extend through longer wires and instead tunnelling may occur. Conductance of metal-molecule-metal junctions is improved for intimate contacts (*i.e.* strong-coupling) at both ends of the molecule rather than at one end[67]. Results are taken from alkyl chains where intimate contact at both electrodes gave rise to highest conductivity and the inclusion of sulphur atoms in molecules for chemisorption to gold increased the current recorded by a factor of 10 for strong-bonding compared to mechanical-contact. Cases with at least one weak-coupling (*e.g.* physisorbed Langmuir-Blodgett (LB) monolayers or SPM mechanical contact) gave lowest values of conductivity. Asymmetric contacts are also more likely to give contact-induced rectification which means contacts should be chemically equivalent if the effects of the molecular core are to be resolved.

A review of findings concerning metal electrodes and their effect in contact resistance was made by Kushmerick[68]. At least 2 orders of magnitude difference were found between the best (Pt-S) and worst (Ag-S) conducting contacts. Data originated from alkanethiols with varying numbers of methylene units. The contact resistance was found by measuring the resistance along the alkanethiol structure and extrapolating the resistance for zero methylene groups. The contact resistance agreed well with the metal electrode work function, meaning that higher work function metals provided lower contact resistance. Results implied that the Fermi level of the junction was positioned closer to the highest occupied molecular orbital (HOMO) than the lowest occupied molecular orbital (LUMO) and that hole transport was dominant.

Metal-linker assemblies are suited for charge injection and both theoretical and experimental studies suggest selenium (Se) is better than sulphur for electronic coupling to a gold surface[69]. Both isonitrile (-NC) and pyridyl groups have been used for coupling molecules with gold[70]. Palladium-sulphur contacts have also been explored and are predicted to be barrierless[71].

It is highly likely that charge transport through long DNA molecules is influenced by the nature of the molecule-electrode contact. This is very much dependent on the work function of the electrode and the nature of the tunnelling barrier. The work functions of metals are known but it is not clear where DNA lies in relation to these[72]. Charge transfer through a direct 'metal-to-π-orbital' contact will be different to a 'metal-to-DNA backbone' contact, and in turn these will be different to a 'metal-to-protein/DNA' contact[72].

2.9 Summary

This chapter has introduced the concepts of biomolecules for bio-electronic applications. The structure and biological roles of DNA and proteins have been discussed with particular attention paid to the self-assembling properties of DNA-protein complexes. A literature review of others' work has been provided regarding visualisation of DNA and its charge transfer properties.

The effects of the molecule-substrate contact were addressed and it is clear that a controlled strong-bonding approach is highly advantageous in an electrode setup. Since the number of studies taking into account the effect of the DNA-electrode contact is low compared other investigated factors, the work of this thesis is focussed towards using DNA-binding proteins for DNA-electrode coupling. DNA-binding proteins can be selectively positioned along DNA strands; they contain cysteine residues which may have affinity for gold electrodes; and when bound to DNA the protein's conformation could potentially be 'switched' via high additions of proline[20] as conformational changes at Au-S interfaces have already been suggested to influence molecular switching elsewhere. High-resolution AFM is employed for structure analysis of DNA and related molecules and its theory is given in Chapter 3.

2.10 References

---

[1] Genomes. (1999) Brown T.A. BIOS Scientific Publishers, Oxford.

[2] DNA Structure and Function. (1994) Sinden, R.R., Academic Press.

[3] Online resource: www.ncbi.nlm.nih.gov/books

[4] Watson, J.D. and Crick, F.H.C. (1953) Molecular Structure of Nucleic Acids: A Structure for Deoxyribose Nucleic Acid. Nature 171, 737-738.

[5] Peptides: Chemistry and Biology. (2003) Sewald, N. and Jakubke, H. -D., Wiley-VCH Verlag GmbH.

[6] Wery, J.P. and Schevitz, R.W. (1997) New trends in macromolecular X-ray crystallography. Curr. Opin. Chem. Biol. 1, 365–369.

[7] Protein Engineering. (1998) Oxender, D.L. and Fox, C.F. (Editors) Alan R. Liss, INC. New York.

[8] Peptides: Chemistry and Biology (2002) Sewald, N. and Jakubke, H.D., Wiley-VCH.

[9] Bernstein, F.C., Koetzle, T.F., Williams, G.J., Meyer, E.F. Jr, Brice, M.D., Rodgers, J.R., Kennard, O, Shimanouchi, T. and Tasumi, M. (1977) The Protein Data Bank: a computer-based archival file for macromolecular structures. Journal of Molecular Biology 112, 535-542.

[10] Online resource: www.rcsb.org/pdb/

---

[11] Stormo, G. D. and Fields, D.S. (1998) Specificity, free energy and information content in protein–DNA interactions. Trends in Biochem. Sci. 23, 109-113.

[12] Luger, K., Mader, A.W., Richmond, R.K., Sargent, D.F. and Richmond, T.J. (1997) Crystal structure of the nucleosome core particle at 2.8Å resolution. Nature 389, 251–260.

[13] White, C.L., Suto, R.K. and Luger, K. (2001) Structure of the yeast nucleosome core particle reveals fundamental changes in internucleosome interaction. EMBO J. 20, 5207–5218.

[14] Oudet, P., Gross-Bellard, M. and Chambon, P. (1975). Electron microscopic and biochemical evidence that chromatin structure is a repeating unit. Cell 4, 281-300.

[15] Khorasanizadeh, S. (2004) The Nucleosome: From Genomic Organization to Genomic Regulation. Cell 116, 259-272.

[16] Reece, R.J. and Ptashne, M., (1993) Determinants of Binding-Site Specificity Among Yeast C_6 Zinc Cluster Proteins. Science 261, 909-911.

[17] Sellick, C.A. and Reece, R.J. (2003) Modulation of transcription factor function by an amino acid: activation of Put3p by proline. EMBO J. 22 (19), 5147-5153.

[18] Swaminathan, K., Flynn, P., Reece, R.J. and Marmorstein, R. (1997) Crystal structure of a PUT3-DNA complex reveals a novel mechanism for DNA recognition by a protein containing a Zn_2Cys_6 binuclear cluster. Nature Struct. Biol. 4 (9), 751-759.

[19] Schjerling, P. and Holmberg, S. (1996) Comparative amino acid sequence analysis of the C_6 zinc cluster family of transcriptional regulators. Nucleic Acids. Res. 24 (23) 4599-4607.

[20] Sellick, C.A. and Reece, R.J. (2005) Eukaryotic transcription factors as direct nutrient sensors. Trends in Biochem. Sci. 30 (7), 405-412.

[21] Feynman, R. (1959) Lecture at the Annual Meeting of the American Physical Society (California Institute of Technology, Dec. 1959).

[22] Woodcock, C.L. and Horowitz, R.A. (1997) Electron microscopy of chromatin. METHODS: A Comparison to Methods in Enzymology 12, 84–95.

[23] Colton, R.J., Engel, A., Frommer, J.E, Gaub, H.E., Gewirth, R., Guckenberger, R., Heckl, W.M., Parkinson, B. and Rabe, J.,Eds., (1998) Procedures in Scanning Probe Microscopies, Wiley, England.

[24] Fotiadis, D., Scheuring, S., Muller, S.A., Englel, A. and Muller, D.J. (2002) Imaging and manipulation of biological structures with the AFM. Micron 33, 385–397.

[25] Ikai, A. (1996) STM and AFM of bio/organic molecules and structures. Surf. Sci. Reports 26, 261-332.

[26] Reich, Z., Kapon, R., Nevo, R, Pilpel, Y., Zmoro, S. and Scolnik Y. (2001) Scanning force microscopy in the applied biological sciences. Biotechnology Advances 19, 451-485.

[27] Beebe, T.P., Wilson, T. E., Ogletree, D.F., Katz, J.E., Balhorn, R., Salmeron, M.B. and Siekhaus W.J. (1989) Direct Observation of Native DNA Structures with the Scanning Tunnelling Microscope. Science 243, 370-243.

[28] Driscoll, R.J., Youngquist, M.G., Baldeschwieler, J.D. (1990) Atomic-scale imaging of DNA using scanning tunnelling microscopy. Nature 346, 294-296.

[29] Clemmer, C.R., Beebe, T.P. (1991) Graphite: A Mimic for DNA and Other Biomolecules in Scanning Tunneling Microscope Studies. Science 251, 640-642.

[30] Cricenti, A., Selci, S., Felici, A.C., Generosi, Gori, E., Djaczenko, W. and Chiarotti, G. (1989) Molecular Structure of DNA by Scanning Tunneling Microscopy. Science 245, 1226-1227.

[31] Tano, T., Tomyo, M., Tabata, H. and Kawai, T. (1998) Scanning Tunneling Microscope Observation and Manipulation of DNA and DNA-Related Molecules in Aqueous Condition. Jap. J. Appl. Phys. 37, 3838-3844.

[32] Tanaka, H., Hamai, C., Kanno, T. and Kawai, T. (1999) High-resolution scanning tunnelling microscopy imaging of DNA molecules on Cu (111) surfaces. Surf. Sci. 432, L611-L616.

[33] Hansma H.G. and Laney D.E. (1996) DNA binding to mica correlates with cationic radius: assay by atomic force microscopy. Biophys J. 70(4) 1933-9.

[34] Thomson, N. H., Kasas, S., Smith, B. L., Hansma, H. G. and Hansma, P. K. (1996) Reversible Binding of DNA to Mica for AFM Imaging. Langmuir 12(24); 5905-5908.

[35] Atomic force microscopy in Cell Biology. (2002) Jena, B. P. and Horber, J. K. H. (Editors).

[36] Handbook of Nanostructured materials and Nanotechnology. (2000) Nalwa, H. S. (Editor) Academic Press.

[37] Hansma, H.G., Vesenka, J., Siegerist, C., Kelderman, G., Morrett, H., Sinsheimer, R.L., Elings V., Bustamante, C. and Hansma, P.K. (1992) Reproducible Imaging and Dissection of Plasmid DNA Under Liquid with the Atomic Force Microscope. Science 256, 1180-1183.

---

[38] Schaper, A., Starink, J.P. and Jovin, T.M. (1994) The scanning force microscopy of DNA in air and in n-propanol using new spreading agents. FEBS letters 355, 91-95.

[39] Han, W., Dlakic, M., Zhu, Y. J., Lindsay, S.M. and Harrington, R.E. (1997) Strained DNA is kinked by low concentrations of Zn^{2+}. Proc. Natl. Acad. Sci. 94, 10565-70.

[40] Medalia, O., Englander, J., Guckenberger, R. and Sperling, J. (2002) AFM imaging in solution of protein-DNA complexes formed on DNA anchored to a gold surface. Ultramicroscopy 90, 103-112.

[41] Arai, T., Tomitori, M., Saito, M. and Tamiya, E. (2002) DNA molecules sticking on a vicinal Si(111) surface observed by noncontact atomic force microscopy. App. Surf. Sci. 188, 474-480.

[42] Maeda, Y., Matsumoto, T. and Kawai, T. (1999) Observation of single- and double-stranded DNA using non-contact atomic force microscopy. App. Surf. Sci. 140, 400-405

[43] Maeda, Y., Matsumoto, T., Tanaka, H. and Kawai, T. (1999) Imaging of the DNA (deoxyribonucleic acid) Double Helix Structure by Noncontact Atomic Force Microscopy. Jap. J. App. Phys. 38, L1211-L1212.

[44] Hansma, H. G., Revenko, I., Kim, K. and Laney, D. E. (1996) Atomic force microscopy of long and short double-stranded, single-stranded and triple-stranded nucleic acids. Nucleic Acids Res. 24 (4), 713-720.

[45] Eley, D. D. and Spivey, D. I. (1962) Semiconductivity of organic substances. Part 9.—Nucleic acid in the dry state. Trans. Faraday Soc. 58, 411-415.

[46] Fink, H.-W., and Schonenberger, C. (1999) Electrical conduction through DNA molecules, Nature, 398, 407-410.

[47] Porath, D., Bezryadin, A., de Vries, S. and Dekker,C. (2000) Direct measurement of electrical transport through DNA molecules. Nature 403, 635-637.

[48] De Pablo, P. J., Moreno-Herrero, F., Colchero, J., Herrero, J.G., Herrero, P., Baro, A. M., Ordejon, P., Soler, J. M., and Artacho, E. (2000) Absence of dc-Conductivity in λ-DNA. Phys. Rev. Lett. 85 (23), 4992-4995.

[49] Storm, A. J., van Noort, J., de Vries, S., and Dekker, C. (2001) Insulating behaviour for DNA molecules between nanoelectrodes at the 100nm length scale. App. Phys. Lett. 79 (23), 3881-3883.

[50] Kleine, H., Wilke, R., Pelargus, Ch., Rott, K., Pulher, A., Reiss, G., Ros, R. and Anselmetti, D. (2004) Absence of intrinsic electric conductivity in single dsDNA molecules. J. Biotech. 112, 91-95.

[51] Gomez-Navarro, C., Moreno-Herrero, F., dePablo, P.J., Colchero, J., Gomez-Herrero, J., Baro, A.M. (2002) Contactless experiments on individual DNA molecules show no evidence for molecular wire behaviour. Proc. Nat. Acid. Sci. USA 99 (13), 8484-8487.

[52] Ha, D. H., Nham, H., Yoo, K.-H, So, H.-M., Lee, H.-Y. and Kawai, T. (2002) Humidity effects on the conductance of the assembly of DNA molecules. Chem. Phys. Lett. 355, 405-409.

[53] Jo, Y. –S., Lee, Y. and Roh, Y. (2003) Current-voltage characteristics of λ- and poly-DNA. Mat. Sci. and Eng. C 23, 841-846.

[54] Iqbal, S.M, Balasundaram, G., Ghosh, S., Bergstrom, D.E., and Bashir, R. (2005) Direct current electrical characterization of ds-DNA in nanogap junctions. Appl. Phys. Lett. 86, 153901-3.

[55] Di Ventra M. and Zwolak, M. (2004) DNA Electronics. Encyclopedia of Nanoscience and Nanotechnology. Vol. X, 1-19.www.aspbs.com/enn

[56] Rinaldi, R., Biasco, A., Maruccio, G., Arima, V., Visconti, P., Cingolani, R., Facci, P., De Rienzo, F., Di Felice, R., Molinari, E., Ph. Verbeet, F. and Canters, G. W. (2003) Electronic rectification in protein devices. Appl. Phys. Lett. 82 (3), 472-474.

[57] Davis, J.J., Morgan, D.A., Wrathmell, C.L. and Zhao A. (2004) Scanning probe technology in metalloprotein and biomolecular electronics. 151(2), 37-47.

[58] Alessandrini, A., Salerno, M., Frabboni, S., and Faccia, P. (2005) Single-metalloprotein wet biotransistor. Appl. Phys. Lett. 86, 133902-(1-3).

[59] Biasco, A., Maruccio, G., Visconti, P., Bramanti, A., Calogiuri, P., Cingolani, P. and Rinaldi, R. (2004) Self-chemisorption of azurin on functionalized oxide surfaces for the implementation of biomolecular devices. Mat. Sci. and Eng. C 24, 563–567.

[60] Xu, D., Watt, G.D., Harb, J. N. and Davis, R. C. (2005) Electrical Conductivity of Ferritin Proteins by Conductive AFM. Nanolett. 5 (4), 571-577.

[61] Molecular Electronics. (1992) Ashwell, G.J. (Editor), Wiley.

[62] Li, X.-Q. and Yan, Y.(2001) Electrical transport through individual DNA molecules. Appl. Phys. Lett. 79 (14) 2190-2192.

[63] Intermolecular and Surface Forces. (1991) Israelachvili, J. Academic Press.

[64] Davis, J.J. (2003) Molecular bioelectronics. Phil. Trans. R. Soc. Lond. A. 361, 2807-2825.

[65] Prisco, U., Leung, C., Xirouchaki, C., Jones, C.H., Heath, J.K and Palmer, R.E. (2005) Residue-specific immobilisation of protein molecules by size-selected clusters. J. of R. Soc. Int. 1(3) 169-175.

---

[66] Johansson, A. and Stafstrom, S. (2000) Interactions between molecular wires and a gold surface. Chem. Phys. Lett. 322, 301-306.

[67] Vuillaume, D. and Lenfant, S. (2003) The metal/organic monolayer interface in molecular electronic devices. Microelectronic Eng. 70, 539-550.

[68] Kushmerick, J.G. (2005) Metal-molecule contacts. Materials Today, Jul/Aug. 26-30.

[69] Patrone, L., Palacin, S., Bourgoin, J.P., Lagoute, J., Zambelli, T. and Gauthier, S. (2002) Direct comparison of the electronic coupling efficienct of sulphur and selenium anchoring groups for molecules adsorbed onto gold electrodes. Chemical Physic, 281, 325-332.

[70] Kushmerick, J. G., Naciri, J., Yang, J. C. and Shashidhar, R. (2003) Conductance Scaling of Molecular Wires in Parallel. Nano Lett. 3 (7) 897-900.

[71] Seminario, J. M., De La Cruz, C. E. and Derosa, P. A. (2001) A Theoretical Analysis of Metal-Molecule Contacts J. Am Chem. Soc. 123 (23) 5616-5617.

[72] Endres, R.G., Cox, D.L. and Singh, R.P. (2004) Colloquium: The quest for high-conductance DNA. Rev. Mod. Phys. (76), 195-214.

CHAPTER 3

Scanning Probe Microscopy

3.1 Introduction

Atomic force microscopy (AFM) was developed in 1986 by Binnig *et al.*[1] and shares many features with its predecessor, the scanning tunnelling microscopy (STM). STM is a specialised technique for probing structures at the nanoscale and is based on the quantum mechanical tunnelling behaviour of electrons between a conducting tip and sample. AFM shares a similar purpose, but instead of a tunnel current it makes use of interatomic forces that exist between a tip and sample. These forces are now routinely exploited in AFM, making it an extremely versatile technique for three-dimensional, real-space imaging of almost any sample at the nanoscale (*e.g.* biological cells, single molecules *etc*). It has the unique ability to function as an imaging device and a force sensor and is capable of achieving nanometre resolution in gaseous, vacuum and liquid environments. Data interpretation can be challenging and a fundamental understanding of this surface analysis technique is crucial to interpret experimental results in meaningful way. Scanning probe microscopy (SPM) systems share many features but differ in signal detection mechanisms. In this chapter the principles of scanning tunnelling microscopy are briefly addressed, the principles of atomic forces with their application to atomic force microscopy are described and details of signal detection and instrumentation for AFM are given.

3.2 Scanning Tunnelling Microscopy

The scanning tunnelling microscope (STM) was invented in 1982 by Binnig et al.[2] and allows the visualization of regions of high electron density. From this, the positions of individual atoms and molecules on the surface of a lattice can be inferred. A conductive tip (a piece of metal wire) is brought within close proximity to a conductive sample and a bias voltage V is applied. At sufficiently close tip-sample separations (*e.g.* a few atomic diameters) quantum mechanics allows electrons to traverse the energy barrier at the interface of materials due to a bias voltage imposed between the two. Thus, a small number of electrons travel from one conducting material to the other, across the tip-sample gap, via quantum mechanic tunnelling[3].

The tunnelling current I depends on the tip-sample separation and decays exponentially with the barrier width (tip-sample separation) z,

$$I \propto e^{-2kz} \tag{3.1}$$

where k describes the wave vector which is a function of energy and applied voltage

$$k = \frac{\sqrt{2m(V-E)}}{\hbar} \tag{3.2}$$

V is the potential of the barrier, E is the energy of the electron, m is the mass of an electron and $\hbar$ is Planck's constant divided by 2π. Tunnelling current is highly dependent on z distance: a variation of just in of 1 Å in z between tip and a metal sample gives rise to an order of magnitude change in current. Tip-sample separations can therefore be measured via variations in tunnel current. Two commonly used modes of imaging are *constant-height* and *constant-current* mode. During *constant-height* mode, the tip-sample separation is fixed and variations in tunnel current are recorded. Higher tunnel currents are given by brighter contrast. For *constant-current* mode a constant tunnel current is maintained via the feedback system and the scanner's z-position is recorded. Higher topographical features are given by brighter intensity in constant current mode although both electronic and topographical properties of the sample influence the final image result. Electronic properties of relatively flat surfaces are usually probed in *constant-height* mode and topographic structures are observed in *constant-current* mode. Tunnel current, bias voltage, probe size and shape, imaging environment, tip-adsorbate and adsorbate-substrate interactions are all influential factors.

Although *constant-current* mode is used for the imaging of biological adsorbates, both electronic and topographical properties of the sample will contribute to the final result. AFM overcomes this dilemma so that topographical features of bulky biological molecules can be mapped by monitoring the tip-sample forces without electronic contributions.

3.3 Principles of Tip-Sample Forces

Atomic force microscopy is based on the detection of forces between a tip and sample. These forces are highly dependent on the tip-sample separations as shown in

Figure 3.1. At tip-sample contact, interactions are dominated by *short-range* repulsive forces; at increased distances, *longer-range* attractive forces take over[3].

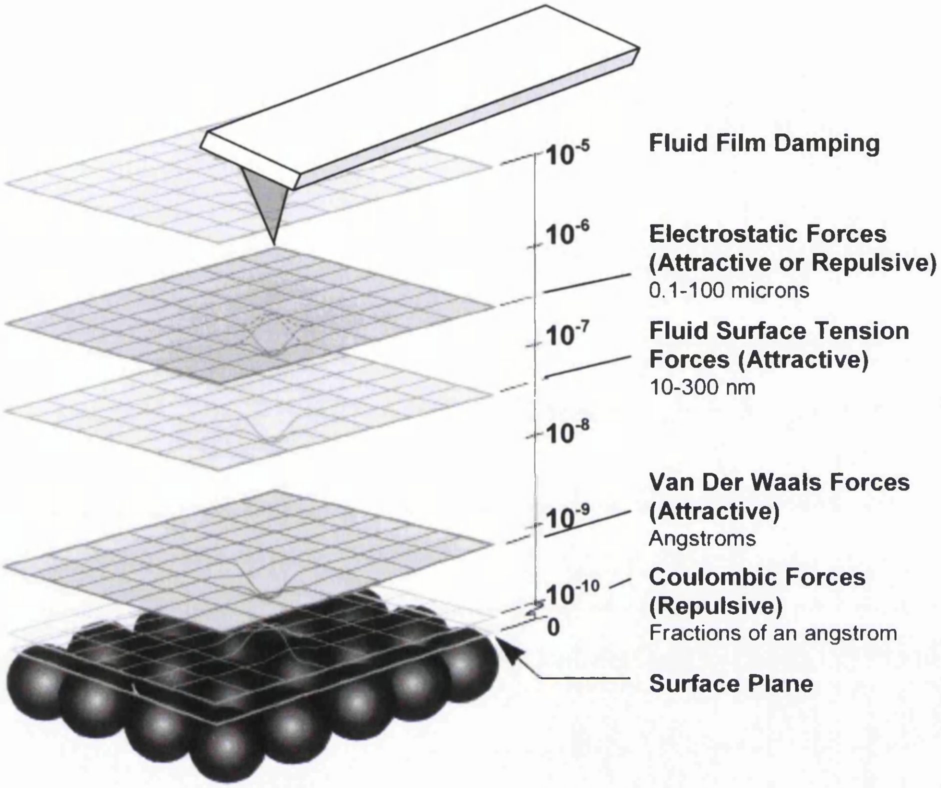

Figure 3.1. Different forces are associated with different tip-sample separations. At small separations, the interactions are predominantly short-range and repulsive. At increased separations attractive forces reign.

3.3.1 Short-Range Interactions

Short-range interactions are predominantly repulsive and are sufficiently strong to deflect macroscopic structures such as AFM cantilevers if they are placed within a few nm. Van der Waals (VdW) interactions have three components: polarization, induction and dispersion[3]. Polarizations are permanent dipole moments such as those occurring in water and $BaTiO_3$. Induction concerns induced dipoles and dispersion refers to instantaneous fluctuations of electrons occurring at the frequency of light causing optical dispersion. Material properties dictate their VdW potential and the interaction forces.

For two identical gas molecules, the VdW potential is expressed as

$$U_{vdw} = -\left(\frac{1}{4\pi\varepsilon_0}\right)^2 \left(\frac{\mu^4}{3kT} + 2\mu^2\alpha + \frac{3\alpha^2\hbar\omega}{4}\right)\frac{1}{z^6} \qquad \textbf{(3.3)}$$

where μ is the dipole moment, T is temperature, α is polarizability, ε_0 is the permittivity of free space, and $\hbar\omega$ is the ground state of electrons. Assuming that dispersion dominates and is isotropic, additive and non-retarded, an approximation of the interaction is used for more complex systems. For this case, the VdW potential between two atoms is $-C/z^6$; between an atom and a flat surface is $-C/z^3$; between two planes is $-A/12\rho z^2$ and between a sphere and plane is $-AR/6z$ where z is the distance between the two objects, R is the radius of the sphere, A is the Hamaker constant and C is a constant or *London coefficient.* As well as repulsive terms the complete interaction includes attractive terms. The Hamaker constant embodies the properties of materials (including collective interactions and polarization if calculated from dielectric and optical properties) and is given as

$$A \approx \pi^2 C\rho_1\rho_2 = \left(\frac{3\alpha^2\hbar\omega}{4(4\pi\varepsilon_o)^2}\right)$$

or,

$$A = \frac{3kT}{4}\left(\frac{\varepsilon_1-\varepsilon_3}{\varepsilon_1+\varepsilon_3}\right)\left(\frac{\varepsilon_2-\varepsilon_3}{\varepsilon_2+\varepsilon_3}\right) + \frac{3\hbar\omega}{8\sqrt{2}}\left[\frac{(n_1^2-n_3^2)(n_2^2-n_3^2)}{(n_1^2+n_3^2)^{1/2}(n_2^2+n_3^2)^{1/2}[(n_1^2+n_3^2)^{1/2}(n_2^2+n_3^2)^{1/2}]}\right] \qquad \textbf{(3.4)}$$

where ρ is the density, k is Boltzmann's constant, T is temperature, ε_i is the dielectric constant in medium i (*i.e.* (1) sample, (2) tip, (3) material separating them) and n_i is refractive index. For most solids the Hamaker constant is of the order of 10^{-19} J. Figure 3.2 shows the result of an interaction between two identical gas molecules.

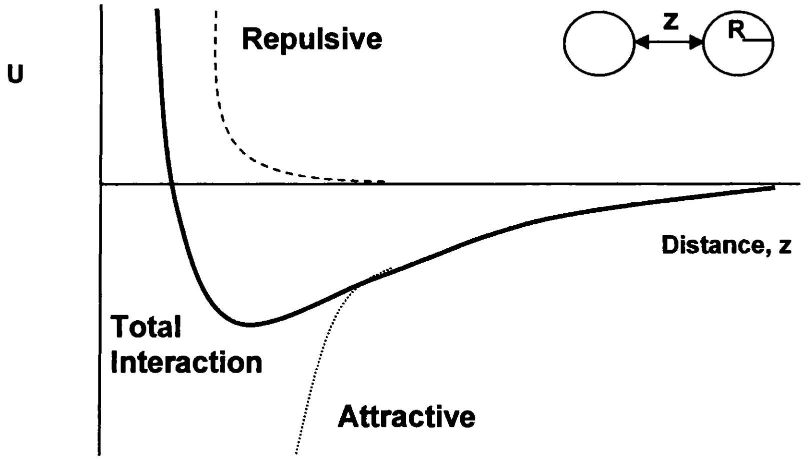

Figure 3.2. A schematic to show the total interaction between two identical molecules at separation z.

The relationships linking the potential, force (which is measurable with AFM) and force gradient are given in the following table:

		For a Spring	**For a sphere-plane,** $z << R$
Potential	U	$= 1/2\ kz^2$	$\propto 1/z$
Force	$-dU/dz$	$= -kz$	$\propto -1/z^2$
Force Gradient	$-d^2U/dz^2$	$= -k$	$\propto -1/z^3$

Image resolution is related to the slope of the potential curve so that atomic resolution is only possible at small tip-sample distances. Forces as low as 10^{-15} N have been measured with AFM although theoretical predictions imply forces at 10^{-18} N should be detectable[3,4].

3.3.2 Long-Range Interactions

In addition to the short-range forces existing between two objects' surfaces, long-range interactions are also present. Long-range interactions include electrostatic attraction or repulsion, current-induced or static-magnetic, and capillary forces caused by surface energy of water condensed between the tip and sample. At small tip-sample separations, long-range force contributions are small. However, as the tip-sample distance increases, long-range forces become more significant. The difference in decay length of short- and long-range forces provides a means of distinguishing the two types of interaction. Simplified relations concerning forces experienced by a tip above a homogeneous surface for electrostatic and magnetic interactions are described in Eq. 3.5 & 3.6 respectively:

$$F_{electrostatic} = -\frac{1}{2}(\Delta V)^2 \frac{\partial C}{\partial z} \tag{3.5}$$

$$F_{magnetostatic} = \nabla\left(m \bullet B_{sample}\right) \tag{3.6}$$

The difference in potential between sample and tip is given by ΔV, the tip-sample capacitance is denoted by C as a function of z, the magnetic field emanating from the sample surface is B_{sample} and the magnetic dipole of the tip is given by m. Note that specialised conducting or magnetic AFM tips are required for electric or magnetic field applications so that electrostatic force imaging (EFM) and magnetic force imaging (MFM) can be performed.

3.3.3 AFM Imaging

At the heart of AFM operation is the detection of forces between a probe tip and sample. Force interactions are measured via deflections of a cantilever tip in response to surface properties. Cantilever deflections are kept constant by varying the vertical position of the tip during constant force mode to give maps of surface topography. This is static, deflection mode and is not the most sensitive mode of imaging. Dynamic modes can be used which make use of the oscillatory or vibrational cantilever properties. Both cantilever material and dimensions influence its oscillatory properties and the resonance is located by oscillating the cantilever over a range of frequencies and measuring its root mean square (RMS) response (Figure 3.3).

By measuring the change in amplitude, both the magnitude and sign of the force gradient can be found for the case when the cantilever is initially oscillated away from its resonance. A constant force gradient image is produced by varying the vertical position of the tip so that the amplitude of oscillation at a specific frequency remains constant.

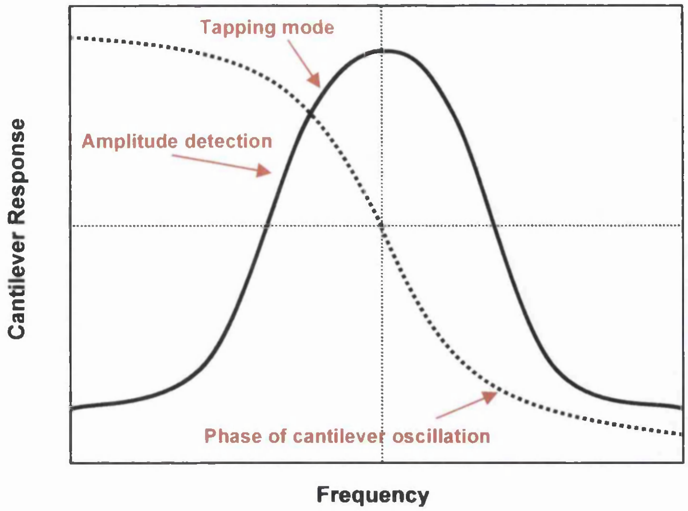

Figure 3.3. The frequency response of dynamic cantilever. Maximum amplitude is reached at the cantilever's resonant frequency. The second (dotted) line represents the phase of the cantilever oscillation.

Quality factors (or Q-factors) are attributed to oscillating cantilevers and are defined as the ratio of peak height at resonance to peak width at the full-width half maximum (FWHM). The Q-factor is dependent on the particular tip and can be modified via the surrounding medium. Oscillating the tip in certain liquids or vacuum environment can adjust Q by several orders of magnitude. High Q-factors improve signal-to-noise ratios but can also increase response times. Furthermore, dynamic modes are generally considered less damaging for soft surfaces or those with weakly bound adsorbates.

Both frequency and phase shifts can be used as imaging signals for surface maps although theoretically any force which produces measurable cantilever deflections or changes in resonant frequency can be used for imaging.

This section has introduced the principles of atomic forces and the ways in which they may be detected with AFM. The next section describes the AFM instrumentation necessary for signal detection before the modes of operation are re-examined in more depth.

3.4 AFM Instrumentation

3.4.1 General Description

Scanning probe microscopes have five essential components: the tip, scanner, detector, an electronic control system and a vibration isolation system. For AFM, a cantilever tip (or force sensor) is positioned over a sample placed on a piezo-scanner. Imaging signals are derived from cantilever deflections that are measured by laser reflections from the cantilever on to a position-sensitive photodiode (PSPD) as shown in Figure 3.4.

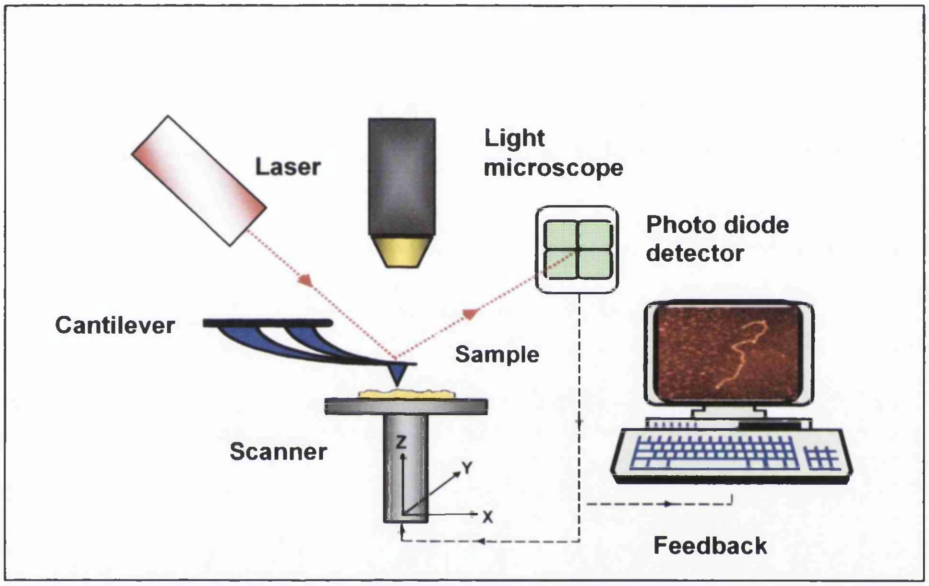

Figure 3.4. A schematic showing signal detection in AFM[5].

3.4.2 The Force Sensor

The principle of AFM is to detect, measure and control the interactions between a force sensor and sample to gain insight to the sample's properties. Therefore, the force sensor is a key component in this process and determines the ultimate resolution achievable. AFM tips are mounted on small flexible cantilevers to form unified probes. These are commercially available and ready for use. Tip shape and sharpness are important as they determine the image resolution achievable and present-day silicon technology and micro-fabrication allow cantilever tips (Si and Si_3N_4) to be fabricated in batches on whole Si wafers. These methods are highly reproducible, less labour intensive and their size can be significantly reduced compared to the first ever probes which were hand-made from sharpened wire or pieces of diamond glued to a metal foil or wire cantilever. When brought within 20 nm of a surface, it is important that the force sensor responds to the attractive and repulsive forces of tip-sample interaction in some detectable way. The force sensor is described below, firstly in terms of their cantilever properties, and secondly its tip geometry.

3.4.2.1 Cantilever Properties

Cantilevers are used to measure tip-sample interactions. Two cantilever geometries are currently available: V-shape and beam (Figure 3.5).

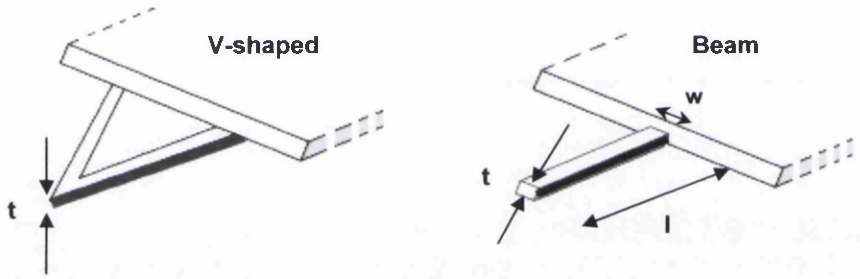

Figure 3.5. Cantilever geometries: V-shaped and beam.

The mechanical properties of cantilever tips are defined by the geometry, dimensions and the material used. The force constant (or spring constant) k and resonance frequency (fundamental eigenfrequency) f_o of the beam cantilever are given by

$$k = \frac{E}{4}\left(\frac{wt^3}{l^3}\right) \tag{3.7}$$

and

$$f_0 = \frac{1}{2\pi}\sqrt{\frac{E}{\rho}}\frac{t}{l^2} = \frac{1}{2\pi}\sqrt{\frac{k}{m_{eff}}} \quad . \tag{3.8}$$

The cantilever is conceptually treated as a classical, one-dimensional, lightly loaded, “fixed-free” beam. Young’s modulus is given by E, the density of the chosen cantilever material is given by ρ, and cantilever width, thickness and length are given by ω, t and l respectively. By varying these parameters, cantilevers can be fabricated with k = 0.01-200 N/m, and f_o= 1-400 kHz. Manufacturers’ guidance are rough estimates and properties will vary significantly across cantilevers on a single wafer. For contact-mode, where large forces could be unintentionally applied to the surface, cantilevers with low spring constants ($k < 1$ N/m) are used. For dynamic modes, stiffer cantilevers ($k > 5$ N/m) with $f_o > 100$ kHz are favoured. High resonant frequencies ensure an adequate signal-to-noise ratio is achieved with minimum probability of cantilevers sticking to surfaces.

Two methods are used to drive the cantilever: acoustic and magnetic drive. For acoustic drive, an oscillator (frequency ω) supplies a voltage drive to a piezoelectric actuator (lead zirconium titanate). Sound waves are generated in the cantilever holder. The frequency ranges from 10 kHz to MHz, corresponding to long wavelength modes that act at the base of the cantilever. When the driving frequency approaches a bending mode resonance of the cantilever, the cantilever is forced into bending and is detected by the PSPD as an *ac* signal. For magnetic drive, an alternating current (frequency ω) is passed through a solenoid in close proximity to a cantilever coated with a magnetic film. The base remains stationary and bending of the cantilever is induced either via magnetostriction or magnetic interaction of film moment and applied field. Thus, a bending torque is initiated. Using magnetic drive, the cantilever can be driven at any frequency though it has been shown that less noise is associated with magnetic drive in liquid[3]. For acoustic drive, displacements of the cantilever base only occur at mechanical resonances of that component and so the frequency may be limited[3].

3.4.2.2. Tip Shape

The basic tip geometries are pyramidal, conical and tetrahedral. All geometries are available in Si and SiO_2 with conical being the favourite. Si_3N_4 are usually pyramidal. Purchased probes are ready for use although they can be sharpened or chemically modified depending on the required application. Tip radius of curvature r, sidewall angles θ and tip length l are key properties (Figure 3.6).

The tip apex is approximated by a hemisphere with radius of curvature r (*i.e.* not atomically sharp). The actual sharpness is difficult to measure accurately and estimates are made during manufacture. Imaging conditions are likely to influence the resolution achievable and the best means of gauging tip sharpness is to scan a standard reference sample. Both the sidewall angles and length influence scanning of steep slopes, trenches and surface pits. (*e.g.* for accurate measurement of a 1 μm deep and narrow trench, the tip must be narrow enough to totally penetrate the gap otherwise the trench is underestimated).

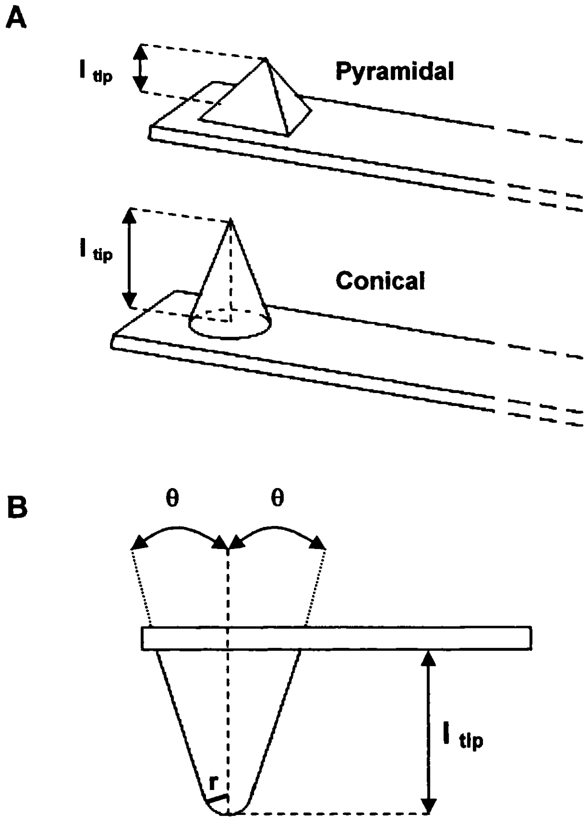

Figure 3.6. The geometry of AFM tips. (A) Pyramidal and conical. (B) Parameters used for defining individual tips: tip length l $_{tip}$, radius of curvature r, and sidewall angle θ.

For contact mode AFM, pyramidal tips are often used. These are made from Si_3N_4 and have a standard sidewall angle of 35°. The radius of curvature for a standard Si_3N_4 tip is 20-60 nm and can be sharpened. Such tips are very resilient although they are not suited for imaging deep, narrow features. Atomic scale contrast has been observed but with a highly specialised practical set-up (*e.g.* using low temperatures where the coefficients of thermal expansion are small, and the long-range attractive forces are cancelled using an electromagnetic force applied to the cantilever)[3,6]. For Si tips, the radius of curvature, sidewall angles and aspect ratios can be modified through etching or focus ion beam (FIB) to give smaller radii <20 nm and significantly lower sidewall angles. A typical force sensor used for dynamic modes of AFM is shown in Figure 3.7. For both TM- and NC-AFM, similar tips are used although those for NC-AFM tend to have shorter, stiffer cantilevers. Deep, narrow gaps may be accessible for tip sidewalls approaching 0°. *Si* probes are stiffer than silicon nitride cantilevers, having larger force constants and resonant frequencies.

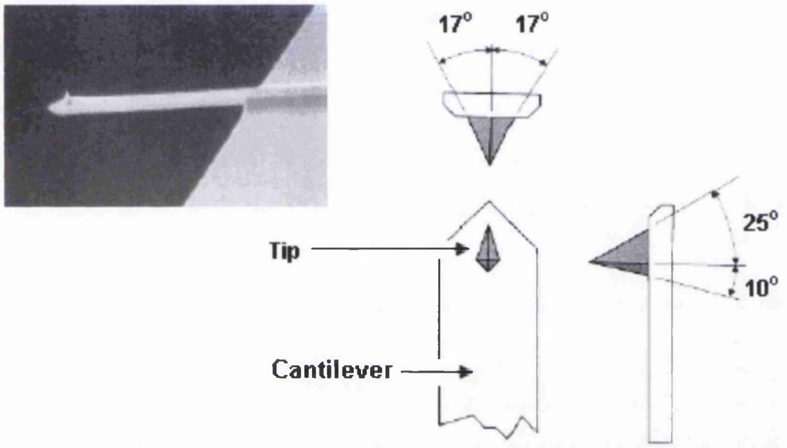

Figure 3.7. A silicon probe for tapping-mode AFM. Tip and cantilever are formed by etching a single silicon crystal and is optionally coated with Al for high reflectivity. The typical cantilever properties are spring constant = 20-100 N/m, resonant frequency = 200-400 kHz, cantilever length = 125μm and a (desired) tip radius of curvature = 5-10 nm.

Depending on the application, tips can be modified with metal coatings (*e.g.* for magnetic force microscopy (MFM), electrostatic force microscopy (EFM) and scanning capacitance microscopy (SCM)) or functionalised (for chemical force microscopy) for probing chemical and molecular interactions.

3.4.2.3 Signal Measurement

Intermolecular forces act between the tip and sample causing the cantilever to bend and flex in response to the surface as the tip is raster scanned across the sample. In order to measure cantilever deflections, a laser beam is reflected from the cantilever coated with a reflective metal (*Au* or *Al*) on to the position-sensitive photodiode (PSPD) as shown in Figure 3.8. The PSPD tracks changes in tip position with great precision. Measured signals provide a means of feedback and are derived from the normal force. These signals are used for maintaining appropriate tip-sample separations via the piezo scanner.

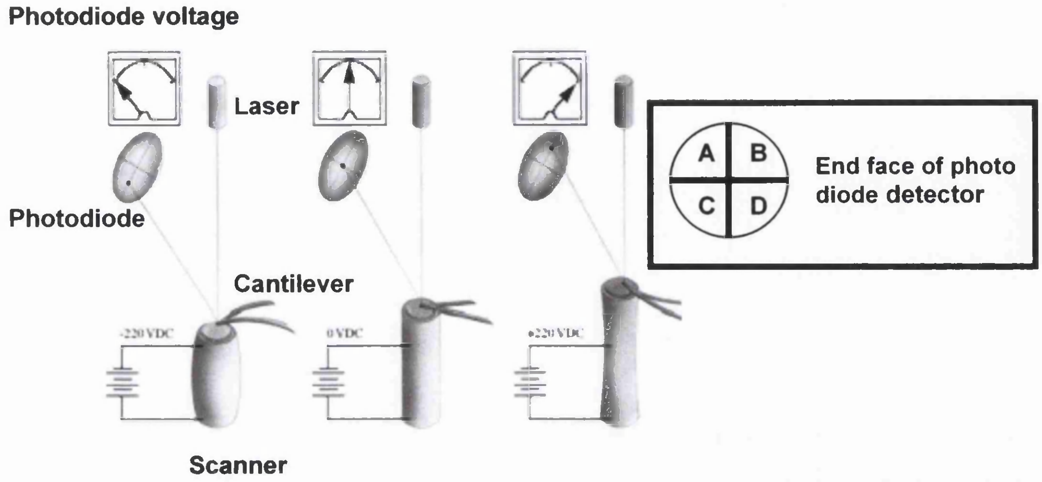

Figure 3.8. Measurement of cantilever deflections in AFM. As the force sensor tip bends and flexes in response to the surface, cantilever deflections are measured via reflections of laser beam on to a position-sensitive photodiode. Variations in tip oscillation and position are quantified by the ratio of signals in the photodiode quadrants[7].

The four-segmented diode measures vertical motion:

$$Z = (A + C) - (B + D) \ ,$$

and lateral motion:

$$X = (A + B) - (C + D) \, .$$

Inter-atomic forces, frictional, magnetic and electrostatic forces all act to attract or repel the tip and feedback for Z produces topographic data and images are built up as the tip is scanned in close proximity to a surface in a raster pattern. The lateral signal X can be used for local friction measurement.

Optical levers are capable of atomic resolution when coupled with appropriate apparatus in noise-free environments (*i.e* free from thermal, electronic and vibrational noise). In such an environment, the ‘laser shot noise’ influences the smallest signal detectable on the PSPD but with adequate laser power, the shot noise is vastly minimised. In practice, image resolution is affected by the tip profile, fluid layers and thermal movement (sub-angstrom resolution is only possible at low temperatures).

3.5 Modes of Operation

Several AFM modes have been developed with aims of increasing the resolution achievable and their versatility. The tip-sample separation is different for each mode (Figure 3.9).

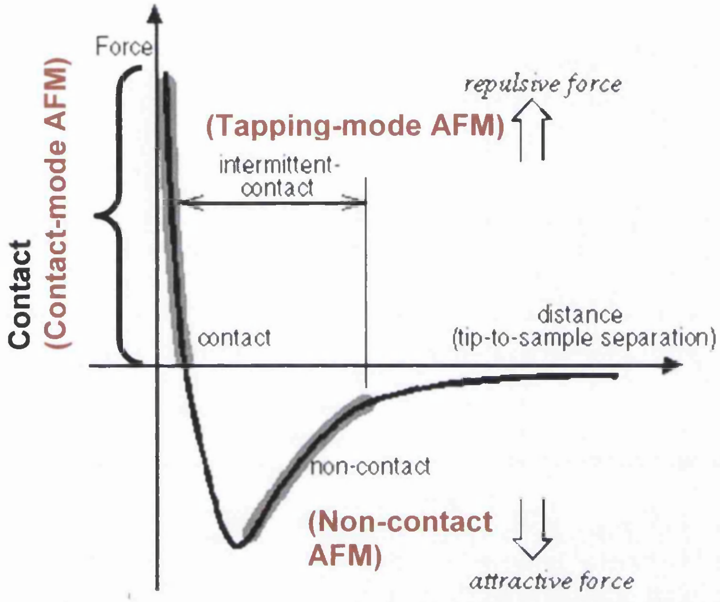

Figure 3.9. During contact-mode, the tip-sample forces are short-range and repulsive. For non-contact mode, forces are predominantly longer-range and attractive. During tapping mode, both of short- and longer-range forces are exploited.

For contact-mode, the tip is positioned within a few angstroms of the sample surface in the repulsive force regime. At increased separations the tip-sample forces become attractive and dynamic modes of AFM are used for force detection. Different AFM modes are suited to different sample compositions and environments. The modes are distinguished as either static-AFM (contact-mode or ‘dc’ mode) or dynamic-AFM (intermittent- and non-contact modes or ‘ac’ mode) as aforementioned. Cantilevers are oscillated above surfaces in dynamic modes and are especially useful for studying soft materials when contact-mode would otherwise cause specimen damage.

Force measurement is used as the feedback signal in the static mode whilst amplitude and frequency modulation are used for signal detection in the dynamic modes. Amplitude modulation is typically used for tapping-mode AFM. Frequency modulation is used for non-contact AFM in vacuum.

Note that *non-contact* refers to the fact that no permanent deformation or wear is caused to either the front atom of the tip or sample during AFM scanning.

3.5.1 Static AFM

In contact-mode AFM the tip is brought into contact with the substrate and the force acting between tip and sample F_{ts} is used as the imaging signal. This force is repulsive and induces a cantilever deflection q' where

$$q' = \frac{F_{ts}}{k} \ . \tag{3.9}$$

Deflections are designed to be significantly larger than the deformations made to the sample by using suitable k values for cantilevers (0.01 N/m to 5 N/m) compared to the interatomic spring constants of solids (10 N/m to 100 N/m). In other words, the cantilever is soft compared to the bulk atoms in both tip and sample. Deflections are measured using a PSPD and a feedback loop maintains a pre-set constant deflection by continually adjusting the z-position of the cantilever tip such that the surface topography is followed during scanning with constant force. True atomic resolution has been recorded using static AFM but the setup is not straightforward. Materials with low thermal expansion coefficients should be used or low temperature scanning should be performed to reduce thermal expansion coefficients and the tip can be immersed in liquid to cancel the effect of long-range attractive forces. For contact-mode AFM, data is given in terms of a topography map $z(x, y, F_{ts} = const)$.

3.5.2 Dynamic AFM

Both tapping- and non-contact modes are dynamic modes of AFM. Cantilevers are mounted on actuators and deliberately oscillated. A general description of force detection using oscillating cantilevers was given in section 3.3.3 and the next sections re-examine signal detection in more depth in terms of amplitude and frequency modulation.

3.5.2.1 Amplitude Modulation

Amplitude modulation (AM) is favoured for tapping-mode AFM[8]. A piezo stack is driven with constant amplitude A_{drive} and constant frequency f_{drive} so that it excites the cantilever's substrate vertically and the cantilever tip oscillates in free air with frequency near its resonance f_0 with amplitude 20-100 nm. As the oscillating cantilever-tip is moved towards the surface the amplitude decreases as the tip lightly "taps" on the sample and strongly interacts with the surface at the bottom of its cycle only. Elastic and inelastic interactions change the amplitude and phase of the cantilever as the piezo stack continues to excite the cantilever's substrate with the same energy. A constant RMS of oscillation signal is measured and a sinusoidal electronic signal generated. Feedback loops act on these signals to maintain a constant oscillation amplitude and a constant "setpoint" is maintained via vertical positioning of the scanner at each x and y data point by comparing signals to the amplitude stored by the computer to form the topographic image of the sample surface. Changes in amplitude do not happen instantaneously with tip-sample interactions but at timescale τ_{AM}

$$\tau_{AM} \approx \frac{2Q}{f_0}. \tag{3.10}$$

Q values can reach 100,000 in vacuum and as a result AM is slow. Nevertheless, TM-AFM is fast in ambient and liquid environments. Cantilevers are usually stiff enough to overcome capillary forces present whilst imaging in air. The resonant frequency for TM in air is typically ≥ 100 kHz. In liquid the cantilever is damped by the fluid and is driven at a frequency matching that of an acoustic mode of the fluid cell not the cantilever's resonance in free air. Low forces are used for imaging of biological molecules to minimise sample deformation. Alternatively, the sample is made stiffer by cooling to liquid nitrogen temperatures (cryo-AFM). In both environments images are produced by mapping the vertical motion of scanner at each lateral data point as it acts to maintain a constant oscillation amplitude. The key advantage of tapping-mode over contact-mode is the elimination of high lateral shear forces. Interactions between the tip and the surface depend not only on sample topography but also on characteristics such as hardness, elasticity and adhesion. The movements of the cantilever tip are therefore dependent on these properties as well as topographic structure.

Phase imaging is related to the phase shift of the sinusoidal oscillation between the driving signal as applied to the cantilever and the actual cantilever oscillation[8].

Mechanical properties such as sample elasticity can damp the cantilever's oscillations resulting in this shift in phase. Phase imaging can be performed by recording the phase shift during normal tapping mode operation. Sensitivity to the sample's mechanical properties is useful for distinguishing sample composition such as polymers with different components with varying stiffness. The key features of amplitude-modulated TM-AFM can be summarised:

- The cantilever is oscillated at a fixed frequency close to the resonant frequency with large amplitude of oscillation.
- Changes in *amplitude* and the *phase* are used as feedback signals.
- Implemented at a close range in ambient conditions involving repulsive tip-sample interaction (difficult to obtain atomic resolution).
- Change in amplitude in AM mode does not occur instantaneously with change in tip-sample interaction, but on a timescale $\tau_{AM} \approx \frac{2Q}{f_0}$.
- The use of high Q-factors reduces noise but also slows down the AM mode.

3.5.2.2 Frequency Modulation

In many AFM systems a cantilever touches the surface at some point during scanning. However, weak inter-atomic forces are still detectable a few angstroms away from the surface if a suitable detection system is used. Frequency-modulated (FM) AFM detects these weak attractive forces and overcomes the lengthy timescales associated with amplitude modulation[6,8,9,10]. The cantilever is oscillated above a sample surface with a small, constant amplitude at a frequency larger than its resonant frequency. Weak attractive forces between the tip and sample influence the oscillation frequency. The imaging signal is phase shifted and subject to automatic gain control before being fed back to the cantilever via the actuator in positive feedback (Figure 3.10).

Surface topography is traced out as feedback electronics act maintain a pre-set frequency shift. The high sensitivity to interaction forces gives rise to outstanding spatial resolution and typical tip-sample forces in NC-AFM are less than 1 nN.

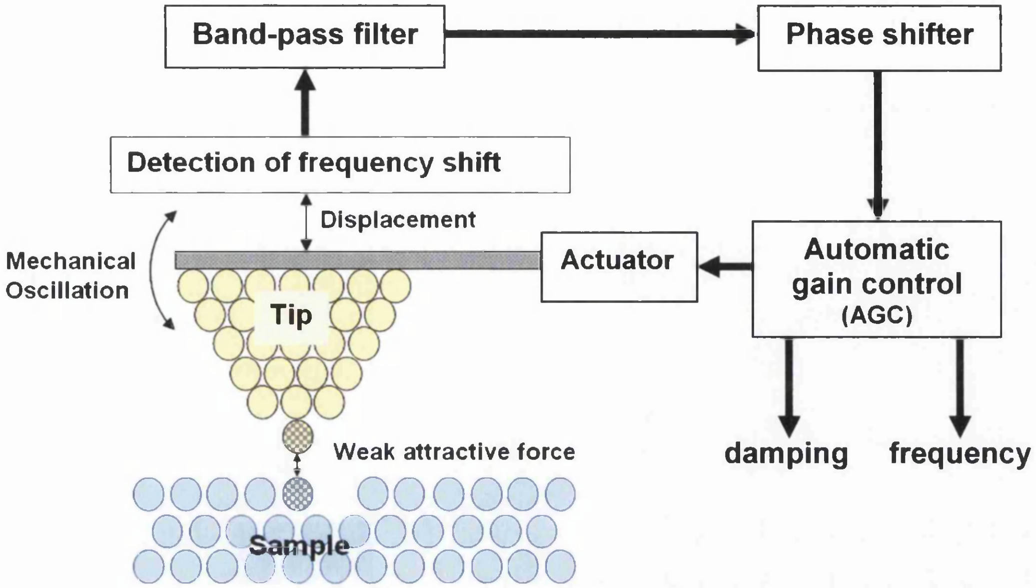

Figure 3.10. A schematic to show frequency modulation in NC-AFM.

NC-AFM is performed in ultra-high vacuum (UHV). VdW, electrostatic and magnetic forces can be detected up to 100 nm from the surface. A frequency shift is induced from these forces and is measured relative to its reference driving frequency (Figure 3.11).

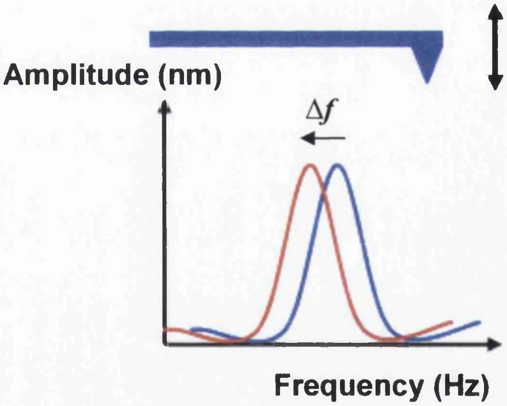

Figure 3.11. The frequency shift (Δf) is measured relative to the reference frequency (f_0) during non-contact AFM.

Controlled positive feedback is applied to a cantilever with eigenfrequency f_0 and spring constant k such that it oscillates with constant amplitude A (Figure 3.12). When the phase shift φ between the driving signal and the actual cantilever motion is $\varphi = \pi/2$ then $f = f_0$. However, a change in f takes place due to tip-sample forces such that $f = f_0 + \Delta f$. A relationship is established between measured frequency shifts and tip-sample interactions. As the tip is brought close to a sample, the potential energy (V_{ts}) between tip and sample causes a force (F_{ts}) between the tip and sample in the z-direction where

$$F_{ts} = \frac{-\partial V_{ts}}{\partial z} \tag{3.11}$$

and a tip-sample spring constant (k_{ts}) can be defined

$$k_{ts} = \frac{-\partial F_{ts}}{\partial z}\left(= \frac{-\partial^2 V_{ts}}{\partial z^2}\right). \tag{3.12}$$

F_{ts} or a quantity derived from it can be used as the imaging signal for AFM. (Note, F_{ts} has both short- and long-range contributions).

During the oscillation cycle assuming the force gradient k_{ts} is constant the frequency shift is be given by

$$\Delta f = f_0 \frac{k_{ts}}{2k}. \tag{3.13}$$

The oscillator circuit is important in frequency-modulated AFM and directs cantilever behaviour. Cantilevers are treated as damped harmonic oscillators that are driven externally. For sinusoidal excitations of cantilever (quality factor $Q >> 1$) the magnitude of the response of cantilever (*i.e.* its amplitude A) can be expressed as

$$|A| = \frac{|A_{drive}|}{\sqrt{\left(1 - \frac{f_{drive}^2}{f_0^2}\right)^2 + \frac{f_{drive}^2}{f_0^2 Q^2}}}, \tag{3.14}$$

where A_{drive} and f_{drive} are the driving amplitude and frequency respectively. The phase between driving and measured signals is given by

$$\varphi = \arctan\left[\frac{f_{drive}}{Qf_0\left(1 - \frac{f_{drive}^2}{f_0^2}\right)}\right]. \tag{3.15}$$

The oscillator circuit allows controlled positive feedback with $\varphi = \pi/2$ so that a constant cantilever oscillation amplitude is achieved. Note that the driving frequency is not freely chosen but is influenced by f_0, Q, phase angle φ and tip-sample forces. Electronics for controlling the oscillator and frequency demodulator are crucial components and further details can be found elsewhere[10].

In linking frequency shifts to physical tip-sample interactions, oscillating cantilevers are described as weakly disturbed harmonic oscillators. However, during classic FM-AFM, k_{ts} is not constant but varies by orders of magnitude in a single oscillation cycle. A perturbation approach is required for the calculation of the frequency shift Δf. A text-book interpretation of NC-AFM is given in Figure 3.12. It shows the deflection $q'(t)$ of the cantilever tip as it is oscillated with amplitude A, at a separation $q(t)$ from the sample. The nearest point to sample is $q = d$ and $q(t) = q'(t) + d + A$.

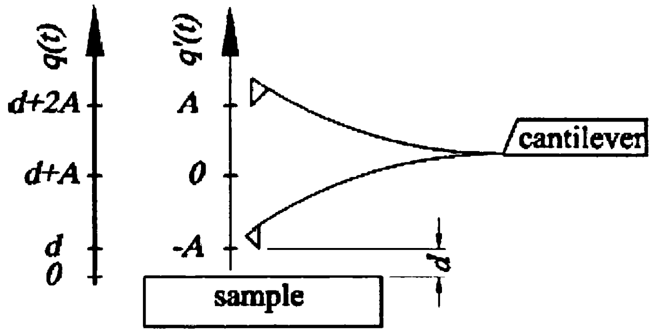

Figure 3.12. A text-book schematic of an oscillating cantilever[6]. The amplitude is denoted by A and minimum tip-sample distance by d.

The Hamiltonian of cantilever is

$$H = \frac{p^2}{2m^*} + \frac{kq'^2}{2} + V_{ts}(q) \tag{3.16}$$

where

$$p = m^* + \frac{dq'^2}{dt}. \tag{3.17}$$

Unperturbed motion is given by

$$q'(t) = A\cos(2\pi f_0 t) \tag{3.18}$$

with frequency

$$f_0 = \frac{1}{2\pi}\sqrt{\frac{k}{m*}}\,. \tag{3.19}$$

In-depth derivations for Δf have been made in the past[6,10] and a brief summary of findings is given here. The first derivation of Δf was given by Giessibl[11] in 1997 using canonical perturbations theory. With brackets indicating averaging over one oscillation cycle, the outcome for Δf was

$$\Delta f = -\frac{f_0}{kA^2}\langle F_{ts} q'\rangle\,. \tag{3.20}$$

A second method involved solving Newton's equations of motions for cantilever motion with effective mass $\mu*$ and spring constant k

$$\mu*\frac{d^2q'}{dt^2} = -kq' + F_{ts}(q') \tag{3.21}$$

where cantilever motion is assumed periodic and is expressed as a Fourier series with fundamental frequency f:

$$q'(t) = \sum_{m\ 0}^{\infty} \mathrm{a_m}\cos(m2\pi f t)\,. \tag{3.22}$$

And after various mathematical operations a result equivalent to Eq. 3.20 was found for Δf.

The above equations are concerned with large amplitudes. If they are integrated by by parts, they are transformed back to resemble Eq. 3.13:

$$\Delta f = f_0\frac{\langle k_{ts}(z)\rangle}{2k} \tag{3.23}$$

where

$$\langle k_{ts}(z)\rangle = \frac{1}{\frac{\pi}{2}A^2}\int_{-A}^{A} k_{ts}(z-q')\sqrt{A^2-q'^2}\,dq'\,. \tag{3.24}$$

This expression resembles that of $\Delta f = f_0 \frac{k_{ts}}{2k}$ (Eq. 3.13) but k_{ts} is exchanged for a weighted average $\langle k_{ts} \rangle$: forces with short-range are given more weight than long-range forces at small amplitudes (Eq. 3.20-3.22 consider large amplitudes only)[6,10]. The conclusion made is that the sensitivity of AFM to forces of a particular range can be controlled via its oscillation amplitude. For small amplitudes the short-range forces can be weighted more than longer range; for larger amplitudes, long-range forces can be given more weight.

In summary, NC-AFM uses feedback signals derived from the force induced shift in resonance frequency of the oscillating cantilever due to its interaction with the surface for regulating the tip-sample separation:

- The cantilever is oscillated slightly above its resonant frequency with fixed amplitude of oscillation.
- Changes in the oscillation frequency are used as the feedback signal.
- The frequency of the oscillations is influenced by the VdW attraction force between the tip and surface.
- The tip does not touch the sample and NC-AFM is performed in vacuum.
- Atomic resolution is obtainable.
- The change in eigenfrequency (f_0) occurs inside a single oscillation on a timescale $\tau_{FM} \approx \frac{1}{f_0}$.
- As the interaction forces are much weaker than in tapping mode, cantilevers are driven at small amplitudes to increase sensitivity.
- Cantilever frequency can:
  - decrease (VdW forces)
  - increase (magnetic/ electrostatic forces).

The six key parameters for frequency-modulated NC-AFM in vacuum are:

1. **<u>Cantilever spring constant</u> (k):** The tip is mounted on a spring and if the cantilever stiffness below a certain value, the tip can suddenly *jump-to-contact* whilst approaching the sample.

2. **Cantilever eigenfrequency (f_0):** The cantilever has eigenfrequency f_0 and is controlled with positive feedback so that it oscillates with constant amplitude A.
3. **Cantilever quality factor (Q):** Q reaches hundreds of thousands in vacuum (compared to a few hundred in air). Therefore high-Q cantilevers combined with a stiffness ~20 N/m and amplitude $A = 10$ nm can give atomic resolution[9].
4. **Oscillation amplitude (A):** The dependence of frequency shift on amplitude means small amplitudes increase sensitivity to short-range forces. Small amplitudes combined with extremely high spring constant cantilevers are proved to be beneficial.
5. **Frequency shift of cantilever (Δf):** The frequency shift (Δf) is related to the cantilever spring constant (k):

$$\frac{\Delta f}{f} = \sqrt{1 + \frac{1}{k} . \frac{\partial F}{\partial z}} - 1 \approx \frac{1}{2k} . \frac{\partial F}{dz}$$

6. **Bias voltage between tip and sample (V_{tip}):** This is useful if for example electro-static force microscopy and conducting probes are used.

Parameters **1-3** are dependent on the type of cantilever and parameters **4-6** are freely adjustable.

3.6 Additional Features

3.6.1 Piezoelectric Scanners

Scanners are essential components of all SPMs and typically have a tube configuration made from a piezoelectric material as shown in Figure 3.13. Both inner and outer surfaces of the tube of piezoelectric material are coated with a thin metal electrode while the outer surface is split into four electrically isolated sections. Operation is based on the behaviour of the tube in response to applied voltages: those applied across the tube give lateral scanning; voltages applied between the inside and outside of the tube give vertical movement. Scanners are characterised by their scan range and resonant frequency.

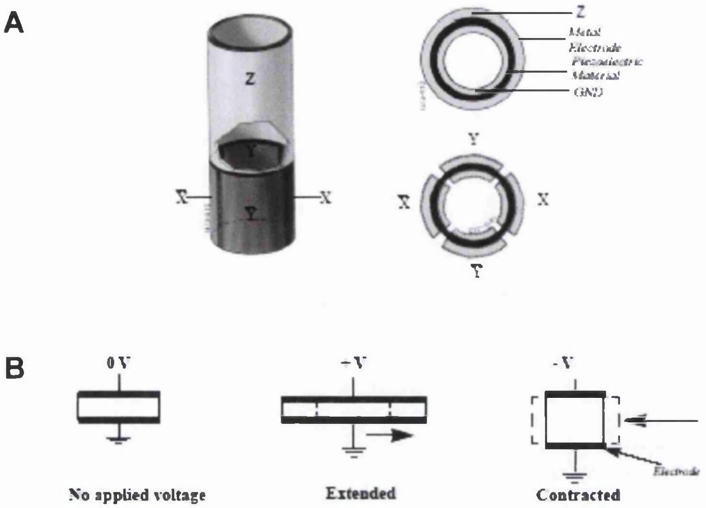

Figure 3.13. (A) Tube scanners are made from piezoelectric material and are spit into four electrically isolated sections. (B) Motion is based on behaviour of the material as voltages are applied.

3.6.2 Vibration Isolation

The desire for high resolution imaging in SPM imposes limits on noise levels. For SPM resolution of 0.01 nm (0.1 Å) vertically and 0.1 nm (1 Å) laterally, noise must be limited to 0.001 nm (0.01 Å) in z and 0.01 nm (0.1 Å) in x and y directions. Mechanical vibrations are the largest components of noise and these low frequency vibrations are minimised by levitating the whole system on an air table. High frequency vibrations (from piezo elements' resonances) are removed with electrical filters without affecting imaging signals.

3.6.3 Data Analysis and Image Processing

Any artefacts acquired during the scanning process must be removed from images if they are to be of any use. Standard routines exist for image processing.

SPM data consists of x, y coordinates associated with a number representing the intensity at that point. Image arrays have size 128×128, 256×256, 512×512 *etc.* and to resolve structures of interest there should be a sufficient density of information. Standard routines exist for image processing which compensate for instrumental defects *etc.* All images possess a deviation in the background plane incurred by the impossibility to align the tip exactly perpendicular to the sample.

This background slope is removed by calculating a least squares fit and then removing it from the data. Left remaining is: $z' = A*(x) + B*(y)$ where A and B are constants. A curved background may result from nonlinearities in the scanner or very low frequency vibrations. This is compensated by using a polynomial of order *n* for the subtraction of that specific plane, $z' = A*(x^n) + B*(y^n)$ where $n \leq 4$ (typically $n \leq 2$) . Plane subtraction is not the same as rotating a plane (a stepped structure is altered to a sawtooth using plane subtraction). 'Whole plane', 'line by line' and 'partial plane' subtractions are used. A plane in the *x*-direction can be removed without affecting the *y*-direction.

3.7 Summary

This chapter has provided the theory of tip-sample forces and how their presence may be exploited for atomic force microscopy. Methods of signal detection have been reviewed with particular emphasis on the lesser-known non-contact, frequency-modulated AFM. The instrumentation needed for AFM has been discussed and details regarding the particular AFM systems used in this work are given in Chapter 4.

3.8 References

---

[1] Binnig, G., Quate, C. F. and Gerbers, C. (1986) Atomic force microscope, Phys. Rev. Lett. 56 (9), 930-933.

[2] Binnig, G., Rohrer, H., Gerber, C. and Weibel, E. (1982) Surface studies by scanning tunneling microscopy. Phys. Rev. Lett. 49, 57–61.

[3] Basic Principles of Scanning Probe Microscopy. (2001) Bonnell, D. (editor).

[4] Smith, D.P.E. (1995) Limits of force microscopy. Review of Scientific Instruments 66 (5)3191-3195.

[5] Bowen, W. R., Lovitt, R.W. and Wright, C.J. (2000) Application of atomic force microscopy to the study of micromechanical properties of biological materials. Biotech. Lett. 22, 893-903.

[6] Giessibl, F.J. (2003) Advances in atomic force microscopy. Rev. Mod. Phys. 75, 949-983.

[7] Digital Instruments: Scanning Probe Microscopy Training Notebook Version 3 (2000).

[8] Garcia, R. and Perez, R. (2002) Dynamic atomic force microscopy methods. Surf. Sci. Rep. 47, 197-301.

[9] Albrecht, T. R., Grutter, P., Horne, H. K. and Rugar, D. (1991) Frequency modulation detection using high-Q cantilevers for enhanced force microscope sensitivity, J. Appl. Phys. 69, 668–673.

[10] Noncontact Atomic Force Microscopy. (2002) Morita,S., R.Wiesendanger, R., and Meyer, E. (editors). Springer.

[11] Giessibl, F. J. (1997) Forces and frequency shifts in atomic resolution dynamic force microscopy. Phys. Rev. B 56, 16 010–16 015.

CHAPTER 4

Experimental Techniques

4.1 Introduction

The practical aspects of this work are addressed in this chapter in terms of substrate preparation and AFM operation. Atomically flat, well-defined and contaminant-free substrates are necessary for successful, high-resolution imaging of biomolecules and it is advantageous that substrates are chemically inert against O_2. Mica and template-stripped gold fulfil these criteria and were prepared for high-resolution imaging of biomolecules. A method of probing DNA's conductivity was required and so gold electrodes were fabricated on silicon dioxide (SiO_2) substrates. The Omicron Variable Temperature (VT) Beam Deflection AFM was used for high-resolution non-contact mode imaging of biomolecules in UHV. The Dimension 3100 AFM system was used for imaging samples in air. Operation of the AFM systems is explained in terms of their apparatus and feedback mechanisms.

4.2 Substrate Preparation

4.2.1 Mica

Muscovite mica has extremely low surface roughness and is a popular substrate for supporting biomolecules during SPM analysis. It is an insulating, layered material having strong bonds in two dimensions and weak bonds in the third. Several types exist with the main component being SiO_4–tetrahedra. Mica is easily cleaved in air using adhesive tape to expose large atomically flat areas extending up to several millimetres. Mica is purchased at relatively low cost (Goodfellows), is easily stored and samples can be repeatedly cleaved for re-use.

The surface roughness of mica was verified with AFM giving RMS roughness of 0.104 nm for 2 μm x 2 μm (Figure 4.1).

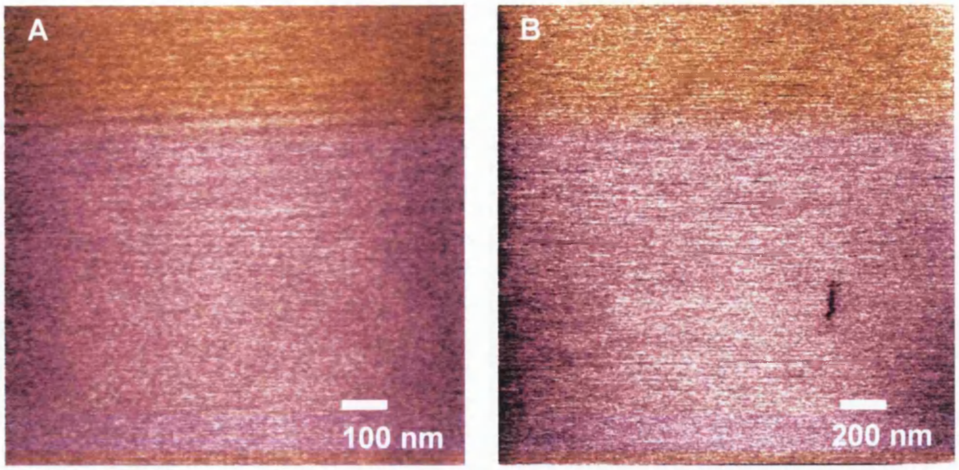

Figure 4.1. NC-AFM of atomically flat mica (A) 1 µm x 1 µm area, maximum height 0.3 nm. (B) 2 µm x 2 µm scan with RMS roughness 0.104 nm.

4.2.2 Template-Stripped Gold

The realisation of ultra-flat electrically conducting substrates for imaging and manipulation of nano-sized structures is highly significant for investigating the electronic properties of biomolecules for applications in bio-electronics. Thin-film gold substrates have been used by others[1] and were fabricated in this work. Gold thicknesses of around 10-20 nm were deposited on mica with the intention of providing flat areas for bio-molecular imaging and means of testing the conductivity of DNA using conducting-AFM (C-AFM) over gold-mica steps. Thin-film gold substrates showed apparently low RMS surface roughness (~0.59 nm for a scan area 1.1 µm x 1.1 µm) when measured with TM-AFM. However, upon deposition of DNA diluted in water (~µl amounts) the samples became rough (Fig. 4.2). The increase in RMS surface roughness to ~2.33 nm for a scan area 1 µm x 1 µm suggested gold was loosened from the mica and for this reason samples could not be used for imaging or electrical measurement.

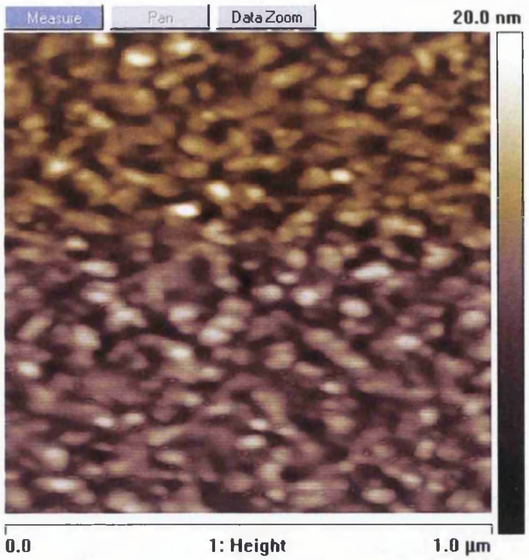

Figure 4.2. TM-AFM of a thin gold film on mica after liquid deposition RMS roughness ~2.33 nm for scan area 1 µm x 1 µm.

Ultra-flat gold samples were successfully produced using a more complex 'template-stripped gold' (TSG) method[2] (Figure 4.3). Gold was evaporated on to a freshly cleaved, preheated (300°C, 5 hours) mica sheet (5 cm x 5 cm). A several hundred nanometre thickness of gold was deposited on to the mica during the deposition procedure using an Edwards Evaporator at 10^{-6} mbar.

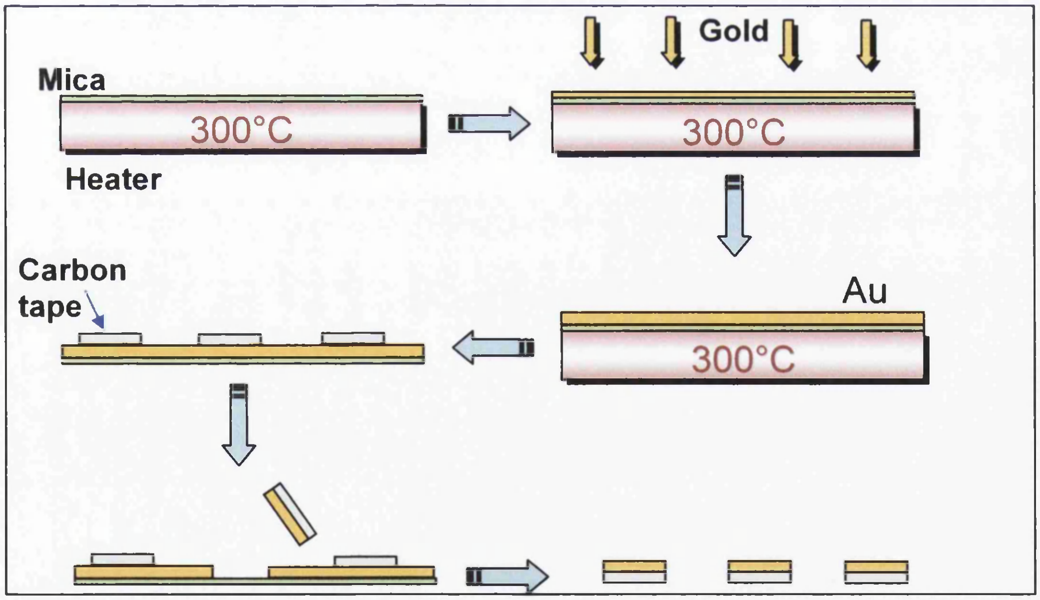

Figure 4.3. Schematic to show fabrication of flat gold substrates. Freshly cleaved mica is heated to 300°C, ~3-5hrs. Gold is evaporated to thickness ≥200 nm. Samples are cooled and fixed gold side down on metal plates. Mica is carefully lifted off to expose a flat, clean gold surface.

The gold-mica sheet was subsequently cut into 1 cm^2 pieces. Samples were fixed gold-side down on metal plates using carbon adhesive pads. Prior to use, mica was carefully peeled off using sharp tweezers and revealed a flat gold surface. Conductivity tests were performed to ensure no mica was left remaining. These gold substrates have very low surface roughness as measured with NC-AFM (Figure 4.4) yielding a root mean square value of 0.198 nm for a scan size 5 μm x 5 μm.

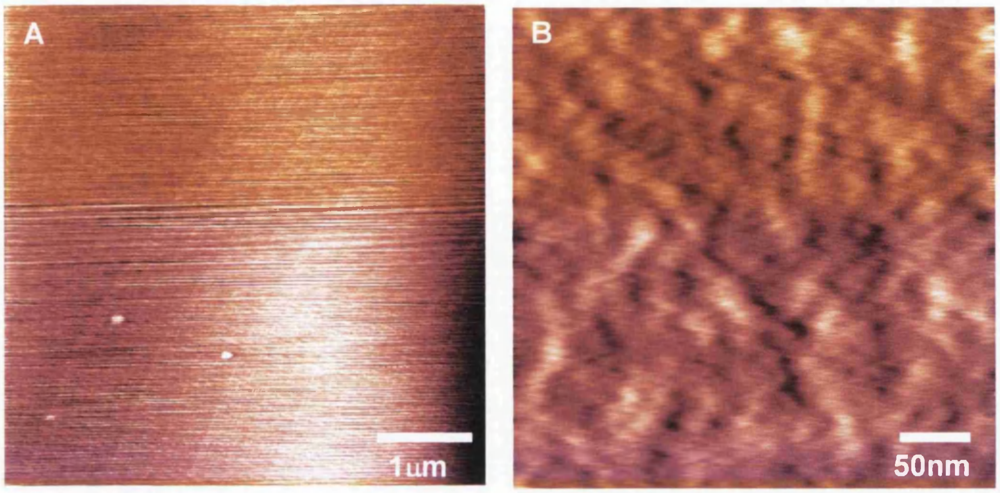

Figure 4.4. NC-AFM of bare template-stripped gold. (A) Scan area 5 μm x 5 μm with low RMS roughness 0.198 nm (mean roughness 0.142 nm). (B) Zoom view, 316 nm x 316 nm with RMS roughness 0.184 nm (mean roughness 0.147nm).

4.2.3 Gold Electrodes

Electrodes necessary for probing DNA's conductivity were designed and fabricated using electron-beam lithography (EBL) by J. Kettle at Cardiff University[3]. EBL is a specialised technique for creating the fine patterning for integrated circuits in present-day electronic applications such as MOSFETs[4,5]. A beam of electrons is scanned across a surface covered with an electron-sensitive resist film and are deposited in a desired pattern of the resist film. The de Broglie wavelength of electrons is less than 1 Å and therefore overcomes the wavelength limitations imposed by photolithography.

The principle of EBL is based on electron interactions with organic compounds either via fragmentation (positive resist) or cross-linking (negative resist) and the ability to successfully predict these interactions since the resolution is not only affected by the electron beam itself but by secondary electrons generated via inelastic forward and back-scattering off the substrate. At present, high-resolution EBL is routinely performed using its direct writing ability to create miniature devices. Figure 4.5A illustrates the fabrication process for a 'Hole array' structure.

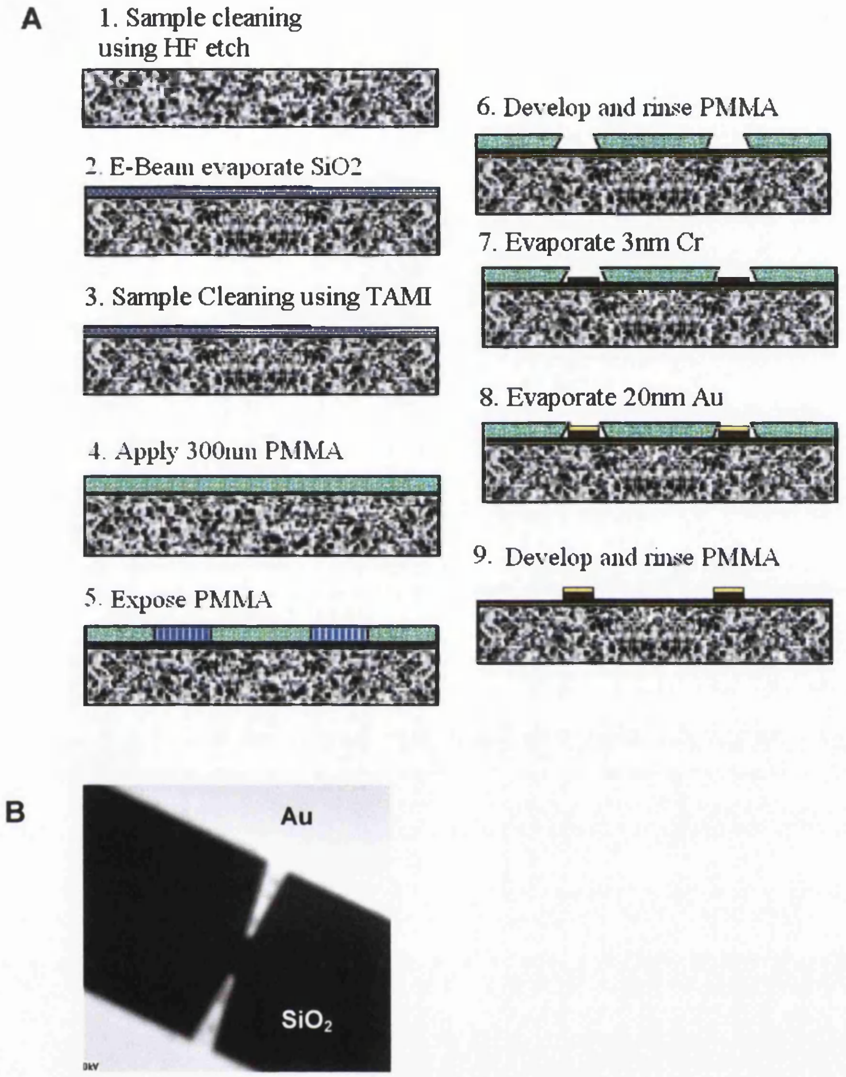

Figure 4.5. Electron-beam lithography (EBL). (A)The fabrication process of a Hole array. (B) An SEM image of typical electrodes

Firstly undoped, cleaved and polished silicon is cleaned (Fig. 4.5A, step 1) so that any organic residues are removed. A four-solvent method removes contaminants of particular molecular weights: 5 minutes of preheated agitated stirring at 120 °C in Trichloroethene, Acetone, Methanol and lastly Isopropanol. The oxide layer is removed with hydrofluoric acid (HF): 5% HF and 10 sec sample dips, and a wetting test performed. Next, a thick layer of e-beam evaporated SiO_2 (~600 nm) is deposited at a rate of 2-4 $Ås^{-1}$ using a 5 kV electron beam in vacuum of 2-4 x 10^{-6} Torr (step 2). Samples are cooled (~2 hrs) and cleaned (step 3). A thin gold layer is deposited on the sample edge to prevent sample charging in the SEM chamber and allows focussing which is not otherwise possible on SiO_2. Next, a 100 nm thick Polymethyl methacrylate (PMMA) is applied via spinning (step 4) using 950 K PMMA and 4 % solid chlorobenzene solvent. The resist mixture is poured onto the silicon wafer and spun at 6000 rpm for 45 sec. The thickness of these transparent films is accurately measured using non-contact, spectro-reflectometry. Substrates are baked at 180 °C for 3 mins and resist thickness remains constant at about 100 nm. Samples are transferred to the EBL system, the vacuum pumped down to 5×10^{-5} torr and exposure done at 20-30 kV at doses 200-350 $\mu C/cm^2$ (step 5). Dosage, pattern size, beam current, spot size all affect exposure and takes ~30 min for normal hole array structures. The chamber is let to air and developed in 1:3 Methyl isobutyl ketone (MIBK) (step 6) and rinsed in isopropanol (IPA), 30 sec. Samples are blown dry with nitrogen. Next, electrode designs are patterned into the PMMA film. Evaporation of 3 nm of chromium (Cr) and then 20-40 nm of gold (Au) are done at 2×10^{-6} torr (steps 7 & 8). Au adheres much better to Cr than to SiO_2 and so substrates with underlying Cr are more resilient. Metals should not be evaporated onto vertical sidewalls of the PMMA cavities. Samples are removed from the system and soaked in acetone for ~1 hr (step 9). If the PMMA hasn't directly lifted off, heating in acetone and agitation via stirring and then ultrasonic agitation is performed. Mica was used instead of silicon during initial attempts but problems were encountered during fabrication and end-products proved unsuitable. Electrodes created on SiO_2 were successfully fabricated and subjected to SEM (*e.g.* Fig. 4.5B), AFM studies and I-V measurement. These results are shown in Chapter 6.

4.2.4 Bio-Molecules

- **DNA samples:** DNA samples were prepared under the supervision of Dr. R. S. Conlan within the School of Medicine at Swansea University[6]. For DNA experiments, 2-kbp and 2.5-kbp linear DNA fragments were amplified from plasmid DNA by polymerase chain reaction (PCR) using Taq polymerase, and M13 forward and reverse primers. PCR products were purified using PCR clean up columns (Qiagen) following the manufacturers recommendations. Amplified DNA was eluted from columns using nuclease free, distilled and deionised water and adjusted to a final concentration ~10 ng/μl. Various concentrations were used including 100 ng/μl but for individual strand observation 10 ng/μl was favoured. The length of the DNA was verified using gel electrophoresis. 2 -5 μl droplets of DNA were deposited in the central region of the chosen substrate centre (typically a 1 cm^2 mica substrate) and left for ~15 min before drying with nitrogen gas.

- **Nucleosome samples:** For the nucleosome work, sonicated chromatin samples were provided courtesy of Drs Y. Teng and Y. Yu of the Department of Pathology at Cardiff University[7]. Intact nucleosomes and chromatin samples were prepared from wild-type FT5 yeast (*Saccharomyces cerevisiae*)[8] as described by Kuras and Struhl[9]. Cells were grown overnight in rich media yeast peptone 2% dextrose to an A550 of 1.5. Purified sonicated chromatin samples were diluted 1:1000 in water before being imaged. A single 2 μl droplet of the nucleosome-containing solution was deposited at the centre of a 1 cm^2 mica substrate and left for 5 min without further treatment. Nitrogen gas was used to remove any remaining liquid from the samples. No rinsing was performed.

- **PUT3-related samples:** Plasmid DNA (~2.5-kbp) containing one PUT3 binding sequence was kindly supplied by Prof. R. J. Reece of the Faculty of Life Sciences, Manchester University[10] along with a separate supply PUT3p protein. The plasmid pRJR130 contained a single PUT3 binding site closed into the 'BamHI-HinDIII' restriction enzyme sites of the plasmid pSP72. The specific PUT3 probe used was the double-stranded oligonucleotide:

5' –GATCCCC**CGGGAAGCGCTTCCCG**GGAAGCT- 3'.

The region red/black/red represents a high-affinity PUT3 binding site[11]. In Swansea, this plasmid DNA was cut using different enzymes in preparation for anticipated experiments. Specific digestion sites serve as reference points for the relative positioning of the protein binding sequence along the DNA strand. These sites are shown in Figure 4.6. Further information concerning the vector circle map, its sequence and reference points can be found at the promega website[12].

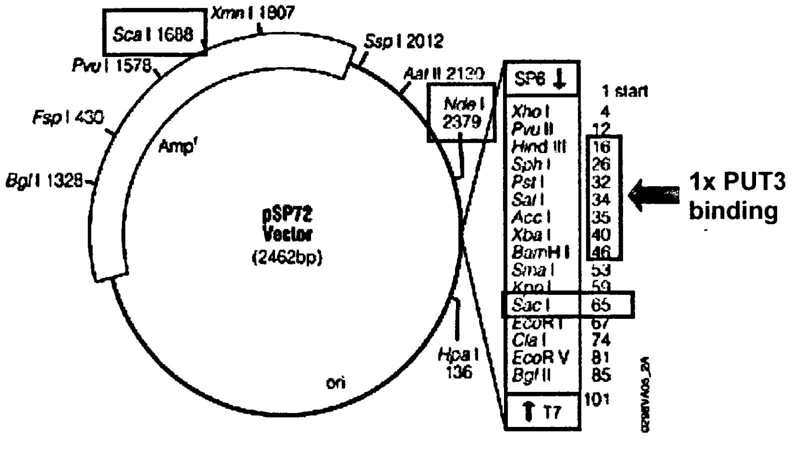

Figure 4.6. The plasmid DNA (2462-bp) containing recognition sites for enzyme digestion. The three sites highlighted in blue were used in this work, cutting the DNA with enzymes Sacl, Scal and Ndel at 65, 1688 and 2379 base-pairs respectively. The single PUT3 binding site is included between bases 16-46.

Enzyme *SacI* was used to cut the plasmid at base-pair 65 for positioning the binding sequence near one end of the DNA strand. Enzyme *ScaI* was used to cut the plasmid at base-pair 1688 for positioning the binding site in the central region of the strand of DNA for one set of experiments. Enzyme *Nde I* was used for digestion at a different site, cutting it at 2379-bp. A second binding site was introduced to the 2462-bp DNA molecule such that the end-product contained binding sites near both ends. Specially designed primers were necessary for this case. The primers needed for amplification were designed as follows:

5' ATTTAGGTGACACTATAGAACTCG 3'

-this primer is known as 'SP 6' and is an *RNA polymerase promoter*, and

5' CGGGAAGCGCTTCCCGTGACGGGCTTGTCTGCTC 3'.

The PCR reaction was performed and the new DNA strand length checked with gel electrophoresis. For a successful amplification, several PCR attempts were made using different annealing temperatures.

Protein was supplied at concentration ~0.35 mg/ml in a reaction buffer containing: 20mM HEPES-KOH (pH 7.5), 150 mM NaCl, 10% glycerol, 10 μM $ZnCl_2$. This PUT3 molecule binds with high affinity to a particular 16-bp sequence of DNA under certain conditions. Therefore a new buffer was made up (20 mM HEPES-KOH (pH 8.0), 150 mM NaCl, 10% (v/v) Glycerol, 5 mM $MgCl_2$, 10 μM $ZnSO_4$).

DNA and protein samples were mixed in the presence of buffer (~30 mins) for binding to occur.

4.3 The Omicron VT Beam Deflection AFM

4.3.1 General Description

The Variable Temperature (VT) Beam Deflection AFM scanner is housed in an analysis chamber and allows NC-AFM to be performed under UHV conditions. A pressure of approximately 8 x 10^{-11} mbar is normally attainable after baking the system. The system is also capable of cooling and heating of samples (from 25 K to 1500 K). A high quality vibration decoupling system crucial for the high-resolution studies, is incorporated into the AFM system. Four soft springs protected by columns are used to suspend the AFM base plate (Figure 4.7).

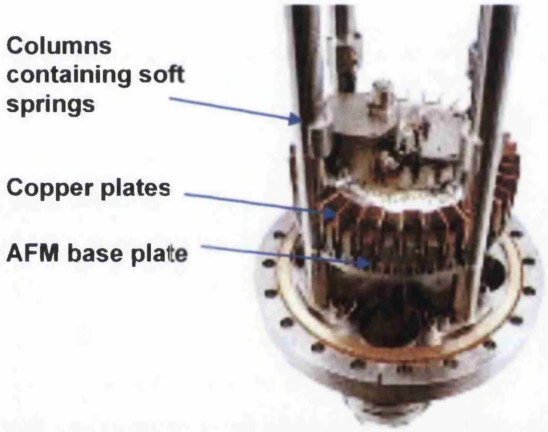

Figure 4.7. A side view of VT Beam Deflection AFM system. The AFM base plate is surrounded by copper plates which come down in between permanent magnets in a nearly non-periodic eddy current damping mechanism.

The spring suspension system has resonance of ~2 Hz; vibrations of this suspension system are intercepted using a *nearly non-periodic eddy current damping mechanism*[13]. This consists of a ring of copper plates which surrounds the AFM base plates and comes down in between permanent magnets.

The Omicron UHV STM and AFM system is shown in Figure 4.8. Samples and tips are introduced to the UHV analysis chamber via a fast entry load lock. Once placed into the load lock, a turbo pump is used to create a vacuum in the 10^{-5} mbar range. The valve isolating the load lock and analysis chamber is then opened and the sample admitted to the UHV chamber and the pressure allowed to recover.

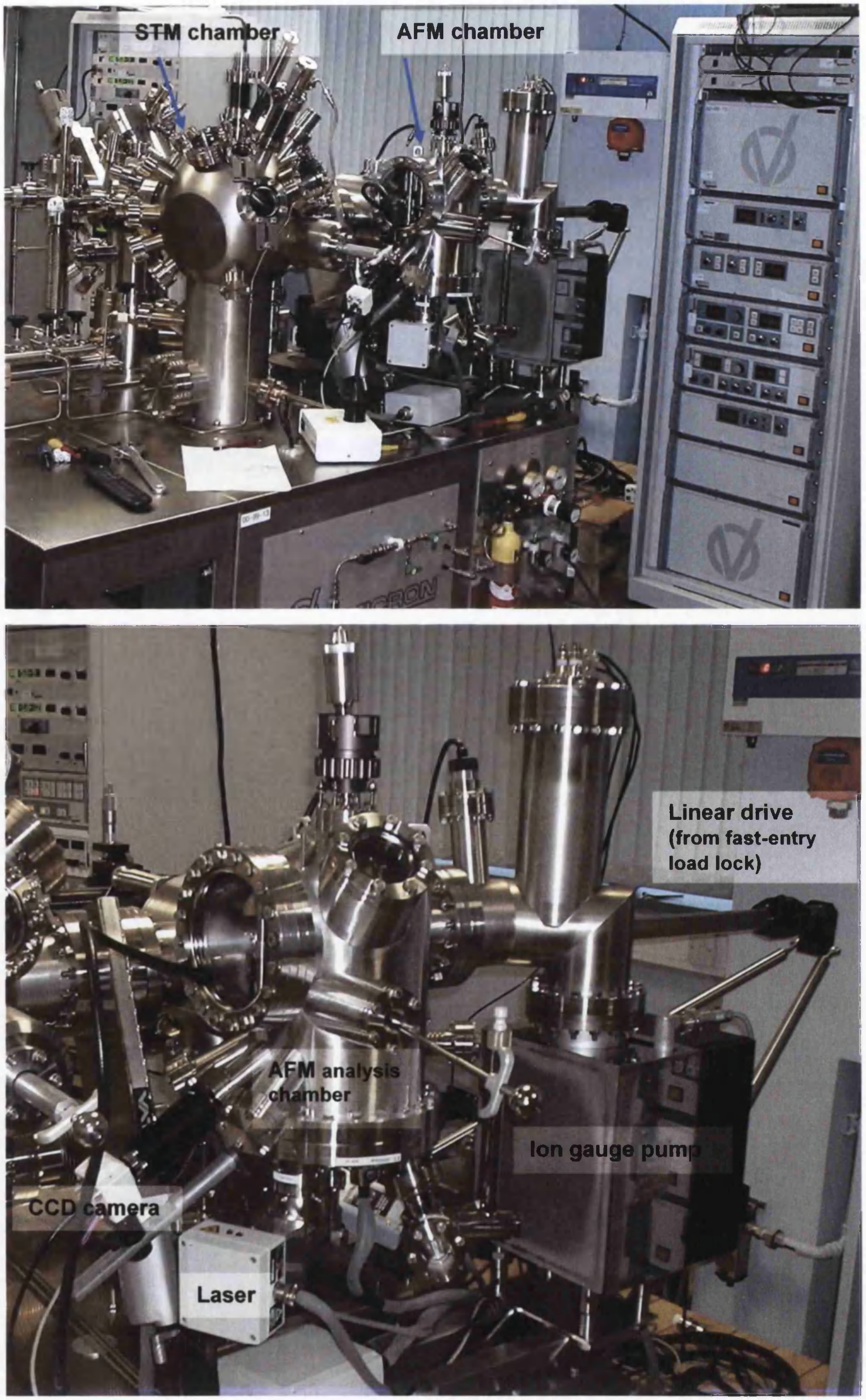

Figure 4.8. The Omicron STM and AFM systems (*top*). The VT Beam Deflection AFM system (*bottom*).

4.3.2 Sample and Tip Positioning

Omicron tip holders are used for mounting cantilever tips and stainless steel plates are used for mounting samples. The princer grip wobblestick is used for tip and sample handling once in the UHV. Samples are transferred sideways to a fixed position at the stage. The cantilever tip is brought close to the sample using the scanner. A 3-axes linear piezo motor positions the scanner using slip/stick effects that are related to inertial forces as the piezo is driven in fast/slow sequence. Sliders, magnetically coupled to three shear piezos, driven with a sawtooth voltage input are transported during slow piezo movements and slip during fast piezo motion due to their inert mass. Slip/stick effects are used for movements parallel to the sample surface (X & Y), perpendicular to the surface (Z) and light beam adjustments (LX, LY & PSPD).

Manual coarse movements bring the tip to close proximity of the sample and is followed by a step-by-step approach depending on whether contact or non-contact mode is used. Note that after a coarse approach the surface is only just in reach of the tip (coarse step width ≤0.2 μm compared to Z-range of the scanner > 1 μm) and so the fine positioning piezo must be adjusted to have full range available during scanning.

4.3.3 Tip Scanner

The scanner is a single tube with maximum scan range of about 10 μm x 10 μm and Z-travel of about 1.5 μm (Figure 4.9). Resolution better than 0.01 nm in Z-direction is possible. Scanner sensitivities are suited to atomic resolution for scan areas under 100 nm x 100 nm; long-distances (~several μm) are less accurate. Piezo sensitivities in X & Y = 18 nm/V and Z = 10 nm/V.

Cantilever tips are manufactured as a single unit. The sharpness of the cantilever tip is important for high-resolution experiments. The cantilever material is highly doped Si which dissipates static charge.

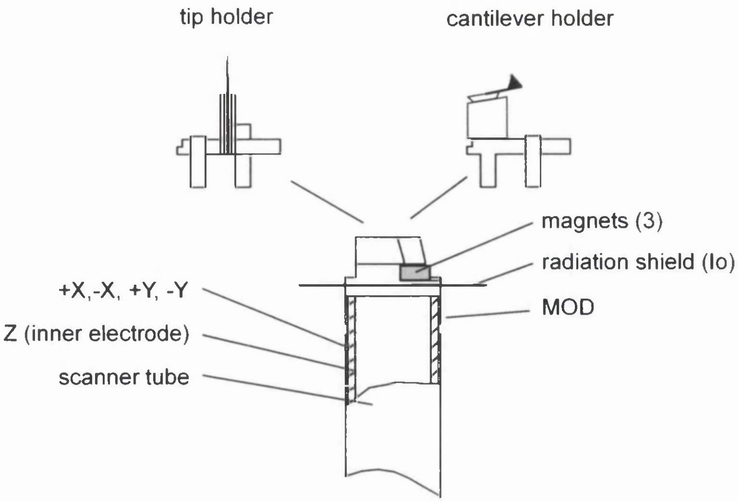

Figure 4.9. The VT AFM tip scanner.

A typical NC-AFM cantilever has length 125 μm, width 30 μm, force constant 42 N/m, resonant frequency ~ 330 kHz (NanoSensors). A point-probe silicon cantilever tip is shown in Figure 4.10. The tip is chemically inert and has high mechanical Q-factor for high sensitivity. Ideally the radius of curvature is < 10 nm.

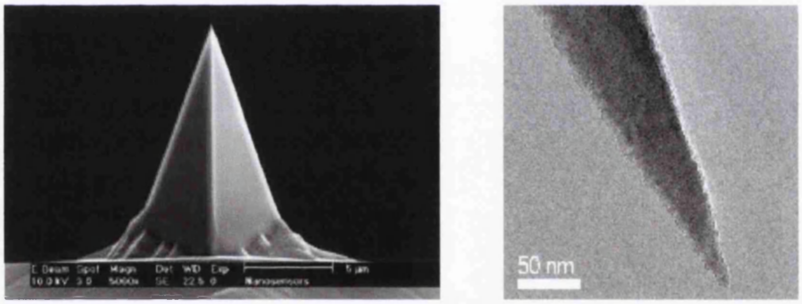

Cantilever data:

Technical Data	Nominal Value	Specified Range
Thickness /μm	1.8	1.0 - 2.5
Width /μm	30	22.5 - 37.5
Length /μm	50	45 - 55
Force Constant /(N/m)	140	6 - 270
Resonance Frequency /kHz	1100	500 - 1700

Figure 4.10. Cantilever tips used for NC-AFM. A typical silicon cantilever tip (*left*). A very high resonant frequency probe (PPP-NCVH AFM) (*right*).

4.3.4 Feedback Control System

AFM is based on the surface-induced deflections of a cantilever. Deflections are measured via laser beam reflection from the cantilever to the position sensitive photo-detector (PSPD).

For contact mode AFM the feedback source is the normal force between tip and surface and a force set-point is software selectable.

- $F_{SET} > 0$ REPULSIVE FORCE
- $F_{SET} < 0$ ATTRACTIVE FORCE

F_{SET} is set as positive for approach and contact between tip and sample. After approach negative values may be used if adhesive samples are used but if contact is lost the regulator cannot regain contact with negative F_{SET}.

For non-contact AFM, feedback is derived from a force induced shift in resonance frequency of an oscillating cantilever. An FM detector identifies the frequency difference (Δf) between the cantilever (f_{OSC}) and a reference oscillator (f_{REF}). For a non-interacting cantilever, $\Delta f = 0$, the reference is automatically set by the software:

$$f_{REF} = f_{OSC} + 455kHz \qquad \textbf{(4.1)}$$

Signals are converted in to analogue output voltage proportional to Δf:

$$Delta\,f\ \mathrm{OUT} = 5mV\,/\,Hz.(f_{REF} - f_{OSC} - f_{INT}) \qquad \textbf{(4.2)}$$

where f_{INT} = intermediate frequency ($\approx 455kHz$). Assuming the reference oscillator is set to the right frequency initially, the FM detector monitors changes in cantilever resonance frequency. For non-contact mode, a pre-selected frequency shift is maintained with the SPM regulator. Cantilever frequency can both decrease and increase from Van der Waals forces and magnetic/electro-static forces respectively. As the resonance curve in air is broad and flat, non-contact AFM is performed in UHV to protect the cantilever and surface.

It is essential that the laser is properly aligned on to the cantilever during both modes of AFM operation. The laser beam generated in the Light Unit passes through the base flange to the microscope chamber using an optical fibre and is aligned as shown in Figure 4.11

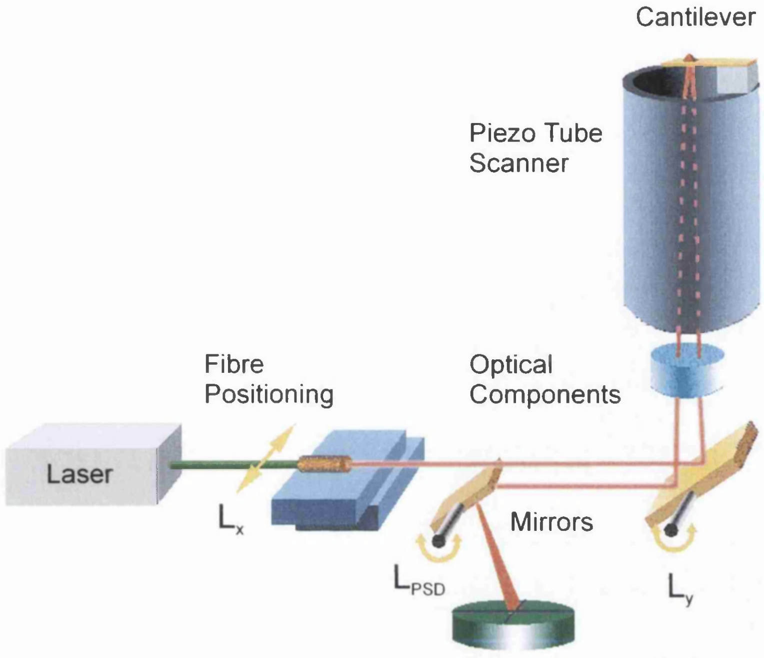

Figure 4.11. Schematic diagram of optical deflection for the Omicron AFM.

The primary beam is positioned on to the cantilever firstly in the x-direction with a micro slide and secondly in the y-direction with a rotating mirror. With the use of a CCD camera the laser spot is visible on the ceramic cantilever holder (Figure 4.12). Assuming the laser beam has been threaded through the scanner piezo tube, the beam is made to hit the cantilever such that a maximum intensity is recorded on the PSPD.

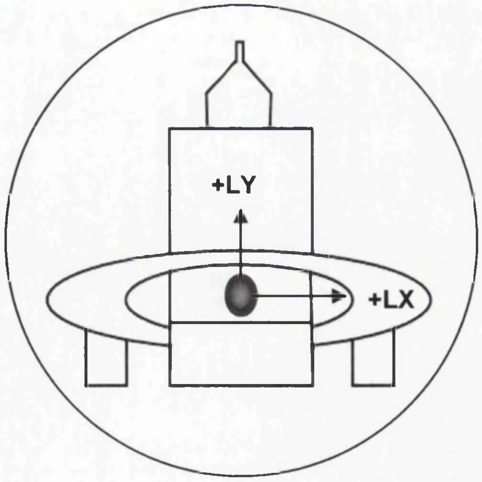

Figure 4.12. CCD Camera view of cantilever through flange during of laser alignment.

Laser beam positioning is performed with a remote box. Once the beam is visible on the ceramic block of the holder the spot can be positioned directly on the cantilever by using left/right (LX) movements and upwards (LY). A small intensity should be detectable on the PSPD as the first reflex (if nearly zero, secondary reflections are likely). A maximum signal is achieved on the PSPD using single steps of alignment.

The L_{PSD} mirror is used for optimisation of the secondary beam. For zero tip-sample interaction, the secondary beam should be positioned at the PSPD centre (Figure 4.13). Different signals are yielded depending on the nature of the interaction. Normal forces move the laser beam vertically and lateral forces move the signal horizontally.

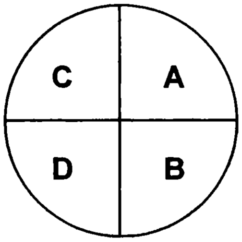

$$FN = [(A + C) - (B + D)] \times 5$$

Figure 4.13. Position sensitive photo-detector with output signal definition for the normal force (*i.e.* vertical movement of beam only).

The secondary beam is positioned at the vertical centre of the detector by adjusting vertical mirror L_{PSD}. The laser power I_{total} should always be slightly above 2V. I_{total}>2.5 V gives bleeding into other PSPD quadrants; I_{total} < 2.0 V induces excitation problems in non-contact mode. After the beam has been positioned on the cantilever, primary beam fine-tuning is useful for confirm the maximum signal intensity on the PSPD. Beam adjustments are also necessary when cantilevers are changed.

4.3.5 AFM Electronics and Software

Figure 4.14 shows regulation of Z-distance and amplitude in NC-AFM in schematic form. The cantilever is a free, self-starting oscillator having a set-point regulated amplitude. A regenerative loop of positive feedback is used for compensation of tip-sample energy losses.

The frequency shift Δf is used as the feedback signal in Z-distance regulation and is strongly dependent on the tip-sample separation. It is desirable to monitor cantilever resonance frequency and damping is checked using a fast sweep oscilloscope.

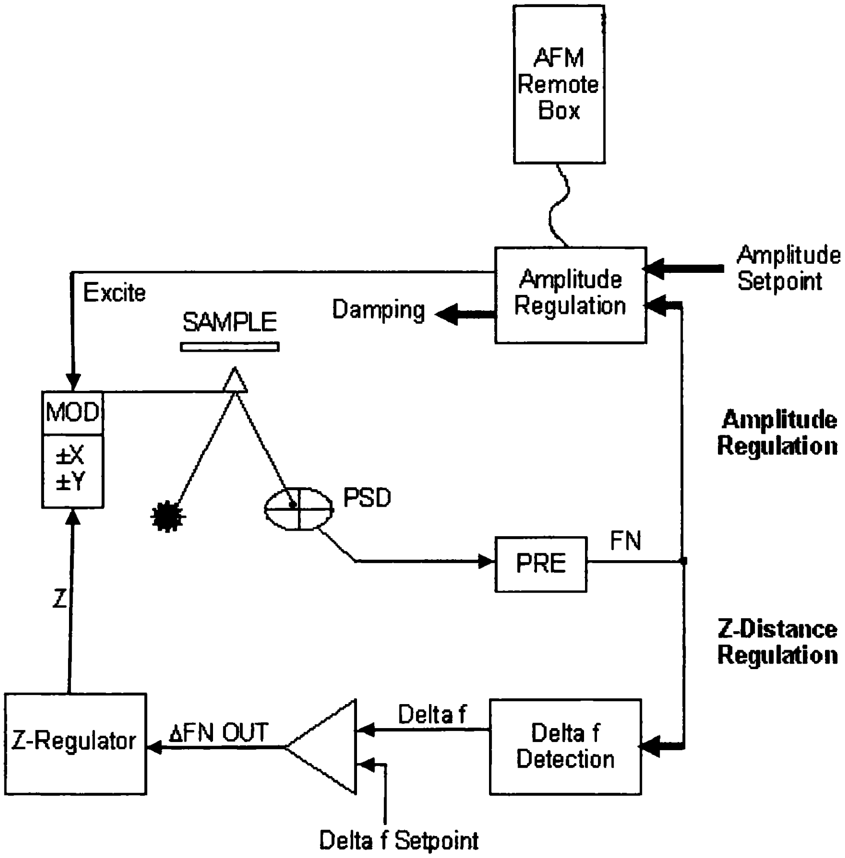

Figure 4.14. Regulation of NC-AFM and feedback electronics.

The electronics controlling the AFM system are contained in a rack mounting case and are controlled by PC via a PCI interface card. The system consists of a pre-amplifier, feedback control for Z-distance and amplitude regulation and circuitry for scan control. By varying the feedback signal Δf the tip-sample distance is altered. Fast or slow tip responses can be realised via integral and proportional gain controls. The software used to control the AFM was Omicron's SCALA PRO software and allowed real time manipulation of the AFM parameters, data acquisition and data analysis. Further reading can be found in the manufacturers' handbook[13].

4.4 Dimension 3100 AFM

4.4.1 General Description

The Digital Instruments' Dimension 3100 AFM was used for imaging samples in air to support data gained from NC-AFM. The AFM is mounted on a vibration isolation table and covered with an acoustic hood. Tapping-mode was favoured for imaging soft samples although the system is capable of several others modes (*e.g* contact- & conducting-AFM.).

4.4.2 Sample and Tip Positioning

All Digital Instruments scanners consist of a single tube with five or more independently operated piezo elements. In common with the Omicron system, the tip is raster scanned over a fixed sample.

4.4.3 Feedback Control System

In common with Omicron AFM system, the Dimension 3100 uses feedback signals derived from laser deflections onto a photodiode. The beam path is shown in Figure 4.15.

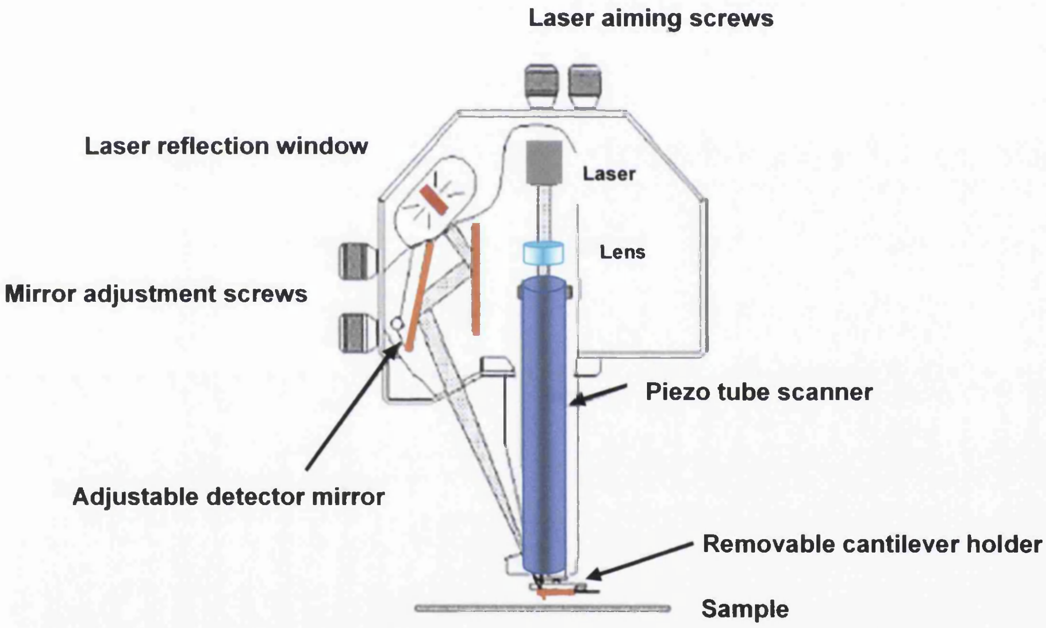

Figure 4.15. Schematic diagram of optical deflection for the Dimension 3100 AFM.

The beam is aligned on the back of the cantilever using the *laser aiming screws* to give a sum signal of about 4 V. The PSPD signal is centralised on the laser reflection window using *mirror adjustment screws* to give vertical deflection of 0 V. The cantilever frequency is tuned using PC controls. Optics are used to focus on the both tip and surface to find the desired area for scanning. An appropriate amplitude set-point is chosen for TM-AFM and an auto approach activated.

The Dimension 3100 uses amplitude modulation in the feedback loop (Figure 4.16).

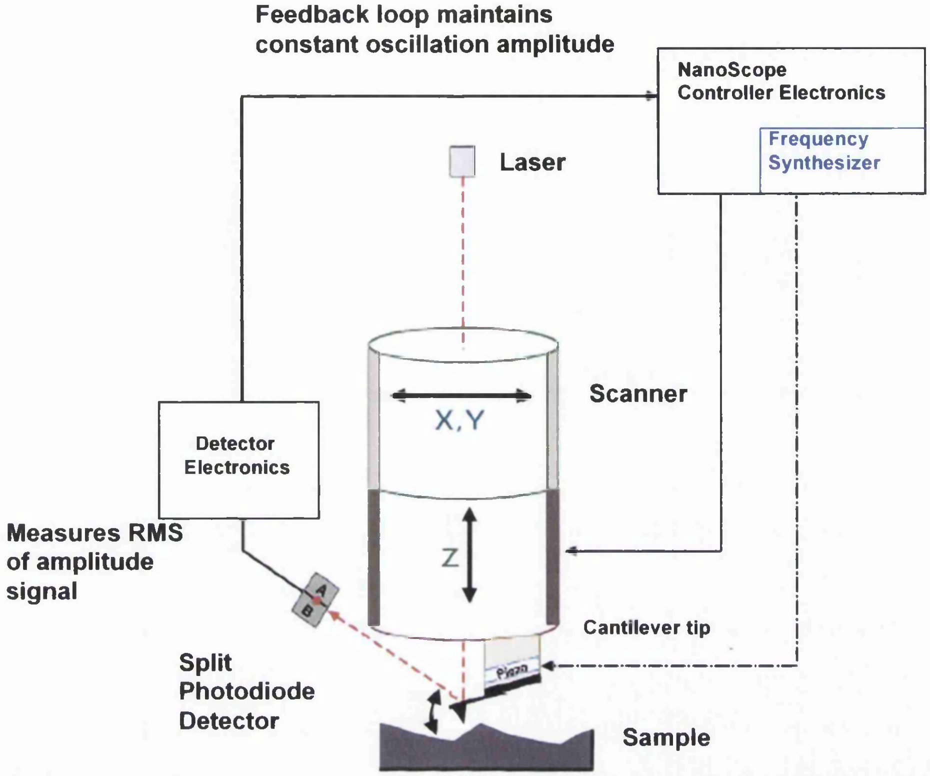

Figure 4.16. TM-AFM feedback via amplitude modulation.

4.4.4 AFM Electronics and Software

The microscope is controlled via PC with Digital Instruments' NanoScope software and a controller. Figure 4.17 depicts the electronics and feedback loops controlling Dimension 3100 operation in schematic form.

Further information regarding this AFM can be found in the manufacturers' notebook[14].

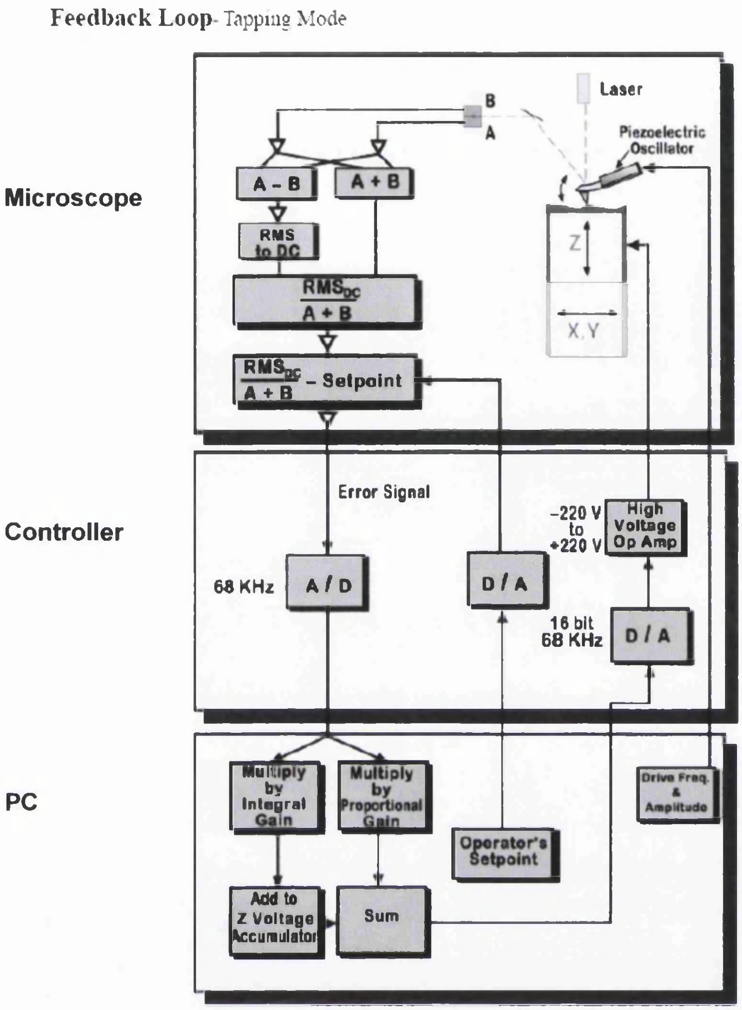

Figure 4.17. Feedback electronics for TM-AFM operation.

4.5 Summary

The techniques presented in this chapter were chosen for their suitability in aiding high-resolution studies of biomolecules. NC-AFM experiments performed in a controlled UHV environment yielded data with exceptional quality and therefore this technique was necessary to accurately study the chosen samples of interest. TM-AFM was invaluable for rapid scanning of samples during optimisation processes and imaging of electrodes for subsequent I-V studies. Both systems were capable of high-quality, reproducible imaging and were proved successful choices for the experiments.

4.6 References

[1] Medalia, O., Englander, J., Guckenberger, R. and Sperling, J. (2002) AFM imaging in solution of protein-DNA complexes formed on DNA anchored to a gold surface. Ultramicroscopy 90, 103-112.
[2] Hegner, M., Wagner, P. and Semenza, G. (1993) Ultralarge atomically flat template-stripped Au surfaces for scanning probe microscopy. Surf. Sci. 291, 39–46.
[3] Kettle, J. Multidisciplinary Nanotechnology Centre, School of Engineering, Swansea University and Richard Perks, School of Engineering, Cardiff University.
[4] Kretz, J. and Dreekornsfeld, L. (2002) Process integration of 20nm electron beam lithography and nanopatterning for ultimate MOSFET device fabrication. Microelec. Eng. 607, 61-62.
[5] Kedzierski, J., Xuan, P., Subramanian, V., Bokor, J., King, T and Hu, C. (2002) A 20nm gate-length ultra-thin body p-MOSFET with silicide source/drain. Superlattices and Microstruct. 445, 28(5/6).
[6] Conlan, R.S., Bowen, A. and Gonzalez, D., School of Medicine, Swansea University.
[7] Teng, Y and Yu, Y., Department of Pathology, UWCM, Cardiff, UK.
[8] Tzamarias, D. and Struhl, K. (1994) Functional dissection of the yeast cyc8-tup1 transcriptional co-repressor complex. Nature 369, 758–761.
[9] Kuras, L. and Struhl, K. (1999) Binding of TBP to promoters in vivo is stimulated by activators and requires Pol II holoenzyme. Nature 399, 609–613.
[10] Reece, R., Faculty of Life Sciences, University of Manchester, UK.
[11] Sellick, C.A. and Reece, R.J. (2003) Modulation of transcription factor function by an amino acid: activation of Put3p by proline. EMBO J. 22(19), 5147-5153.
[12] Online resource: www.promega.com
[13] Omicron Nanotechnology: The VT Beam Deflection AFM User's Guide & Service Manual (2003).
[14] Digital Instruments: Scanning Probe Microscopy Training Notebook Version 3 (2000).

CHAPTER 5

Visualisation of Biological Molecules

5.1 Introduction

Structural knowledge of biological molecules is vital for understanding their behaviour in science. This knowledge can be applied in different situations leading to future developments of the present day technologies. Prior to the invention of SPM, various techniques were developed to elucidate molecular structures (*e.g.* X-ray crystallography and cryo-electron microscopy (cryo-EM)). However, for X-ray crystallography, crystallised samples are required and for cryo-EM, the signal-to-noise ratio can be relatively low. Atomic force microscopy (AFM) is a valuable technique that provides useful structural information regarding individual, nano-sized molecules without such lengthy sample preparation; data averaging over large numbers of molecules is not required and experiments can be performed under liquid, air or vacuum conditions.

The modes of intermittent- and non-contact AFM operation were described in Chapters 3 & 4 and in this chapter, the results of atomic force microscopy applied to DNA and protein structures are presented along with a detailed dimension analysis. In particular, this chapter demonstrates the quality of frequency-modulated (FM) NC-AFM imaging of single biological structures. Emphasis is directed towards the usefulness of TM-AFM when performed in air on similar samples which provides a valuable comparison with NC-AFM. TM-AFM is regarded as more versatile for scanning larger areas in shorter timescales due to the absence of the vacuum environment. TM-AFM complements other imaging techniques and allows one a more rapid 'turnover' of samples.

In the course of this work, several STM experiments were performed using an desktop STM (EasyScan). Tapping-mode AFM studies were performed using a Dimension 3100 AFM. Non-contact AFM imaging experiments were performed using an Omicron Variable Temperature (VT) Beam Deflection AFM system and formed the main body of high-resolution imaging of DNA and protein. These visualisation studies of individual molecules directly adsorbed onto atomically flat and electrically conducting substrates are of key interest for the subsequent exploration of their charge transfer properties.

5.2 Sample Preparation

For successful imaging of biological molecules, the supporting substrates need to be clean and atomically flat. Both graphite and mica were cleaved with adhesive tape prior to each experiment revealing clean, atomically flat areas for the deposition of biomolecules. The substrates were re-used many times after cleaving. Gold surfaces were fabricated using a template-stripped gold technique as described in Chapter 4. These substrates were suitable for single-use only.

Biological samples were prepared as described in Chapter 4 (Section 4.2.4). For DNA experiments, 2-kbp and 2.5-kbp linear DNA fragments were amplified and purified. 2 -5 μl droplets of DNA were deposited in the central region of the chosen substrate centre (typically a 1 cm^2 mica substrate) and left for ~15 minutes before drying with nitrogen gas.

For nucleosome work, intact nucleosomes and chromatin samples were prepared from wild-type FT5 yeast (*Saccharomyces cerevisiae*). Further details can be found in Chapter 4. A single 2 μl droplet of the nucleosome-containing solution was deposited at the centre of a 1 cm^2 mica substrate and left for 5 minutes without further treatment. Nitrogen gas was used to remove any remaining liquid from the samples. No rinsing was performed.

Prepared samples were transferred into the sample stage for STM and TM-AFM ready for imaging or transferred in the UHV chamber for NC-AFM.

5.3 STM Studies of DNA on Graphite and Gold Substrates

STM was used to visualise 2-kbp DNA strands deposited on freshly cleaved HOPG and gold substrates. Sample preparation consisted of 2 μl depositions of DNA diluted with pure water to concentration ~10 ng/μl deposited in the central region of a substrate surface, left for 15 minutes, and dried with nitrogen gas. A number of features were visible during the scan although it should be noted that surface features of HOPG may mimic the structure of biomolecules. Figure 5.1 shows examples of imaging performed with STM. Substrates were scanned prior to deposition and changed significantly after material deposition and surface adsorbates are clearly visible.

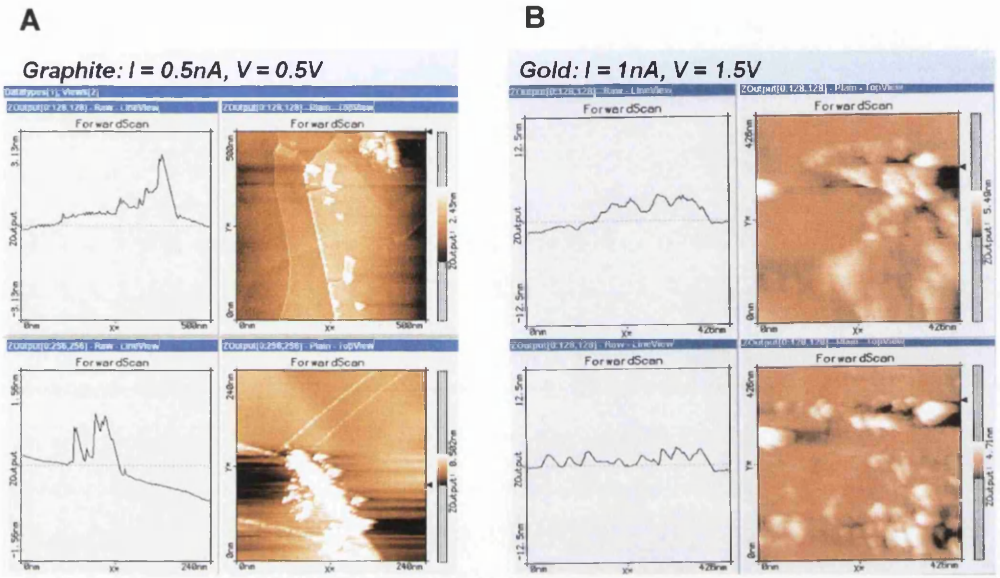

Figure 5.1. STM images: 2-kbp DNA deposited on (A) graphite (HOPG) and (B) gold substrates and imaged in air. Adsorbates are visible with height 1-5 nm.

The height of the adsorbates appears to be ~1-2 nm on graphite substrates and ~5 nm on gold. It is difficult to ascertain whether the observed features are definitely DNA since surface features of graphite can be confused with adsorbates and the bare gold surfaces were relatively rough. Several attempts at point spectroscopy were performed where the tip was moved over an adsorbate, the feedback mechanism disengaged and the tip bias modulated such that an increase in tunnel current was recorded. This process appeared to transform the structure somewhat for the gold images (see *top-right* image compared to *bottom-right*) which implies the adsorbates are ‘soft’ as they are affected by variations in tunnel current and not features of the surface itself. For control experiments performed on bare gold, point spectroscopy did not result in altered images. For this work, imaging was performed in air and contamination is one possible factor. High-resolution STM has been reported by Tanaka *et al.*[1] using flat clean, copper substrates in UHV (Figure 5.2). Specialised pulse-injection valves were required to transfer biological material into the UHV chamber to maintain cleanliness, prevent the clean metal surface oxidising and perform imaging at ~95K. Compared with the work of this thesis where the height of adsorbates was 1-5 nm as measured with STM (Fig. 5.1), Tanaka *et al.* reported higher resolution images with the topographic height for the plasmid DNA at 0.2-0.5 nm and strand diameter of 2-4 nm depending on the tip condition. The high-resolution images of Fig. 5.2 show internal structures are resolved with periodicity 2.6-3.7 nm and compare well to the Watson-Crick DNA of ~3.4 nm.

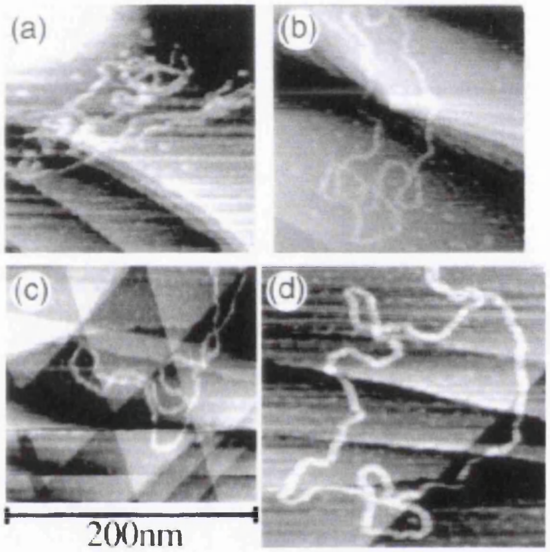

Figure 5.2. Examples of scanning tunnelling microscopy images reprinted from Tanaka *et al.*[1] of 2739 base-paired double-stranded plasmid DNA after pulse injection on Cu(111) in UHV and observed at ~95K. In addition to the DNA, steps and dislocations of the copper in the background are clearly visible.

STM probes the electronic states and therefore the measured height may not necessarily correspond to the actual topographic height of the DNA skeleton. STM contrast corresponds to the density of states near the Fermi level arising from the hybrization of metallic states with the molecules' states. Thus, the prerequisite for imaging with STM is being an electrically conducting substrate. Combining this need with unknown or undetermined electronic properties of biomolecules may invoke difficulties in data interpretation. On the other hand, AFM does not rely on the electron transfer through materials whose electron carrying properties are not yet known and does not require specialised injection valves, nor low temperatures.

For AFM data acquisition, feedback signals are derived from the forces between a cantilever tip and substrate rather than electron tunnelling. These are solely determined by tip-sample interactions which in turn are strongly dependent on surface topography. In this way, a tip follows surface contours and the topography can be mapped. Both electrically conducting and insulating substrates can be scanned at ambient temperature during AFM, thus broadening the range of imaging substrates. STM was not used in subsequent experiments and AFM was the preferred imaging mechanism.

5.4 AFM Studies of DNA on Mica Substrates

Tapping-mode and non-contact mode AFM were used to visualise DNA. Equivalent samples were prepared on mica substrates. A comparison is made in terms of the resolution achievable with each mode.

5.4.1 TM-AFM Imaging

Images of 2.5-kbp DNA fragments adsorbed on mica and scanned in air with TM-AFM are given in Figure 5.3.

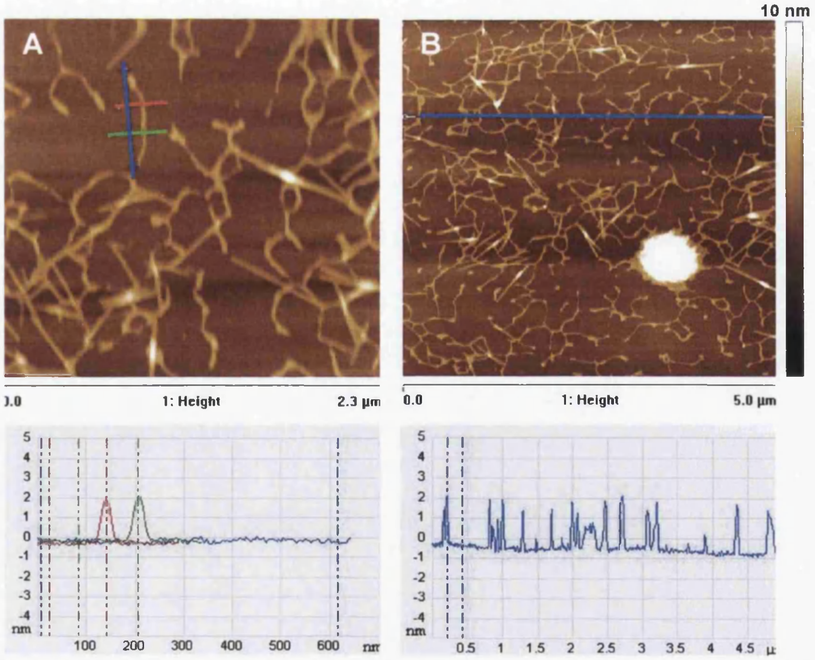

Figure 5.3. TM-AFM images of DNA networks. (A) Scan area 2.3 µm x 2.3 µm. The DNA height is 2 nm as shown by the line profiles. The length of the strand into the network is ~600 nm. (B) Scan area 5 µm x 5 µm. Random networks are clearly visible where DNA strands are lying of top of each other. A large mass is visible where DNA has 'clumped' together due to the high concentration.

Many DNA strands have combined to form random networks. The average height of the DNA in these networks is 1-2 nm as shown in the line profiles. This value agrees with the accepted value of 2 nm as determined with X-ray crystallography. As well as highly concentrated samples, end-to-end aggregation and partial separation of strands can aid the formation of networks. (End-to-end aggregation is reported to be a consequence of favourable free energies of base-stacking whilst in solution comparable to kT ~ 0.6 kcal/mol[2]).

Figure 5.4 shows individual, well-defined DNA strands dispersed over mica. Each strand has topographic height of 0.5-1 nm and measured width ~30 nm. Their measured length is 700 nm and agrees well with the calculated length of a 2.5-kbp molecule of 875 nm as there are some kinks and folds within them. At this resolution, small oligonucleotides and salts are visible in the background. Whilst the height measurements are low compared to the accepted diameter of 2 nm the measured widths are relatively large. The sharpness of the cantilever tip limits the resolution achievable for lateral measurements and since it is in intermittent-contact mode of operation, it is possible that the tip is compressing the molecules somewhat so that they appear broader. Strands are highly distinguishable against the background but the helix nature is not discernable.

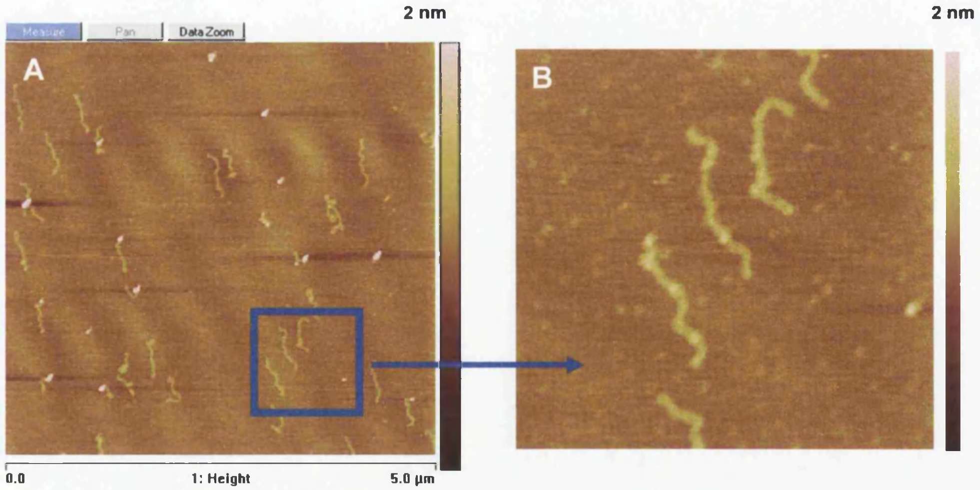

Figure 5.4. TM-AFM images of individual DNA strands on mica. (A) 5 µm x 5 µm scan showing many DNA strands (B) 1.5 µm x 1.5 µm scan showing three individual DNA molecules each having of approximately length 700 nm which when allowing for the kinks agrees well with the calculated length of a 2.5-kbp molecule.

Following the deposition of DNA molecules on to mica, the conformation of DNA can change as it undergoes the transition from three- to two-dimensions. Furthermore, the number of conformations that DNA could possibly adopt is greatly reduced due to the loss of one degree of freedom.

In 1996, Rivetti *et al.*[3] studied the deposition process of DNA molecules onto a mica surface for imaging under the atomic force microscope. Two types of molecule-surface interactions were described[3]: (i) molecules are free to equilibrate on the surface before becoming captured in a certain conformation, or (ii) the equilibration stage is omitted so that molecules are trapped on the surface with conformations resembling the actual 3D conformation. If the appropriate conditions are used, DNA molecules are able to equilibrate on a freshly cleaved mica surface (as in an ideal 2D solution). However, if DNA molecules are deposited on glow-discharged mica or H^+-exchanged mica they do not equilibrate at the surface but appear as simple projections onto a surface plane, suggesting they are kinetically trapped. Findings showed the number of DNA molecules bound to the surface was shown to be proportional to the square-root of the deposition time t. This indicated that DNA molecules diffused to the surface and on reaching it, they could not return into the solution (*i.e.* irreversibly adsorbed). Analyses of the mean-square end-to-end distance $< R^2 >$ and mean-square bend angle between two chain segments $< \theta^2 >$ showed that if DNA molecules were deposited in low salt solutions onto freshly cleaved mica they did equilibrate on the surface. Findings also showed that protein-end labelled DNA fragments deposited onto freshly cleaved mica were able to equilibrate on the surface even with the additional protein-surface interaction (*i.e.* proteins attached to both ends of the DNA did not stop molecules from equilibrating freely onto the surface during the deposition). Conversely, if glow-discharged or H^+-exchanged mica were used, molecules were unable to equilibrate and molecule conformations resembled 3D projections onto the plane.

In view of these findings and the fact that freshly cleaved mica was used in the work of this thesis, it is likely that the DNA molecules are equilibrated onto the mica surface rather than kinetically trapped.

5.4.2 NC- AFM Imaging

NC-AFM was used to for similar imaging of DNA adsorbed on mica but in UHV with base pressure 3×10^{-10} mbar base pressure. Figure 5.5 shows results of a highly concentrated sample (~100 ng/μl).

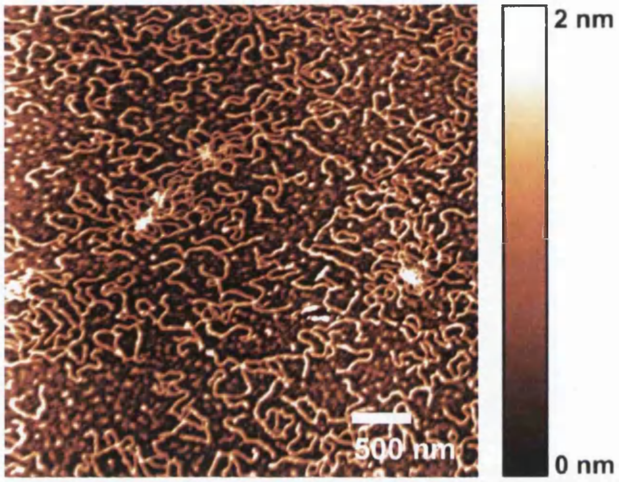

Figure 5.5. NC-AFM of concentrated DNA (~100 ng/μl). The strand-like nature of DNA is discernable despite being densely packed.

Fig. 5.5 shows that high concentrations of DNA are not only easy to scan with TM-AFM but are readily imaged with NC-AFM Again many DNA strands are visible, some of which have combined to form random networks with some similarity to Fig. 5.3. Some tip-sample interference may be expected for molecules associated with other molecules rather than the surface but for DNA there were none observed.

To explore the resolving power of NC-AFM, single molecules were examined using a lower concentration (~10 ng/μl). Fig. 5.6A shows individual strands are evenly dispersed over the substrate which can then be examined in more detail, Fig. 5.6B-D. Here, the high-resolution capabilities of NC-AFM are truly revealed. By zooming in to individual molecules, the helical nature of the DNA is highly discernable. The height contrast of the maxima and minima correspond to the helix, and its pitch can be compared to that determined via X-ray crystallography. For the most common structure, B-DNA, in 92% humidity the pitch is known to be ~3.4 nm for 10-bp[8] (or ~3.5 nm for 10.5-bp[4]).

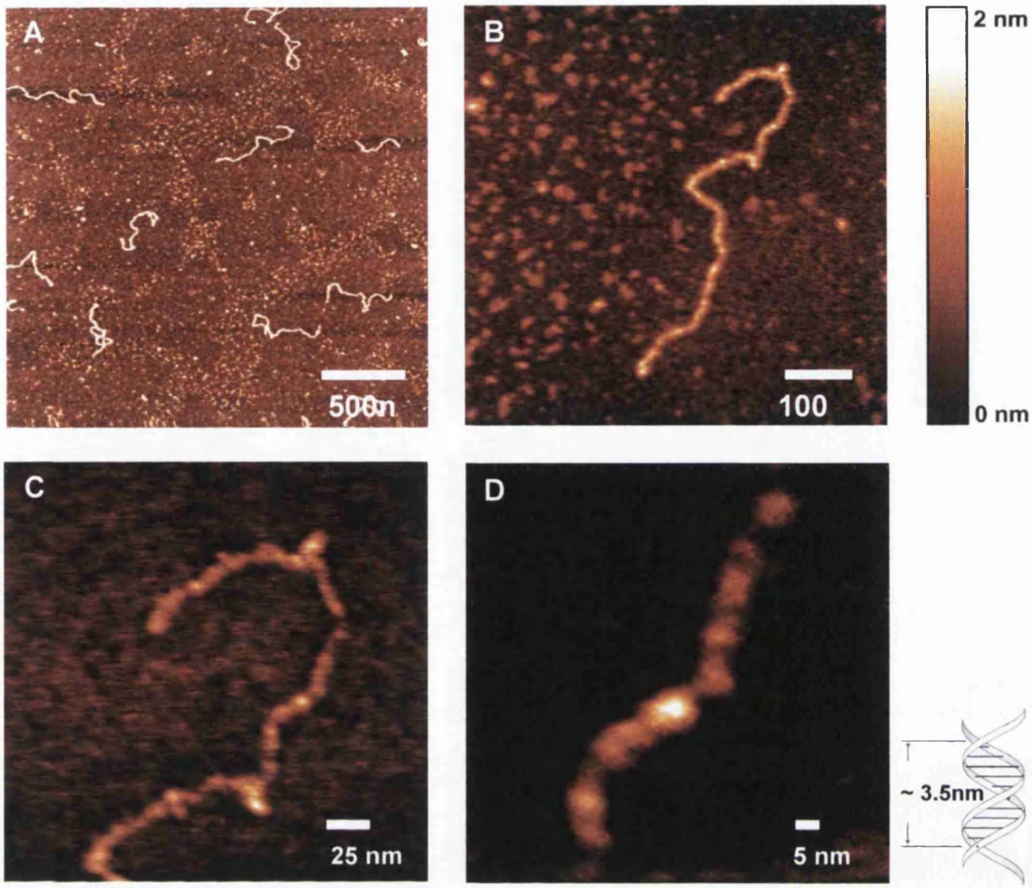

Figure 5.6. NC-AFM images of ~2-kbp double-stranded DNA deposited on mica and imaged in UHV with base pressure 3×10^{-10} mbar. (A) A wide area scan showing individual DNA strands randomly dispersed on a flat mica background. (B)-(D) Zooming in to one particular structure ultimately revealing the helix periodicity at high-resolution. Cantilever resonant frequency ~330 kHz, with pre-set frequency shift (Δf) set at approximately -50Hz. (Images captured with 400 points/line).

Some variation in pitch is expected due to the UHV environment and method of probing it. The average pitch measured for the DNA shown in Fig. 5.6C is 3.0 nm, (standard deviation 0.71 nm) which compares to the pitch of ~3.4 nm for 10 base-pairs as described by Watson and Crick[8]. Note that scanning probe microscopy measurements are obviously dependent on the flexibility of the DNA molecules and interactions with a surface as well as the UHV environment.

Compared with others work (i) Tanaka *et al.*[1] reported that DNA strands deposited on copper in UHV had internal structure with periodicity of 2.6-3.7 nm, (ii) Arai *et al.*[5] reported a pitch value of ~7 nm using NC-AFM on DNA on Si(111) in UHV and (iii) Sugawara *et al.*[6] reported a pitch value of 33 Å (3.3 nm) for DNA on mica using

NC-AFM -but this was using a specialised, super-sharpened cantilever tip (radius of curvature 20 Å) on a sample that had been thermally annealed at a temperature lower than 100 °C for 48 hours in UHV.

Figure 5.7 shows additional scans of individual DNA strands; long molecules ~2000-bp (Fig. 5.7A, B) and a much shorter length ~300-bp (Fig. 5.7C). Once again, the structures are highly defined against the background and detail is seen along the molecules themselves.

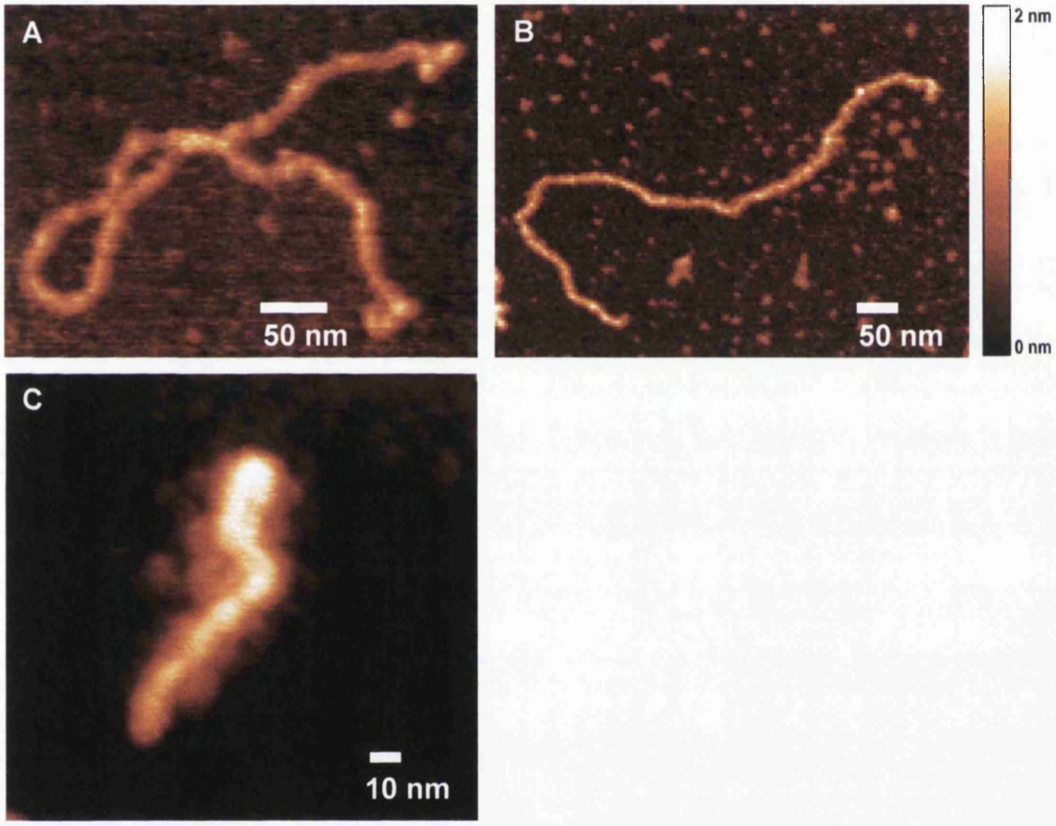

Figure 5.7. High-resolution images of individual DNA molecules (A-B) Double stranded DNA (dsDNA) of length 2000-bp (C) A short strand of dsDNA consisting of ~300-bp.

In Fig. 5.7A it is possible to see the manner in which the molecules folds back and crosses over itself after the lay-down event. Small fragments, possibly oligonucleotides or salt residues, are distributed evenly on the mica surface and exist in close proximity to the strands as shown in Fig. 5.7B. The shorter strand in Fig. 5.7C appears straighter than the longer molecules. DNA molecules of this length (~100 nm) are readily resolved with NC-AFM.

Figure 5.8 shows random networks of DNA at high-resolution which can be later compared to networks on gold. Fig. 5.8A shows at least 5 strands that have combined to form the network. The helical nature becomes evident by continually zooming into the region indicated. An example of a line profile between successive maxima is given in Fig. 5.8C to compare with the helix mode (Fig. 5.8D).

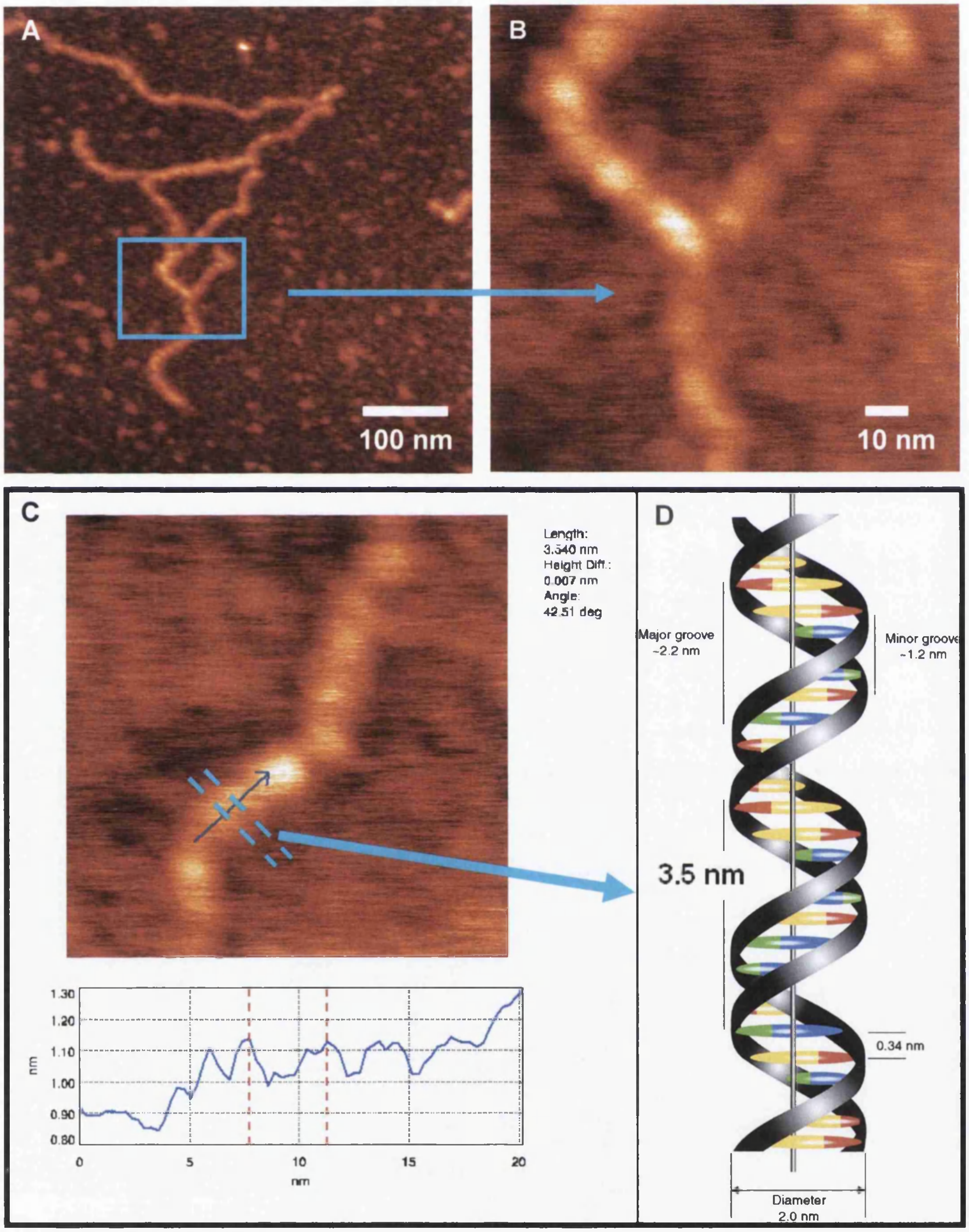

Figure 5.8. (A) Random networks of DNA form where strands are lying across one another. (B) A high-resolution scan of the helix structure. (C) Measurements of the helix periodicity and its associated line profile. (D) Schematic to indicate the periodicity of the molecule. (Images captured with 400 points/line).

Fig. 5.5-5.8 have shown the high-resolution capabilities of NC-AFM. The helical nature is visible with internal structure periodicity comparable to others' pitch values as aforementioned. The high-resolution imaging is made possible from the combined effects of the chosen non-contact mode, a sharp cantilever tip and the vacuum environment.

Dehydration causes a reduction in helical periodicity from a transition of B-DNA to A-DNA[7,8]. B-DNA is the most commonly found form as identified via X-ray diffraction of DNA fibres in 92% humidity; A-DNA was deduced by X-ray diffraction at 75% relative humidity and is the more compact form. Specific recognition areas for proteins, chemicals and drugs to interact are provided by the distinct major and minor grooves of the helix. The grooves in A-DNA are not as deep as B-DNA and bases are tilted more. The B-to-A transition implies a reduction in length of up to 1.5-bp per helix turn with slightly increase diameter of 0.3 nm. It is therefore feasible that dehydrated molecules will appear slightly shorter than expected. Long DNA strands are likely to find increased adhesion sites which may aid conservation of the B-DNA following dehydration. Since the molecules in this study are considered long (~2000-bp) this effect can be neglected. The approximate length measured for each strands is ~ 700 nm which agrees with that expected for a 2000-bp molecule. Short strands of DNA (300-bp) (Fig. 5.6C) are also clearly defined. Shorter pieces (*e.g.* 100-200-bp) of dsDNA can form rods on mica and molecules of this length were not used in this work. Even shorter strands of single-stranded DNA (ssDNA) (~ 50-bp) are reported as difficult to distinguish as regular rods, sometimes appearing as globular formations[2] which could be mistaken as salts *etc.*

5.4.3 Comparison of NC- and TM- AFM Imaging

When NC-AFM images of DNA samples are compared to TM-AFM, it is apparent that highest resolution is achieved using NC-AFM. Frequency-modulated NC-AFM in vacuum reveals more sub-structure than tapping mode since the NC-AFM tip is more sensitive to tip-sample interactions. During TM-AFM in air, water layers are also present which may mask the helix nature from the cantilever tip. This limits the resolution achievable compared to the NC mode which is performed in a totally dry

UHV environment. NC-AFM is capable of resolving the helical nature of DNA and furthermore it is possible to observe the manner in which the molecule folds and crosses over itself (Fig. 5.7).

In the past, divalent cations were used to anchor large DNA molecules on mica[9]. A bridge forms between these cations and the negatively charged phosphate backbone of DNA. There are some DNA fragments, oligonucleotides or ions remaining from purification and are shown to be surrounding the DNA strands in previous images but these are likely be present in all experiments. Although AFM imaging was stable and reproducible for both TM and NC modes, the added advantage of NC mode is that molecules were apparently unaffected by the tip (*i.e.* not displaced or significantly flattened) and a width measurement of 10 nm was closer to the accepted diameter of DNA (*i.e.* being around one third that of TM). TM-AFM was performed in air and so water layers may contribute to the larger measurements. Lateral resolution is also influenced by factors such as tip-size, tip-sample separation and tip-sample forces. Broadening effects due to the finite tip size are observed in most AFM images and as a result, lateral resolution of AFM is hard to define[10]. Images are created with a non-linear character due to multiple interacting regions between the tip and sample[10]. Sharp tips and/or software algorithms can be used to minimise tip-broadening effects[11,12,13,14] so that lateral dimensions are closer to expected values. Technique such as etching are used to modify the tip properties (*i.e.* decrease the radius of curvature and/or sidewall angles) to increase the resolution achievable.

Firstly, these results reinforce the valuable *non-contact* behaviour and secondly, they show that normal NC-AFM cantilevers can be used for scanning soft samples with imaging parameters not dissimilar to those used for hard surfaces like bare mica. The outcome of this comparison study is that NC-AFM is proven to resolve biological structures in more detail than TM-AFM and this claim is supported by others' published observations[15]. The unparalleled quality of imaging soft structures with NC-AFM provides the motivation behind choosing it for subsequent experiments with lesser-known structures and to observe effects of alternative supporting substrates (*e.g.* electrical conductors).

5.5 High-Resolution NC-AFM Studies of DNA on Gold Substrates

DNA has been routinely imaged on mica substrates and now for the first time imaging of DNA deposited on atomically flat gold substrates without chemical modification of molecule or substrate by using NC-AFM[17]. Details concerning the fabrication of the flat gold can be found in Chapter 4. Approximately 15 minutes was allowed for the DNA to adsorb to this hydrophobic surface before drying with nitrogen gas. Hydrophobic surfaces are inert to water: they do not bind to water molecules through ionic or hydrogen bonds. Lenses of water are formed on the surface as water molecules are reorientated to allow hydrogen bonding to still take place between them. Tetrahedrally coordinated water molecules may also link themselves around just about any shape or size of inert molecule[16]. Analyses of chemically unmodified dsDNA molecules show that an untreated gold surface provides an ideal background for imaging deposited DNA molecules, as shown in Figure 5.9. The images clearly show maxima and minima corresponding to the helical nature of DNA.

Measurements made for five individual DNA molecules show that the length is 700 nm which is in good agreement with the calculated length of 680 nm for a linear 2-kbp DNA molecule. The resolution achieved using NC-AFM surpasses that reported by other means and these results were published in 2005[17]. Analyses of 15 separate dsDNA molecules from five separately prepared samples gives an average height of 1.37 nm (standard deviation 0.19 nm). This lower than expected value of height is likely to be due the effects of the UHV. Sample dehydration has already been estimated reduce the height of DNA strands by 0.6 nm[18]. Where DNA molecules are lying across one another the height increases correspondingly.

Certain factors are likely to contribute to a larger than expected lateral diameter measurement of 12 nm. The finite tip width leads to a tip convolution effect; individual molecules are adsorbed on to a surface rather than free in solution implying lateral spread occurs to fully adsorb on to the gold substrate; and the UHV environment may remove excess water layers which would otherwise be present when imaging in air. Despite the difference between the observed and expected lateral dimension, NC-AFM imaging produced high-resolution detail of the double helix structure of DNA, and clearly offers an alternative to cryo-EM and tapping mode AFM in terms of sample preparation, image resolution and reproducibility.

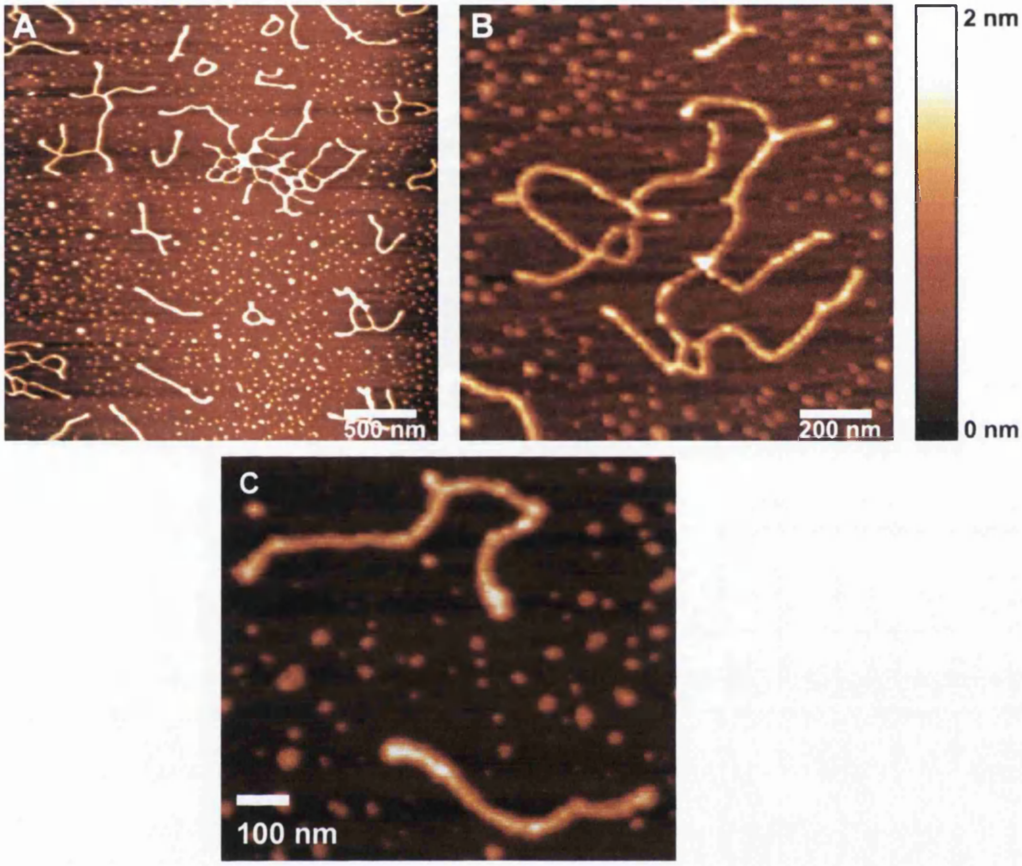

Figure 5.9. NC-AFM images taken under UHV conditions of dsDNA (2000-bp) on atomically flat gold surface. (A) Large area scan of DNA on a gold substrate. (B) Randomly formed DNA network adsorbed on to gold. The helical structure is evident along the DNA length. Interestingly, exclusion regions appear to surround long DNA molecules, small fragments do not appear in close proximity to DNA molecules. This characteristic is prominent on hydrophobic gold substrates. (Published results[17]).

On a gold substrate DNA molecules form a random network (Fig 5.9A, B) which is much more pronounced than previously observed on mica for the same concentration. A randomly formed DNA network consisting of at least nine separate molecules is shown at high magnification in Fig. 5.9B. Interestingly, small fragments (possibly small oligonucleotides or salt residues) are excluded within close proximity of DNA strands which may be a result of charge repulsion. This contrasts with images obtained on hydrophilic mica (*e.g.* Fig. 5.6) where the immediate adsorption of DNA appears to inhibit the formation of the exclusion zones. Individual strands of DNA are also observed with lower frequency and are shown in Fig. 5.9C. Note, that a charge can interact with a neutral surface (or molecule) because of the field reflected by the surface (or molecule) on it becoming polarized[16]. For example, a DNA fragment (*charge Q*) at a distance *D* from a neutral gold surface may interact with it because of the field reflected by the surface. The reflected field is equivalent to an *image charge* (*Q'*) at a distance *2D* from *Q*. Also, a dipole near a surface encounters an image of itself reflected by the surface, and two surfaces will 'see' reflected images of each other. These effects give rise to the Van der Waals (VdW) forces between them and could possible contribute to the phenomenon of exclusion zones as observed on gold in Fig.5.9.

The gold surfaces used in this work were exposed to air and have hydrophobic properties and as a result interactions with hydrophilic molecules is significantly reduced. However, the advantage of gold substrates when used in conjunction with more invasive modes of AFM is that it is available for chemisorption of biological structures that contain free thiol groups or proteins containing cysteine residues. Structures like DNA can be anchored through their termini to gold using thiol groups while still allowing their inner regions to be accessible for simultaneous interaction with other molecules and their imaging. AFM has been applied to DNA anchored on gold substrates and results are reprinted from Medalia *et al.*[19] in Figure 5.10 and provides a useful comparison to the author's observations of NC-AFM of DNA on gold.

In the work of Medalia *et al.* DNA was modified to include a terminal thiol linker at the 5'-ends of DNA strands and DNA could be observed when chemisorbed to the Au surface but those unmodified samples could not be seen. Modified DNA molecules of ~300 nm (900-bp) and ~700 nm (2450-bp) were observed and anchorage allowed imaging in liquid so that proteins could interact with surface-bound DNA. Molecules were ~5 nm wide at the ends with height 1.5-2.5 nm, which become wider, may disappear and occasionally reappear with width 10-20 nm. This implies that despite anchorage at the ends, the middle regions are free to move in solution and may result in blurring. This approach is useful for immobilisation of DNA at the surface in cases where DNA would otherwise not be observable.

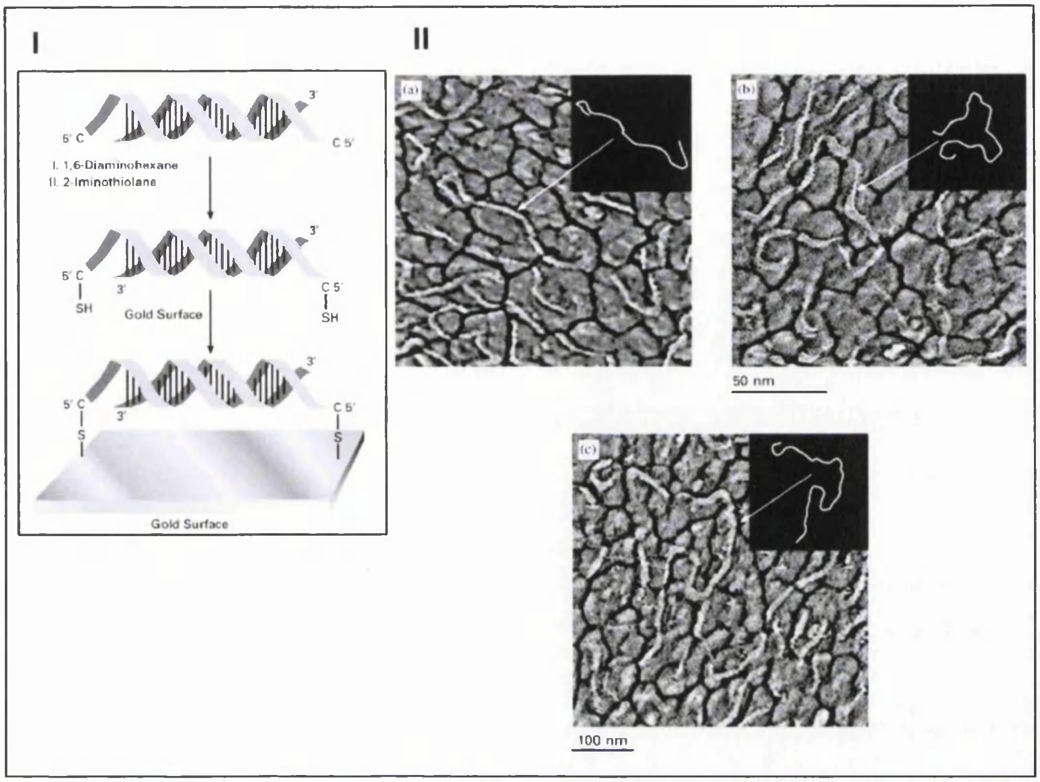

Figure 5.10. Images reprinted from Medalia *et al.*[19] (I) Preparation of DNA using a cytidine residue within a 5' –overhand sequence, transaminated with 1,6-Diaminohexane, then thiolated with 2-iminothiolate giving a thiolated DNA fragments which anchor to gold substrates. (II) AFM imaging of DNA fragments anchored to gold surfaces (a,b) Tapping mode of a 900-bp fragment and (c) 2450-bp fragment.

In comparison, the gold used in this thesis appears much smoother in the background and DNA is highly discernable with comparable height and width where no modification is made to either molecule or substrate.

5.6 High-Resolution NC-AFM Studies of Nucleosome Proteins

DNA is packaged by histone proteins in eukaryotic cells forming nucleosomes which secure DNA through degrees of folding into chromatin fibres[20]. Regularly repeating nucleosomes are considered the basic sub-unit of chromatin and the structure has been determined through X-ray crystallography[21,22]. Conventional AFM imaging of biomolecules involves depositing samples on atomically flat mica and so mica was the chosen substrate for nucleosome as well as DNA investigations. Others have already performed nucleosome studies but with TM-AFM[23] and an example is given in Figure 5.11. In Fig. 5.11A, the DNA strand is visible with at least 4 protrusions along it corresponding to the nucleosome proteins. In Fig. 5.11B, the DNA extending from nucleosomes is clearly visible although no surface detail is evident within the nucleosomes themselves. The limited resolution may be due to the imaging method or thin water layers which are typically present when experiments are performed in air. Fig. 5.11 provides a means of comparison for nucleosomes observed with TM-AFM and with the NC mode of imaging from this thesis.

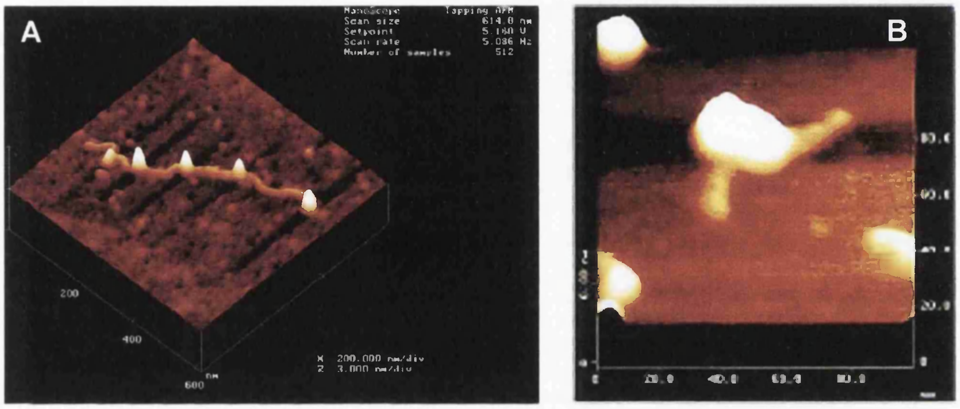

Figure 5.11. Reprinted from M.H. Sato et al. (1999) *Atomic force microscopy sees nucleosome positioning and histone H1-induced compaction in reconstituted chromatin*. FEBS letters, 452, 267-271. Nucleosomes are clearly spaced along a strand of DNA in (A) whilst an isolated nucleosome is examined in (B). In (B) the entry and exit DNA pathways to the protein are visible, but no further detail is discernable on the protein itself such as the wrapping of DNA.

For this thesis, images were captured of intact nucleosomes and chromatin samples were prepared from wild-type FT5 yeast (*Saccharomyces cerevisiae*)[24] as described by Kuras and Struhl[25] (Chapter 4, Section 4.2.4). Purified sonicated chromatin samples were diluted 1:1000 in water before being imaged. A single 2 μl droplet of the nucleosome-containing solution was deposited at the centre of a 1 cm^2 mica substrate and left for 5 min without further treatment. Nitrogen gas was used to remove remaining liquid and the samples were transferred into UHV with base pressure at 3×10^{-10} mbar. Three independently prepared samples of chromatin were used during the course of the experiments, although many others were performed at various sonication levels and concentrations.

5.6.1 Single and Di-Nucleosomes

Figure 5.12 shows NC-AFM studies of nucleosomes adsorbed on to mica substrates and imaged under UHV conditions. At low resolution, intact mono and di-nucleosomes isolated from yeast can be seen, randomly dispersed over the mica (Fig. 5.12A). High-resolution imaging of the highlighted dinucleosome clearly shows detailed structure of these two nucleosomes (Fig. 5.12B).

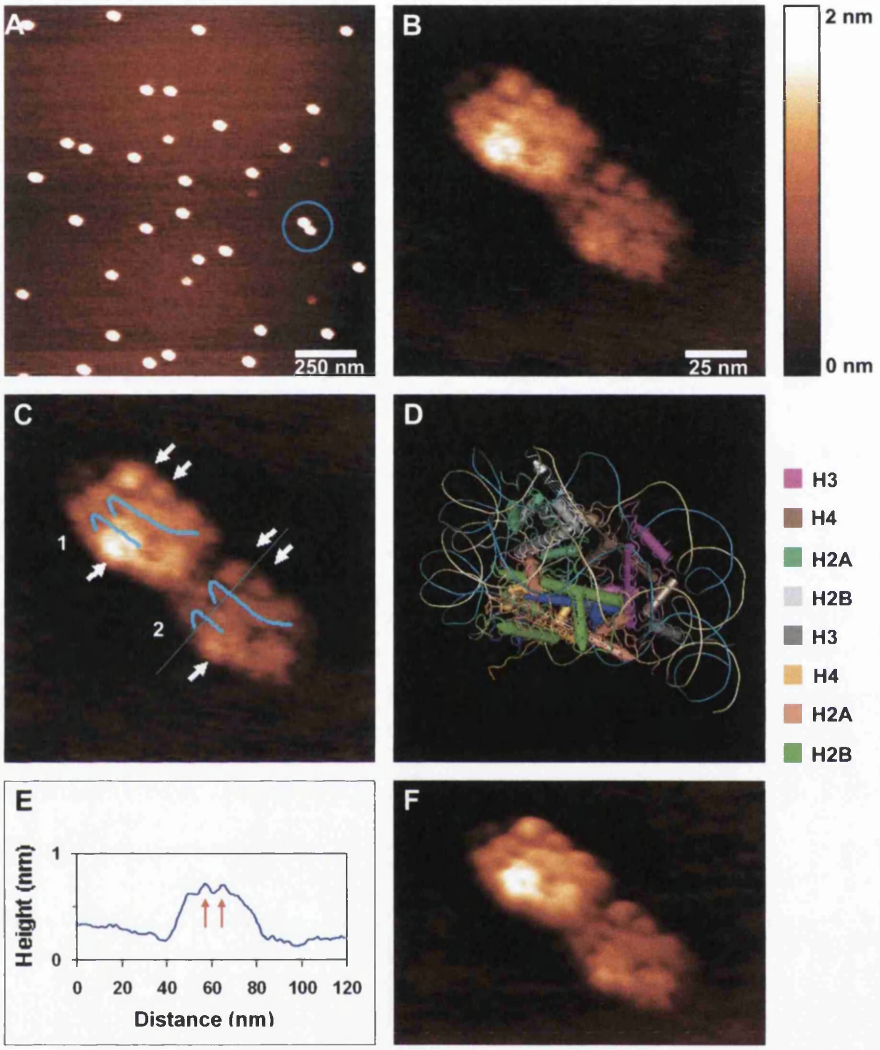

Figure 5.12. NC-AFM of nucleosome structures adsorbed on mica under UHV conditions. (A) Large area scan of mono- and di-nucleosomes randomly deposited on atomically flat mica surface. (B) High-resolution scan of dinucleosome depicted in A. (C) DNA pathway around nucleosome core octamer (blue) correspond to that shown in the simple model derived from the nucleosome crystal structure. Arrows (white) indicate extensions out of the core region. The blue line across nucleosome '2' represents the location of the profile shown in E. (D) The crystal structure of the *Saccharomyces cerevisiae* core nucleosome particle (Protein Data Bank accession number 1ID3) from modelled NCBI Cn3D 4.1 software and oriented with the NC-AFM nucleosome in B. (E) A line profile taken across the dinucleosome (blue line) denotes peaks (red arrows) possibly DNA, having width 3–4 nm. (F) A three-dimensional perspective of the dinucleosome. (Published results[17]).

The nucleosomes in Fig. 5.12B both lie in the same plane and may form an intact dinucleosome. Fig. 5.12C demonstrates how the DNA could be arranged in relation to the nucleosome core. The 3.1Å resolution crystal structure for the *Saccharomyces cerevisiae* nucleosome[22] shows how the histone protein octamer, consisting of two molecules of each core histones (H2A, H2B, H3 and H4), is assembled into a highly ordered structure around which DNA is coiled to form the nucleosome. Since yeast nucleosome cores are very closely packed with linker regions only 15–20-bp in length[22], it is feasible the nucleosomes in Fig. 5.12B are still joined with DNA (height 0.2-0.5 nm).

Alignment of the NC-AFM nucleosome image in Fig. 5.12C with an image derived from X-ray crystal data of a reconstituted yeast nucleosome[22] in Fig. 5.12D (NCBI Cn3D 4.1 software[26]) clearly shows the very high degree of similarity between the two structures which have been oriented on the basis of dimension analysis of super-coiled DNA wrapped around the core histones. For the X-ray model DNA coils are depicted in blue and gold. Within the core, histone H2B (light grey) is nearest the top of the nucleosome and H4 (orange) is at the base to match areas of low/high mass densities of the NC-AFM data.

A line profile across one nucleosome in the structure (blue line, Fig. 5.12C) reveals two height maxima as shown in Fig. 5.12E (highlighted with red arrows) having width 3–4 nm, which correspond to DNA wrapped twice around the histone octamer. The distance between the two DNA strands was 5–7 nm. The measured lateral dimensions of nucleosomes 1 and 2 are 36 nm and the height is 1.2 nm. This compares to the 11 nm lateral dimension for the known nucleosome core particle[27]. Direct comparison between calculated and measured values is difficult since factors such as sample preparation, chemical treatment and controlled UHV environment have to be considered. The differences in lateral dimensions between these measurements and crystal structure data could possibly be attributed to the presence of complete N-terminal ‘tail’ domains of the histone proteins (arrows, Fig. 5.12C), accounting for additional histone mass protruding from the nucleosome core[28]. Alternatively, measurements may vary from expected values as the structures extend as they fully adsorb on to the mica surface resulting in a decrease in nucleosome height. Although the direct comparison between measurements taken using NC-AFM and those calculated using X-ray crystallography are limited with the nucleosome structure, it is clear that NC-AFM reproducibly offers superior structural information when compared to conventional TM-AFM (Fig. 5.11). In future, NC-AFM may complement techniques such as X-ray crystallography and provide high-resolution structural information for biomolecules such as proteins that cannot be crystallised.

5.6.2 Array of Nucleosomes

Chromatin subjected to sonication for a reduced time typically resulted in the ordered nucleosome arrays shown in Figure 5.13.

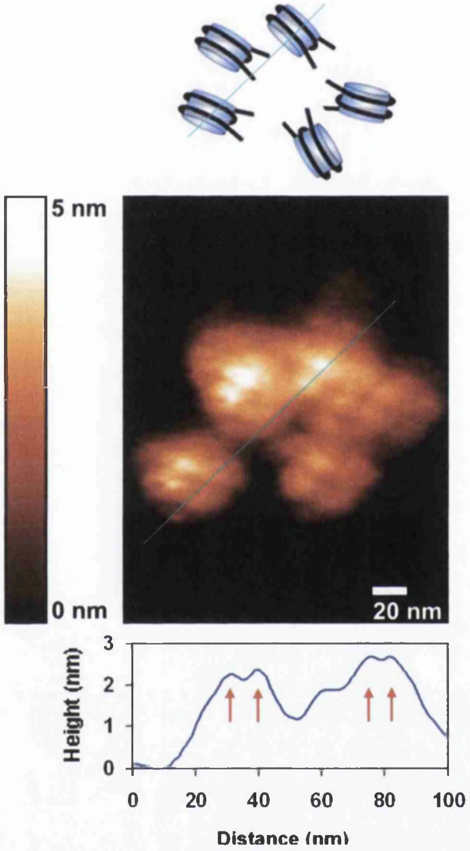

Figure 5.13. An array of 5 nucleosomes adsorbed on mica. A simple model proposes the relative orientation of each nucleosome. A line profile (graph) depicts peaks (4 red arrows) corresponding to DNA maxima as presented in the nucleosome model and actual nucleosome array. (Published results[17]).

The diameter of each nucleosome in the array is approximately 26–30 nm whilst the height is 2–3 nm. This suggests that the nucleosomes are less prone to spreading, possibly due to the interactions between adjacent nucleosomes in a larger macromolecular structure[29]. A simple model at the top of Fig. 5.13 depicts the ordered arrangement of the nucleosomes which is derived from various line profiles taken across each nucleosome. The line profile shown through two nucleosomes (blue line) reveals 4 peaks corresponding to the packaged DNA with each having width 3–4 nm. The reproducibility of NC-AFM is supported through analysis of more than 22 single nucleosomes from different samples.

Using these randomly chosen structures, the average nucleosome height is 1.38 nm, standard deviation 0.27 nm. The average diameter of a nucleosome is 33.17 nm, standard deviation 4.12 nm. Analyses of 12 nucleosomes show height peaks corresponding to DNA wrapping around the nucleosome core. The average DNA width (based on 12 random nucleosomes, 2 DNA measurements per nucleosome) is 3.17 nm, standard deviation 0.39 nm. The reproducibility of experiments shows that NC-AFM is a reliable technique for imaging biological material. Although the presence of salt affects the histone-DNA interactions[30,31], transitions from condensed states to open structures are essential for processes such as transcription and DNA replication[29,32]. In this work, concentrated chromatin was prepared in a salt concentration of 150 mM sodium chloride and subsequently diluted 1:1000 in water (to 0.15mM NaCl) and immediately imaged thereby minimising conformational changes. Nucleosome structure is maintained and reinforced through experimental data. Dilution is required to minimise undesired interaction of highly charged particles with the imaging mechanism.

It is noted that the generation of single strand DNA breaks by the sonication process used to prepare nucleosome samples is possible. However, it is clear that the integrity of the nucleosome has been maintained as determined by the structure revealed. DNA when integrated into a nucleosome is known to be highly resistant to DNA cleavage as is exemplified by pioneering experiments into nucleosome structure, where high concentration deoxyribonuclease (DNAase) treatment of nucleosomes did not result in the degradation of DNA associated with histone proteins[8]. DNAase itself is an enzyme protein used to cut DNA at every phosphodiester bond: regions either side of the compacted nucleosome (*i.e.* the genes) are sensitive to DNAase and are affected but not those associated with histones. This effect is thought to be significant in the expression of particular genes. This issue appears to be supported through NC-AFM images whereby their structural integrity is maintained.

Until now, the high-resolution capabilities of NC-AFM with respect to biological molecules have been established using comparitive studies to their accepted values and to results of other modes of SPM (STM and TM-AFM). Imaging has been performed on a new, alternative substrate to mica (*i.e.* gold) without chemical modification. The structures studied so far are well defined and analyses closely agree with data gained by other means (*e.g.* X-ray crystallography). The close correlation between expected values and experimental data provides the motivation for the next study where high-resolution NC-AFM was applied to molecules whose structure is not wholly defined, namely the DNA-binding protein PUT3.

5.7 AFM Studies of DNA-Binding Proteins

DNA-binding proteins and their significance in biological systems and their potential in bio-electronic applications were described in Chapter 2. Although X-ray diffraction provides information regarding the positions of atoms in structures and gel electrophoresis gives information regarding the length and shape of DNA molecules, many copies of the same molecule are required. However, SPM techniques allow single molecules to be studied. DNA-binding proteins were chosen for this work due to their self-assembling and controllable binding properties with potential use in bio-electronics. AFM was used to visualise a PUT3, DNA-protein complex in both vacuum and air environments and although much is known about the conditions for site-specific binding *etc.* the majority of this data is gained from X-ray crystallography. This particular protein has never been probed with SPM to the knowledge of the author and furthermore, only the binding domain (PUT3, which is a small fraction of the whole protein) has been subject to X-ray crystallography so that the whole protein structure (PUT3p) is undefined at the present time.

In summarising the main features of PUT3p protein (or Proline Utilisation Trans-Activator), it is a DNA-binding protein that binds to DNA in its dimer form. The full-length tagged PUT3 protein is ~116 kDa[33] (dimer size 232 kDa). The structural properties and binding determinants of DNA-binding proteins have been studied giving rise to a number of publications[34,35,36]. Schematics of the PUT3 binding domain are shown in Figure 5.14.

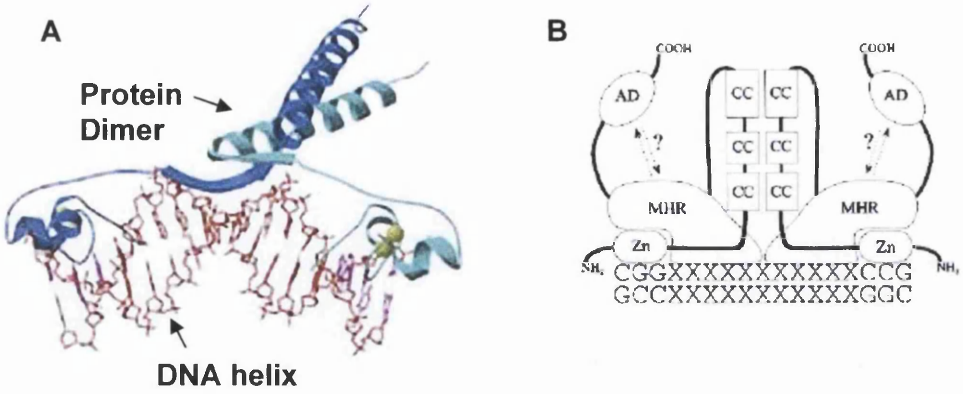

Figure 5.14. (A) A schematic of the yeast PUT3 transcriptional activator protein bound to DNA. [1ZME] The PUT3 protein is a member of the GAL4 family of fungal transcription factors and contains a conserved Zn_2Cys_6 binuclear cluster domain and that bind as homodimers to DNA targets containing 2 conserved DNA half-sites. *"The crystal structure shows how the PUT3 homodimer assumes an asymmetric structure to intercalate amino-acid residues into the DNA minor groove to bend the DNA and position the Zn_2Cys_6 domains to bind the two CGG half sites (purple). The Zn atoms which stabilize the Zn_2Cys_6 domains are shown in yellow"* Nat. Struct. Biol. 1997; 4: 751-9. (B) A second schematic shows a prototypic C_6 zinc cluster protein which recognises the CGG triplets and the spacing between them. Coiled-coils (CC) aid dimerisation. MHR regions prevent binding with inappropriate sequences.

This particular protein is known to undergo binding to DNA strands during gene expression. Furthermore, the protein adopts an 'activated' conformation in the presence of proline (at concentration ~5 mM) and such an alteration in conformation could provide a potential 'switching' mechanism as suggested in Chapter 2. For example, computers are controlled by transistors that switch signals *on* and *off* rapidly and/or amplify small currents and voltages.

5.7.1 Preparation of DNA, Protein and Buffer

Plasmid DNA already containing the specific binding sequence was kindly supplied by Prof. R. J. Reece, University of Manchester along with a separate supply PUT3p protein[37]. The specific PUT3 probe used in the DNA was the double-stranded oligonucleotide shown below:

5' –GATCCCCCGG**GAAGCGCTTC**CCGGGAAGCT- 3'.

The region red/black/red represents a high-affinity PUT3 binding site[33]. In Swansea, this plasmid DNA was cut using different enzymes in preparation for anticipated experiments (Figure 5.15). Specific digestion sites served as reference points for the relative positioning of the protein binding sequences. Enzyme *SacI* was used to cut the plasmid at base-pair 65 for positioning the binding sequence near one end of the

DNA strand; enzyme *ScaI* was used to cut the plasmid at base-pair 1688 for positioning the binding site in the central region of the strand of DNA. Ezyme *Nde I* was used for digestion at a different site, cutting it at 2379-bp so that a second binding site could be introduced such that the end-product contained binding sites near both ends. Further details of sample preparations can be found in Chapter 4.

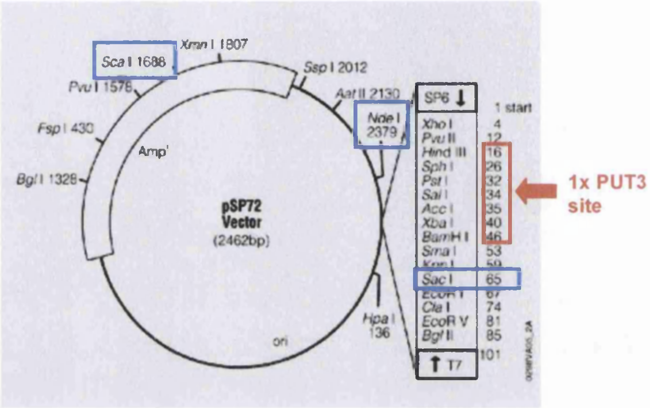

Figure 5.15. The plasmid DNA (2462-bp) containing recognition sites for enzyme digestion. The three sites highlighted in blue were used in this work, cutting the DNA with enzymes Sac1, Sca1 and Nde1 at 65, 1688 and 2379 base-pairs respectively. The single PUT3 binding site is included between bases 16-46.

PUT3 protein was supplied at concentration ~0.35 mg/ml in a reaction buffer containing: 20mM HEPES-KOH (pH 7.5), 150 mM NaCl, 10% glycerol, 10 μM $ZnCl_2$, and binds with high affinity to a particular 16-bp sequence of DNA in the presence of a binding-buffer: 20 mM HEPES-KOH (pH 8.0), 150 mM NaCl, 10% (v/v) Glycerol, 5 mM $MgCl_2$, 10 μM $ZnSO_4$. The binding-buffer was prepared and scanned with NC-AFM. The heights of buffer particles were found to be small and diameters much smaller than that of proteins. A scan taken of the buffer is shown in Figure 5.16.

The DNA-protein binding reaction is known to be reversible and occurs at room temperature and it was anticipated that preferential binding of the protein at these high-affinity sites would be manifest through AFM work.

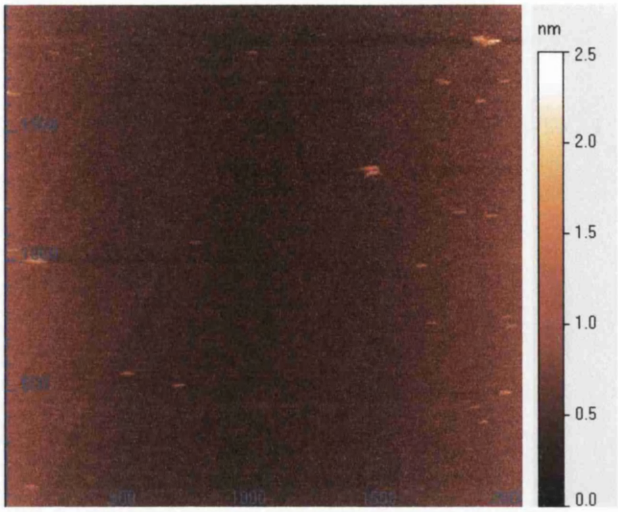

Figure 5.16. A NC-AFM image (2 µm x 2 µm) of the reaction buffer deposited on mica, showing small particles with height ~1 nm. This buffer was later used for PUT3-DNA binding.

5.7.2 Imaging PUT3

Despite the fact that detailed structural knowledge has been derived from X-ray crystallography and its binding characteristics gained from mobility shift assays/gels, this is the first time to the author's knowledge that SPM has been applied to examine this particular protein. It was not known whether the protein would interact or 'stick' sufficiently to imaging substrates for SPM to be performed, as surface treatment is a necessary prerequisite in many studies. Furthermore, it was unknown whether the 'stickiness' of the protein would cause interference with the imaging mechanism. In view of these uncertainties a considerable number of experiments were performed involving a number of protein, DNA, and buffer concentrations with the aim of visualising the protein clearly and reproducible with AFM. The protein concentration (as indicated by a gel) was ~0.35 mg/ml and dilutions were made with deionised water to disperse the molecules. 2-5 µl amounts were deposited on to a freshly cleaved atomically flat mica substrate and left for approximately 10-15 minutes without further treatment. Remaining liquid was removed using high purity N_2 gas. The protein samples were subjected to both NC- and TM-AFM imaging.

5.7.2.1 NC-AFM on Mica

Protein samples were transferred to ultra-high vacuum (UHV) with base pressure at 3 x 10^{-10} mbar and scanned. One successful experimental result is shown in Figure 5.17

and although the visualisation represents protein when diluted in water before deposition on to mica, immense difficulties were encountered in gaining stable and reproducible imaging of this sample. Imaging parameters needed constant attention to prevent the tip-sample interference sample and imaging artefacts. The height of the protein specimen in Fig. 5.17 is ~11 nm with corresponding width, as indicated in blue, ~70 nm.

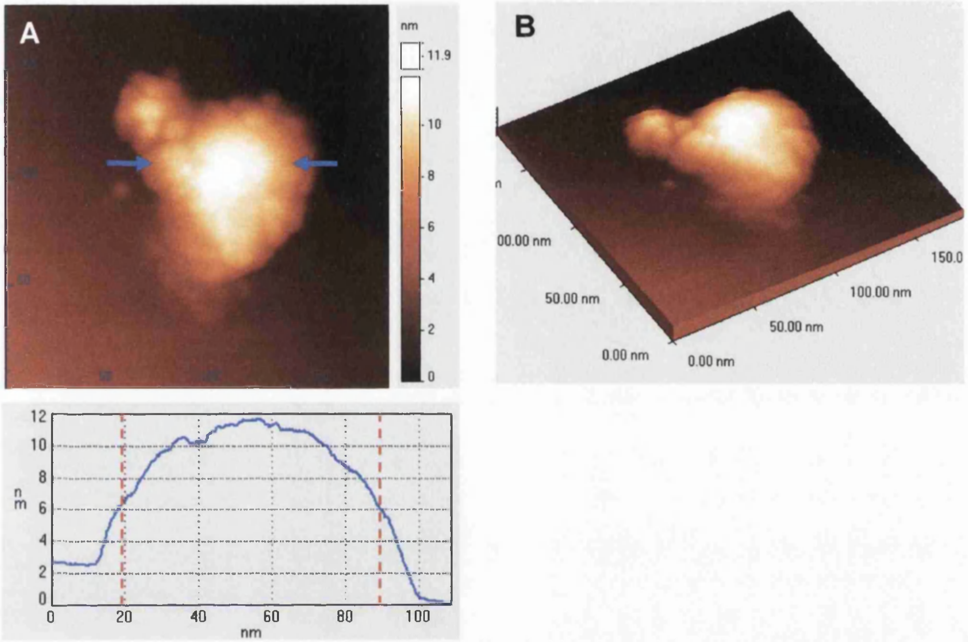

Figure 5.17. (A) The PUT3 protein structure. The diameter at the location indicated is ~70 nm with maximum height ~11 nm. There is a small lobe attached to the large mass, possibly corresponding to the binding domain. This structure is considered large for a single protein and is likely to be in its dimer form, or larger. (B) A 3D perspective of PUT3 dimer. For this image, 1 µl protein (at 0.35 mg/ml) was diluted with 100 µl of water and then deposited on mica.

As the mass of a full-length tagged PUT3 protein is ~116 kDa[33], the mass of a dimer would be expected be ~232 kDa. Using the conversion $1\,Da = 1\,u = 1.660\,538\,73\times10^{-27}\,kg$ and protein density is $\sim 1.4\ \mathrm{g/cm^3}$, the expected volume of a PUT3 dimer is $\sim 275\ \mathrm{nm}^3$. Approximating the PUT3 dimer as a sphere in space with $\text{volume} = \frac{4}{3}\pi r^3$ gives an expected radius of ~ 4 nm (*i.e.* diameter ~ 8 nm). Although this diameter value is comparable to the PUT3 height measurement of Fig.5.17 (~11 nm), the lateral measurements reveal much larger values (~70 nm). Therefore, the structure shown in Fig. 5.17 is likely to be an aggregate of PUT3 proteins (*e.g.* several dimers spread over the surface).

5.7.2.2 TM-AFM on Mica

TM-AFM was used to scan the proteins at lower resolution and this section presents images of PUT3 protein obtained using tapping mode operating in air. Similar sample preparation was carried out: 1 µl PUT3 was diluted in 50 µl water, then 2 µl deposited at the centre of mica, left 15 minutes and dried with N_2. Examples of results are given in Figure 5.18.

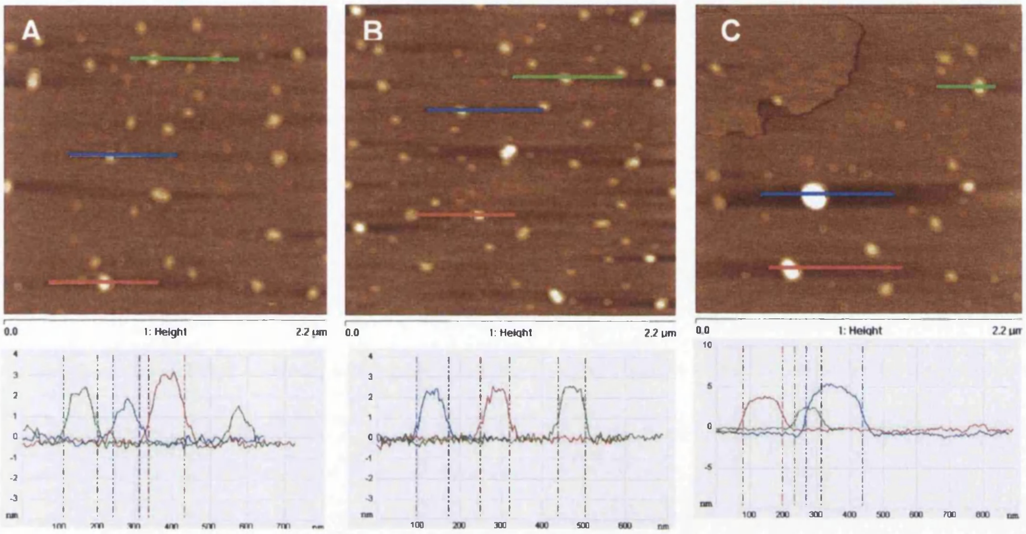

Figure 5.18. (A) TM-AFM of PUT3 proteins in the absence of DNA. (A) The line profiles as indicated give the following diameters: green ~91 nm, blue ~73 nm, and red ~ 95 nm. For these cases, the topographic height varies up to 5 nm. (B) Diameters: green ~78 nm, blue ~78 nm and red ~82 nm, all with height 2-3 nm. (C) Larger clusters of proteins, with diameters given: green ~ 82 nm, blue >160 nm and red 121 nm. Height of the clusters is ~5 nm.

A range of protein diameters (~70-90 nm) is observed. Even larger structures are also visible where proteins have clustered together (diameters $\geq$ 160 nm). The frequency of protein size is depicted in Figure 5.19 in histogram format. The most frequently measured protein size as measured with TM-AFM lies within the range of 50-75 nm with measured height between 2 and 2.5 nm. This data supports that found for NC-AFM (Fig. 5.17) where the measured diameter was 70 nm and height 11 nm. As the diameter prediction for a spherical-shaped PUT3 dimer was ~ 8 nm (Section 5.7.2.1), these results also suggest that larger aggregates of PUT3 are being formed.

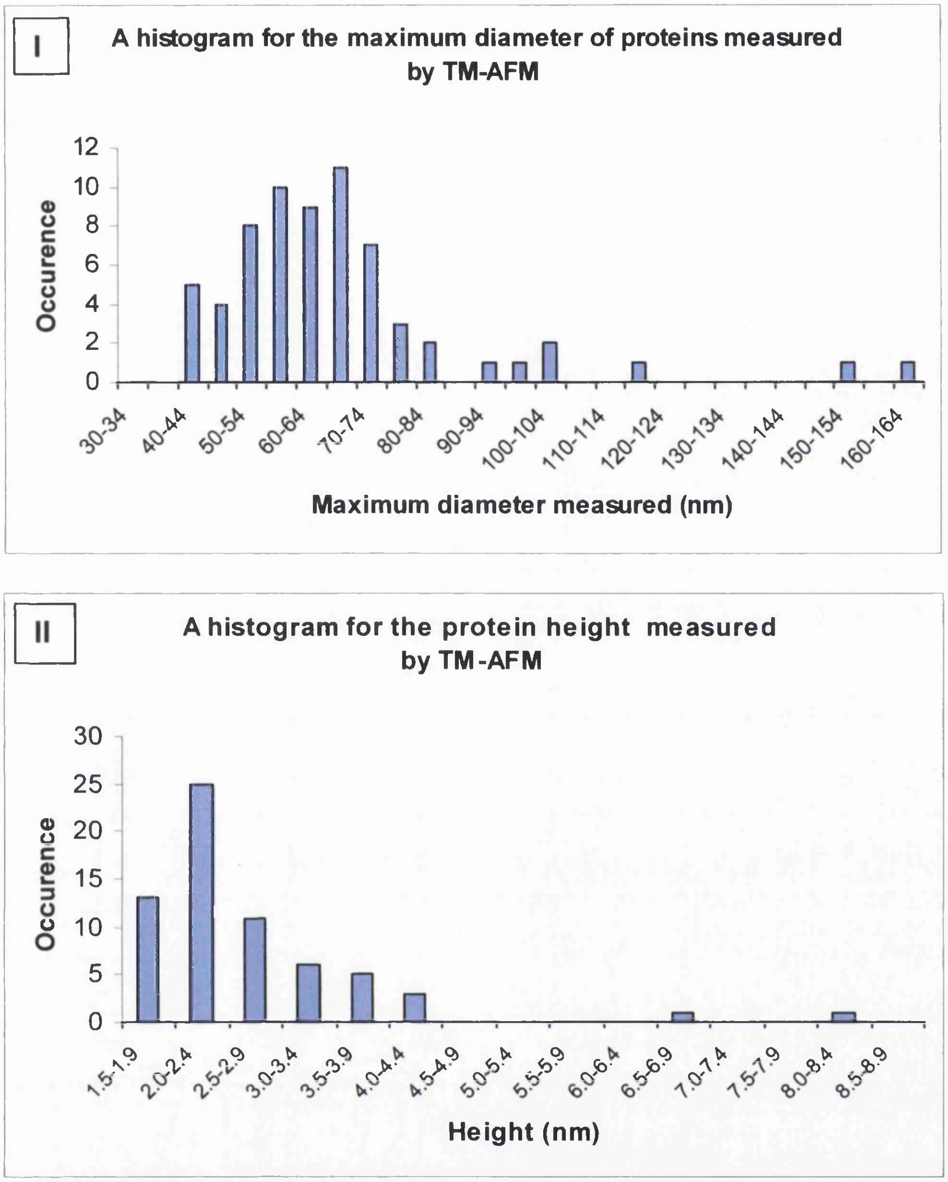

Figure 5.19. Histograms showing the frequency of protein (I) diameter and (II) height measured with TM-AFM.

The noticeable higher height measurement in NC-AFM is likely to be due to the non-contact nature of the AFM mechanism, whereas for TM-AFM the tip is likely to be 'tapping' the soft molecules into the surface thereby compressing them somewhat. Less imaging difficulties were encountered with TM-AFM and imaging was highly reproducible but at low resolution.

5.7.3 NC-AFM of DNA strands with Protein Binding Sites

The 2.5-kbp DNA strand containing the 16-bp binding sequence was scanned in the presence of buffer particles using NC-AFM. Again, difficulties were encountered with the tip picking up particles and imaging parameters required frequent adjustment. One of the successful results is shown in Figure 5.20. Results yielded a lower than expected height of 0.8-1.0 nm, presumably due to the presence of the buffer, with measured diameter 20 nm and approximate length of ~860 nm. This compares favourably to a calculated length of 875 nm for a 2.5-kbp molecule.

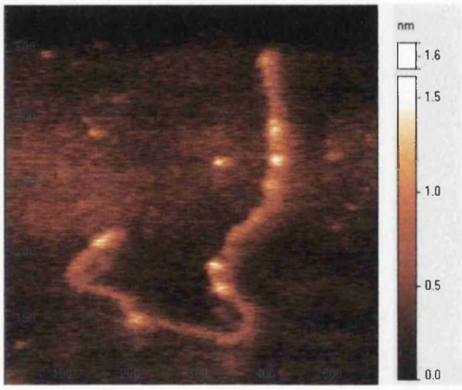

Figure 5.20. An individual strand of DNA diluted in buffer with scan size 550 nm x 550 nm. The height of the DNA strand is 0.8-1.0 nm. A blurring effect is noticeable and attributed to the presence of buffer.

The DNA was mixed with buffer to see its effects on the imaging of DNA which is straightforward when diluted in water. A buffer-induced blurring is indeed encountered and attributed to the presence of charge particles within the buffer.

5.7.4 DNA with PUT3

5.7.4.1 NC-AFM on Mica: A Comparison Study of Normal and High Frequency Cantilevers

Despite many trial-and-error experiments it was proved notoriously difficult to image molecules prepared in buffer using normal NC-AFM cantilevers. The spring constant for these cantilevers is 42 N/m and oscillating frequency ~750 kHz. These problems were attributed to strong tip-sample forces causing the tip to pick up particles or jump-to-contact. Very few single strands of DNA could be observed, which were thought to coil up if the concentration was high. Figure 5.21 shows the only successful NC-AFM scan of protein with DNA using a normal NC-AFM cantilever.

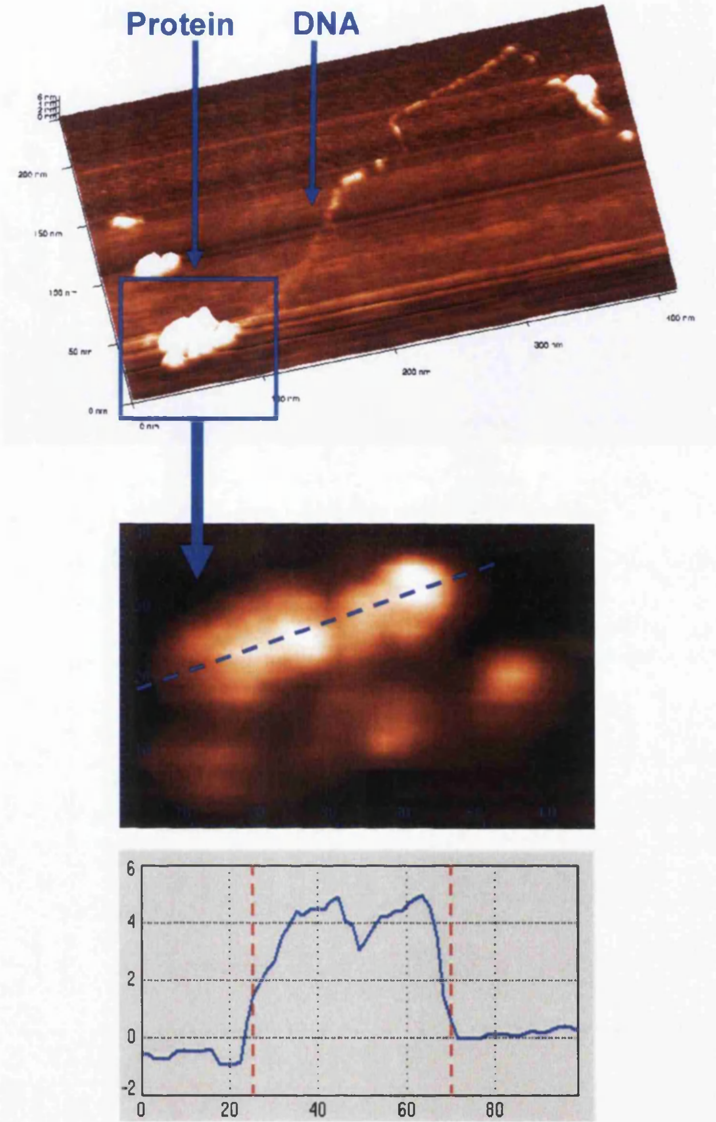

Figure 5.21. The only NC-AFM image of PUT3 bound with DNA using a normal NC-AFM cantilever. Problems were associated with stable, reproducible imaging as the proteins and buffer were causing tip instabilities. The frequency shift (Δf) was set relatively low between -25 and -40 Hz. The protein height is ~5-6 nm and of width ~60 nm (see zoom view and line profile) and situated along a DNA strand of length ~500 nm, excluding coils/folds at the other end. The zoom into the protein shows a number of features, and consists of at least 2 proteins attached to the DNA. Note, problems were encountered in imaging, and a large number of protein DNA and buffer concentrations were used. For this particular image the following amounts were used: 1μl DNA (10 ng/μl), 1μl PUT3 (0.35 mg/ml) 8 μl buffer and 490 μl water. The large amount of water minimised the presence of the charged particles in the buffer although structures were difficult to find.

For the imaging in Fig. 5.21, the sample was prepared using 1μl DNA (10 ng/μl), 1μl PUT3 (0.35 mg/ml), 8 μl buffer and 490 μl water. The large amount of water minimised the presence of the charged particles in the buffer although structures were difficult to find. DNA was cut with Sca 1 at 1688-bp, thereby positioning the binding site within approximately 270 nm from one end, out of a whole length of 2462-bp. In Fig.5.21, the proteins appear to be bonded to the DNA strand but appear to be much closer to the end than expected. This implies the DNA which should be extending further than the protein has either folded up (as the opposite end appears to be), has been severed during deposition, or simply that protein-binding has occurred at a similar recognition site with lower affinity. Nevertheless, this observation of proteins associating with DNA is still advantageous for conductivity studies. These initial experiments exposed problems finding proteins associated with DNA with the current setup employed. Although NC-AFM is considered a non-contact method of imaging, the imaging quality of initially good, sharp cantilevers was found to deteriorate when various concentrations of protein and buffer were used. The process to get a single image of DNA associated with protein was extremely time-consuming and so methods were sought for overcoming these difficulties.

To explain the process occurring it is necessary to consider what happens in terms of the tip-sample forces. Besides attractive Van der Waals forces, chemical bonding can occur between tip and sample. These forces are attractive for spaces greater than the equilibrium distance. The tip, mounted on a spring can jump-to-contact if the stiffness of the cantilever is sufficiently low. The jump-to-contact is avoided by oscillating cantilevers with larger amplitude. However, energy needs to be supplied to the cantilever during each oscillation and if hysteresis occurs amplitude control can be difficult. A high spring constant is a second option. Very high spring constant silicon cantilevers can be purchased[38] with force constant (k) in the range 6-270 N/m and resonant frequency 500-1700 kHz. (Nominal values 140 N/m and 1100 kHz respectively.) For the studies in this thesis, very high spring constant cantilevers could be used without any significant developments made to the AFM system although they had previously been unused in any experiments. In this thesis, the chosen cantilever had resonant frequency ~612 kHz and oscillating frequency of 1069 kHz. The problems associated with imaging were remedied and DNA molecules having proteins attached were imaged successfully. The high spring constant cantilever overcame problems associated with tip-sample interference is therefore extremely useful.

Figure 5.22 shows scanning of DNA associated with protein that is reproducible using the high-spring constant cantilever. The proteins are relatively large and each appears to have a small lobe extending out (to the right) from the larger mass, indicating a similarity to Fig. 5.17. The lobe is not always visible and is likely to depend on its orientation with respect to DNA when first bound in solution and how it adsorbs to the surface following deposition.

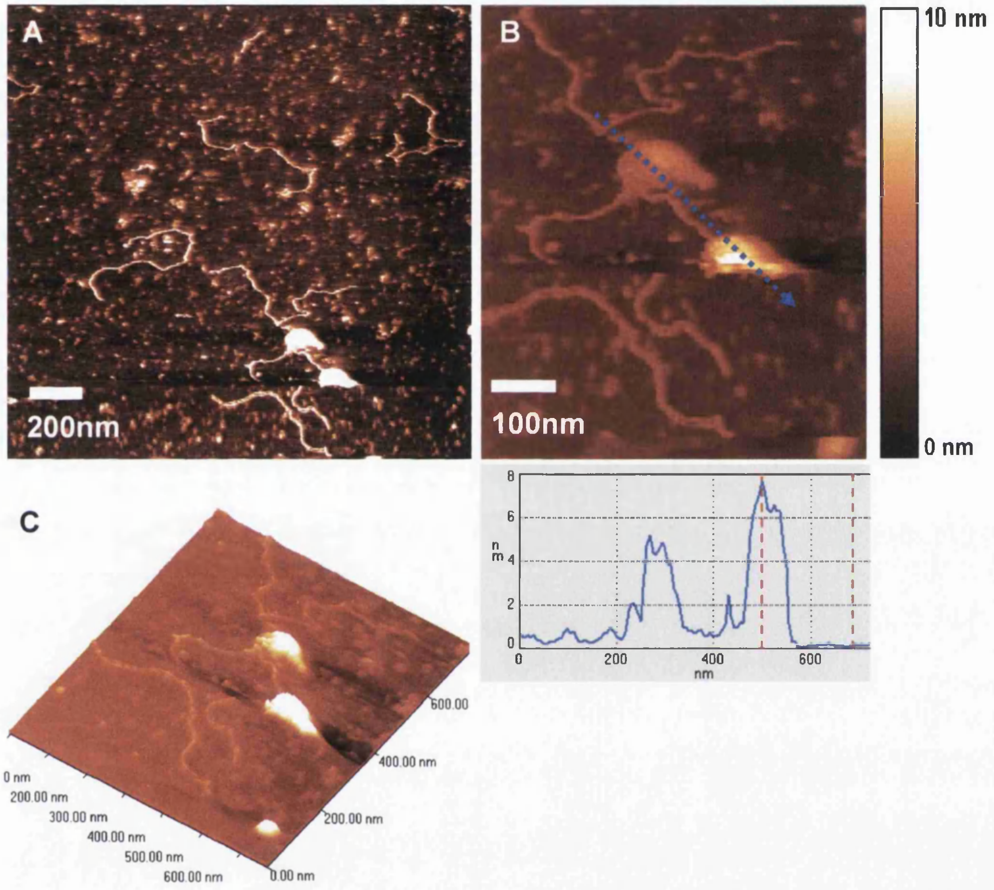

Figure 5.22. NC-AFM scans of DNA associated with protein. (A) A wide area scan showing at least 6 DNA strands. (B) A high-resolution image showing DNA strands associated protein. Note again that the proteins are relatively large and it is feasible that clumping is occurring. The measured height of the proteins is 5-8 nm. For these images, the concentrations of DNA, protein and buffer were followed as much as possible to that specified[33] with the incubation time doubled from 30 min to 1 hr at room temperature for maximum binding. Images were captured with a high frequency cantilever having resonant frequency ~612 kHz (reference frequency 1069 kHz) with oscillating with amplitude 0.4V and $\Delta f \approx$ -70 Hz.

One protein is associated with DNA near the end of the strand in Fig. 5.22 and another is associated about halfway along and is likely to be interacting with a separate DNA strand. This positioning along the DNA is expected since the binding site sequence of this DNA is situated close to one of the ends. Although a high spring constant cantilever is used for imaging samples containing proteins and buffer particles, there are still slight problems as shown in Fig. 5.22B when the cantilever encounters the protein mid-way through the scan where a small effect is seen. Feedback is maintained and the tip is able to carry on scanning. Numerous experiments were performed to capture DNA associated with protein and additional results are shown in Figure 5.23.

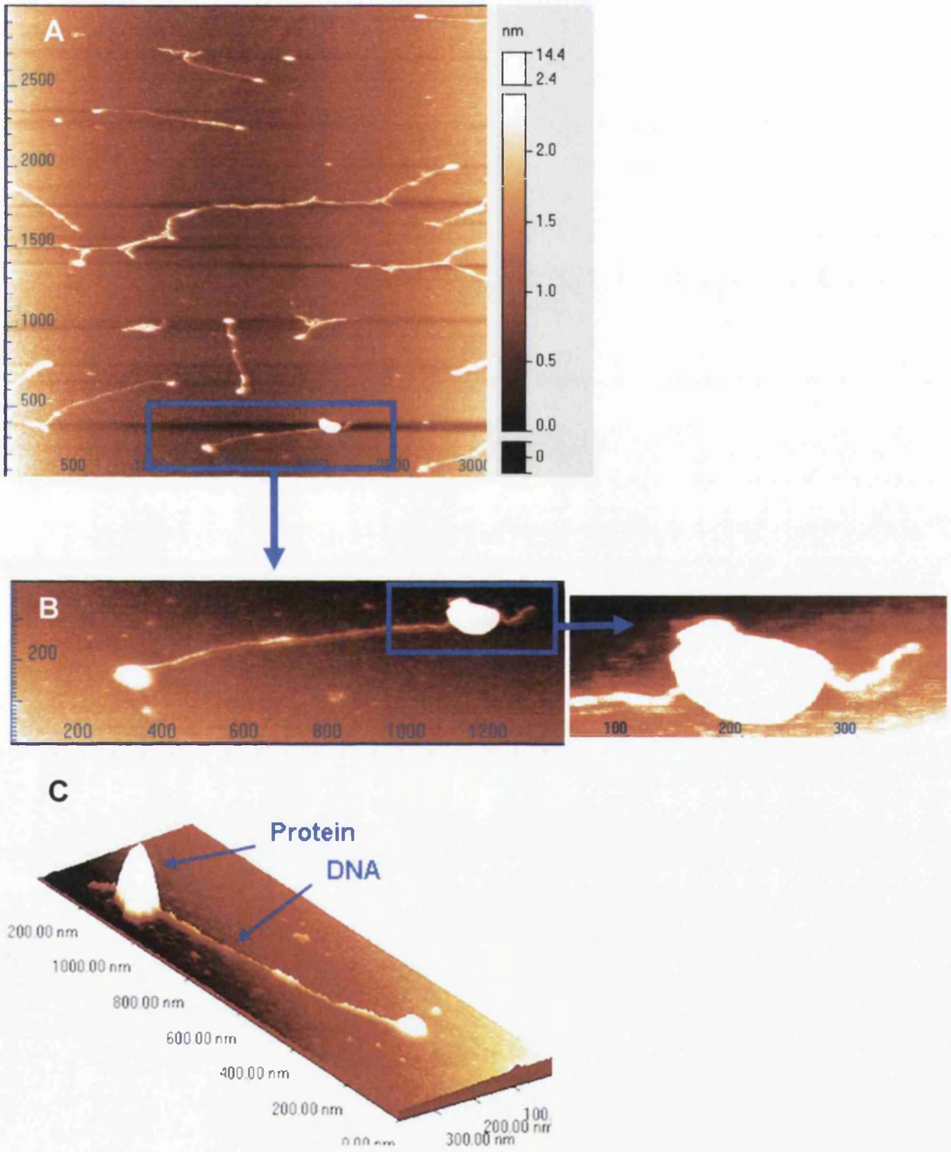

Figure 5.23. NC-AFM of DNA mixed with protein. (A) A wide area scan 3 μm x 3 μm with numerous stands of DNA visible. (B) A zoom in to one of these structures reveals a DNA with its associated protein and (C) A 3D perspective showing the relative height of protein to DNA. The protein height is ~12 nm whilst the DNA has height ~1 nm and length ~1000 nm which is close to the expected value of 875 nm for a 2.5-kbp molecule. For these particular images, the amplitude set to 0.3 V and Δf = -120 Hz.

Fig. 5.23 clearly shows a single DNA strand with a significant mass attached which is very likely to be protein. The protein is relatively large and once again appears to have a small lobe attached (top of protein, Fig. 5.23B) and this supports the observation recorded in Fig. 5.17-22. For this case DNA should extend past the protein-binding site by an extra ~270 nm. A tail does indeed extend by ~110 nm from the edge of the large protein. This implies site-specific binding is occurring, with the large protein extending out further from the binding site centre. Figure 5.24 shows results from additional scans of the same substrate.

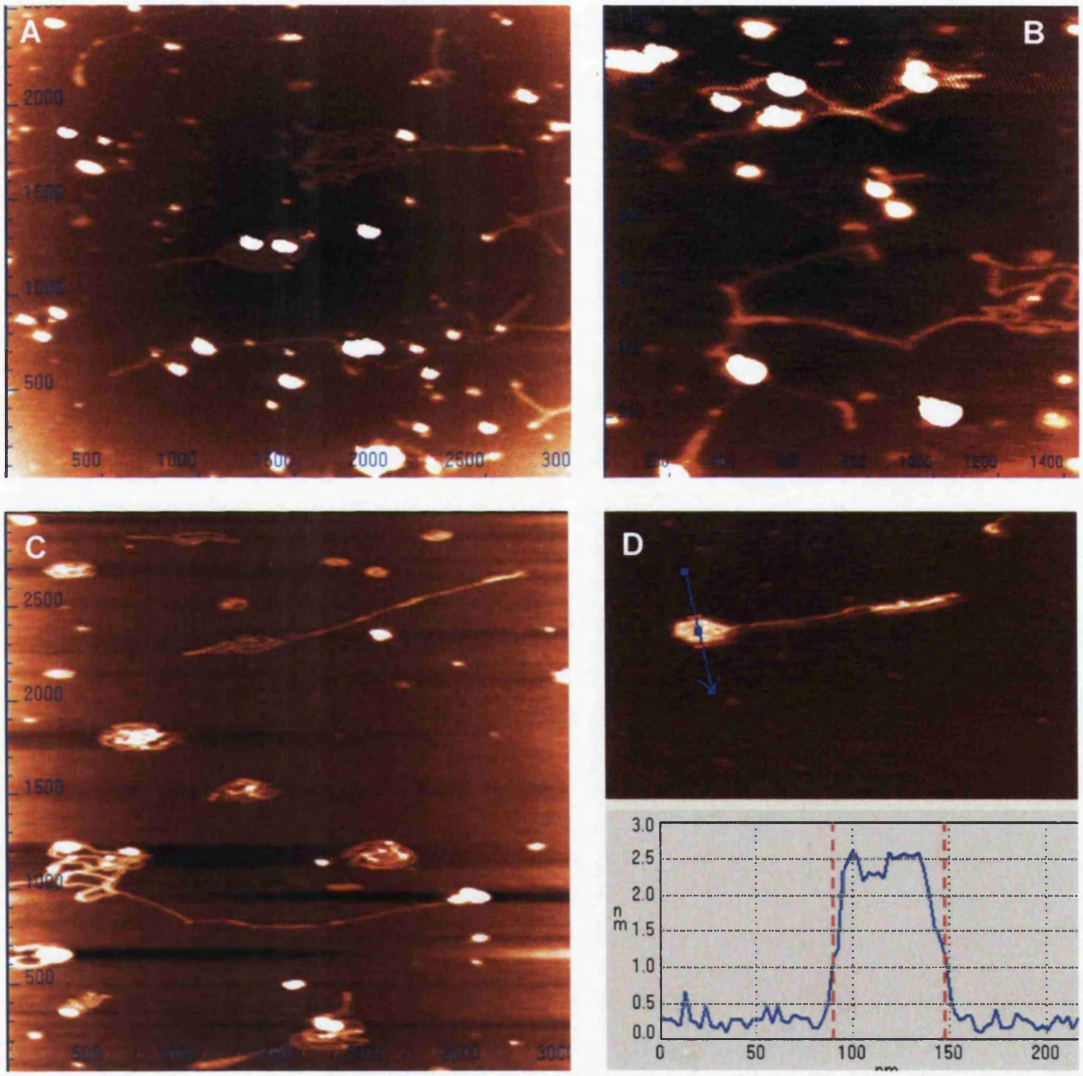

Figure 5.24. NC-AFM of DNA mixed with protein (A) Scan area 3μm x 2.5μm. (B) 1.45μm x 1.45μm. The proteins appear in white and are larger in height, masking the DNA strands in comparison. The protein height (in white) are ~9-15 nm, and diameter between 90-140 nm. (C) Scan area of 3 μm x 3 μm showing coiling at the ends of some DNA molecules and many are coiled up completely, possible due to protein/buffer effects as this was not seen for on other samples. DNA height is 0.7-0.9 .(D) A line profile showing the possible attachment of a protein, although only ~2.5 nm in height but its position and line profile across is gives width ~60 nm which is expected for protein.

Aggregates are present at the ends of some DNA molecules in Fig. 5.24 and are likely to be proteins and/or coils of DNA due to its long length. In general, the dimensions of DNA coils appear to be less than that of protein. Histograms representing the occurrence of protein diameters and heights as measured with NC-AFM are given in Figure 5.25. A range of dimensions are recorded for the proteins and measurements suggest that clusters are formed which consist of two or more proteins.

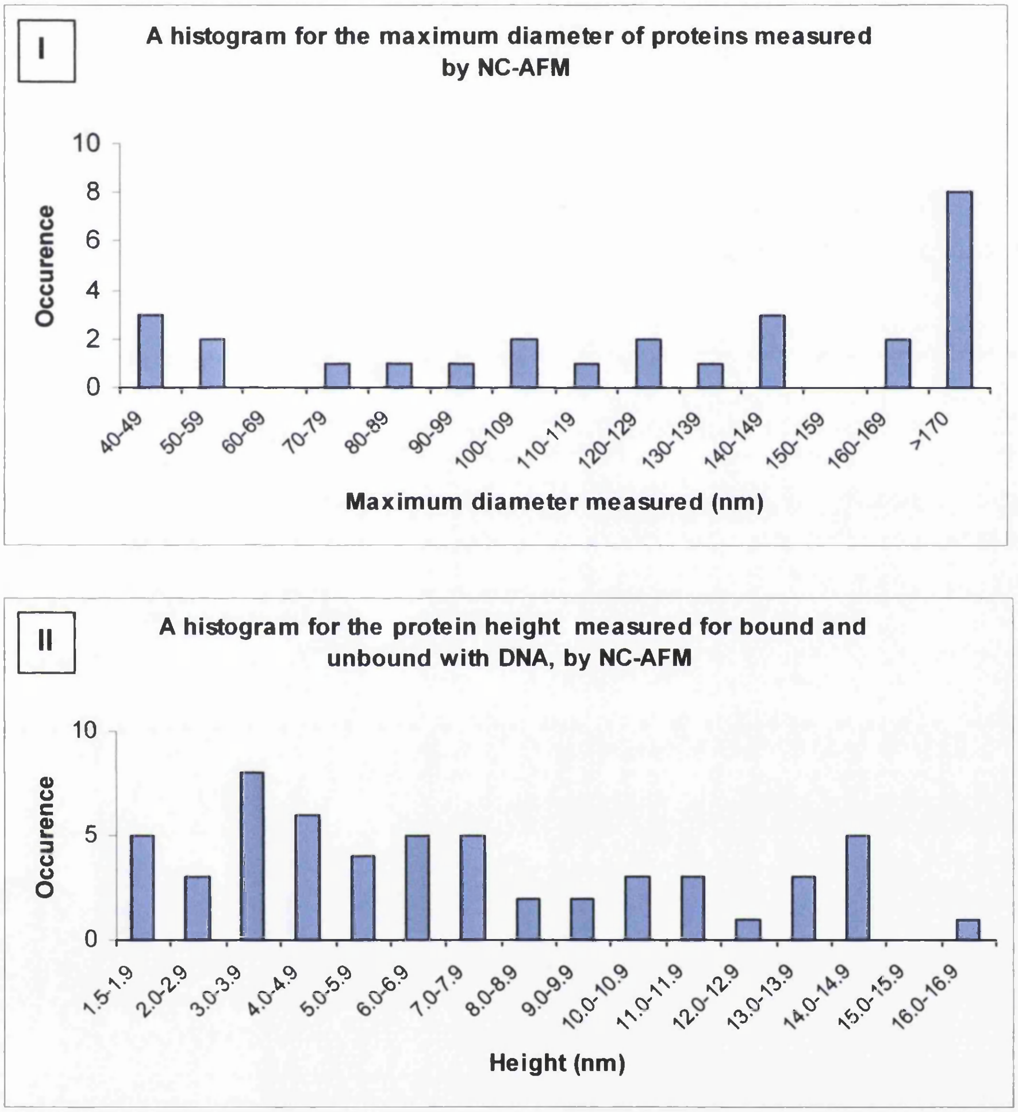

Figure 5.25. Histograms showing the frequency of protein (I) diameters and (II) heights as measured with NC-AFM. Note, diameters strongly depend on tip shape and through the course of this work, many cantilevers were used therefore some variation is expected although height measurements are considered more useful.

Compared to results with TM-AFM (Fig. 5.19) broad, flat distributions are observed with NC-AFM. In general, the heights of proteins measured with NC-AFM (Fig.

5.25) are larger than for TM-AFM and sample compression could possible account for lower height values recorded using TM-AFM.

5.7.4.2 TM-AFM on Mica

Proteins mixed with the DNA containing an additional binding site were imaged with TM-AFM and results are shown in Figure 5.26. This structure which contains two binding sites will be useful in conjunction with electrodes when probing DNA's conductivity.

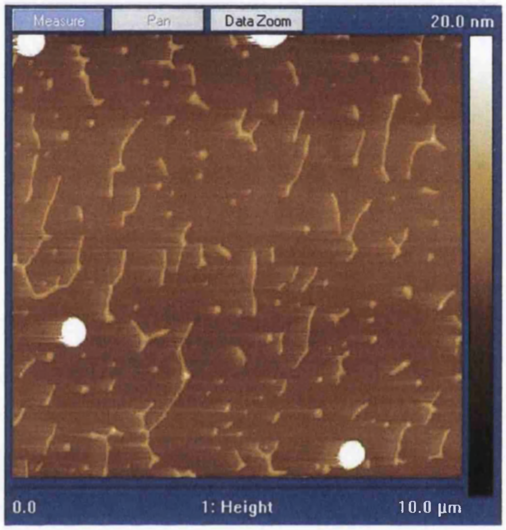

Figure 5.26. A large area TM-AFM scan of DNA mixed with protein in the presence of buffer. Many DNA strands are visible forming random networks.

There are many DNA strands of different lengths in Fig. 5.26 and fragmentation may have occurred during sample preparation. Many strands appear to be associated with protein as there is noticeable widening at the ends of molecules where the binding sites are situated. There is some noticeable blurring in the resulting images which may be due a fast scanning speed but also the presence of buffer particles. Several individual strands are imaged at higher resolution in Figure 5.27. A protein is likely to be attached to the DNA at the bottom of the image Fig. 5.27A having large width ~150 nm compared to the measured DNA width of ~50 nm. Again the protein appears to extend slightly in a lobe shape at the very base of the structure and this was noticed during NC-AFM studies.

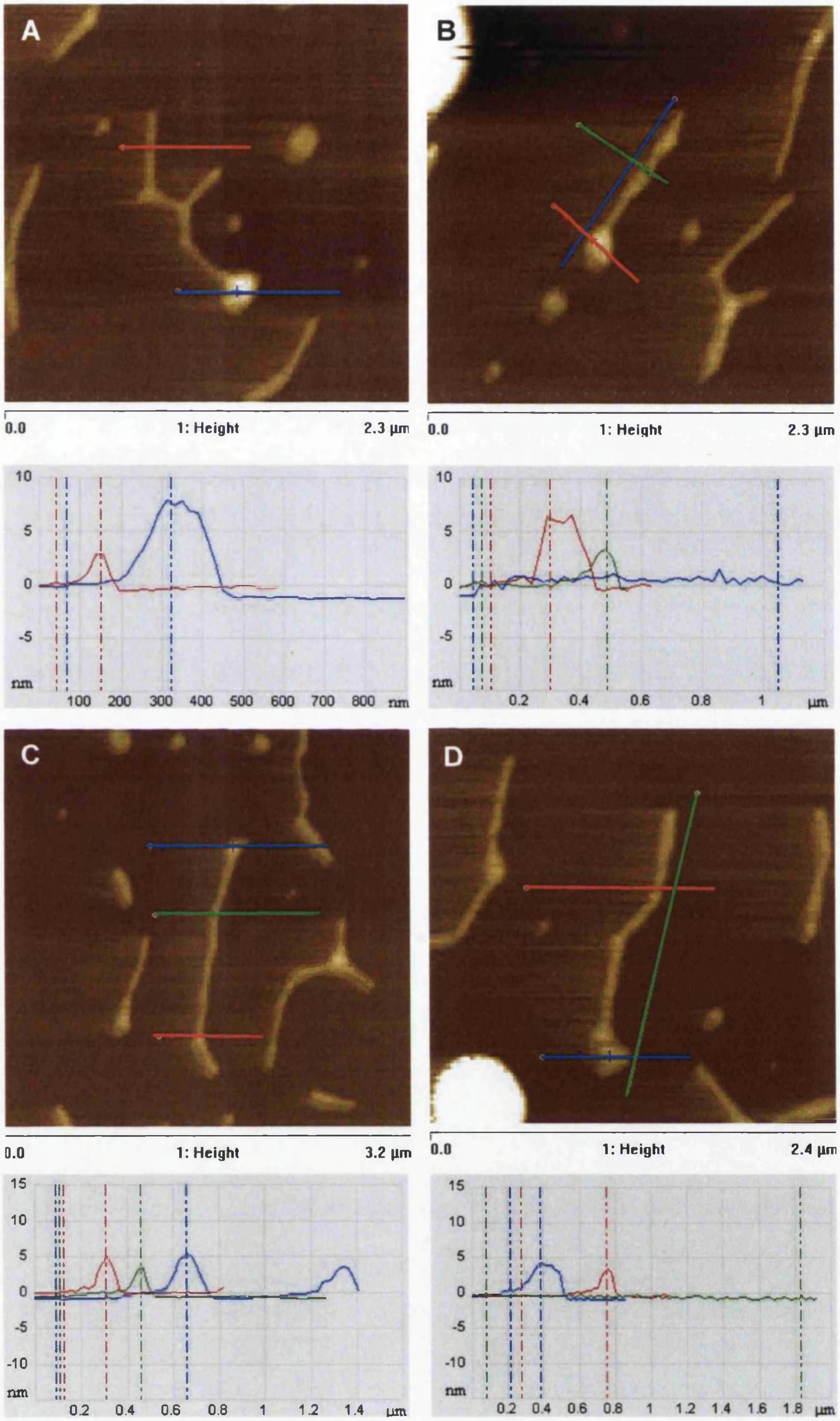

Figure 5.27. TM-AFM of DNA mixed with protein in the presence of buffer. The line profiles as indicated give the following measurements: (A) DNA height = 2.7 nm (red), protein height = 7.5 nm (blue), (B) DNA height = 3.1 nm (green) and length = 1 µm (blue) protein height = 6.5 nm (red). (C) DNA height = 4 nm (green), protein height = 6.2 nm (top, blue), 4.9 nm (lower, red). (D) DNA height = 3.3 nm (red) and length = 1.8 µm (green), and protein height = 3.9 nm (blue). The DNA has noticeable widening at some places and these are likely to be proteins.

There is a slight decrease in imaging quality recorded when samples are prepared in buffer as the tip picks up particles and 'double-tip' images are experienced. The effect of buffer is not so extreme that alternative cantilevers are necessary as with NC-AFM.

DNA strands containing a PUT3 binding sequence have been reported to have a 6° bend near the binding region in the absence of protein[35]. This bend may be due to the specific arrangements of the bases and aid proteins in their recognition of the correct binding site. After binding, the bend is reported to increase to 46° towards the major groove of the PUT3-bound DNA. However, this is difficult to measure since the DNA molecules are themselves flexible and those molecules appear to have numerous kinks in the absence of protein. If measurable, this protein-induced bend would be highly informative when there is some ambiguity about whether the protein is bound or not. In many images, multiple DNA strands have linked together, end-to-end and this angle is difficult to detect.

The buffer containing ions is required for proteins to bind with the DNA and certain cations are known to increase the efficiency of binding DNA with mica. However, at an inappropriate concentration they may affect the nucleic acid structure by substituting physiological counterions and in turn may prove detrimental to binding proteins. Zn^{2+} ions have been linked to kinking in DNA[39] and this may provide another reason (besides it long length) for DNA to coil at the ends when mixed in a buffer containing Zn^{2+} and protein. Effects as low as 10 μM Zn^{2+} may persist. Zn^{2+} associates predominantly with bases and Mg^{2+} interacts primarily with phosphates.

5.7.4.3 TM-AFM on Gold

Until this point DNA and protein experiments have been successfully imaged on mica substrates with TM-AFM. However, for electronic investigations, electrically conducting substrates are necessary so that their electronic properties may be studied. It is already known that DNA does not bond well with gold and it was only possible to image strands on gold using the non-contact mode of AFM in UHV. Typically anchoring groups are used for TM-AFM studies. However, for this work, it is extremely beneficial if proteins act as anchoring groups for DNA. The PUT3 protein was combined with DNA in the presence of buffer and deposited on template-stripped gold (TSG) substrates. TM-AFM did reveal strands of DNA on the gold surface and are shown in Figure 5.28.

There is some thickening along the strands and these are likely to be protein. Of the eight strands shown in Fig. 5.28A, four have length between 680-900 nm, which is agreeable for the DNA length. Assuming proteins are situated near the ends of the strands they are likely to add to the length compared to those without protein. The strand height measured roughly at the mid-point is 3-4 nm. Length measurements of four other strands are in the range 400-450 nm and maybe due to DNA coiling or folding back on itself, again heights are ~3-4 nm. These observed heights are larger than the ~2 nm observed on mica and implies the DNA does not spread out to adsorb strongly to the gold as for mica.

Three strands are imaged separately in Fig. 5.28B-E. In Fig.5.28B there is a large feature near the end of one strand having height ~10 nm compared to the rest of the strand ~2-3 nm high. In Fig. 5.28C-E there is some thickening along the DNA strands where protein should be situated. The gold background appears different from mica and a phase image is given in Fig. 5.28F. When comparing the images of Fig. 5.28 with those obtained with NC-AFM, there is a clear difference in the amount of detail resolved. With TM-AFM, strand-like features are clearly visible but without any surface detail. Molecules appear wider during TM scanning which is likely to be due to the combined effects of water layers, the presence of protein and buffer, and the tip shape and sensitivity.

When imaging has been reported using thiol groups in liquid, it was suggested that fixing molecules at the ends might allow movement of the middle sections which could account for larger than expected width measurements. However, these samples were dried and so large widths are likely to be due to DNA bundles and/or protein attachments possibly all along the DNA lengths.

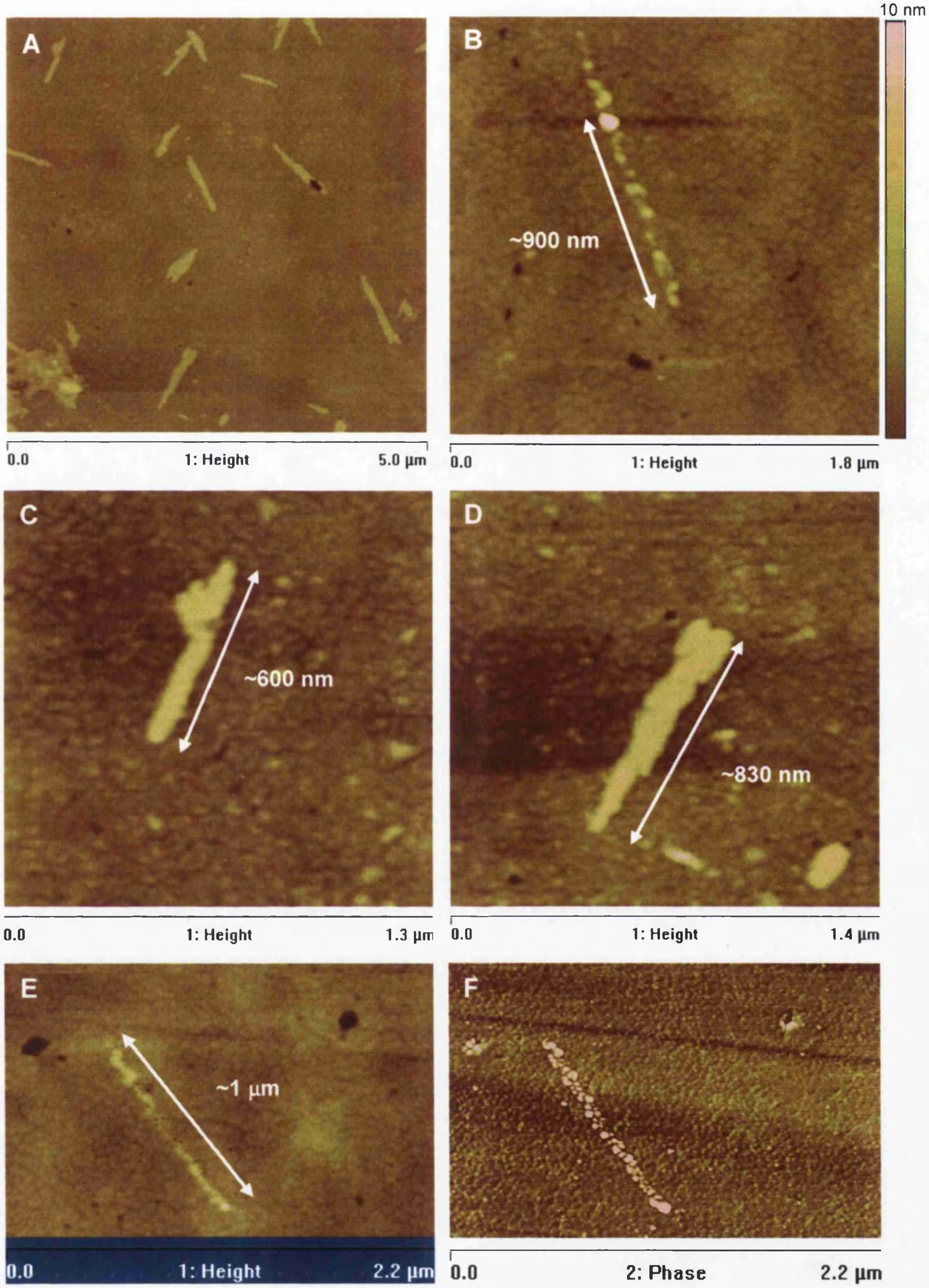

Figure 5.28. TM-AFM scans of DNA and protein strands in the presence of buffer on TSG substrates (512 points/line). (A) Wide area scan showing at least 8 strands of DNA. (B) An individual DNA strand showing a protrusion that is likely to be a protein. (C) A second individual DNA strand accompanied by the corresponding phase image. DNA strands are highly visible against the Au background. Height and width differ along the molecules and it is unclear whether the whole protein is bound with the DNA to provide an anchor to the gold surface.

Note that other binding sites might also be present within the DNA strands where the binding affinity is lower (*e.g.* sites similar to CCG triplets and/or slightly different spacings[34]) and so non-specific binding may be taking place.

Pure DNA could not be visualised on gold substrates using TM-AFM. However, DNA could be visualised on gold when samples were prepared in buffer with PUT3 protein using TM-AFM. This implies that protein helps anchor DNA to the gold and means it could be exploited for self-assembling applications and electrode measurements.

5.8 Summary

This chapter has demonstrated the immense potential for frequency-modulated NC-AFM in high-resolution imaging studies of biological structures. For the first time gold has proved a useful substrate for DNA studies and it can be used without chemical treatments thereby reinforcing the fact that lateral forces are minimised with NC-AFM. NC-AFM was applied not only to DNA but proteins and their associated DNA complexes. Detail of structure was revealed that is not accessible with other SPM systems especially in the absence of low temperatures and chemical fixation. An unexpected and practical outcome of this study is that high-spring constant cantilevers are very useful for protein work to prevent cantilevers jumping-to-contact and this will aid future observations of biological molecules. In addition to the high-resolution capabilities of NC-AFM, TM-AFM proved invaluable for imaging of samples in short timescales to support the data gained through NC-AFM.

This chapter has shown it is indeed possible to design structures which 'self-assemble' via the positioning of high-affinity protein-binding sites along DNA molecules, and observe them individually with NC-AFM. From the data gained, proteins did not always bind in the exact position predicted -sample preparation is one factor of influence and the way molecules adsorb to the surface, as well as the possibility of lower affinity binding sites being present elsewhere in the 2.5-kbp molecule. The next step, having successfully performed the necessary observations of individual DNA strands associated with proteins in a stable and reproducible manner, was to probe their I-V characteristics and this is the subject of Chapter 6.

5.9 References

[1] Tanaka, H., Hama, C., Kanno, T. and Kawai, T. (1999) High-resolution scanning tunneling microscopy imaging of DNA molecules on Cu(111) surfaces. Surf. Sci. 432, L611–L616.

[2] Hansma, H.G., Revenko, I., Kim, K. and Laney, D. E. (1996) Atomic force microscopy of long and short double-stranded, single-stranded and triple-stranded nucleic acids. Nucleic Acids Res. 24 (4) 713-720.

[3] Rivetti, C., Guthold, M. and Bustamante, C. (1996) Scanning Force Microscopy of DNA Deposited onto Mica: Equilibration versus Kinetic Trapping Studied by Statistical Polymer Chain Analysis. J. Mol. Biol. 264, 919–932.

[4] DNA Structure and Function. (1994) Sinden, R.R., Academic Press.

[5] Arai, T., Tomitori, M., Saito, M. and Tamiya, E. (2002) DNA molecules sticking on a vicinal Si(111) surface observed by noncontact atomic force microscopy. App. Surf. Sci. 188, 474-480.

[6] Noncontact Atomic Force Microscopy. (2002) Morita,S., R.Wiesendanger, R., and Meyer, E. (editors). Springer.

[7] Atomic force microscopy in Cell Biology. (2002) Jena, B. P. and Horber, J. K. H. (Editors).

[8] Genomes. (1999) Brown T.A. BIOS Scientific Publishers, Oxford.

[9] Hansma H.G. and Laney D.E. (1996) DNA binding to mica correlates with cationic radius: assay by atomic force microscopy. Biophys J. 70(4) 1933-9.

[10] Garcia, R. and Perez, R. (2002) Dynamic atomic force microscopy methods. Surf. Sci. Rep. 47, 197-301.

[11] Keller, D. and Frank, F.S. (1993) Envelope reconstruction of probe microscope images. Surf. Sci. 294, 409-419.

[12] Vesenka, J., Manne, S., Giberson, R., Maersh, T. and Henderson, E. (1993) Colloidal gold particles as an incompressible atomic force microscope imaging standard for assessing the compressibility of biomolecules. Biophys. J.65, 992-997.

[13] Biscarini, F. and Levy, P. (1997) Nanoscale caliper for direct measurement of scanning force probes. Appl. Phys. Lett. 71, 888-890.

[14] Tranchida, D., Piccarolo, S. and Deblieck, R.A.C. (2006) Some experimental issues of AFM tip blind estimation: the effect of noise and resolution. Meas. Sci. Technol. 17 (2006) 2630–2636.

[15] Maeda, Y., Matsumoto, T., and Kawai, T. (1999) Observation of single- and double-stranded DNA using non-contact atomic force microscopy. Appl. Surf. Sci. 140, 400–405.

[16] Intermolecular and Surface Forces. (1991) Israelachvili, J. Academic Press.

[17] Davies, E., Teng, K.S., Conlan, R.S. and Wilks, S.P. (2005) Ultra-high resolution imaging of DNA and nucleosomes using non-contact atomic force microscopy. FEBS Lett. 579, 1702-1706.

[18] Van Hulst, N.F, Garcia-Parajo, M., Moers, M.F., Veerman, M.H.P. and Ruiter, A.G.T. (1997) Near-field fluorescence imaging of genetic material: toward the molecular limit. J. Struct. Biol. 119, 222-231.

[19] Medalia, O., Englander, J., Guckenberger, R., Sperling, J. (2002) AFM imaging in solution of protein-DNA complexes formed on DNA anchored to a gold surface. Ultramicroscopy 90, 103-112.

[20] Zlatanova, J. (2003) Forcing chromatin. J. Biol. Chem. 278, 23213–16.

[21] Luger, K., Mader, A.W., Richmond, R.K., Sargent, D.F. and Richmond, T.J. (1997) Crystal structure of the nucleosome core particle at 2.8 Å resolution. Nature 389, 251–260.

[22] White, C.L., Suto, R.K. and Luger, K. (2001) Structure of the yeast nucleosome core particle reveals fundamental changes in internucleosome interaction. EMBO J. 20, 5207–5218.

[23] Sato, M.H., Ura, K., Hohmura, K. I., Tokumasu, F., Yoshimura, S.H., Hanaoka, F. and Takeyasu, K. (1999) Atomic force microscopy sees nucleosome positioning and histone H1-induced compaction in reconstituted chromatin. FEBS Lett. 452, 267-271.

[24] Tzamarias, D. and Struhl, K. (1994) Functional dissection of the yeast cyc8-tup1 transcriptional co-repressor complex. Nature 369, 758–761.

[25] Kuras, L. and Struhl, K. (1999) Binding of TBP to promoters in vivo is stimulated by activators and requires Pol II holoenzyme. Nature 399, 609–613.

[26] Hogue, C.W.V. (1997) Cn3D: a new generation of three-dimensional molecular structure viewer. Trends Biochem. Sci. 22, 314–316.

[27] Khorasanizadeh, S. (2004) The nucleosome: from genomic organization to genomic regulation. Cell 116, 259–272.

[28] Luger, K. and Richmond, T.J. (1998) The histone tails of the nucleosome. Curr. Opin. Genet. Dev. 8, 140–146.

---

[29] Zlatanova, J., Leuba, S.H. and van Holde, K. (1998) Chromatin fiber structure: morphology, molecular determinants, structural transitions. Biophys. J. 74, 2554–2566.

[30] Riehm, M.R. and Harrington, R.E. (1989) Histone-histone interaction mediates chromatin unfolding at physiological ionic strength. Biochemistry 28, 5787–5793.

[31] Xiao, X.W. and Cole, R.D. (1989) Chromatin aggregation changes substantially as pH varies within the physiological range. J. Biol. Chem. 264, 11653–11657.

[32] Wu, J. and Grunstein, M. (2000) 25 years after the nucleosome model: chromatin modifications. TIBS 25, 619–623.

[33] Sellick, C.A. and Reece, R.J. (2003) Modulation of transcription factor function by an amino acid: activation of Put3p by proline. EMBO J. 22(19), 5147-5153.

[34] Reece, R.J., Ptashne, M. (1993) Determinants of Binding-Site Specificity Among Yeast C_6 Zinc Cluster Proteins. Science 261, 909-911.

[35] Swaminathan, K., Flynn, P., Reece, R.J. and Marmorstein, R. (1997) Crystal structure of a PUT3-DNA complex reveals a novel mechanism for DNA recognition by a protein containing a Zn_2Cys_6 binuclear cluster. Nat. Struct. Bio. 4(9), 751-759.

[36] Des Etages, S. A. G., Falvey, D.A., Reece, R.J. and Brandriss, M.C. (1996) Functional Analysis of the PUT3 Transcriptional Activator of the Proline Utilization Pathway in Saccharomyces cerevisiae. Genetics 142, 1069-1082.

[37] Reece, R., Faculty of Life Sciences, University of Manchester, UK.

[38] Online resource: www.nanosensors.com/PPP-NCVH.htm

[39] Han, W., Dlakic, M., Zhu, Y. J., Lindsay, S.M. and Harrington, R.E. (1997) Strained DNA is kinked by low concentrations of Zn^{2+}. Proc. Natl. Acad. Sci. USA 94, 10565-10570.

CHAPTER 6

Electrical Measurement of Biological Molecules

6.1 Introduction

The high-resolution capabilities of NC-AFM have proved particularly useful for studies of DNA, protein and their associated complexes. The current-voltage (I-V) properties of DNA and associated proteins are now considered in this chapter. Despite the numerous studies of DNA's conductivity performed under a variety of conditions by others, the results are not conclusive. This is not surprising when one considers the vast number of ways used for preparing samples and the methods used for probing them. The emphasis of this work is placed on the effect of the physical contact between the DNA and the metal electrode. Thiol groups are commonly used because they have a high affinity for gold and a strong covalent bond is formed when thiolated DNA is incubated with a gold substrate. This anchoring is sufficient for imaging DNA with TM-AFM in liquid and examples of others' work were shown in Chapter 5. It is suggested that while thiol groups based on the sulphur's affinity for gold are ideal for fixing molecules for their observation with TM (as unmodified strands are only loosely adhered to the surface and are affected by tip-sample forces) they may not be the best anchoring group for electrical measurements on the DNA itself. The novel suggestion is to use protein as an alternative anchoring group. The adhesion of peptides comprised of single-species amino acids with inorganic substrates has been studied elsewhere[1]. Increased adhesion was found for peptides comprised of polar-charged amino acids to the material surfaces Si_3N_4, SiO_2 and AlGaAs -but none of the amino acids gave any preference for bonding with Au (or Pt, Ti or Pd). The pH is one particular factor affecting the adhesion process and it has been suggested that bonding to substrates could be promoted or suppressed for certain species of amino acids via pH control. Other studies have suggested that whole proteins containing cysteine residues can be chemisorbed and oriented onto gold substrates for stable AFM imaging[2] and may help to explain the author's observations of proteins with DNA on gold substrates in the previous chapter.

Proteins associate with DNA under certain conditions forming DNA-protein complexes as shown in Chapter 5. Basic histone proteins combine with DNA forming nucleosomes that are found in cell nuclei and their binding is not thought to be highly sequence-specific. DNA unwinding can occur and its conformation largely depends on the cell's activities. On the other hand, DNA-binding proteins are able to distinguish DNA sites and bind to it under the correct physiological conditions. This allows one some control over the protein's binding position relative to the DNA strand. Using the knowledge gained previously where two protein binding sites were built-in to each end of a DNA strand, it is now feasible to use each protein as an anchoring group in an electrode set-up. This means that the physical contact and therefore the charge transfer properties between the DNA and gold could be affected or even enhanced by the protein. If current measurements are enhanced, designs for self-assembling protein-DNA contacts could be used in future bio-electronics.

The idea of probing DNA modified with protein using an electrode setup is relatively straightforward. Similar electrode setups have been used by others for current-voltage characterisation of many interesting molecules. The setup is used here to determine the effect of protein anchoring groups on DNA's conducting properties. The first challenge encountered is the fabrication of electrodes with the correct spacing for the size of the molecule. Specialised equipment was needed and so electrode fabrication was carried out with electron-beam lithography (EBL) (Chapter 4). Initially gold electrodes (which do not form oxide layers) were fabricated on mica and afterwards on SiO_2. SEM and AFM imaging was used to check gap sizes and cleanliness. This is the first time to the authors' knowledge that I-V measurements have been performed on the PUT3p protein itself and when bonded with DNA. A comparison is made between unmodified DNA and protein-bound-DNA in terms of their I-V measurements and is followed by an in-depth discussion of the likely implications of this work.

6.2 Sample Preparation

6.2.1 DNA and Protein

DNA and protein samples were prepared for conductivity measurements in the same way as for high-resolution imaging (Chapter 5). High and low concentrations of DNA were used, dilutions were made with water and buffer, with- and without- the presence of protein for a comparative study.

6.2.2. Electrodes

Initially thin gold films were evaporated on mica as described in Chapter 4. A metal mask was used to form a gold-mica step over which DNA could be deposited and I-V measurements performed. AFM scanning of these surfaces showed low surface roughness. The Au-mica slope was gradual and ideal for depositing DNA. However, since the Au edge was not abrupt, small particles of gold were found extending further on the mica side of the substrate. Upon deposition of liquid (~μl amounts) the gold was loosened, roughness increased tremendously and many substrates proved unusable. If they had been stable they would have provided a means of combining I-V characterisation and imaging studies using a conducting-AFM probe as others have described for different molecules. Alternative methods were sought and electrode arrays were fabricated on mica substrates by J. Kettle[3] using EBL. Mica was the first choice as a base for electrodes because of its electrically insulating nature and extremely low surface roughness as already shown with AFM imaging of biomolecules. However, mica was found not to be a suitable base for electrode fabrication. Problems were encountered during patterning and the gold metal began peeling off it during later stages of fabrication despite attempts to use a chromium base layer prior to the evaporation of gold (this is known to increase adhesion of Au on SiO_2 substrates).

Although mica has been used as a substrate for electrode fabrication in current literature[4], the majority of experiments reported are performed using either gold[5,6,7] or platinum[4,8] on SiO_2 substrates. As a result, gold electrodes were fabricated on insulating SiO_2 for this work. The gap between electrodes was specified to be less than the DNA strand length (~875 nm) for bridging to occur. Figure 6.1 shows SEM images of an array of 5 electrode pads with electrodes. The electrode gap was unexpectedly large (*i.e.* > 1 μm) for narrow electrodes (Fig.6.1B). These electrodes have a gap larger than the DNA length but may still be useful for I-V analysis of highly concentrated DNA when networks are formed or for longer DNA strands. For smaller gaps to be realized (~300 nm), a wide electrode base was necessary (Fig. 6.1C). Here, there is an increased probability that individual DNA strands will align themselves across the electrode gap. The electrodes in Fig. 6.1C have gap size ~300 nm and are more suited for measurements on this DNA.

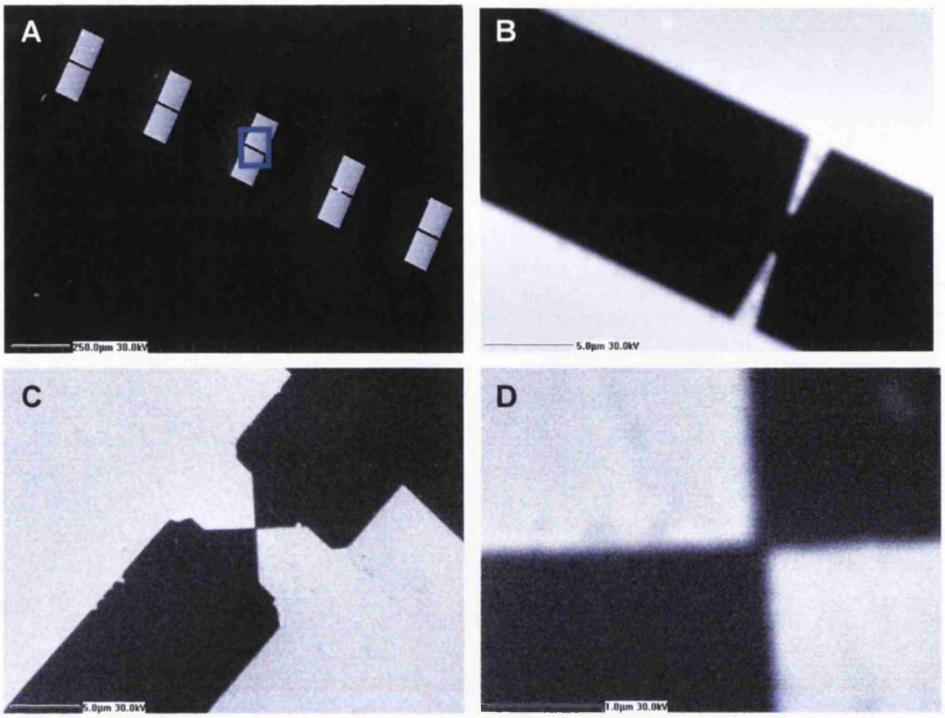

Figure 6.1. SEM images of gold electrodes fabricated on SiO_2 with EBL. (A) An array of electrode pads with the location of the narrow gap indicated (blue). (B) Electrodes with narrow bases resulted in unexpectedly large gaps, >1 µm. (C-D) Electrodes with wide bases had small gap sizes ~300 nm.

Before depositing biological materials on these electrodes, wire-bonding was necessary for connections to external circuitry and so electrodes were extended into large pads. The gap between wire-bonding sites was redesigned to be 1500 µm (1.5 mm) for AFM scanner access (Figure 6.2). The electrodes of Fig.6.2C allowed access for the AFM scanner and so gap sizes could be checked as well as sample cleanliness. A high resistance of ~100 Ω was measured for a set of joined electrodes but is negligible compared to the expected value of DNA.

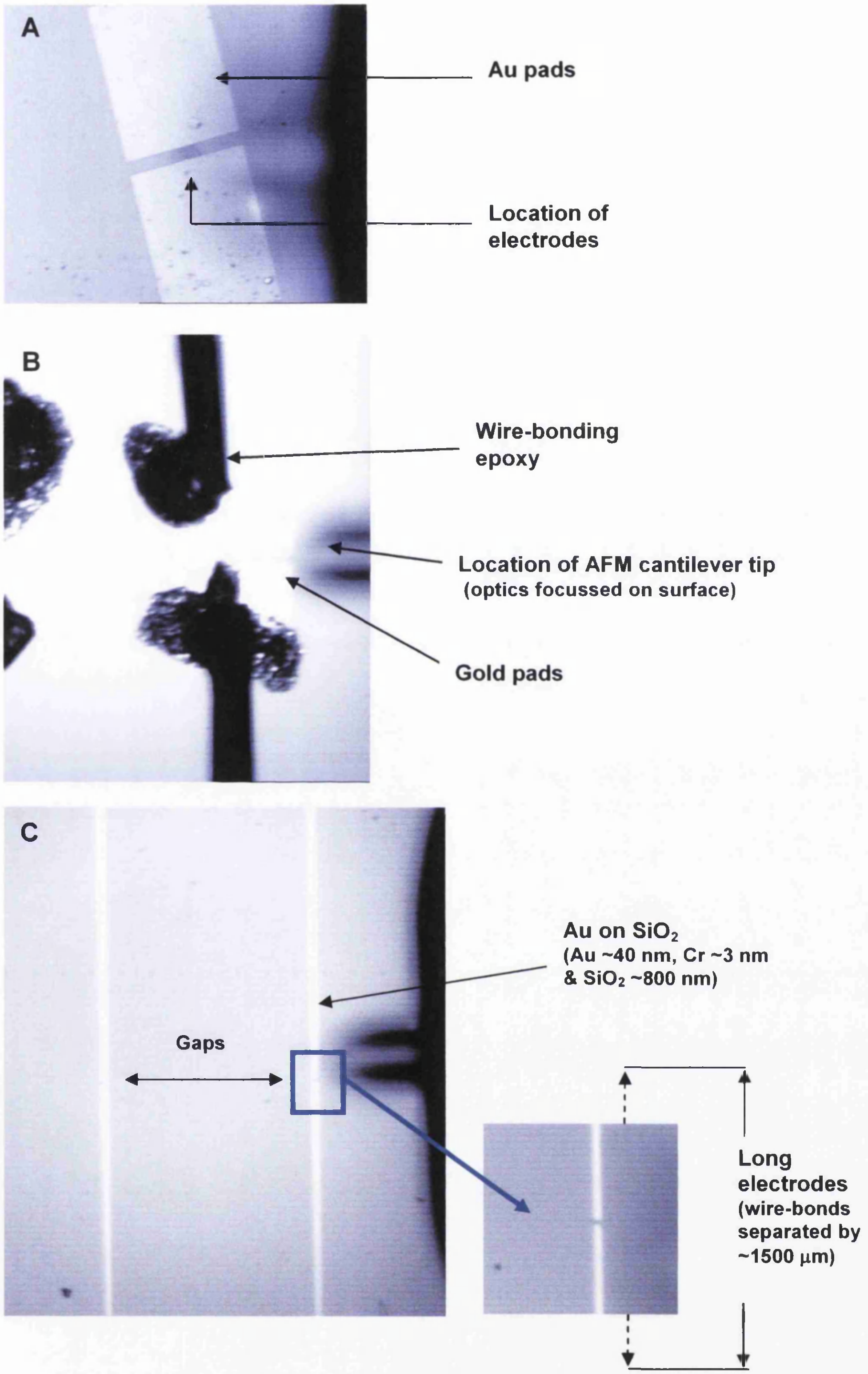

Figure 6.2. Optical microscope images of electrode pads on SiO_2. (A) Before wiring, electrodes are easily accessible with AFM. (B) After wiring-bonding, access is limited for AFM scanner. (C) Electrodes with wire-bonding sites set 1500 μm apart.

6.3 AFM of Studies of Nano-Spaced Electrodes

6.3.1 Bare Electrodes

Figure 6.3 shows AFM images of electrodes. The EBL design specification was met and resulted in a gap of approximately 300 nm.

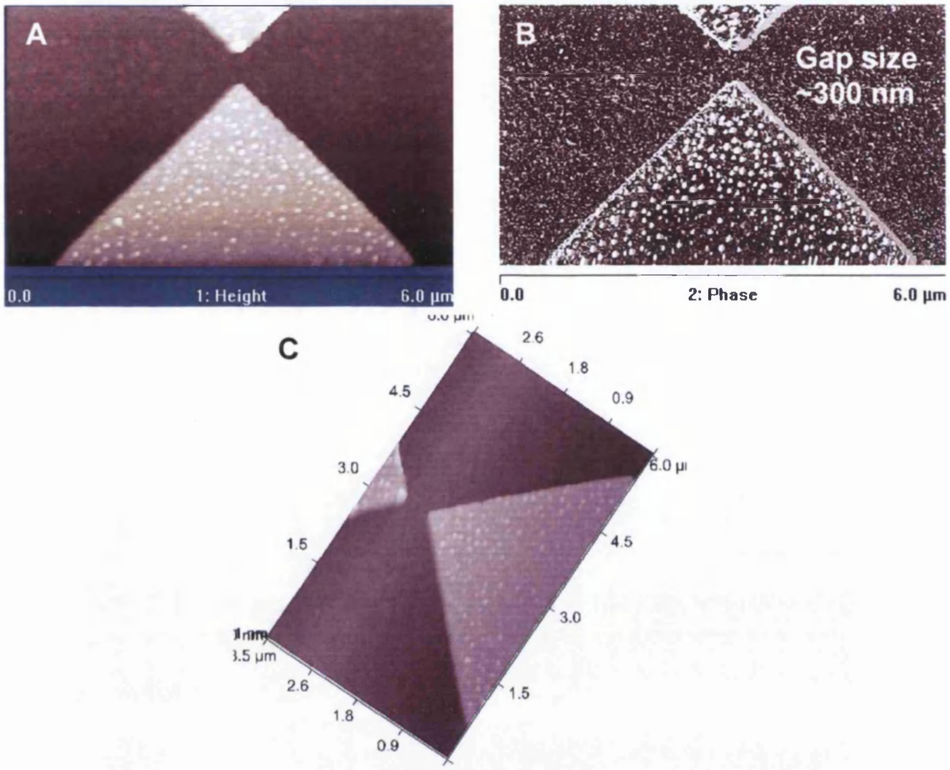

Figure 6.3. TM-AFM of gold electrodes with abrupt edges on a clean SiO_2 substrate. (A) Height image. (B) Phase image. (C) 3D perspective.

DNA molecules that contain 2.5-kbp are ~875nm in length and there is a high probability that they will bridge an electrode gap of ~300 nm. Therefore, the electrodes in Fig. 6.3 have a gap size that is well-suited for probing the conductivity of this DNA. A region near the one electrode was scanned and images are shown in Figure 6.4. Although electrodes were cleaned extensively in solvents after fabrication to remove PMMA, the SiO_2 surface was unexpectedly rough with RMS roughness ~1.42 nm for 1 µm x 1 µm. Depositions were made and experiments were performed in attempt to distinguish DNA strands from the SiO_2 background. Results are given in the next section.

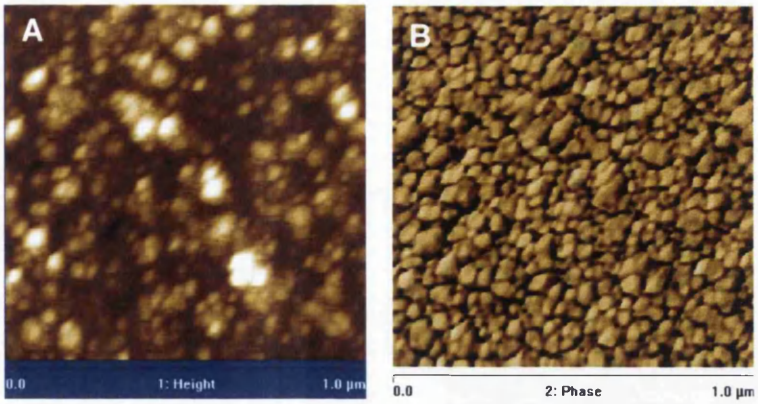

Figure 6.4. TM-AFM of SiO_2. (A) Surface topography image. (B) Phase image. The RMS roughness was 1.42 nm for a scan size 1 µm x 1 µm.

6.3.2 Electrodes with DNA

Figure 6.5 shows electrodes after the deposition of highly concentrated DNA (50 ng/µl).

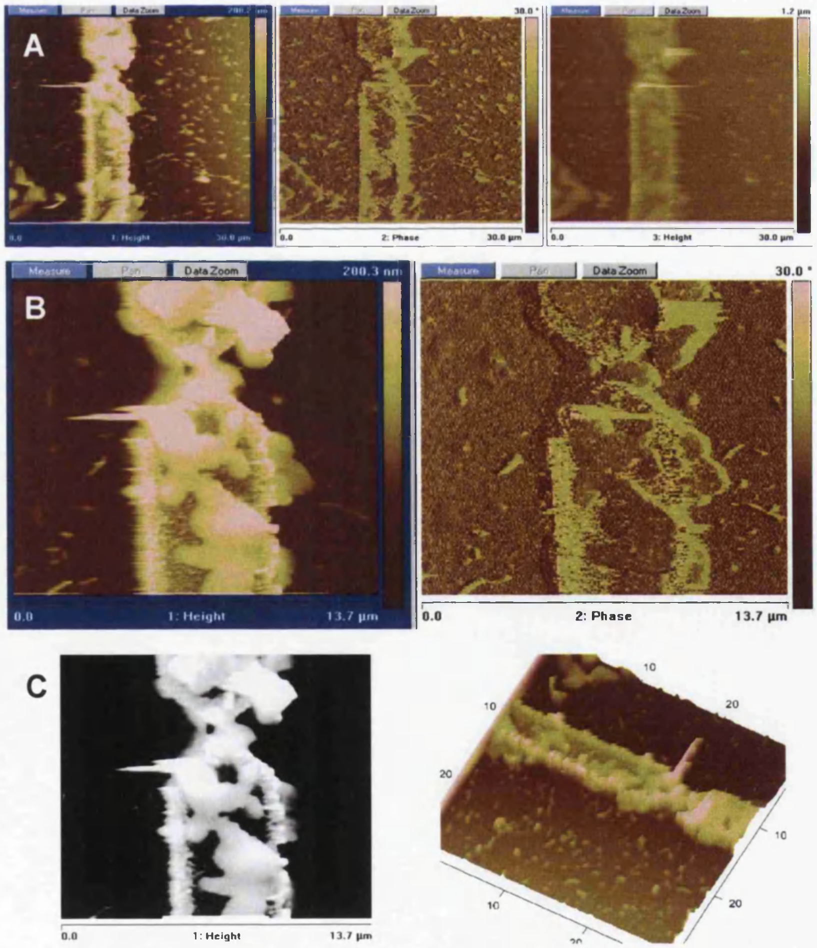

Figure 6.5. Electrodes with DNA deposited. (A) Topography and phase images showing electrodes and biomolecules on the SiO_2. (B) The electrode gap is filled with DNA. (C) High contrast image. D) A 3D perspective. Image blurring may be a result of weakly adsorbed molecules.

The tip was moved progressively into the electrode gap with the intention of resolving single DNA strands (Fig. 6.5A, B). The contrast was altered (Fig. 6.5C) and 3D perspectives used (Fig. 6.5D). The gap was not visible as DNA molecules were amassed over it.

Figure 6.5 has shown the successful result of DNA bridging electrodes despite the combined effects of the large electrode height, rough SiO_2 and lateral forces of TM-AFM causing movement of weakly adsorbed molecules (*i.e.* causing image blurring). Line profiles of the DNA on the surrounding SiO_2 are given in Figure 6.6.

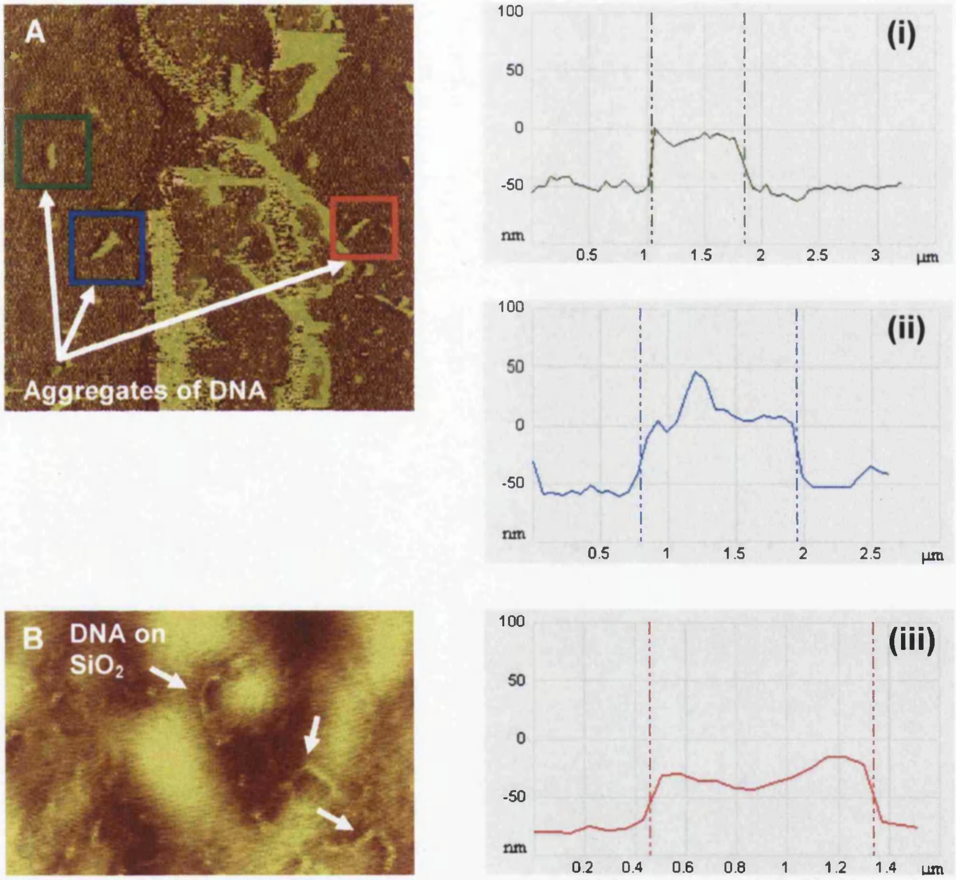

Figure 6.6. Phase images and line profiles of DNA on SiO_2. (i) blue ~1.1 µm, (ii) green ~880 nm, (iii) red ~970 nm. Profiles (i-iii) have large height owing to the underlying rough surface and aggregation effects. (B) DNA strands are also present on the SiO_2 but are almost totally masked by surface features.

DNA structures highlighted in Fig.6.6A (length ~1 µm) are in good agreement with the size expected for DNA (~875 nm). Height measurements are large (~50 nm) and are attributed to the combined effects of the uneven SiO_2 topography and DNA aggregation (*e.g.* DNA bundles).

Difficulties were encountered in distinguishing single strands of DNA from the background. They are present but can only be observed after image processing (Fig. 6.6B). As liquid depositions were made to cover the electrodes, similar structures are likely to be distributed across the whole electrode substrate including the electrode gap. Figure 6.7 shows a second example of electrodes with DNA deposited.

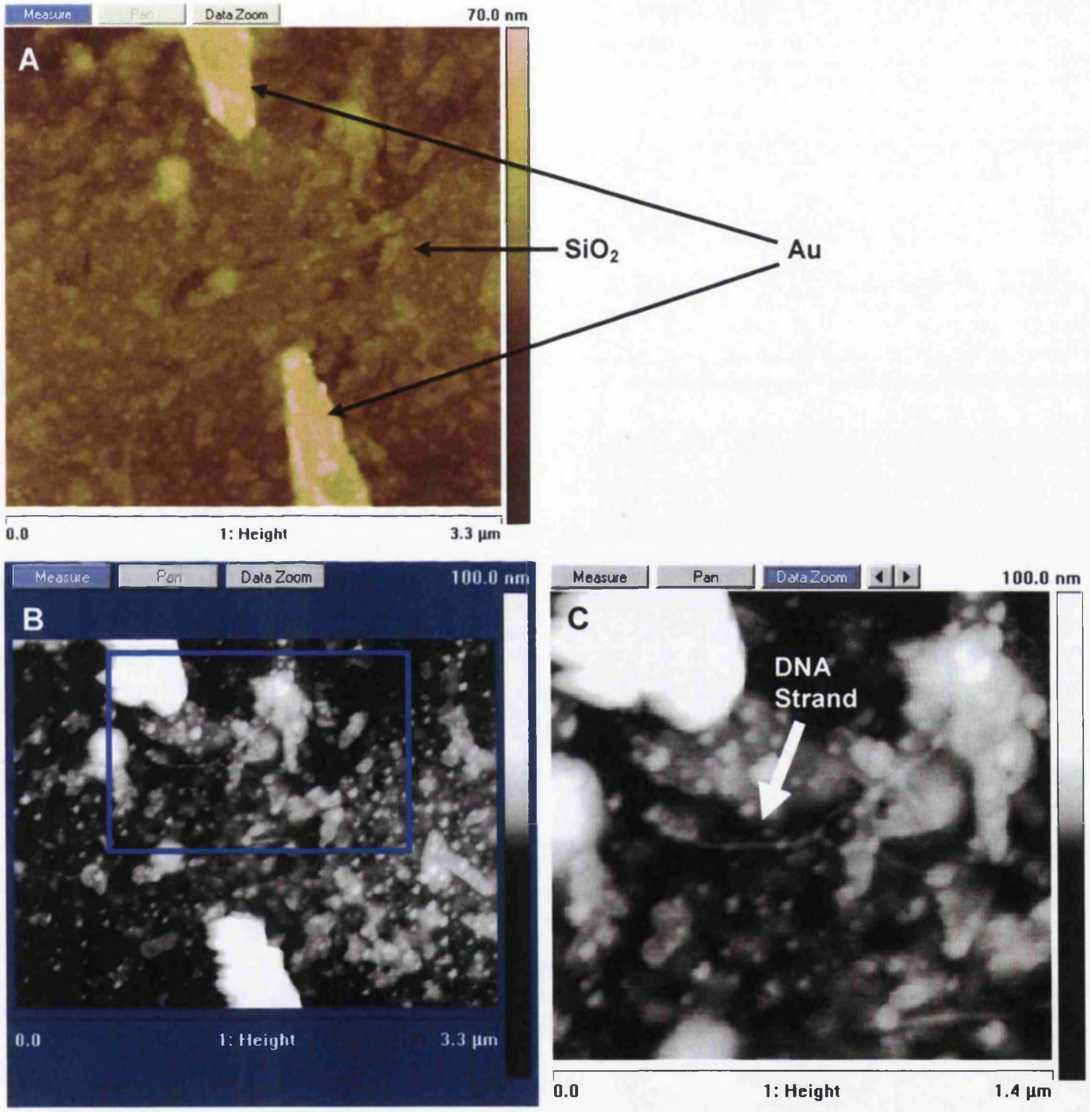

Figure 6.7. AFM of electrodes after DNA deposition. (A) Under normal scanning, the DNA is masked by the height of the Au. (B) DNA is visible after contrast adjustment. The area indicated (blue) is scanned at high-resolution in (C).

To resolve individual strands at the electrode gap without too much tip-sample interference, a much lower concentration was used. Under normal scanning conditions DNA is not visible even though the background slope is removed (Fig. 6.7A). However, high contrast image processing does allow the strand like nature of DNA to be observed (Fig. 6.7B, C). The height of the strands DNA is 1.5-4 nm.

The long, linear structure of DNA is advantageous for distinguishing it from the background after image processing but any other structures such as globular proteins are not distinguishable on this surface due to the rough SiO_2 topography. A line profile of the DNA is given in Figure 6.8.

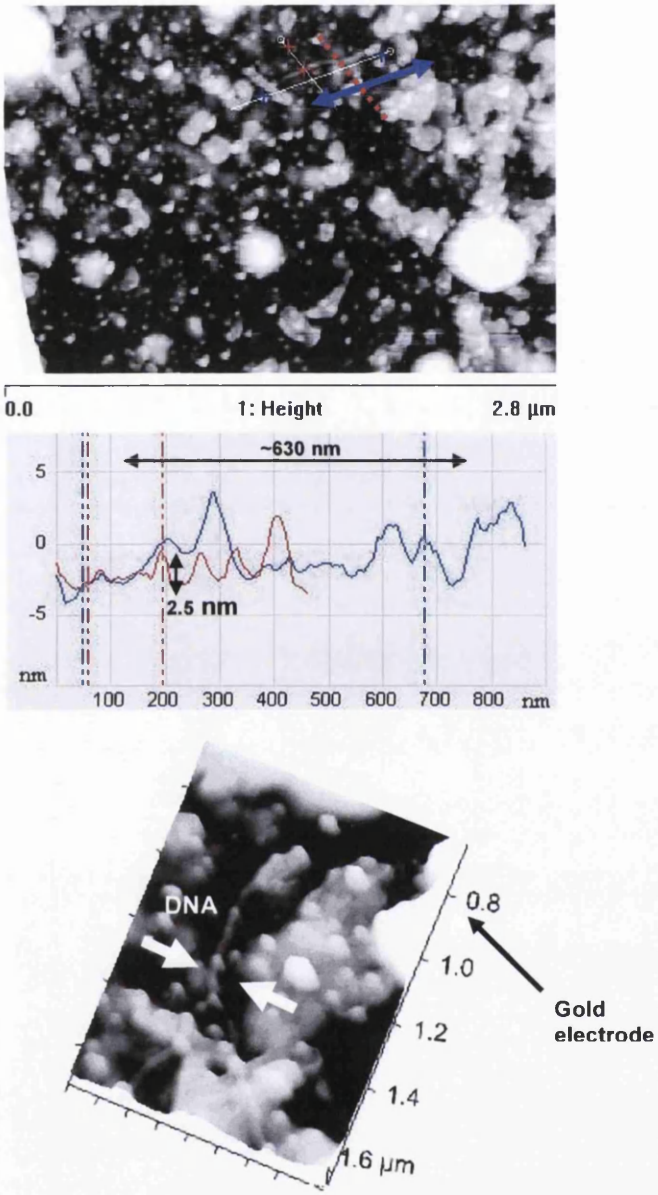

Figure 6.8. DNA strands on SiO_2. Strand length is approximately 630 nm (blue); strand height is 2.5 nm (red).

Following the aforementioned observations of DNA on electrodes, experiments were performed with the aim of comparing DNA's current-carrying properties with and without the presence of DNA-binding proteins. It was shown in Chapter 5 that the protein PUT3 binds with DNA and these complexes have an affinity for gold. A comparison study was therefore performed across samples containing DNA and those containing DNA-protein complexes.

6.4 I-V Measurement of DNA-Protein Complexes

6.4.1 General Description

The work of this thesis was aimed at determining the feasibility of using DNA-binding proteins to provide the necessary intimate contact between the DNA and the metal electrode for improvement of DNA's overall conductivity. For the ideal case, DNA should traverse the electrode gap with proteins acting as anchoring groups that bind preferentially to the gold electrodes as shown in Figure 6.9.

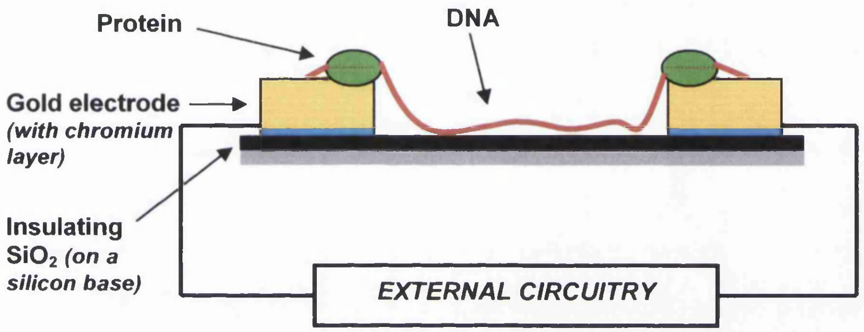

Figure 6.9. The setup for I-V measurements on DNA with protein anchoring groups.

A comparative study was performed to compare I-V measurements under equivalent conditions to determine the effect of proteins on DNA's current measurements. I-V measurements were made using three pairs of electrodes. (Gap sizes: ~250 nm and ~300 nm as measured with AFM, and ~300 nm as measured with SEM). Gold electrodes with an underlying chromium layer for adhesion of gold to electrically insulating SiO_2 were found to be the most resilient for I-V measurements and allowed cleaning for repeated use. Electrodes were used in conjunction with a HEWLETT PACKARD 4142B power supply and KARL SUSS MP4 probe station which is widely used for characterisation of semiconductor devices. Experiments were performed under equivalent conditions as much as possible. (*i.e.* constant temperature, amount deposited, length of time left to adsorb/dry, same experimental apparatus, same cables *etc.*). The key difference was the actual content of the solution deposited. It was noted that high voltage sweeps (-10 V to 10 V) caused irreversible damage to electrodes.

6.4.2 I-V Measurements

A summary of the overall results obtained is provided in Figure 6.10 as a log plot of current at +5 V as a function of sample composition. Although current was recorded as a function of voltage as it was swept from -5 V to +5 V, the main divergence in current between samples occurred at +5 V. Current values at +5 V were also less affected by noise than those at -5 V. The log plot firstly introduces the magnitudes of current recorded and the general trend over 23 labelled results, and secondly it allows one to examine each data point in more detail for a comparison study regarding the effect of protein on DNA's conductivity. Results are discussed in the sections that follow and examples of individual data recordings are provided.

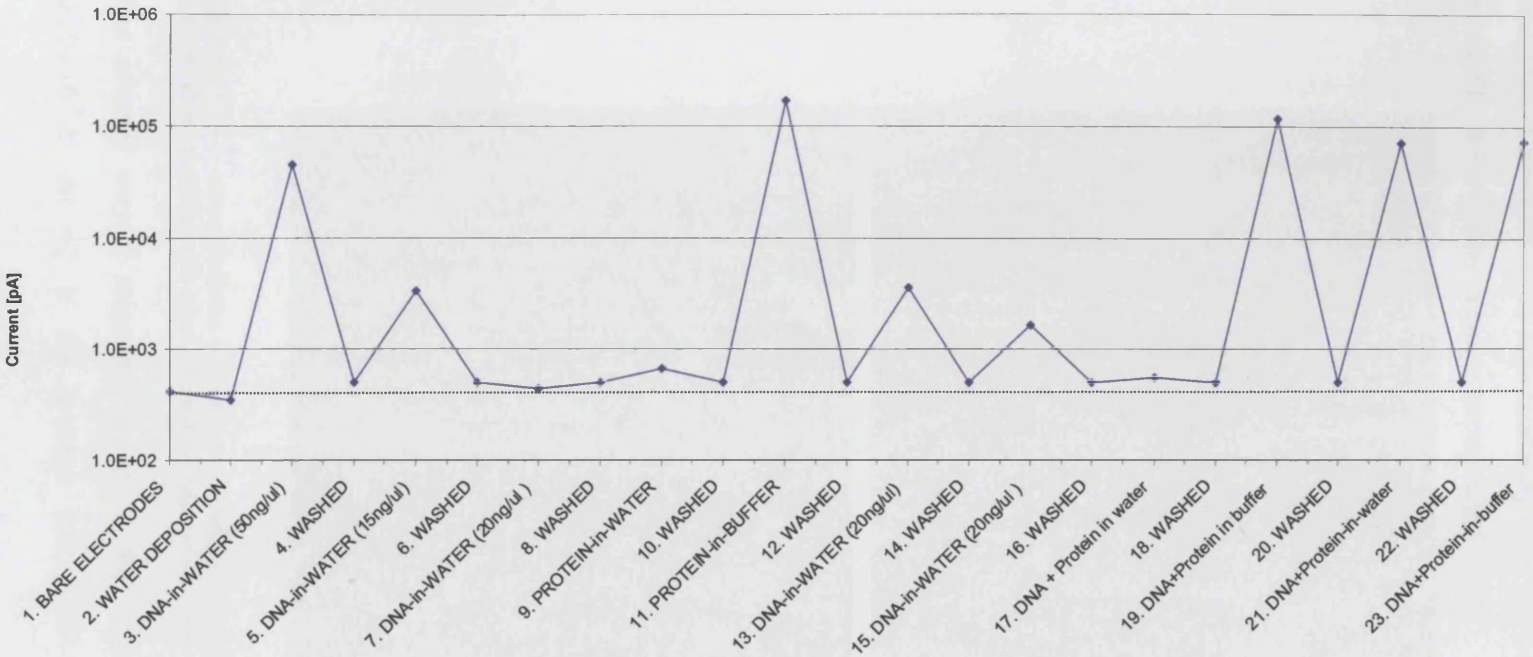

Figure 6.10. A summary of current readings of DNA-related samples at +5 V. Experiments were performed at room temperature in air.

6.4.2.1 Bare Electrodes

Control experiments were performed at the outset using bare, dry electrodes in a dark environment (Figure 6.11). The voltage was swept from -5 V to 5 V and the current automatically recorded at 0.05 V increments (*i.e.* 201 points per voltage sweep). A background noise level of approximately ±0.5 nA was present (data entry 1, Fig. 6.10). Fig. 6.11A shows a single experimental result.

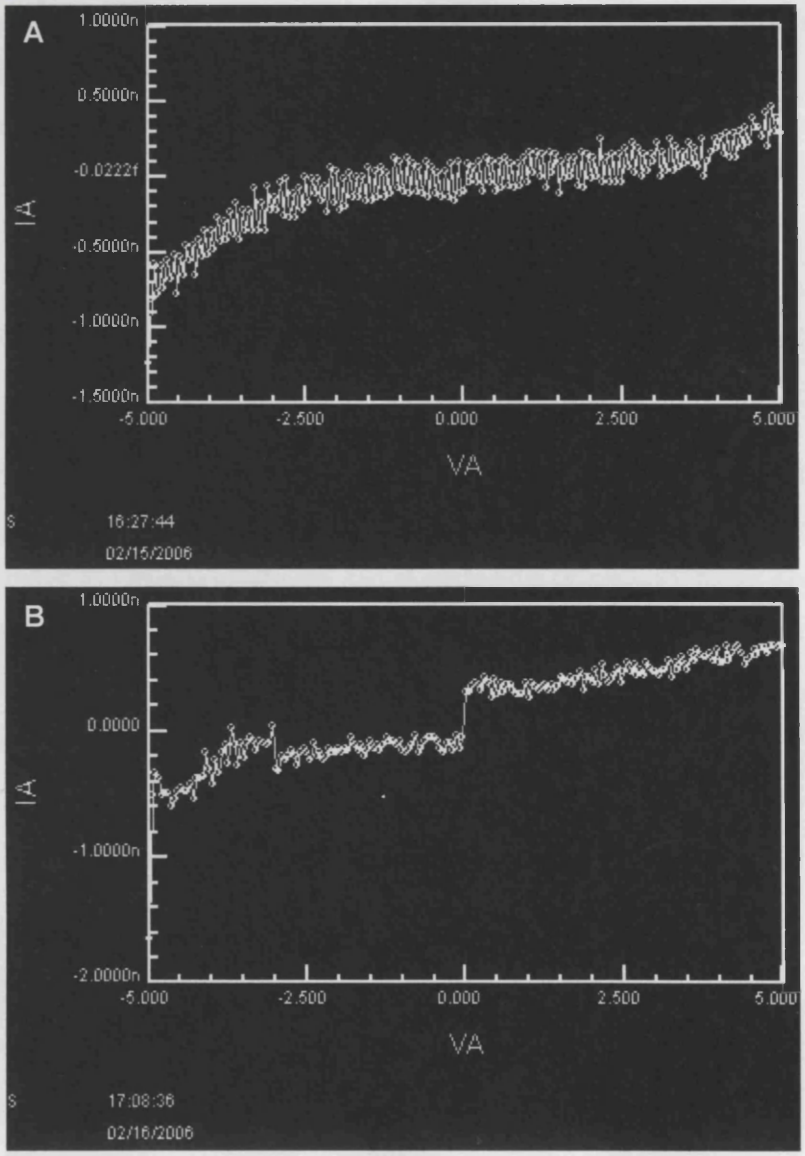

Figure 6.11. I-V characteristics of clean electrodes in a dark environment. (A) Bare electrodes, prior to all depositions. (B) After water deposition and drying.

The average current measured at +5 V was 0.42×10^{-9} A, standard deviation 0.20×10^{-9} A. At +2 V the average was 0.07×10^{-9} A, standard deviation

0.17×10^{-9} A. Measurements were made after rinsing with water: pure deionised water was deposited, left for 15 mins and dried with N_2 gas. Note, the same water was used for DNA dilution. An example of the I-V measurement is shown in Fig. 6.11B. Current readings closely matched those of the bare, dry electrodes -the average current at +5 V was 0.35×10^{-9} A, standard deviation 0.22×10^{-9} A (data entry 2, Fig. 6.10). Experiments with DNA and protein were performed and following each deposition, electrodes were washed with copious amounts of ethanol and water. Tissue was used to draw remaining liquid to the edge of the substrate and electrodes were dried with N_2 gas. Crucially, current readings returned to this background control level always after cleaning (data entries 4, 6, 8, 10, 12, 14, 16, 18, 20, 22, Fig. 6.10).

6.4.2.2 Electrodes with DNA across Gap

- ***DNA, prepared in water***

Following the deposition of concentrated DNA (~50 ng/μl) current readings were greatly elevated from the background level as shown by Figure 6.12. Such readings were attributed to DNA bridging the gap in its bundle or network form. The average current measured at +5 V was 45.03×10^{-9} A, standard deviation 3.37×10^{-9} A (data entry 3, Fig. 6.10)

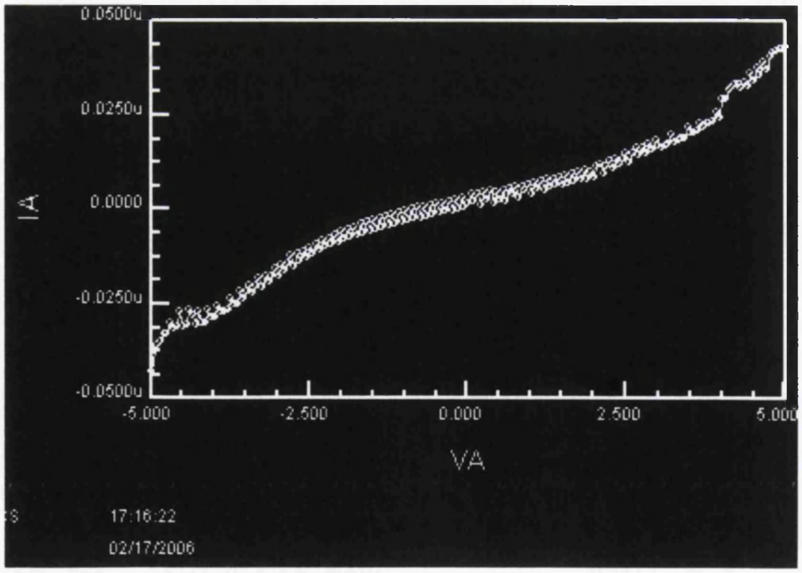

Figure 6.12. I-V data for concentrated DNA (~50 ng/μl).

To decrease the amount of aggregation, a lower concentration of DNA was used (~15 ng/μl). Again, an increase from the background level of current was observed as shown in Figure 6.13. For this case, the average current at +5 V was 3.36×10^{-9} A, standard deviation 0.35×10^{-9} A (data entry 5, Fig. 6.10).

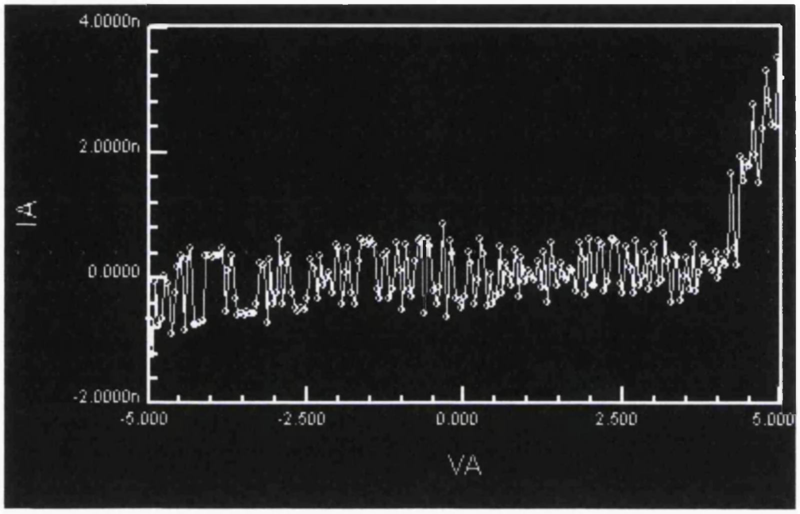

Figure 6.13. A single data recording for diluted DNA (~15 ng/μl).

Measurements were also made using a less dilute sample of DNA (20 ng/μl) and initially readings similar to the background level were measured (data entry 7, Fig. 6.10) but current was elevated in two later experiments (data entries 13, 15, Fig. 6.10). The average currents for these cases were 3.61×10^{-9} A, standard deviation 1.17×10^{-9} A and secondly 1.64×10^{-9} A, standard deviation 0.38×10^{-9} A. A single I-V measurement is shown in Figure 6.14.

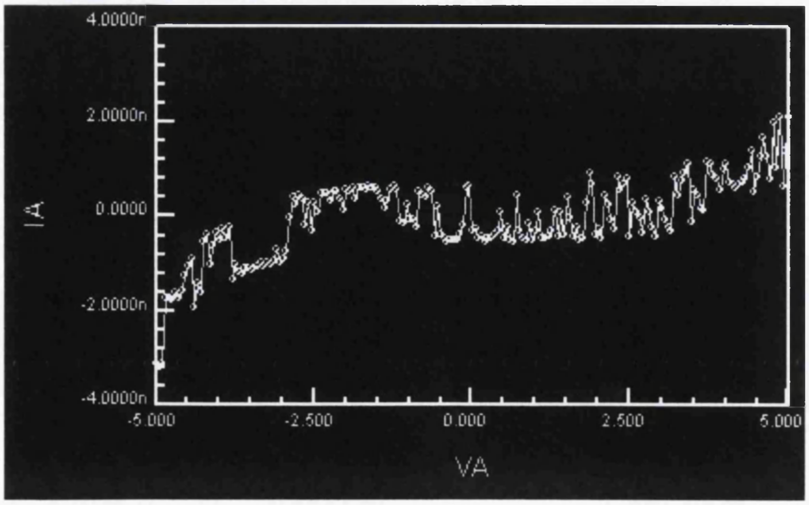

Figure 6.14. A single data recording for DNA (~20 ng/μl).

Whilst concentrated DNA (50 ng/μl) gave the highest current readings, lower concentrations (15-20 ng/μl) also give rise current readings higher than the background. DNA at concentration 20 ng/μl was therefore chosen for experiments involving protein. It is twice as concentrated as that used for individual strand imaging (Chapter 5) but it is necessary to ensure a high probability of DNA bridging the electrode gap.

6.4.2.3 Electrodes with Protein and DNA across Gap

- ***Protein, prepared in water and buffer***

During this comparison study I-V measurements were performed on protein diluted in water and protein diluted in buffer. For protein diluted in water, readings were only slightly elevated above the background level (data entry 9, fig 6.10). At +5 V, the average current reading was 0.67×10^{-9} A, standard deviation 0.41×10^{-9} A. An experimental result is shown in Fig. 6.15A.

Protein diluted into buffer gave significant current readings (data entry 11, fig 6.10). At +5V, the average current was 168.91×10^{-9} A, standard deviation 1.63×10^{-9} A (Fig. 6.15B). This increase of current was not seen for proteins prepared in water and implied that the presence of buffer particles improved protein conductivity possibly by 'doping' individual proteins or causing them to aggregate into larger structures (*e.g.* tetramers) –sufficiently large structures could bridge the electrode gap and give rise to significant currents.

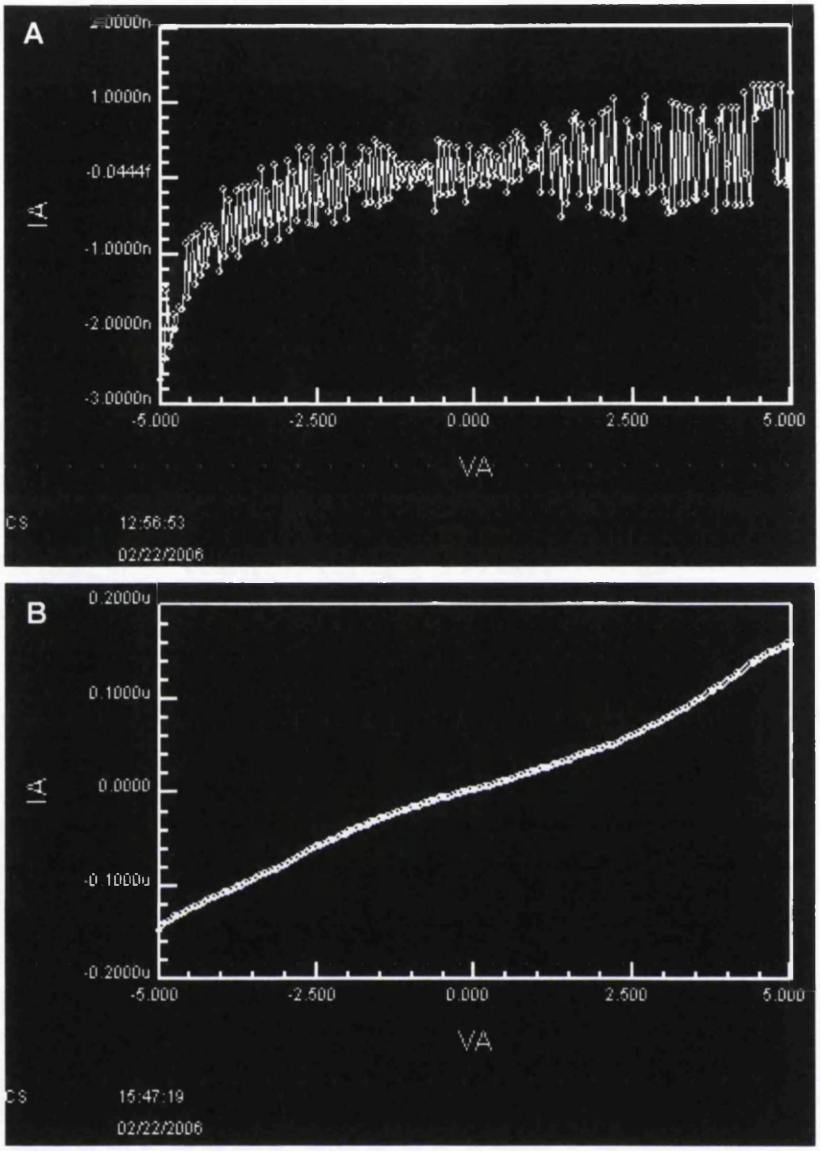

Figure 6.15. I-V data for protein. (A) Diluted in water. (B) Diluted in buffer.

- ***DNA and Protein, prepared in water***

DNA and protein were mixed in water before deposition. For the first case, the average current measured at +5 V was similar to the background level at 0.55×10^{-9} A, standard deviation 0.21×10^{-9} A (data label 17, Fig. 6.10). For the second case, (data entry 21 Fig. 6.10) significant currents were recorded. The average current was 71.75×10^{-9} A, standard deviation 11.59×10^{-9} A. I-V records of these results are shown in Figures 6.16 and 6.17 respectively.

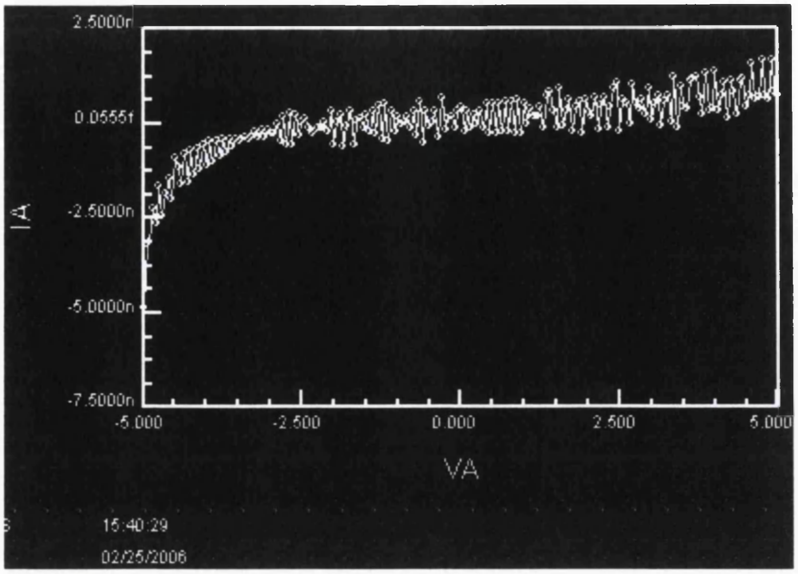

Figure 6.16. An example of I-V data recorded for DNA prepared with protein in water. Readings similar to the background levels were observed.

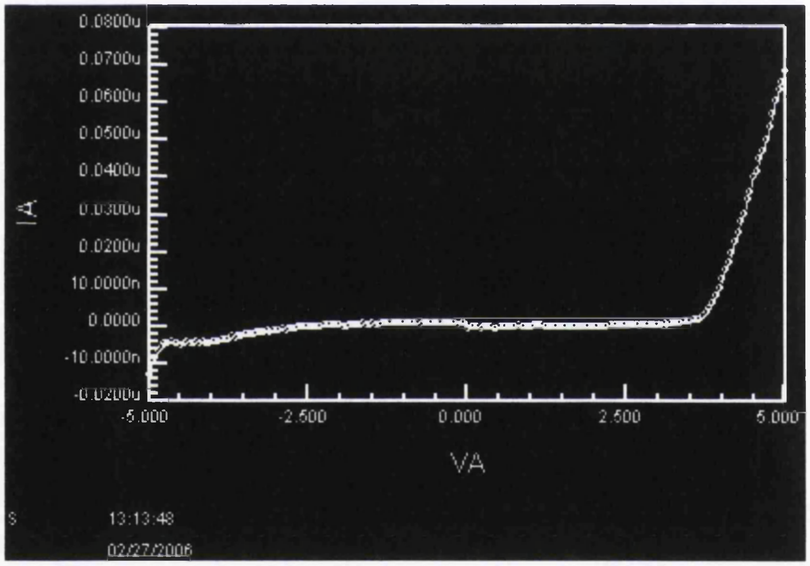

Figure 6.17. A second example of I-V data recorded for DNA prepared in water. Significant currents were measured.

Although considerable currents were measured for DNA mixed with protein in water, binding usually occurs in the presence of buffer. DNA-protein PUT3 complexes could not be visualised without the presence of buffer during preparation in Chapter 5. Experiments were therefore repeated using DNA and protein mixed in buffer.

- ***DNA and Protein, prepared in buffer***

Large current values were obtained for DNA mixed with protein in buffer. For the first case, an average current was 115.36×10^{-9} A, standard deviation 17.25×10^{-9} A (data label 19, Fig. 6.10) was found which is similar to that obtained when DNA was mixed with protein in water. For the second case, the average current was 73.62×10^{-9} A, standard deviation 28.75×10^{-9} A (data entry 23, Fig. 6.14). Examples of I-V measurements are shown in Figures 6.18 and 6.19 respectively.

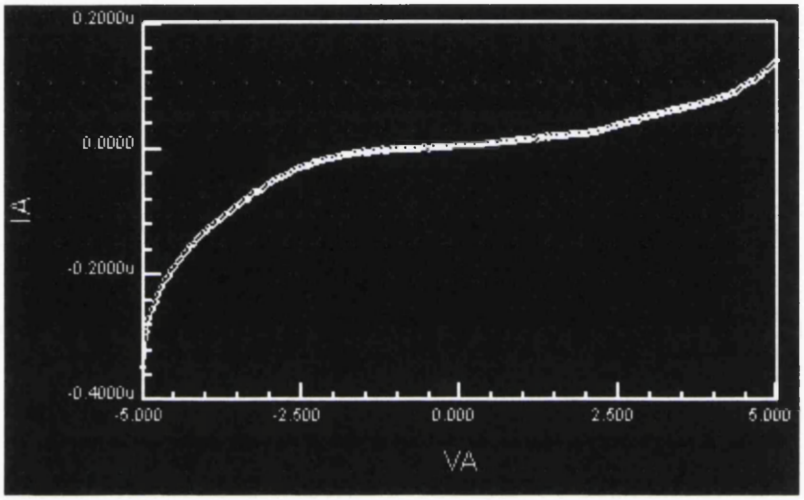

Figure 6.18. An example of a data recording for DNA prepared with protein in buffer. Large currents were measured.

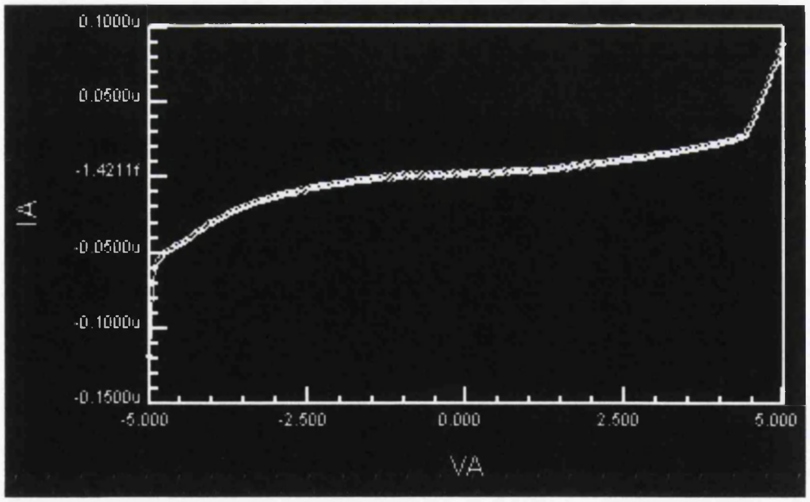

Figure 6.19. A second example of a data recording for DNA prepared with protein in buffer. Again, large currents were measured.

From Fig. 6.18 and 6.19, the presence of buffer appears to improve current readings when compared to DNA with protein mixed in water (fig 6.16 and 6.17).

Results presented up to this point have provided the core data necessary for determining the effect of protein on DNA's conductivity. Next, a comparison is made in terms of the currents recorded for each sample composition.

6.4.3 Comparison of I-V Measurements

Current values recorded at +5 V and +2 V are listed in Results Tables A-C, Figure 6.20. These tables are useful for accurate comparisons to be made across various sample compositions and for conclusions to be drawn about the effect of protein on DNA's conductivity. Data is presented in terms of average current, standard deviation and maximum and minimum current for each sample composition. Results are quoted at voltage +5 V (Table A, Fig. 6.20), at voltage +2 V (Table B, Fig. 6.20) and in order of increasing current (lowest to highest) at +5 V (Table C, Fig. 6.20).

Table A
At +5 V

Sample Composition	*Average Current (A) at +5 V*	*Standard Deviation (A)*	*Number of Readings*	*Minimum Current (A)*	*Maximum Current (A)*
Bare Electrodes	0.42×10^{-9}	0.20×10^{-9}	7	1.00×10^{-10}	6.60×10^{-10}
Water	0.35×10^{-9}	0.22×10^{-9}	5	1.20×10^{-10}	6.80×10^{-10}
DNA (50ng/μ), concentrated	45.03×10^{-9}	3.37×10^{-9}	7	3.99×10^{-8}	4.85×10^{-8}
DNA (15ng/μ), dilute_1	3.36×10^{-9}	0.35×10^{-9}	5	-1.4×10^{-10}	7.4×10^{-10}
DNA (20ng/μ), dilute_1	0.44×10^{-9}	0.40×10^{-9}	5	-1.20×10^{-10}	7.60×10^{-10}
DNA (20ng/μ), dilute_2	3.61×10^{-9}	1.17×10^{-9}	5	1.88×10^{-9}	4.58×10^{-9}
DNA (20ng/μ), dilute_3	1.64×10^{-9}	0.38×10^{-9}	5	1.04×10^{-9}	2.08×10^{-9}
Protein in water	0.67×10^{-9}	0.41×10^{-9}	4	2.60×10^{-10}	1.12×10^{-9}
Protein in buffer	168.91×10^{-9}	1.63×10^{-9}	5	1.55×10^{-7}	1.956×10^{-7}
DNA (20ng/μl) with Protein mixed in water_1	0.55×10^{-9}	0.21×10^{-9}	2	4.00×10^{-10}	7.00×10^{-10}
DNA (20ng/μl) with Protein mixed in water_2	71.75×10^{-9}	11.59×10^{-9}	5	6.29×10^{-8}	9.15×10^{-8}
DNA (20ng/μl) with Protein mixed in buffer_1	115.36×10^{-9}	17.25×10^{-9}	5	9.44×10^{-8}	1.38×10^{-7}
DNA (20ng/μl) with Protein mixed in buffer_2	73.62×10^{-9}	28.75×10^{-9}	5	4.33×10^{-8}	1.16×10^{-7}

Figure 6.20A. Table of results to show current measurements at +5 V.

Table B
At +2 V

Sample Composition	*Average Current (A) at +2 V*	*Standard Deviation (A)*	*Number of Readings*	*Minimum Current (A)*	*Maximum Current (A)*
Bare Electrodes	0.07×10^{-9}	0.17×10^{-9}	7	-3.80×10^{-10}	8.0×10^{-11}
Water	0.14×10^{-9}	0.15×10^{-9}	5	0	3.80×10^{-10}
DNA (50ng/µl), concentrated	0.11×10^{-9}	3.36×10^{-9}	7	7.22×10^{-9}	1.59×10^{-8}
DNA (15ng/µl), dilute_1	0.20×10^{-9}	0.38×10^{-9}	5	-3.80×10^{-10}	6.60×10^{-10}
DNA (20ng/µl), dilute_1	0.40×10^{-9}	0.28×10^{-9}	5	8.00×10^{-10}	6.00×10^{-10}
DNA (20ng/µl), dilute_2	0.09×10^{-9}	0.64×10^{-9}	5	-5.20×10^{-10}	8.80×10^{-10}
DNA (20ng/µl), dilute_3	0.22×10^{-9}	0.39×10^{-9}	5	-2.80×10^{-10}	6.60×10^{-10}
Protein in water	0.54×10^{-9}	0.40×10^{-9}	4	-2.00×10^{-11}	8.40×10^{-10}
Protein in buffer	6.58×10^{-9}	1.10×10^{-9}	5	5.50×10^{-9}	8.40×10^{-9}
DNA (20ng/µl) with Protein mixed in water_1	0.29×10^{-9}	0.14×10^{-9}	2	2.80×10^{-10}	3.00×10^{-10}
DNA (20ng/µl) with Protein mixed in water_2	0.03×10^{-9}	0.17×10^{-9}	5	2.40×10^{-10}	2.20×10^{-10}
DNA (20ng/µl) with Protein mixed in buffer_1	0.26×10^{-9}	3.75×10^{-9}	5	2.21×10^{-8}	3.11×10^{-8}
DNA (20ng/µl) with Protein mixed in buffer_2	7.17×10^{-9}	2.52×10^{-9}	5	4.52×10^{-9}	1.13×10^{-8}

Figure 6.20B. Table of results to show current measurements at +2 V.

Table C

Order of Current at +5V (lowest to highest)	***Sample Composition***	***Average Current (A) at +5 V***	***Average Current (A) at +2 V***	***Number of Readings***
0	**Water**	0.35×10^{-9}	0.13×10^{-9}	5
1	**DNA (20ng/µl), dilute_1**	0.44×10^{-9}	0.40×10^{-9}	5
2	**DNA (20ng/µl) with Protein mixed in water_1**	0.55×10^{-9}	0.29×10^{-9}	2
3	**Protein in water**	0.67×10^{-9}	0.54×10^{-9}	4
4	**DNA (20ng/µl), dilute_3**	1.64×10^{-9}	0.22×10^{-9}	5
5	**DNA (15ng/µl), dilute_1**	3.36×10^{-9}	0.20×10^{-9}	5
6	**DNA (20ng/µl), dilute_2**	3.61×10^{-9}	0.09×10^{-9}	5
7	**DNA (50ng/µl), concentrated**	45.03×10^{-9}	0.11×10^{-9}	7
8	**DNA (20ng/µl) with Protein mixed in water_2**	71.75×10^{-9}	0.03×10^{-9}	5
9	**DNA (20ng/µl) with Protein mixed in buffer_2**	73.62×10^{-9}	7.17×10^{-9}	5
10	**DNA (20ng/µl) with Protein mixed in buffer_1**	115.36×10^{-9}	0.26×10^{-9}	5
11	**Protein in buffer**	168.91×10^{-9}	6.58×10^{-9}	5

Figure 6.20C. Table of results to show sample depositions in order of increasing current at +5 V.

From the data presented in Tables A-C (Fig. 6.20) and the log plot (Fig. 6.10) it is clear that biological molecules do give rise to measurable currents. The average currents at +5 V are better for observing differences between samples compared to those recorded at +2 V (Tables A, B in Fig. 20). At +2 V, the trend cannot be observed as the majority of readings are indistinguishable from the background. At +5V, proteins prepared in buffer contribute to the highest current reading (position 11, Table C, 168.91×10^{-9} A). Next highest are DNA-protein complexes mixed in buffer (position 10 and 9, $I = 115.36\times10^{-9}$ A and $I = 73.62\times10^{-9}$ A) followed by DNA-protein mixed water (position 8, $I = 71.75\times10^{-9}$ A). Current is lessened for 'concentrated' DNA (position 7, $I = 45.03\times10^{-9}$ A) followed by 'dilute' DNA (positions 6, 5, 4, $I = 3.61\times10^{-9}$ A to 1.64×10^{-9} A) and proteins diluted in water (position 3, $I = 0.67\times10^{-9}$ A). Current readings similar to the background control level were encountered for the two remaining samples (DNA with protein in water, position 2, $I = 0.55\times10^{-9}$ A and dilute DNA, position 1, $I = 0.44\times10^{-9}$ A) and it is unlikely that any molecules are bridging the gap electrode. Several observations can be made:

- Firstly, the effect of DNA concentration is apparent. Concentrated DNA (50ng/μl) gave rise to a large current peak (data entry 3, Fig. 6.10) while lesser peaks were seen for lower concentrations DNA (data entries 5, 7, 13, 15). DNA aggregation was likely to contribute to the highest current reading (*e.g.* DNA ropes/bundles) whilst individual strands were more likely to bridge the gap at lower concentrations.

- Secondly, significant current peaks were revealed for DNA mixed with protein (data entries 19, 21, 28 Fig. 6.10) and protein alone with buffer (data entry 11). When DNA was combined with protein (data entries 17, 19, 21, 23, Fig. 6.10) current readings were, on the whole, elevated compared to DNA alone (data entries 5, 7, 13, 15). This suggested that the presence of protein may in fact improve the overall conductivity of DNA.

- Thirdly, the presence of buffer appeared to improve the frequency with which elevated currents were measured for DNA mixed with protein although there was little difference between the actual current magnitudes of the elevated readings. Possibly, DNA-protein binding is occurring without the need for buffer, although buffer *was* necessary for visualisation of individual DNA-protein PUT3 complexes in Chapter 5. Again it was likely that DNA-protein networks were contributing to results rather than individual molecules.

One set of electrodes was used repeatedly to record the aforementioned I-V characteristics of DNA-related samples. Besides these, I-V measurements were performed using two additional sets with the same external circuitry. These electrodes had similar gap sizes: ~250 nm and 300 nm. Similar data trends were observed and to save time, efforts were later concentrated on one particular set of electrodes. This set was subjected to repeated I-V measurements, washing, and AFM scanning in the endeavour to identify the molecules traversing the electrode gap. For highly concentrated DNA the electrode gap was not resolved as DNA appeared to fill the gap; for lower concentrations, DNA strands were revealed in close proximity to the electrodes only after much imaging processing. The imaging process proved extremely time-consuming as the background topography of the SiO_2 obscured observations of DNA and also prevented the identification of protein molecules. Nevertheless, there are several outcomes from the work performed so far and these are discussed below.

6.5 Discussion

The effect of proteins bound to DNA was studied in this project and from the data gained, currents did appear elevated for samples containing DNA and protein compared to DNA alone. Note that elevated current were also observed for protein in buffer without DNA. It was shown in Chapter 5 that protein PUT3p appeared to have an affinity for gold substrates. Similar findings have been reported by others where whole proteins containing cysteine residues or disulphide bridges were chemisorbed directly to Au surfaces[2]. PUT3p contains a Zn_2Cys_6 binuclear cluster that binds to DNA in dimer form at the correct base sequence by wrapping around the DNA in one and one-half turns. It is possible that this protein, having an affinity for gold electrodes, was anchoring DNA at the gold electrodes during their I-V measurement. Furthermore, an 'intimate' contact between the DNA and the metal electrode may be formed which might account for the improved current readings. Less likely is the possibility that DNA is aiding this process by orientating the cysteine-containing zinc clusters towards the gold electrodes as the DNA itself attempts to adsorb to the substrate in the most energetically favourable way. Zinc ions are necessary for DNA-protein binding and may be supplied from the buffer. The buffer may improve current readings by interacting with the DNA strands: Zn^{2+} ions are already known to induce strand kinking and if the interactions are strong enough effects such as 'doping' may occur giving rise to metallic-DNA (M-DNA)[9,10]. Lee *et al.* have recently (in 2006) prepared M-DNA via the specific introduction of Zn^{2+} ions to successfully give rise to metallic behaviour[11]. 'Doping' of protein with these ions is another possibility and one which may explain the increased current readings for protein in buffer compared to protein in water.

It was notoriously difficult to distinguish DNA from the rough SiO_2 background during AFM analysis and contrast adjustment was needed to mask the relatively large electrodes and to reveal the strands against the uneven SiO_2 surface. An in-depth, high-resolution imaging study had already been performed in Chapter 5 and although a number of images were captured of DNA in the vicinity of the electrodes in this chapter, high resolution AFM imaging of the electrode gap would ideally aid support explanations of results measurements if alternatives to SiO_2 could be found.

6.6 References

---

[1] Willett, R.L., Baldwin, K.W., West, K.W., Pfeiffer, L.N. (2005) Differential adhesion of amino acids to inorganic surfaces. PNAS 102 (22), 7817-7822.

[2] Prisco, U., Leung, C., Xirouchaki, C., Jones, C.H., Heath, J.K and Palmer, R.E. (2005) Residue-specific immobilisation of protein molecules by size-selected clusters. J. of R. Soc. Int. 1(3) 169-175.

[3] Kettle, J. Multidisciplinary Nanotechnology Centre, School of Engineering, Swansea University and Richard Perks of The School of Engineering, Cardiff University.

[4] Storm, A.J., van Noort, J., de Vries, S., Dekker, C. (1999) Insulating behaviour for DNA molecules between nanoelectrodes at the 100 nm length scale. Appl. Phys. Lett. 79 (23), 3881-3.

[5] Iqbal, S.M., Balasundaram, G., Ghosh, S., Bergstrom, D.E., and Bashir, R. (2005) Direct current electrical characterization of ds-DNA in nanogap junctions. Appl. Phys. Lett. 86, 153901-3.

[6] Asare, D, Chen, H., Heremans, J.J. and Soghomonian, V. (2003) Comparative current-voltage characteristics of nicked and repaired λ-DNA. Appl. Phys. Lett. 82(26), 4800-2.

[7] Jo, Y. S., Lee, Y. and Roh, Y. (2003) Current-voltage characteristics of λ- and poly-DNA. Mat. Sci & Eng. C 23, 841-846.

[8] Kleine, H., Wilke, R., Pelargus, C., Rott, K., Pulher, A., Reiss, G., Ros, R. and Anselmetti, D. (2004) Absence of intrinsic electric conductivity in single dsDNA molecules. J. Biotechnol. 112, 91-95.

[9] Aich, P., Labiuk, S.L., Tari, L. W., Delbaere, L.J.T., Roesler, W.J., Falk, K. J., Steer, R.P. and Lee, J.S. (1999) M-DNA: A Complex Between Divalent Metal Ions and DNA which Behaves as a Molecular Wire. J. Mol. Biol. 294, 477-485.

---

[10] Richter, J. (2003) Metallization of DNA. Physica E 16(2), 157-173.

[11] Lee, J.M., Ahn, S.K., Kim, K.S., Lee, Y., Roh, Y. (2006) Comparison of electrical properties of M- and λ-DNA attached on the Au metal electrodes with nanogap. Thin Solid Films (*in press*).

CHAPTER 7

Conclusions

In the work of this thesis, the feasibility of utilising DNA and protein complexes in future nano-devices was investigated. These particular biomolecules were chosen for their small size (*e.g.* the diameter of DNA is 2 nm) and their inherent self-assembling properties. Thus, these biomolecules could possibly be used as nano-device components and help to overcome the problems associated with the fabrication of smaller electronic devices. As quoted by Wong *et al.*[1] in 2005: "*fabricating and interconnecting sub-nanometre devices at the giga scale is totally beyond our imagination at the present time*". Furthermore, techniques commonly used in molecular biology (*e.g.* PCR and enzyme reactions) give added control over biomolecules' properties, such as the length of DNA fragments and their level of purity. Such levels of control are extremely advantageous if biomolecules are to be fully integrated into electronic devices in future.

During this work, the benefits of frequency-modulated AFM for high-resolution imaging of biological macromolecules have become apparent. Whereas the crystallization of samples is required for X-ray crystallography, it is not required for AFM; protein size is limited for NMR but even large proteins can be imaged with AFM; and unlike cryo-EM where samples are frozen, for AFM, there is a choice of imaging environment (*e.g.* air, liquid or UHV).

Firstly, the high-resolution capabilities of NC-AFM were demonstrated as images of DNA deposited on mica were captured. The helix nature of the molecule was resolved and pitch measurements (~3 nm) were in good agreement with others' values gained using different techniques: high-resolution STM of DNA on copper[2] gave internal structure periodicity of 2.6-3.7 nm and NC-AFM of DNA on silicon[3] gave a pitch value of ~7 nm. Images of DNA on atomically flat gold were captured using NC-AFM without sample or surface chemical treatments. The results reinforced the non-invasive nature of NC-AFM compared with other modes (*i.e.* lateral forces are minimised). For both contact- and tapping-mode AFM experiments involving gold, either the surface is chemically treated or chemically groups are added to DNA fragments to promote binding between molecules and surface. If these preparation steps are not optimised, lateral displacement of molecules can occur as a result of strong, repulsive tip-sample forces. Detail of structure was revealed with NC-AFM that was not accessible with other SPM systems (*i.e.* helix, coiling and kinking of strands). Besides studies on DNA, results have shown the immense potential of NC-AFM for high-resolution imaging of protein. Detailed images of nucleosomes were captured with line profiles indicating peaks of 3-4 nm corresponding to DNA wrapped twice around the nucleosome core. Again, NC-AFM provided higher resolution without the need for low temperatures or chemical fixation. NC-AFM was used to study the DNA-binding protein PUT3p and to the author's knowledge, this was the first time it had been visualised using scanning probe microscopy (SPM). NC-AFM allowed preliminary data to be captured for the PUT3p protein using a new, very high-spring constant cantilever. This technique could possibly be applied in future works to examine to lesser well-known biomolecules, for example those which cannot be crystallised, to gain some structural insight and to complement techniques such as NMR.

Secondly, besides the interest in biomolecular structure, PUT3p was designed to act as an anchoring group between the metal electrode and DNA molecule. Current-voltage (I-V) measurements were performed with the overall aim of investigating the effect of protein on the conductivity of DNA. Analyses of results showed that when concentrated DNA (50 ng/μl) was deposited across electrodes, at +5V significant currents were measured (I ~ 45 nA); for dilute DNA (15-20 ng/μl), current readings were reduced (I = 0.4-3.6 nA). As dilute DNA was mixed with protein, current values were mostly elevated (I = 71-115 nA). The presence of buffer was necessary for DNA-protein binding to occur and it seemed to improve current readings possibly via the incorporation of zinc ions into biomolecules (*i.e.* doping). Factors that may contribute to the results obtained are discussed below.

- **Humidity:** It is feasible that as biomolecules span the electrode gap, they provide a 'pathway' between electrodes. Hydration layers on these samples may contribute to elevated current readings via the continuous exchange of protons (H^+) between adjacent water strands. This effect was postulated by Y. –S. Jo *et* *al.*[4] in 2003 after the conductivity of DNA molecules deposited on gold electrodes was drastically lowered by transferring samples from humid environments into vacuum. The phenomenon was reported as reversible and independent of the charged carrier (electron or hole) through DNA strands, thus implying the dominant conduction mechanism of DNA was via ionic conduction and proton transfer.

In 2006, J.M. Lee *et al.*[5] performed similar experiments using metallic-DNA (M-DNA). DNA fragments with zinc ions already incorporated, 3-kbp in length (~1 μm) concentration 150 ng/μl were deposited on gold electrodes fabricated on SiO_2. The electrode gap size was 150 nm with electrode height 50 nm; a semiconductor parameter analyzer HP4145 used for I-V measurements and an SEM image of bare electrodes recorded. The results showed that after the stable formation of M-DNA conductivity decreased rapidly as the measurement pressure moved into high vacuum range. Again, variations in conductivity readings were attributed to the decrease in humidity due to the vacuum environment (*i.e.* removal of hydration layers otherwise present when performing experiments in air). In terms of actual values, for M-DNA at +3 V, the current measured was ~0.1 mA (100 nA) at atmospheric pressure. In vacuum (10^{-1} Torr) the current was reduced to approximately 0.35 nA. For M-DNA, the linear I-V relationship was maintained across the change from air to vacuum but the slope of the relationship depended on the level of humidity.

Similar humidity effects were also reported in 2004 by Kleine *et al.*[6] following experiments performed in a controlled argon environment (*i.e.* not a vacuum). Here, the conductivity of long DNA molecules was reported to be strongly dependent on the humidity level with capillary condensation of water on DNA molecules giving rise to additional ionic currents.

- **Oxygen level:** In contrast to the findings outlined above, data published in 2002 by H.-Y. Lee *et al.*[7] showed that the conductance of DNA was reportedly controlled by several orders of magnitude using *oxygen-hole doping*. In other words, adsorbed oxygen gas molecules act as electron acceptors which create holes and these act as the dominant charge carriers in DNA. Experiments were performed using DNA of length 0.5-2.9 μm and concentration 25-250 ng/μl deposited on gold electrodes fabricated on SiO_2. The electrode gaps were 100-200 nm and an SEM image showed DNA films formed rod-like structures over the electrodes. For DNA films in air +4 V, the current measured was ~4 nA (R= 1GΩ). In oxygen ambient, conductance increased by a factor of 100. From the control experiments performed, it was reported that the influence of humidity on conduction of DNA films was negligibly small compared to that of oxygen doping. Therefore, it is important to note that experiments performed a vacuum environment will not only change the level of humidity but also the amount of oxygen present.

To compare with the work of this thesis, small (μl) amounts of material at relatively low concentrations (~20 ng/μl) were deposited the electrode gap and left to dry. After 15 minutes, no droplets were visible and samples were thoroughly dried using a nitrogen gas gun (>5 minutes). Note, the same procedure was used for NC-AFM experiments in UHV before entry to load-lock. To minimise the effects of exposure to varying oxygen levels, samples were transferred to the apparatus needed for I-V characterisation in air. Excessive drying of samples was not performed as there is a possibility that residual water molecules play an important role in the internal conformation of DNA strands by interacting with proteins and other DNA strands (*e.g.* some protein-DNA contacts are mediated by water molecules). Excessive drying may alter the internal conformation of biomolecules and weaken bonds between DNA and protein or between the substrate and surface. Hence, for consistency, I-V characteristics were measured in air and at atmospheric pressure throughout.

- **Doping of DNA and PUT3 protein with Zn^{2+} ions:** Zinc ions have been linked to kinking and doping of DNA strands. In 1997, Han *et al.*[5] reported the kinking of DNA in the presence of 1 mM Zn^{2+} and images clearly showed the pronounced effect of zinc ions as circular DNA became square-shaped. Effects as low as 10 μM Zn^{2+} may also persist. Since the protein was supplied in a buffer containing 10 μM $ZnCl_2$ and the binding-buffer used for the work of this thesis contained 10 μM $ZnSO_4$ it is possible that zinc ions present for protein-DNA binding are actually causing strand kinking/coiling by interacting with the DNA. Coiling was noticeable along DNA strands imaged with NC-AFM in the presence of buffer compared to those samples prepared without buffer.

The I-V relationship for metallic-DNA (M-DNA) has been reported as linear[5] and for it to be created divalent zinc ions (Zn^{2+}) are inserted in every base pair of DNA, thereby releasing one proton per base-pair per metal ion. Current literature published by J.M Lee *et al.*[5] suggests that pH control is important when M-DNA is being formed and DNA molecules should be treated at pH values greater than 8.0 if the M-DNA is to display the characteristic linear I-V relationship. The importance of pH control is reiterated by Aich *et al.*[8]

In the work of this thesis, the binding-buffer contained the component HEPES-KOH at pH 8.0. Therefore, it is possible that zinc ions are being inserted into the DNA structure during the 30 minute period allowed for binding although additional research would support this explanation.

- **Protein anchoring groups:** PUT3 proteins were designed to act as anchoring groups between the DNA and gold surface for improvement of the electrical contact. PUT3 contains cysteine residues and data published by Prisco *et al.*[9] in 2005 showed that proteins containing these residues were reported to chemisorb to Au surfaces. The two proteins used were *green fluorescent protein* (GFP) and *human oncostatin.* (OSM). GFP contained two cysteine residues and was displaced by the scanning tip. OSM contained five cysteine residues and was immobilised at the surface. In comparison, a PUT3 protein contains a Zn_2Cys_6 cluster and binds to DNA in dimer form. Dimers then interact and wrap around DNA by one and one-half turns. As DNA strands were manipulated to contain binding sites at both ends, the number of cysteine groups attached to the DNA molecule was increased. DNA strands mixed with PUT3 were successfully visualised on flat gold using TM-AFM whilst DNA strands alone could not be imaged. These results imply than proteins are aiding the anchorage of DNA to gold but it is not possible to say from these results whether the presence of these particular residues is responsible.

- **The protein-gold contact area:** The contact area between the protein and gold is large (~70 nm) compared to the DNA-Au contact (~2 nm). While the presence of cysteines may aid the chemisorption to gold, it is possible that the large mass of the protein may facilitate better charge transport across the metal-molecule interface due to the larger contact area.

It is clear from the above discussion that the conductivity of DNA may be influenced by several factors. Humidity, oxygen level, doping and the presence of protein may all contribute to the results obtained. One major hurdle, which is also shared with others, is to ascertain the true nature of the molecules crossing the gap. In this work, attempts were made to image the electrode gap at high-resolution but this proved impractical due the rough SiO_2 background. Large area scans were captured after sufficiently high concentrations of DNA were used to bridge the gap but it was impossible to identify how many strands were actually present. Fortunately, an in-depth imaging study of DNA and DNA-protein complexes had been performed earlier so that DNA-protein binding was known to take place with high probability and that binding to gold substrates was possible. This novel approach for studying self-assembling DNA-protein complexes suggests there are potential benefits if efforts were continued in future work.

Future Work

This is the first time that (i) PUT3-DNA binding proteins have been visualised with DNA using NC-AFM, and (ii) electrical measurements have been performed on them. Several courses of action could be implemented to build on the results obtained. Firstly, alternative substrates to SiO_2 could be found so that high-resolution imaging of electrodes with DNA deposited could be performed. Substrates should have low surface roughness, be electrically insulating and stable for gold evaporations. This would then encourage simultaneous observation of molecules and their I-V characterisation so that I-V results could be ascribed to the exact nature of the molecules crossing the gap.

Secondly, the I-V characteristics of the DNA-PUT3 protein complexes could be studied in a different environment. Experiments could be performed in a ultra-high vacuum or oxygen-rich environment to ascertain the true effects of humidity and oxygen-hole doping on this particular DNA-protein complex.

Thirdly, a comparative study could be performed using a similar DNA-binding protein (*e.g.* GAL4). GAL4 contains a DNA-binding domain that is similar to PUT3 and binds to a slightly different sequence of DNA[10]. It would be useful to perform high-resolution imaging and I-V characterisation on this protein so that a size comparison could be made with PUT3 to see if (i) large protein clusters are formed, (ii) whether non-specific binding occurs with the DNA, and (iii) if any differences in I-V measurements arise.

Fourthly, it is not yet known how to eliminate random interactions of biomolecules or how to control the efficiency of proteins binding with gold in an electrode set-up. Therefore, it would be advantageous to experiment with different methods of sample preparation. In this work, a buffer was required to visualise PUT3 protein associated with DNA and problems were encountered during AFM imaging: samples containing charged buffer particles and/or protein caused undesirable tip-sample interference. Additional sample preparation steps such as rinsing and/or allowing proteins to equilibrate at the surface before adding DNA could possibly prevent tip-sample interference and also prevent large protein aggregates from forming. In the work of Prisco *et al.*[9] proteins were prevented from aggregating by immobilisation on gold clusters which were deposited on highly oriented pyrolytic graphite using a cluster-beam source. The gold clusters encouraged isolated proteins to be immobilised whilst protein monolayers which can form on large gold surfaces were avoided.

The presence of cysteine residues in a protein does not guarantee that they are available to chemisorb with the surface. For instance, they may be buried deep inside the protein. For this reason it may be useful to create a mutant version of the protein that contains additional cysteine residues that are more accessible to chemisorb to the gold. Proteins could then chemisorb to gold whilst simultaneously binding to DNA. Protein purification tags already use this concept[10]. The *his-tag* is composed of six histidine residues; the DNA encoding these residues are cloned into the target gene such that the protein produced contains six consecutive histidine residues somewhere in its polypeptide sequence; the tag can be located at the extreme amino- or extreme carboxyl-terminal (*i.e.* where it is unlikely to impair the function of the protein). His-tags have high affinity for certain metal ions (*e.g.* nickel) and can then bind with them non-covalently. Proteins modified with tags can then be captured in *immobilized metal ion affinity chromatography* (IMAC)[10].

Finally, the alignment of individual DNA molecules on electrodes could be investigated in future work. Results published in 2005 by Lin *et al.* [11] demonstrated that chemically unmodified DNA molecules could be positioned using AC electric fields. As a non-uniform AC field is applied, a circular flow of liquid is generated that stretches DNA molecules across a gold surface or between gold electrodes. The process is described as controllable so that single molecules can be positioned across electrodes. Similar methods could be investigated to align DNA strands functionalised with PUT3 protein across electrodes in future works.

References

---

[1] Wong, H. and Iwai H. (2005) The road to miniaturization. Physics World (Sept) 40-44.

[2] Tanaka, H., Hama, C., Kanno, T., and Kawai, T. (1999) High-resolution scanning tunneling microscopy imaging of DNA molecules on Cu(111) surfaces. Surf. Sci. 432, L611–L616.

[3] Arai, T., Tomitori, M., Saito, M. and Tamiya, E. (2002) DNA molecules sticking on a vicinal Si(111) surface observed by noncontact atomic force microscopy. App. Surf. Sci. 188, 474-480.

[4] Jo, Y. –S., Lee, Y. and Roh, Y. (2003) Current-voltage characteristics of λ- and poly-DNA. Mat. Sci. and Eng. C 23, 841-846.

[5] Lee, J.M., Ahn, S.K., Kim, K.S., Lee, Y. and Roh, Y. (2006) Comparison of electrical properties of M and λ-DNA attached on the Au metal electrodes with nanogap. Thin Solid Films (in press).

[6] Kleine, H., Wilke, R., Pelargus, Ch., Rott, K., Pulher, A., Reiss, G., Ros, R. and Anselmetti, D. (2004) Absence of intrinsic electric conductivity in single dsDNA molecules. 112, 91-95.

[7] Lee, H.-Y, Tanaka, H., Otsuka, Y., Yoo, K.-H, Lee, J.-O. and Kawai, T. (2002) Control of electrical conduction in DNA using oxygen hole doping. Appl. Phys. Lett. 80 (9)1670-1672.

[8] Aich, P., Labiuk, S.L., Tari, L. W., Delbaere, L.J.T., Roesler, W.J., Falk, K. J., Steer, R.P. and Lee, J.S. (1999) M-DNA: A Complex Between Divalent Metal Ions and DNA which Behaves as a Molecular Wire. J. Mol. Biol. 294, 477-485.

[9] Prisco, U., Leung, C., Xirouchaki, C., Jones, C.H., Heath, J.K and Palmer, R.E. (2005) Residue-specific immobilisation of protein molecules by size-selected clusters. J. of R. Soc. Int. 1(3) 169-175.

[10] Analysis of genes and genomes. (2004) R. J. Reece. Wiley Publishers.

[11] Lin, H.-Y., Tsai, L.-C., Chi, P.-Y. and Chen, C.-D. (2005) Positioning of extended individual molecules on electrodes by non-uniform AC electric fields.